

SANDIA REPORT

SAND88-2473C • UC-13

Unlimited Release

Printed December 1988

AD-A214 581

59th

Shock and Vibration Symposium

Volume IV

Prepared by

Sandia National Laboratories

Albuquerque, New Mexico 87185 and Livermore, California 94550

for the United States Department of Energy

under Contract DE-AC04-76DP00789

Proceedings of a conference sponsored by
The Department of Defense and
The Department of Energy
held in Albuquerque, New Mexico
October 18-20, 1988

DTIC
ELECTRONIC
NOV 07 1989
S 8 D

DISTRIBUTION STATEMENT A

Approved for public release;
Distribution Unlimited

89 11 06 035

SAND88-2473C
Unlimited Release

Distribution
Category UC-13

59th Shock and Vibration Symposium

Volume IV

**Proceedings of a conference sponsored by
The Department of Defense and
The Department of Energy
held in Albuquerque, New Mexico
October 18-20, 1988**



Sandia National Laboratories

SYMPOSIUM MANAGEMENT

Host Representatives:

Mr. David O. Smallwood - Sandia National Laboratories
Mr. Rodney G. Galloway - Air Force Weapons Laboratory

Contract Management:

Mr. David O. Smallwood - Sandia National Laboratories

SYMPOSIUM MANAGER

Henry C. Pusey
4193 Sudley Road
Haymarket, VA 22069

REGISTRATION MANAGER

Sallie C. Pusey

59TH SYMPOSIUM PROGRAM COMMITTEE

Lt. C M Carlin, USN
Defense Nuclear Agency
SPWE
6801 Telegraph Road
Alexandria, VA 22310

Rodney G. Galloway
U.S. Air Force
AFWL/NTES
Kirtland AFB, NM 87117-6008

J. Scott Milne
NASA/GSFC
M/C 302
Greenbelt, MD 20771

Jerome Pearson
U.S. Air Force
AFWAL/FIBG
Wright-Patterson AFB, OH 45433

John A. Robinson
U.S. Army Combat Systems Test Act.
STECS-EN-EV
Aberdeen Proving Ground, MD 21005

Lt. Col. Al Schenker
Defense Nuclear Agency
TTST
Kirtland AFB, NM 87115-5000

David O. Smallwood
Sandia National Laboratories
Division 7544
P.O. Box 5800
Albuquerque, NM 87185

Rudolph H. Volin
Naval Research Laboratory
Code 6337
Washington, DC 20375

COMPILATION OF PROCEEDINGS

Henry C. Pusey
Sallie C. Pusey

PRODUCTION OF PROCEEDINGS

Vibration Institute

Accession For	
NTIS GRA&I	<input checked="checked" type="checkbox"/>
DTIC TAB	<input type="checkbox"/>
Unannounced	<input type="checkbox"/>
Justification	
By	
Distribution/	
Availability Codes	
Dist	Avail and/or Special
A-1	

TABLE OF CONTENTS

Papers Appearing in Volume IV

FEATURED PAPER	1
Validation Testing of Nuclear Survivable Systems	
E. Sevin	3
VIBROACOUSTIC PAYLOAD ENVIRONMENT PREDICTION SYSTEM (VAPEPS)	19
Using the VAPEPS Program to Support the TOPEX Spacecraft Design Effort	
T. D. Scharton and D. L. Kern	21
Statistical Energy Analysis Modeling of Nonstructural Mass on Lightweight Equipment Panels	
Using the VAPEPS Program	
M. L. Slay	37
Stress Estimation and Statistical Energy Analysis of the Magellan Spacecraft Solar Array Using the VAPEPS Program	
G. A. Badilla and V. C. Thomas	49
DYNAMIC MEASUREMENT	61
An Automated Vibration Transducer Calibration System Using Advanced FFT Techniques	
T. Licht and E. Schonthal	63
DYNAMIC CRITERIA	71
Avionics Environmental Reliability	
A. A. Bhungalia and G. Kurylowich	73
MODAL APPLICATIONS	95
Structural Verification Using Modal Frequency Testing: A Nondestructive Evaluation	
T. F. Drouillard, D. N. Iklé and D. K. Gustaveson	97
Model Validation Using Substructure Modal-Testing, Applied to a Large and Very Flexible Wind Turbine	
T. G. Carne, J. P. Lauffer, A. J. Gomez and T. D. Ashwill	119
Analytical Estimation of Earth Penetrator Structural Response and Comparison with Laboratory Shock and Modal Test Data	
R. J. Kipp and V. I. Bateman	133
SHOCK	145
Vertical Launching System Modal Techniques for Shadow Side Effect during Ship Shock Trials	
T. S. Arora and M. E. Pearce	147
Dynamic Response of Pipe Subjected to High Impact Loads	
R. J. Scavuzzo and P. C. Lam	183

DYNAMIC ANALYSIS	195
Bubble Jet Calculations Using the DYSMAS/E Finite Difference Code S. A. Wilkerson and H. Schittke	197
Convergence of Finite Element Frequency Analysis for a Thin Walled Cylinder J. M. Santiago and H. L. Wisniewski	209
Integral Method for Free Edge Plates with Stiffeners B. P. Wang and S. Nomura	241
VIBRATION CONTROL	251
Shock Isolation Using an Active Magnetostrictive Element R. S. Reed	253
Prediction of Modal Characteristics and Harmonic Response of Viscoelastically Damped Structures H. T. Zhou, J. Der Hagopian, G. Ferraris and M. Lalanne	265
New Structure Design Criteria Offer Improved Pointing and Lower Weight L. P. Davis and J. F. Wilson	273
AIRBLAST	
The Effects of Heavy Tungsten Casings on the Airblast Characteristics of a Cylindrical Charge K. A. Marchand and L. M. Vargas	283

Papers Appearing in Volume I

FEATURED PAPERS

Development Testing at Sandia

D. M. Olson

The Quest for $\omega = \sqrt{K/M}$: Notes on the Development of Vibration Analysis

N. F. Rieger

Statistical Energy Analysis: An Overview of Its Development and Engineering Applications

J. E. Manning

DATA BASES

DOE/DOD Environmental Data Bank

C. A. Davidson

GREEDI - The Computerization of the DOE/DOD Environmental Data Bank

C. R. Adams and E. M. Kephart

A Shock and Vibration Database for Military Equipment

R. A. McKinnon

Vibration Data Base for Aircraft and Its Application

M. T. Orth

VIRBROACOUSTIC PAYLOAD ENVIRONMENT PREDICTION SYSTEM (VAPEPS)

The Importance of Non-Resonant and Inplane Vibration Transmission in Statistical Energy Analysis

R. E. Powell and J. E. Manning

Vibroacoustic Response Using the Finite Element Method and Statistical Energy Analysis

F. L. Gloyne

Study of Helium Effect on Spacecraft Random Vibration with VAPEPS Program

Y. A. Lee

Validation of LACE Spacecraft Vibroacoustic Prediction Model

A. A. Salzberg

Comparison of VAPEPS Predictions with IUS Vibroacoustic Data

C. J. Beck

DYNAMIC MEASUREMENT

Prediction and Measurement of the Acoustic Environment of the Airborne Seeker Evaluation
Test System

L. L. Shaw and K. R. Wentz

PVDF Applications in Shock and Vibration Measurements and Control

L. M. Lee, J. P. Berhault, J. P. Chambard and F. Bauer

Inertial Reference and Tracking System for the Measurement of Blast Induced Displacements

P. H. Frisch and R. Pearson

Mechanical Shock Sensors (A Feasibility Study)

D. Frommer, M. Gross and D. Heller

Built-In Mechanical Filter in a Shock Accelerometer

A. S. Chu

Mechanical Impedance Measurements Using Oblique Excitation

L. J. Nucci and J. R. Reed

DYNAMIC CRITERIA

- Simulating Vehicle Dynamics: The Importance of a Valid Forcing Function
G. L. Ferguson
- Underlying Assumptions in the Development of Tracked Vehicle Vibration Schedules
W. H. Connon, III
- Structural Response and Cosmetic Cracking in Residences from Surface Mine Blasting
D. E. Siskind and M. S. Stagg

MODAL APPLICATIONS

- Using Modal Testing to Identify Dynamic Changes in Battle Damaged F-16 Wings
A. B. Pacia
- Modal Identification Using Solid Rocket Motor Static Firing Data – A Case Without Knowing the External Excitation
C. F. Chang and D. Mason
- Nonlinear Systems in Vibration
E. G. Endebrock and N. F. Hunter, Jr.

Papers Appearing in Volume II

DYNAMIC TESTING

- STAR 63F Q-3 Qualification Vibration Test
B. G. Johnson
- Correlation Between Vibration and Computer Operator Response Onboard a UH-1H Helicopter
G. O. White
- Shaker Shock Testing Using Nonstationary Random Transients
T. L. Paez and T. J. Baca
- High Velocity Impact Testing of an Accident Resistant Container Using a Large Centrifuge
J. R. Garcia and R. L. Weatherbee

SHOCK

- Pyrotechnic Shock Data Reduction Procedures and Problems
H. D. Riead
- Time Domain Analysis of Pyrotechnic Shock Utilizing Resonant Beam Test Apparatus
F. Ehorn
- Equipment Limitations in Pyrotechnic Shock Testing
J. W. Rehard and J. Czajkowski
- Shock Response Spectrum Anomalies Which Occur Due to Imperfections in the Data
R. G. Bell and N. T. Davie
- A Fourier Transform for Almost Any Number of Data Points With Reasonable Run-Times
J. B. Cheek
- Shock Spectrum for Classes of Excitations
W. D. Pilkey and M. Rosenstein
- A Technical Procedure for the Optimum Shock Hardening of Aircraft Support Equipment
W. R. Lauderdale, D. Croce and B. C. McNaught
- Boundary Integral Technique for Explosion Bubble Collapse Analysis
S. A. Wilkerson

DYNAMIC ANALYSIS

- Modeling of Vibration Transmission in a Damped Beam Structure Using Statistical Energy Analysis
S. S. Sattinger
- Solar Array Deployment Nonlinear Dynamics Analysis
R. A. Mills
- Experimental Observations of Low and Zero Gravity Nonlinear Fluid-Spacecraft Dynamics
L. D. Peterson
- Vibratory System Dynamic Analysis Using a Graphics Based Self-Formulating Program
J. Alanoly and S. Sankar
- Design of Upper Atmosphere Research Satellite (UARS) Using Transient Loads Analysis
S. Mittal, M. Garnek and C. Stahle
- Analytical Approaches for Determining Effective Weights Used in the Method of Weighted Accelerations for Force Measurements
T. J. Kreitingner, M. Wang and H. L. Schreyer
- Shock Response of a Mine Hunter Due to Sea Ground Mine Explosions - Numerical Simulations
W. E. Pfrang, H. Lütje and J. Freercks
- An Analysis of Newmark Beta Integration for Structural Dynamics
R. L. Bort
- Response of Nonlinear Continuous Systems Subjected to Transient Loads: An Analytical Approach
S. C. Sinha
- Influence of Elastic Coating on the Plastic Deformation of a Beam in Water Subjected to a Shock Wave
A. L. Stiehl and R. C. Haberman
- Approximate Method for Predicting the Permanent Set in a Circular Plate in Water Subjected to a Shock Wave
A. L. Stiehl and R. C. Haberman
- Computer Code SPIDS; Shock Propagation in Ducting System
R. H. Fashbaugh and T. C. Knight

Papers Appearing in Volume III

MACHINERY VIBRATION

- Some Recent Contributions to Mechanical Signature Analysis
R. L. Eshleman
- High Frequency Vibration Analysis for Rotating Equipment and Piping Systems
R. M. Jones
- Diagnosing Problems in Modern 2-Pole Induction Motors
R. M. Kolodziej
- Absolute Ball Bearing Wear Measurements from SSME Turbopump Dynamic Signals
M. J. Hine
- Spectral Normalizing
B. Lundgaard and S. B. Stocking
- Kinematics of a Flexible Length Redundant Robotic Arm
A. Choudhury and J. Genin

VIBRATION CONTROL

Optimization of a Five-Parameter Nonlinear Shock Mount

N. A. Roy and V. H. Neubert

Active Damping Design of Flexible Structures Based on Non Collocated Sensor-Actuator Velocity Feedback

Q. Zhang, S. Shelley, X. N. Lou and R. J. Allemang

Relating Material Properties and Wave Effects in Vibration Isolators

M. C. Reid, S. O. Oyadiji and G. R. Tomlinson

Compensation for Actuator Dynamic Effects Using Model Following Adaptive Control

Q. Zhang, S. Shelley, D. L. Brown and G. L. Slater

Damping and Vibration Control of Unidirectional Composite Beams Using Add-on Viscoelastic Materials

C. T. Sun, B. V. Sankar and V. S. Rao

Creep and Load-Deflection Characteristics of Rubber Element for Vibration Control Devices

E. I. Rivin and B. S. Lee

AIRBLAST

Envelope Models for Finding the Response of Structures in Blast Waves

S. J. C. Dyne and J. K. Hammon

Dynamic Nonlinear Frame Analysis for Blast and Shock

L. M. Bryant, S. D. Campbell and D. Nebuda

Behavior of a Reinforced Concrete Blast Shelter in an Overload Environment

T. R. Slawson and J. L. Davis

Shelter Response in a Simulated 8-KT Nuclear Blast Environment

R. L. Holmes, S. C. Woodson and T. R. Slawson

Blast Induced Liquefaction Field Explosive Tests

H. A. Hassen and W. A. Charlie

GUNS AND PROJECTILES

Wave Coupling and Resonance in Gun Tubes

T. E. Simkin

The Blast Field Produced by a Cannon Having a Perforated Muzzle Brake

G.C. Carofano

Lagrangian Modelling of Blunt Projectile Impacts Against Thick Plates

J. C. Schulz and O. E. R. Heimdahl

Analytical Estimate of Artillery Projectile Balloting Load Based Upon Correlation with Strain Gage Test Data

A. Meyer

FEATURED PAPER

VALIDATION TESTING OF NUCLEAR SURVIVABLE SYSTEMS

Eugene Sevin
Assistant Deputy Under Secretary
Offensive and Space Systems
Office of the Secretary of Defense
The Pentagon, Room 3E129
Washington, DC 20301-3090

Department of Defense policy regarding nuclear hardness validation testing is reviewed. Examples of major programs involving extensive full-size testing are presented in the context of nuclear simulation methods. Implications of using simulation testing to both define nuclear load environments and demonstrate hardening are discussed.

INTRODUCTION

When Henry Pusey called me last July to ask if I'd be interested in speaking at the Symposium, I was wrapping up a panel assignment on test capabilities for validating nuclear hardened space systems, so I felt that I had appropriate material in hand. Our panel had been asked to determine the test capabilities needed to assure, with confidence, the survivability of future nuclear hardened space systems; we were to report on the type of test facilities needed, to identify shortfalls in testing knowledge, technology and capabilities, and to suggest how best to fix any deficiencies. Moreover, just that day I had received a complimentary letter from a distinguished four-star general on our panel's report, so I was feeling fairly mellow.

Well, immediately upon accepting Henry's offer, an equally distinguished four-star general sent word to the effect that our report obviously was the work of the nuclear effects mafia, and that the last thing he needed was three-sigma nuclear effects zealots telling him how to test his satellites. I tried to reach Henry but, cleverly, he had left town. On reflection, however, it seemed that the reasons why our study had provoked such diametrically opposed reactions offered a clue to the proper focus for my discussion today.

It should come as no particular surprise to this audience that our panel focused on the "validation process" itself and the role of testing; in particular, the need for large-scale system-level testing and the fidelity requirements for nuclear simulations were the central issues. We thought the burden of proof lay with the developer; that for critical war-fighting systems, confidence in having met the nuclear hardness design objectives required some amount of meaningful system-level testing. These considerations apply not only to hardened space systems, but quite generally to all types of hardened systems.

I will touch briefly on the Department of Defense's hardness validation policy, review three examples of hardness validation programs, and offer some observations on nuclear effects simulation testing.

DoD HARDNESS VALIDATION POLICY

DoD has an established policy that nuclear survivability and hardness features shall be included in the design, acquisition, and operation of major and nonmajor systems that must perform critical missions in nuclear conflicts. This includes conventional forces, nonstrategic nuclear forces, strategic communications, and intelligence systems. Top-level guidance is contained in DoD Directive 4245.5, "Acquisition of Nuclear Survivable Systems", first issued in 1983 and updated this past July; Army and Air Force regulations predate the DoD directive by five years. DoD policy mandates that a Nuclear Survivability Program dealing with survivability requirements, criteria, validation procedures, and life-cycle maintenance be developed and maintained.

"...(criteria) should be quantified and be amenable to validation by reasonable Test and Evaluation procedures..."

"...(the developer) shall ensure that the nuclear survivability is validated at the appropriate points in development and operational test programs with critical survivability features validated as early as practical. Nuclear hardness shall be validated in realistic system configurations, with a cost-effective combination of underground nuclear testing, simulation testing and analysis. During T&E, the assumptions concerning system performance used in deriving the criteria shall be validated."

(The term "validation" appears five times in this single paragraph.) Finally, the adequacy of the nuclear survivability program is to be judged at critical milestones in the acquisition process, a point to which I will return later.

Each Service has its own regulations for implementing this top-level DoD policy, and there is substantial and growing literature on nuclear survivability from a program management perspective. The Defense Nuclear Agency and the Army's Harry Diamond Laboratories both publish very useful bulletins; DNA's July 1988 Bulletin, Nuclear Survivability, has as its theme, "How to Develop a Nuclear Hardening Program".

With such material to draw upon, and the emphasis given to "validation," one might think it relatively straightforward to set forth a coherent view of the hardness validation process—what it is and how one goes about it. But, of course, this is not the case. People who write policy tend not to be burdened with the consequences. While there are numerous individual examples of hardness validation programs—and, I will cite several—we are a long way from a comprehensive view of the subject. Perhaps this is because of the wide variety of nuclear survivable systems (spacecraft, aircraft, missiles, a great variety of surface and subsurface systems), the broad range of damaging nuclear effects and associated failure modes, and the substantial variation in hardness criteria—from limiting collateral damage to withstanding direct attacks. Still, it is unacceptable that a serious policy have neither standards to measure conformance nor means to enforce its provisions.

Hardness is a characteristic of the system; confidence that the prescribed hardness has been obtained is a judgment based on knowledge of the system and the threat environment. Therefore, hardness validation is a process of information gathering about system behavior under Nuclear Weapons Effects (NWE) environmental stresses. In exploring this process, it is useful to contrast hardness validation with hardness assessment; the terms sound similar, but they are two very different concepts.

Hardness assessment is a process for estimating the system's actual hardness level; the level of the NWE "stress" at which the system reaches its failure threshold. Hardness validation, in contrast, is not (or need not be) about system failure; rather, it is a process for verifying that the system meets its hardness requirement, that it will not fail at or below a specified level of stress. A comprehensive hardness assessment would provide the probability of system failure over the full range of design variables and NWE stresses. Thus, if available, it would suffice as well for hardness validation since the failure probability at criteria stress levels is a direct statement of hardness validation. However, an accurate determination of system failure probability is a very complicated undertaking, and usually beyond the scope of a design effort.

THREE CASE STUDIES

Let me discuss briefly three nuclear survivable systems in which large-scale testing played an important role in hardness validation. All are ground-based systems for which the primary hardening design challenge was to mitigate blast, shock and thermal effects—the Army's hardened tactical shelter (HATS), and two Air Force weapon systems—the hardened mobile launcher (HML) for the Small ICBM, and the superhard silo concept for basing the Peacekeeper missile. At present, the HATS development is complete but no systems have yet been produced; continuation of the HML full-scale development awaits a decision by the next Administration, the superhard silo development was nearly completed when abandoned in favor of basing Peacekeeper on railroad cars. This dismal status report might suggest that nuclear survivable systems face an easier time with threats from overpressure than from fiscal or political pressures; nonetheless, these examples remain interesting case studies from a hardness validation perspective. The wide range of nuclear environment requirements illustrates different simulation challenges, as depicted in Figure 1.

Hardened Tactical Shelter

The Army has a well-conceived approach to developing nuclear survivable equipment. Compliance with specified nuclear survivability criteria is mandated from the beginning of hardware development, through validation tests of equipment during both development and production. The intent is to ensure that battlefield equipment is at least as survivable as the combat personnel required to operate it. Nuclear design environments were developed for the HATS family of hardened shelters (Figure 2) over a range of plausible battlefield scenarios. While the level of hardening is modest by some standards, it substantially exceeds the capability of unhardened shelters.

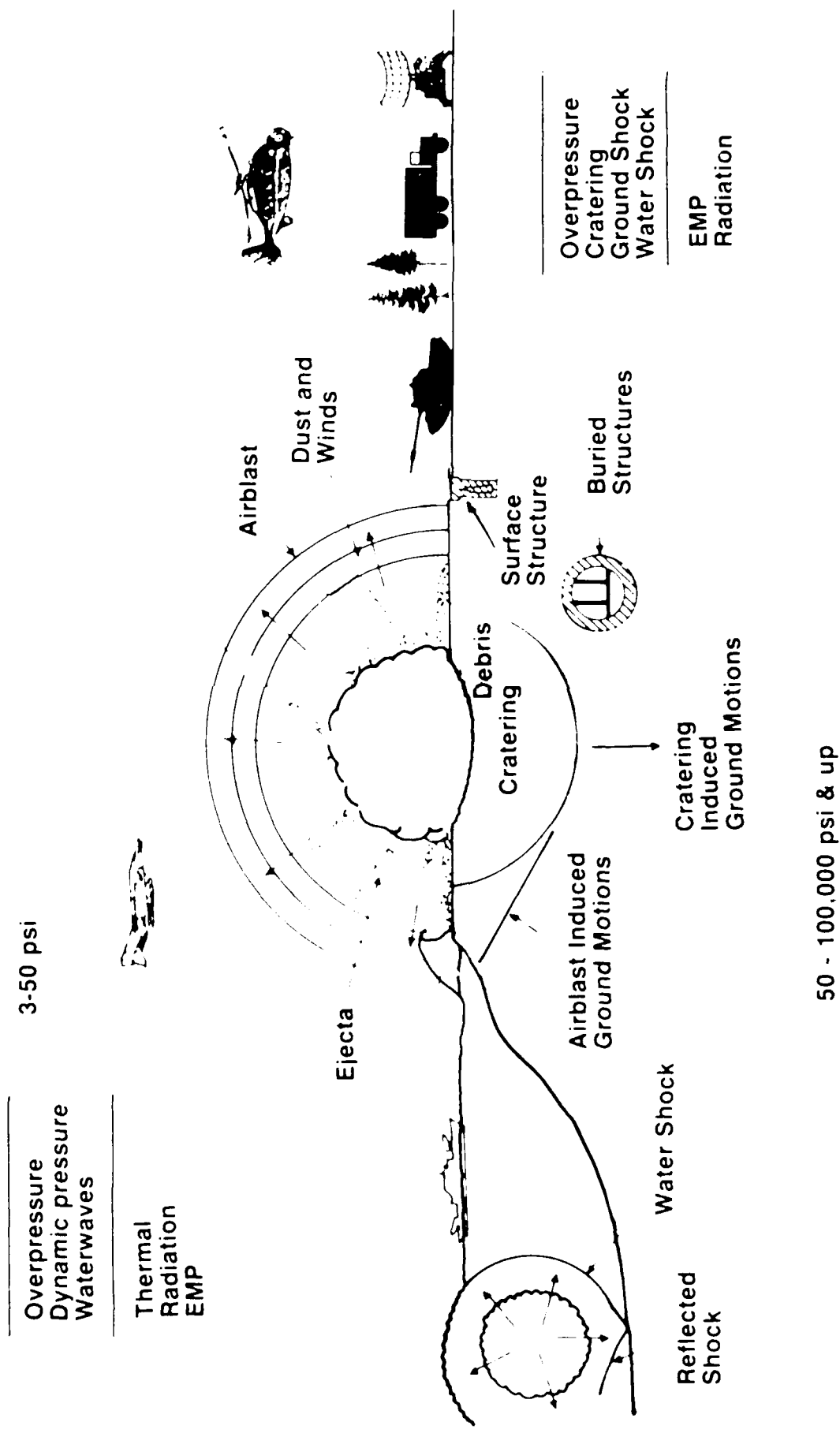
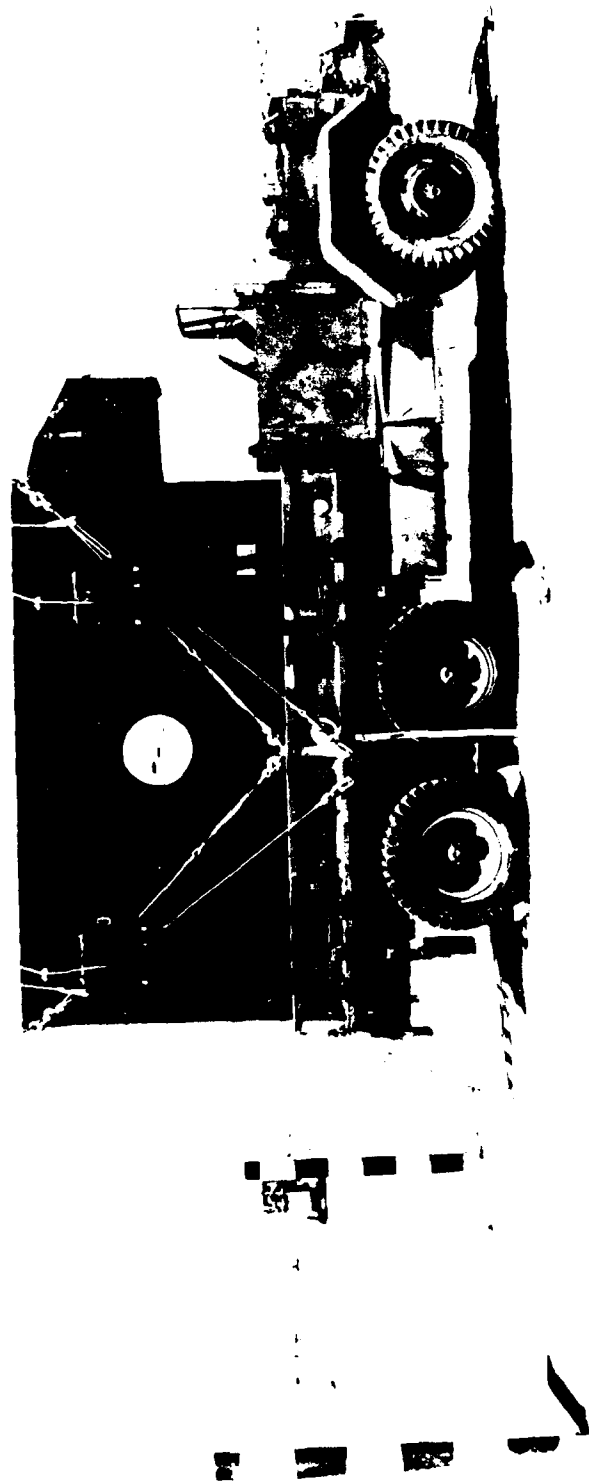


Fig. 1 Blast and Shock Environment



A SPECIALIZED ADVANCED TACTICAL ENCLOSURE
DEVELOPED BY HDL TO INCREASE SURVIVABILITY
OF ARMY C³I SYSTEMS IN NUCLEAR ENVIRONMENTS.

Figure 2 Hardened Tactical Shelter

The HATS is designed to be fully compatible with existing vehicles and shelters. The shelter panels are of sandwich construction with kevlar skin (for ballistic projectile and thermal protection), paper honeycomb core and internal fiberglass stiffeners; an inside aluminum facing provides EMI shield. The shelter is attached to the vehicle with tie-downs and outriggers are used to prevent rotation and translation.

Low pressure nuclear airblast waveforms can be simulated in shock tubes and by hard high explosive (HE) charges. Both techniques are capable of producing exponentially decaying pressure-time waveforms over a range of nuclear yields with high fidelity. Neither device provides significant thermal output, however. While thermal effects can be simulated by various means, combined thermal-blast loading is usually accomplished with HE under field conditions. The need for improved understanding of combined airblast and thermal loading of HATS led to the initiation of large-scale testing early in the development program. About a dozen full-scale tests of HATS were conducted in shock tubes and HE field tests during its development.

Hardened Mobile Launcher

Survivability of the Small ICBM (SICBM) is achieved through mobility, not hardness. The idea of hardening the mobile launcher was born of desire to greatly reduce the land area needed for its deployment. At hardnesses of several tens of psi overpressure, the system can survive a massive barrage attack when deployed randomly on selected military bases. From a hardening perspective, the HATS experience suggests this to be an extremely ambitious undertaking, and it was fully appreciated from the outset that a more radical vehicle design was required. Figure 3 shows the HML design selected for full-scale engineering development in December 1986; not much resemblance to HATS. The HML has outstanding on-road and off-road mobility characteristics, fully meets all of its operational performance specifications, protects the missile, and provides for unattended launch (and costs a fortune).

The HML is hardened structurally against direct airblast effects. Sliding and overturning forces are reduced by aerodynamic streamlining, and resistance to sliding is achieved by exploiting the stabilizing effects of the vertical airblast forces. Clearly, the design requires a detailed understanding of the airblast flow field, including time phasing of the vertical and horizontal airblast components. It is known from atmospheric testing experience that nuclear airblast waveforms and flow fields along the ground are dependent on the height of burst and thermal properties of the ground surface. The radiating fireball heats the ground ahead of the advancing shock wave, causing it to propagate more rapidly along the surface than in the (cooler) air above. This leads to radical changes in the airblast shock structure and increases the aerodynamic drag forces on above-ground objects. There is direct evidence that these so-called thermally precursed flow effects can have a dramatic influence on the response of "drag type" targets such as vehicles.

A novel method was developed to simulate thermally precursed flow in the absence of a suitable thermal source. The underlying premise is that the flow develops as consequence of the air shock propagating along the ground ahead of the main shock. While this is triggered in a nuclear burst by fireball preheating, it

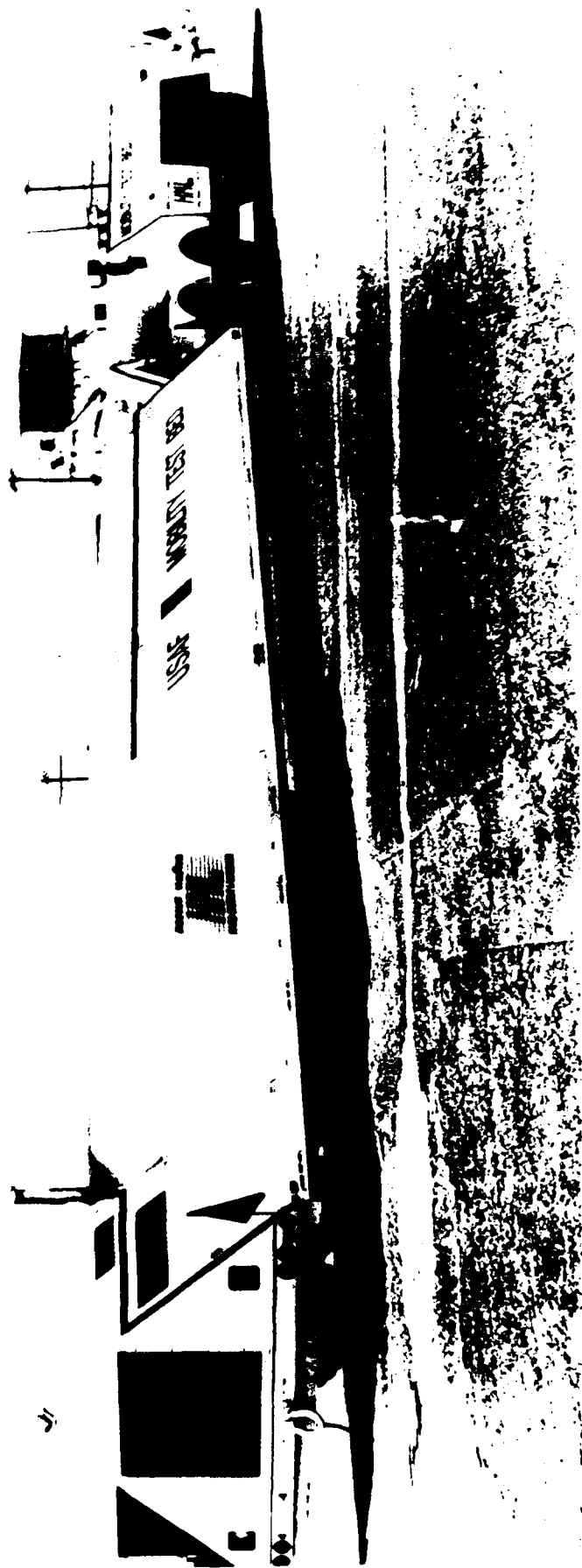


Figure 3 Small ICBM Hardened Mobile Launcher

is not primarily a thermally dominated effect. Thus, it should be possible to replicate the flow in a layered, two-gas system of appropriately different sound speeds. This was accomplished at large scale under field conditions by confining a layer of helium gas along the ground under a thin mylar membrane. The speed of propagation is controlled by the concentration of helium which, in turn, is related to nuclear yield and height of burst through theoretically-based estimates of surface air temperature.

This approach was investigated by means of extensive numerical simulations and comparison with atmospheric nuclear data, tested in laboratory shock tubes at miniature scale, and demonstrated successfully in HE field tests. Figure 4 shows the test setup in the Minor Scale event, an 8-kiloton nuclear equivalent HE source. A 0.5 mil-thick mylar membrane measuring 400 ft wide x 900 ft long x 2 ft high contained helium at 95 percent concentration. Figure 5 is a photograph of the shock structure obtained in this field test. Comparison with data from atmospheric nuclear tests, appropriately scaled, was remarkably good.

On this basis, the test technique was qualified for hardness validation testing. One-fifth geometric scale models of two competing (pre-FSD) HML designs were tested in the Minor Scale event. This was considered to be a successful proof-of-principle test for the HML design concept. Full-scale development of the SICBM and HML has been terminated by this Administration for reasons of affordability, though it is possible that the next Administration will elect to continue development. The Test and Evaluation plan did not call for further large-scale response testing of the HML.

Superhard Silos

Concerns regarding the vulnerability of our silo-based Minuteman ICBM force stem from potential improvements in the accuracy of Soviet missiles. Superhardening—a 25- to 50-fold increase in hardness over our current silos—is a competitive strategy to thwart the effectiveness of Soviet ICBM modernization plans. To achieve the accuracy required against superhard targets would challenge them on major new technology investment, undesirable force structure (especially in view of arms control limits), operational difficulties, and substantial targeting uncertainties.

The feasibility of superhardening rests on a far-reaching reassessment of nuclear weapon effects close-in to the burst; more specifically, high overpressure waveforms, cratering and crater-produced ground motions. An earlier view of these effects suggested that at overpressure loadings of interest, the compressive strength of silo materials would be exceeded and ground motions would far surpass the capabilities of known shock isolation methods; indeed, the conventional view held that current silos were about at the practical limit of hardness.

The atmospheric nuclear data base extends only up to about 1000 psi and predictions of higher overpressures are based on numerical solutions. Recent, more detailed, calculations indicated that overpressure waveforms were substantially more impulsive, decaying to half peak value in a fraction of the time originally thought. Experimental confirmation was obtained by detonating a small nuclear device on the floor of a large, air-filled, underground chamber to simulate an atmospheric surface burst for a short period of time. These results had profound implications for structural hardening once it was recognized that early-time pressure impulse, rather than peak pressure, was the more appropriate



Figure 4 Minor Scale Test Bed

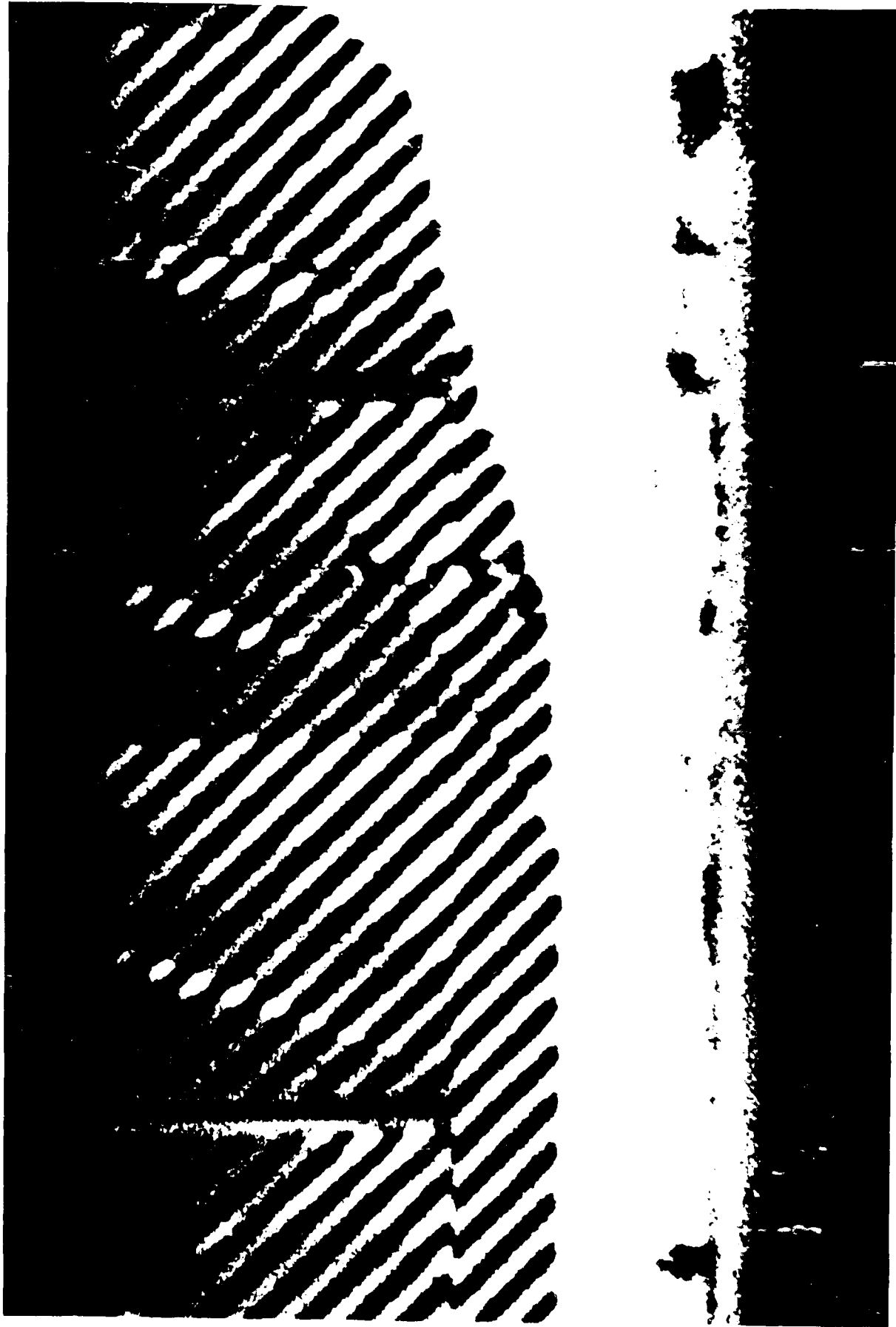


Figure 5 Simulated Thermally Precursed Airblast

damage indicator. With this stimulus, research in superhard construction soon led to radically improved designs.

Cratering and crater-related ground motions also pose significant design challenges for superhardening. Theoretical predictions of crater formation did not agree with the empirical results based on high explosive data and a few large-yield nuclear tests in the Pacific. Theory consistently indicated very much smaller craters and ground motions, as well as a strong dependency on geology.

The underground nuclear "atmospheric" chamber test mentioned earlier not only provided critical airblast data but also demonstrated a new capability for cratering experimentation. The chamber remained intact post-test and measurements of the crater were in good agreement with analytical predictions. A subsequent chamber experiment was conducted with a different near-surface geology and extensive ground motion measurements were obtained; these results also supported the analytical methods. Finally, a two-year geophysical exploration of selected nuclear craters at the Pacific Test Site has brought the empirical basis for yield scaling in line with theoretical expectations.

How did we approach test validation with this substantially changed view of close-in nuclear effects? The nuclear chamber test is not suitable for testing silos, and high explosives cannot achieve nuclear source region pressures. The simulation approach adopted for large-scale testing combines each of these techniques in a sequential, three-stage process. The concept is illustrated in Figure 6. The first stage is represented by the underground "atmospheric" tests, where agreement between predictions and observations of ground motions and final crater dimensions is presumed to substantiate the early-time, hydrodynamic phase of the theory. Stage 2 consists of a high-explosive simulation of the crater, close-in ground motions and airblast. Practical considerations limit this to kiloton-yield equivalence. Termed CARES (Crater and Related Effects), this simulation consists of a high-explosive subsurface charge that replicates the calculated pressure-velocity state at about the 50 kilobar stage of the evolving nuclear crater, and subsequent pressures can be obtained with HE. (At this time, the crater has grown to about five percent of its final volume in a dry geology.) A sequentially detonated surface charge is used to simulate the airblast-coupled ground shock, transitioning into a conventional HEST bed to provide the primary airblast loading on the silo structure. Finally, in Stage 3, the ground motions measured in the CARES experiment are scaled up and reproduced in a large-size HEST-DIHEST configuration to provide a test bed for prototype silo structures.

A fully instrumented CARES test replicating a 2-kiloton surface burst (one-eighth scale for a megaton) provided the experimental rationale for establishing silo ground motion design criteria and designing large-scale HEST beds for silo validation testing. Figure 7 shows the CARES test bed under construction. Subsequently, a large-scale HEST test was conducted on a large-size superhard silo (i.e., full-size for the SICBM or 5/8-size for the Peacekeeper missile) in which both airblast and direct ground motion effects were simulated. A photograph of this silo during construction is shown in Figure 8.

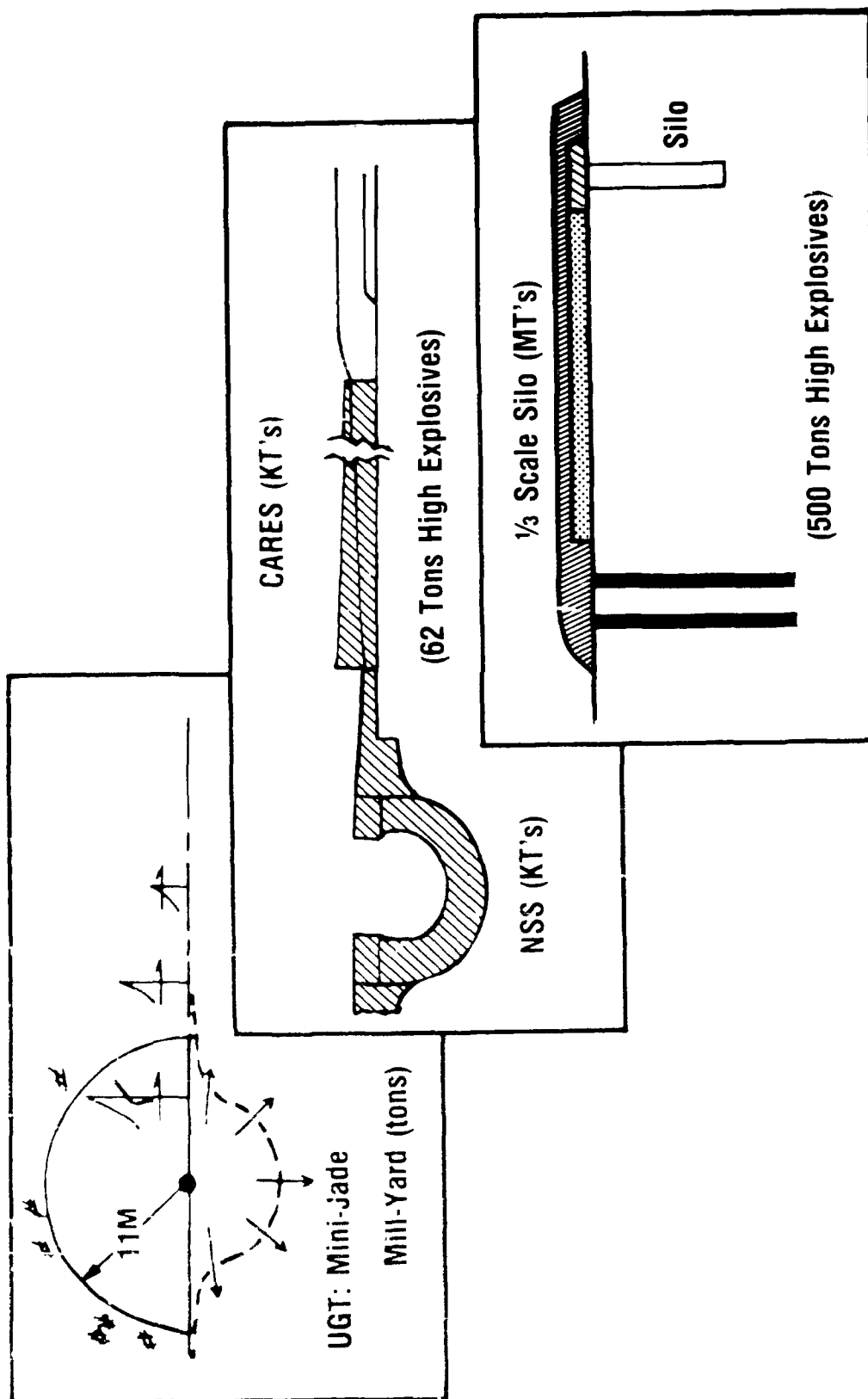


Figure 6 Silo Simulation Development

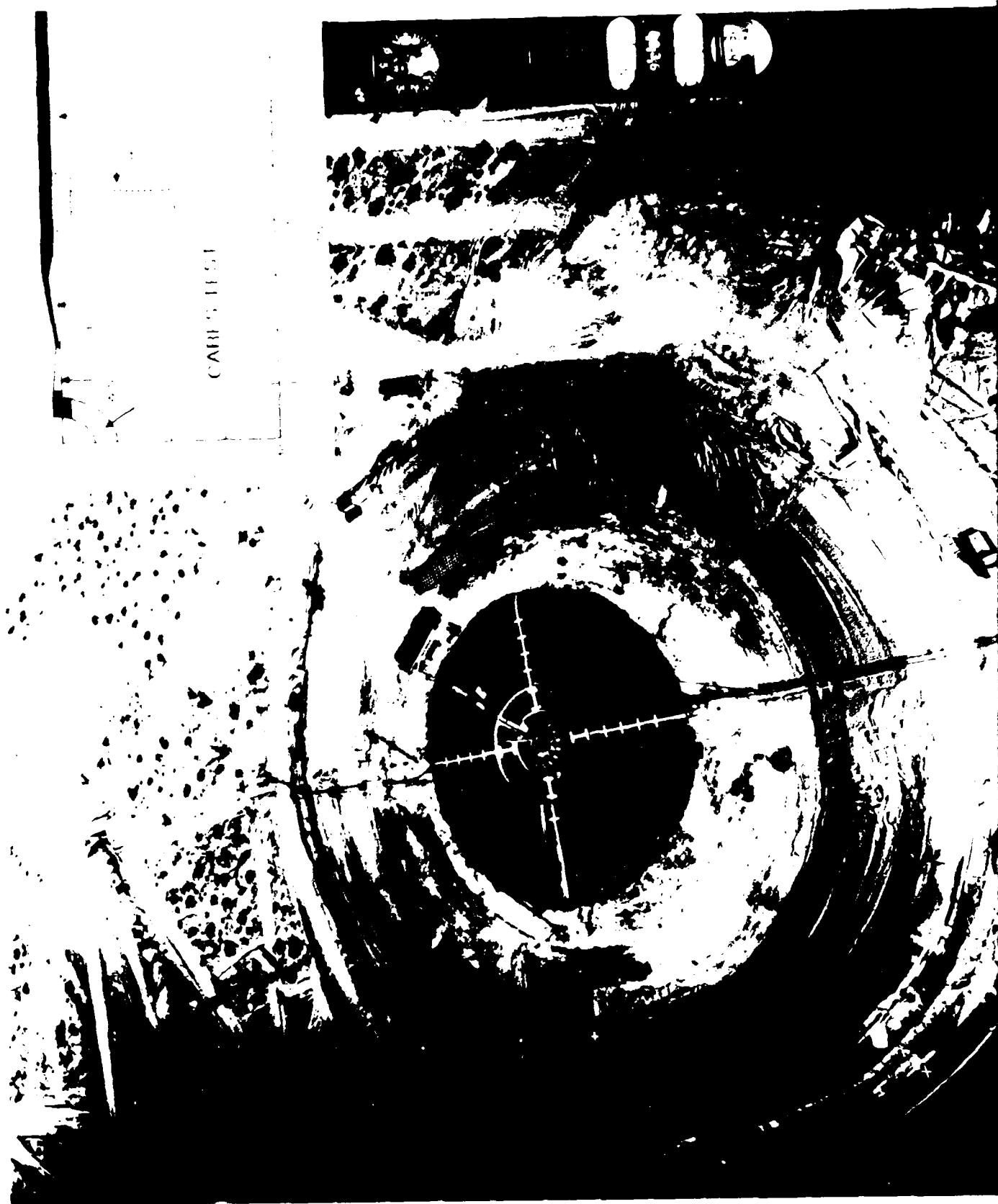


Figure 7 CARES Test Bed

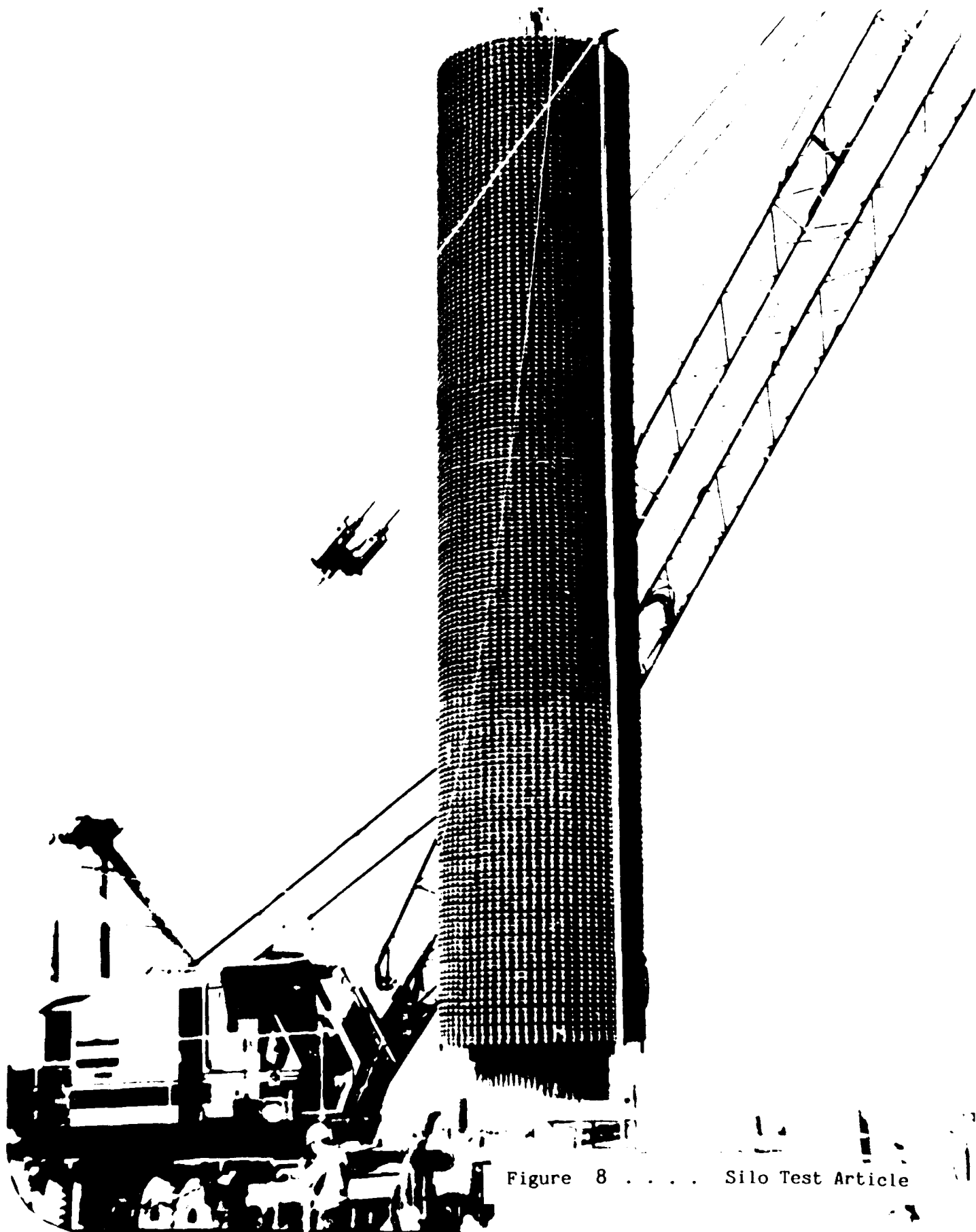


Figure 8 Silo Test Article

OBSERVATIONS

What can be learned about the hardness testing and validation process from these examples? Clearly, each program took a comprehensive approach toward meeting its nuclear hardness requirements; all could serve as role models in this regard. The need for high-fidelity nuclear simulations and testing at large scale was accepted. Indeed, the Air Force programs developed major new airblast and ground shock simulation capabilities to obtain design data and demonstrate hardness proof-of-principle. Is there any reason, then, to doubt that these systems are as survivable as advertised?

At issue principally is the relationship of the test environments to threat-level nuclear environments. The new airblast simulation technique developed for the HML is an important technology breakthrough for studying complex flow fields at large scale. It appears to replicate the essential features of thermally precursed airblast, but the nuclear data base is extremely sparse. Accepting this test technique as a valid simulation of the nuclear environment from which to determine HML design loads and, subsequently, for hardness proof-of-principle demonstration involves a certain leap of faith. The HATS was designed and tested under ideal airblast conditions. While the developers were aware of thermally precursed flow effects, these were not considered to be significant at HATS design overpressure levels. However, recent research stemming from the HML development suggests that this matter needs to be revisited.

In the superhard silo program, a new high-explosive simulation technique (CARES) was used as a surrogate nuclear cratering experiment to establish design ground shock loadings. In turn, a still larger-scale simulator was constructed to produce this environment on a prototype silo which had been to resist these loadings. We are highlighting instances in which the system developer has exercised considerable discretion in interpreting hardness design criteria. And, where one developer may be very imaginative and creative, as surely the Air Force was here, others may be considerably less so. At the same time, we must acknowledge the risk involved in using unproven test procedures. It is possible to be too creative, and we need to remind ourselves from time to time not to get out too far ahead of the state-of-the-art. This is a particularly serious matter when it comes to accepting nuclear simulations as the basis for both design and validation. I know of more than one instance in which a presumably independent test amounted to little more than a mechanical analog of the theory under investigation.

Central to the hardness validation process, it seems to me, is how the rules are made regarding nuclear simulation. A nuclear hardness program plan is a required part of the Test and Evaluation Master Plan (TEMP); the TEMP must be accepted by the Defense Acquisition Board (DAB) at the Concept Demonstration/Validation and Full-Scale Development acquisition milestones. The Assistant to the Secretary of Defense (Atomic Energy), with the help of the Defense Nuclear Agency, is obligated to advise the DAB on the adequacy of the developer's nuclear survivability plan. This strikes me as offering a particularly good opportunity to define and agree upon the rules. Among the tests to be conducted in any hardness validation program, there must be those whose significance depends on being accepted as realistic nuclear simulations—not merely high-explosive "stimulations." Such tests need to be identified in advance, their importance to the validation process made clear, and provisions established to independently "certify" the test bed design for use by the developer. Agreeing in

advance on a simulation test that can serve as a surrogate nuclear test to define design loads and determine response clearly is in the interest of the developer. The developer is relieved of the responsibility of making up the validation rules and is judged only by how well he follows them. It places others in a "put up or shut up" position regarding the scale and fidelity of tests required for validation. The Under Secretary of Defense (Acquisition), as chairman of the Defense Acquisition Board, becomes the rule-maker, and accepts the risk that the rules are later found to be inadequate. That is as it should be.

I don't think that approaching hardness validation in this manner is about to happen anytime soon. The DoD directive dealing with nuclear survivable systems installs a gatekeeper in the acquisition process to advise on the adequacy of the survivability program. The gate has yet to be slammed on a developer for inadequate validation test planning as documented in the TEMP, however deserving. It is likely that the sound of a slamming gate will be the appropriate attention getter!

**VIBROACOUSTIC PAYLOAD
ENVIRONMENT PREDICTION SYSTEM
(VAPEPS)**

USING THE VAPEPS PROGRAM TO SUPPORT THE TOPEX SPACECRAFT DESIGN EFFORT

Terry D. Scharton and Dennis L. Kern

Jet Propulsion Laboratory
California Institute of Technology
Pasadena, CA 91109

The TOPEX instrument module (IM) consists of large, lightweight honeycomb panels which are very responsive to the acoustic loads generated by the Ariane launch vehicle at liftoff. The VAPEPS (Vibroacoustic Payload Environment Prediction System) computer program was utilized to evaluate the effect of TOPEX IM configuration changes on the acoustic response at the panel/instrument interfaces. Acoustic and vibration data for a structure similar to the TOPEX IM were used to calibrate the VAPEPS modeling. TOPEX configuration variations studied were panel size, thickness, weight, and damping. An on-line method of notching random vibration tests has been designed for those TOPEX components for which it is desirable to limit the vibratory force input from the shaker.

INTRODUCTION

Usually aerospace structures are designed to withstand mission dynamic and static loads through an iterative process. Once the design is adequately defined, the structure is analyzed for response to high frequency acoustic loads. The results of this analysis are used to establish random vibration test requirements for the instruments and other hardware supported by the structure. The development of the TOPEX (The Ocean Topography Experiment) spacecraft has presented an unique opportunity to utilize acoustical analyses to help design a spacecraft structure and to develop a notched qualification test spectrum that will accommodate the utilization of vibration sensitive inherited hardware.

The TOPEX spacecraft is the key element in the TOPEX/Poseidon mission being undertaken by the U.S. National Aeronautics and Space Administration (NASA) and the French Centre National d'Etudes Spatiales (CNES) for studying the global ocean circulation from space [1]. The mission will use the techniques of satellite altimetry to make precise and accurate measurements of sea level for several years. The Jet Propulsion Laboratory (JPL) has the responsibility to manage the development of the TOPEX spacecraft system for NASA. Development of the spacecraft has been contracted to the Fairchild Space Company. The spacecraft is being designed for Ariane launch in late 1991/early 1992.

The TOPEX spacecraft will carry both NASA and CNES sensors (instruments). The TOPEX instrument module (IM) consists of large, lightweight honeycomb panels which are very responsive to the acoustic loads generated by the Ariane launch vehicle at liftoff. The sensors themselves are, for the most part, based on inherited designs/hardware which have been qualified to moderate random vibration levels. Based on programmatic considerations, it is not feasible to redesign the sensors to survive high vibration levels. The problem then was to design the IM panels to reduce their response to acoustic loading and to specify a random vibration test which did not unnecessarily overtest the sensors.

The VAPEPS (VibroAcoustic Payload Environment Prediction System) computer program was utilized to evaluate the effect of TOPEX IM configuration changes on the acoustic response at the panel/instrument interfaces [2]. Acoustic and vibration data for a structure similar to the TOPEX IM were used to calibrate the VAPEPS modeling. TOPEX configuration variations studies were panel size, thickness, weight, and damping. An online method of notching random vibration tests has been designed for those TOPEX components for which it is desirable to limit the vibratory force input from the shaker.

SPACECRAFT CONFIGURATION AND VIBROACOUSTIC ENVIRONMENT

The TOPEX spacecraft configuration is depicted in Figure 1. The Multimission Modular Spacecraft (MMS) bus consists of a frame structure supporting the bus subsystem modules. The instrument module (IM) is composed of large aluminum honeycomb core panels. The external panels are arranged to form a box. A center panel runs the length of the box, dividing the IM into two compartments. The panel face sheets are 0.025" thick aluminum and the core is 1.0" thick, with a density of 0.0018 lb/in³. The electronics boxes were grouped onto selected panels to increase the panel mass loading. Other panels were left unloaded. The electronics box arrangement of one of the external panels is shown in Figure 2. This panel carries 12 electronics boxes with a total weight of 171 lbs, for an equipment surface density loading of 0.07 lb/in². Five lengthwise heat pipes are also buried between the face sheets of this panel. The heat pipes are modeled as 1.0" by 0.2" aluminum bars.

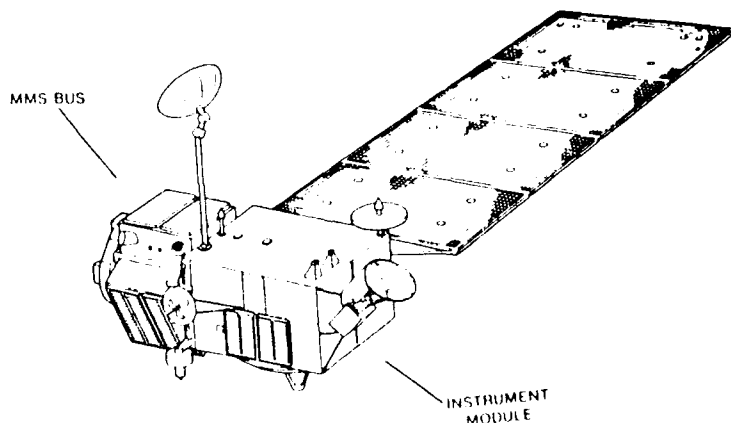


Figure 1. TOPEX Spacecraft Configuration

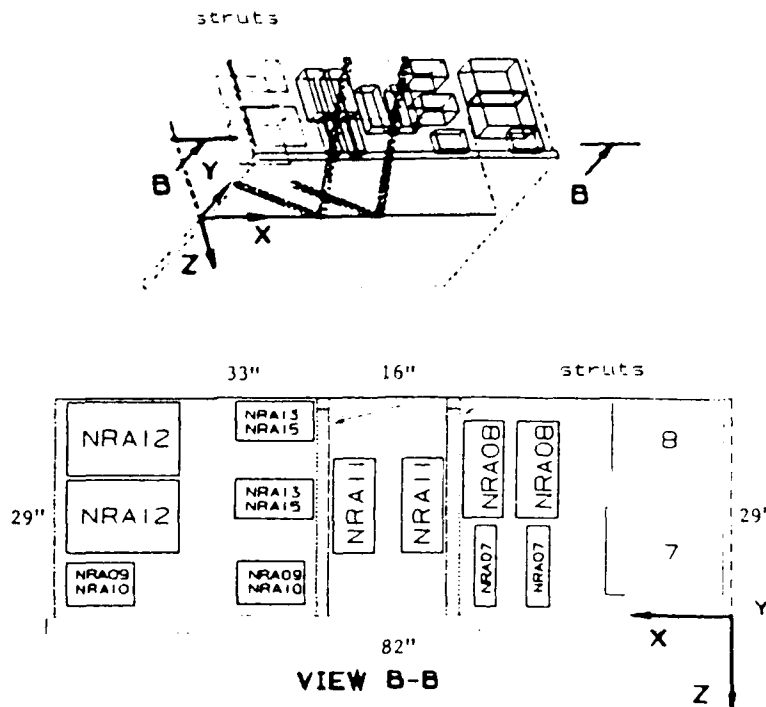


Figure 2. Honeycomb Panel of TOPEX Instrument Module

The predicted one-third octave band flight acoustic levels for the TOPEX spacecraft inside the Ariane launch vehicle shroud are shown in Figure 3. The overall sound pressure level (OASPL) is 142 dB. For comparison, the one-third octave band flight acoustic levels for STS payloads (OASPL of 138 dB) is also shown in the figure. Ariane payload acoustic levels are considerably more severe in the mid frequency range where honeycomb panels are typically most responsive to acoustic excitation (about 200 to 800 Hz). This also covers the frequency range in which instrument sensors and electronics boxes typically exhibit their most damaging dynamic structural responses.

The response of the IM panel described above to the Ariane acoustic environment was predicted employing the SEMOD routine of the VAPEPS (VibroAcoustic Payload Environment Prediction System) program. The SEMOD routine incorporates Statistical Energy Analysis (SEA) to theoretically predict structural responses to acoustic excitation. The SEA technique utilizes energy balance equations to arrive at a spatially averaged response of a structural element over a specific frequency bandwidth. Structural elements are defined by their average physical properties. The predicted spatially averaged random vibration response of the panel is shown in Figure 4. The 95th percentile panel response level, which is predicted in VAPEPS by adding an empirically derived factor to account for the spatial variation across the panel, is also shown. The panel equipment loading was treated as non-structural mass for this prediction.

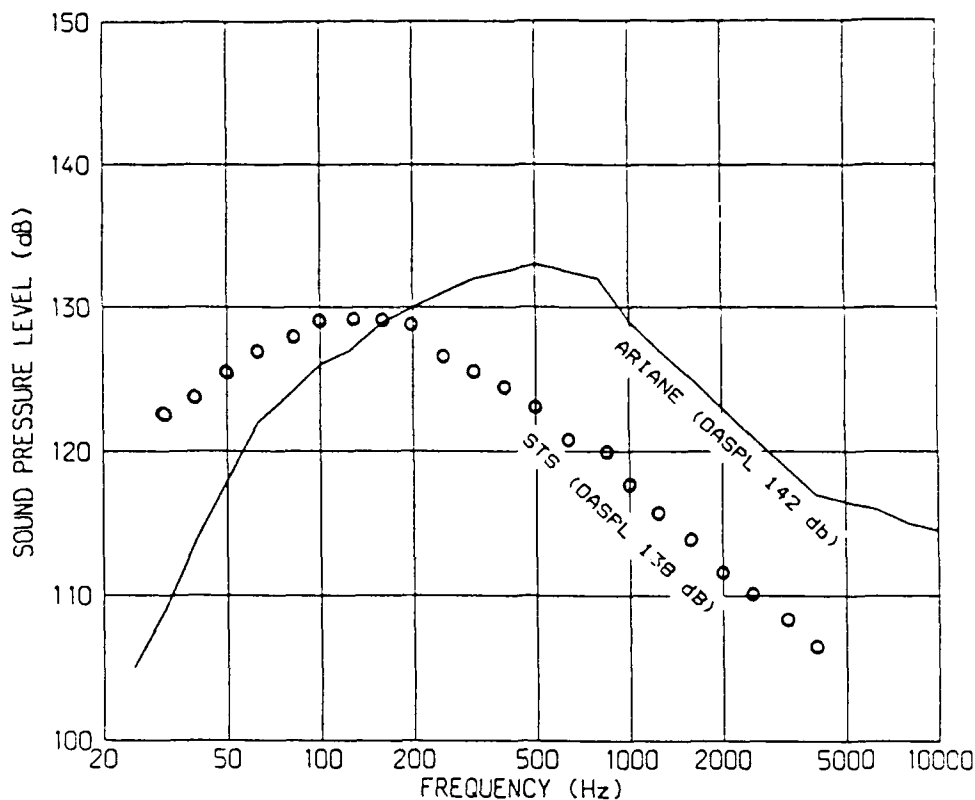


Figure 3. One-Third Octave Acoustic Flight Levels for Ariane Launch Vehicle Inside TOPEX Spacecraft Shroud

As can be seen in Figure 4, the predicted 95th percentile flight random vibration level for the panel mounted equipment peaks at a level of about $0.2 \text{ G}^2/\text{Hz}$. It is standard practice at JPL to add 4 dB to 95th percentile flight acoustic levels and to multiply 95th percentile flight random vibration spectral density levels by a factor of 2.5 for design and qualification/prototyping testing of spacecraft hardware. These random vibration levels significantly exceed the previous qualification levels of the inherited instrument designs.

The TOPEX IM design described above resulted from a reconfiguration which attempted to satisfy the following objectives, listed in order of priority: a) functional requirements, b) structural/acoustic requirements, c) thermal requirements, d) magnetic requirements, and e) accessibility requirements. The acoustic requirements were basically to reduce the random vibration levels at the instruments/panels interfaces to levels compatible with the instruments inherited designs. The following sections describe the efforts undertaken to optimize the IM design for acoustics and to develop instrument random vibration specifications compatible with their inherited designs.

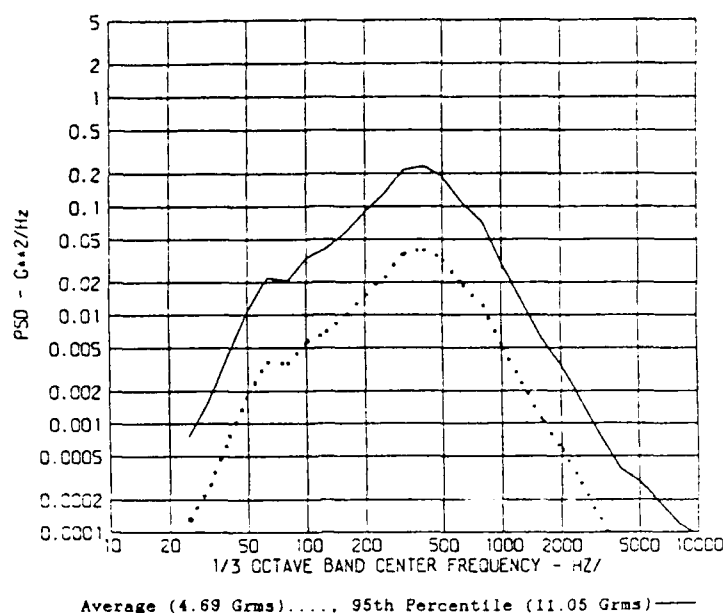


Figure 4. SEMOD Prediction of Flight Random Vibration Levels of TOPEX IM Panel

SENSITIVITY OF VIBROACOUSTIC PREDICTIONS TO DESIGN CHANGES

The VAPEPS SEMOD program was used by Fairchild Space Company (FSC) and JPL to investigate the sensitivity of the acoustic response of the TOPEX Instrument Module (IM) to the IM panel mechanical design parameters. The parameters investigated were: panel thickness, equipment mass, damping, and panel size. In addition, the benefits of constructing the IM as a closed box so that the panels were acoustically excited only on one side was recognized and incorporated into the design selected by FSC.

The sensitivity studies presented herein show the vibroacoustic effects of parameter variations relative to the design configuration selected by FSC for the lower +Y panel of the IM as illustrated in figure 2. This particular panel was chosen as representative of the IM panels. The SEMOD prediction of the 95th percentile flight random vibration for the selected combination of panel design parameters panel is shown in figure 4. This prediction for the selected design parameters is repeated as the solid reference curve in figures 5-8, which show the effects of the parameter variations.

Figure 5 shows the vibroacoustic effect of variations of the IM panel thickness of 0.5", 1.0", 2.0", and 4.0". The selected thickness value was 1.0". Also shown in figure 5 are the corresponding coincidence frequencies at which the panels are best coupled to the acoustic field. Increasing the panel thickness lowers the vibroacoustic response. This reduction results because the ratio of the squared vibration response to squared acoustic pressure is inversely related to panel thickness at any frequency and also because increasing the panel thickness reduces the coincidence frequency below the 500 Hz peak in the acoustic spectrum, see figure 3.

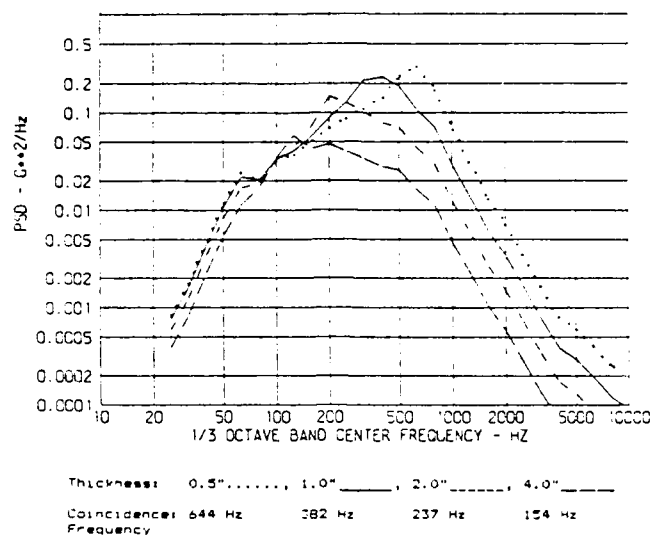


Figure 5. Effect of Panel Core Thickness on 95th Percentile Vibroacoustic Response

Figure 6 shows the vibroacoustic effect of variations of the IM panel equipment mass of 0 lb, 86 lb, 171 lb, and 342 lb. The selected equipment mass value was 171 lb which corresponds to a surface density loading of 0.07 lb/in² for the 2378 in² panel shown in figure 2. The prediction shows that the squared vibration response is reduced in proportion to the ratio of panel weight (approximately 24 lb) to the total panel plus equipment weight. This effect of equipment weight predicted by SEMOD is conservative as discussed in the next paper in this session. The grouping together of the TOPEX IM mounted equipment on a few panels was one of the principal techniques selected by FSC to reduce the vibroacoustic response.

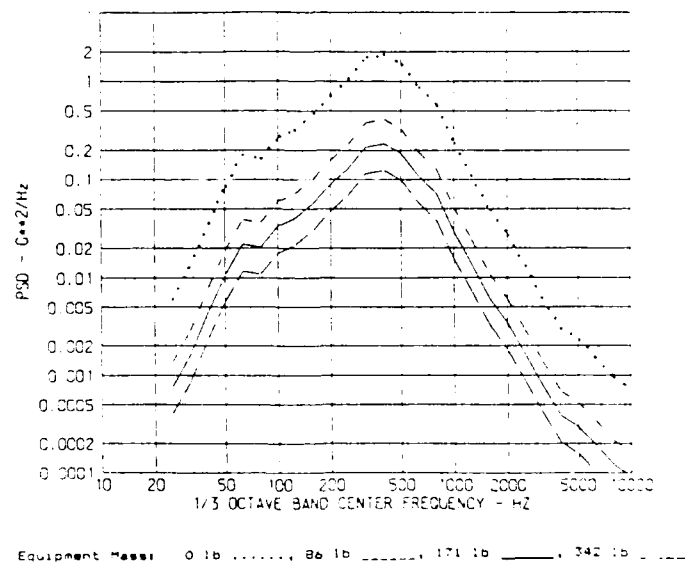


Figure 6. Effect of Panel Equipment Mass on 95th Percentile Vibroacoustic Response

Figure 7 shows the vibroacoustic effect of variations of the IM panel damping loss factor of 0.2, 0.1, 0.05, and 0.025. The selected value was 0.1. The predictions assume that the damping loss factors are inversely related to frequency and the quoted damping loss factors are the values at 300 Hz. It is noted that the damping loss factor is defined as twice the damping ratio or as one over the system Q. The results in figure 7 show that damping has a relatively small effect at the peak in the vibroacoustic spectrum where a reduction would be most beneficial. This is because the honeycomb panels are well coupled to the sound field at the coincidence frequency so that the energy lost through acoustic radiation is comparable to that due to internal damping. In view of the results in figure 7, no effort was made by FSC to increase the panel damping and the damping loss factor was assumed to be 0.1 for the vibroacoustic predictions.

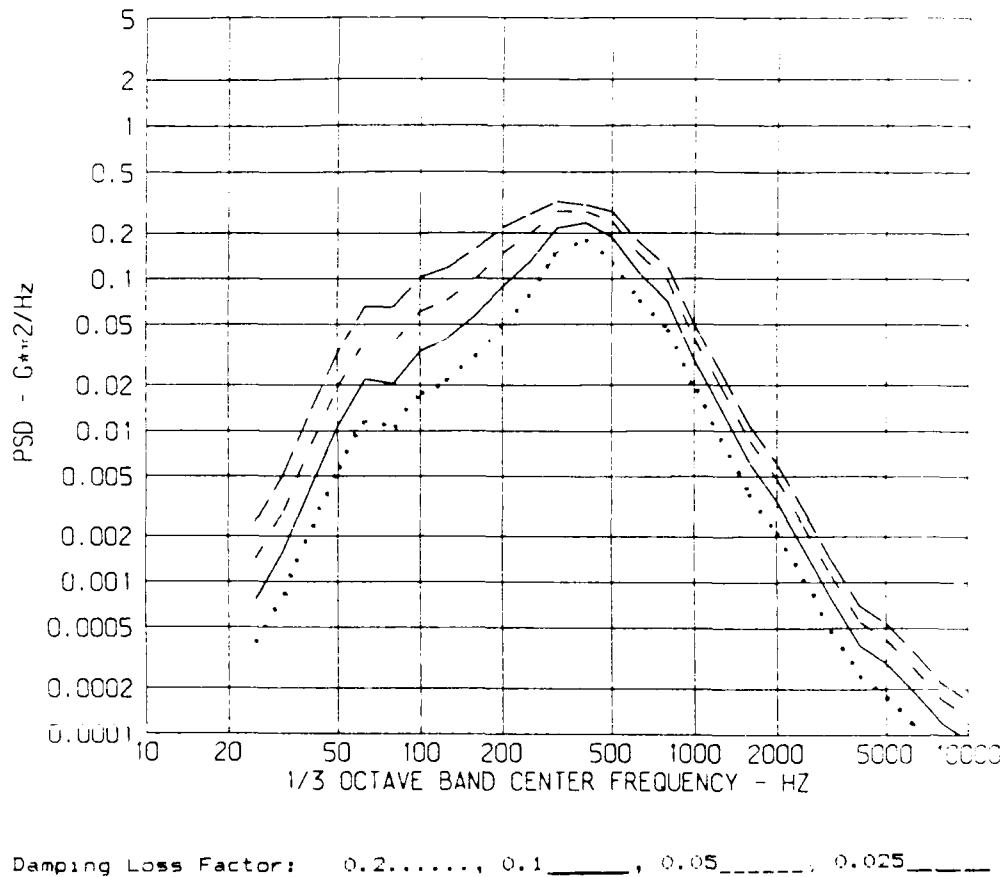
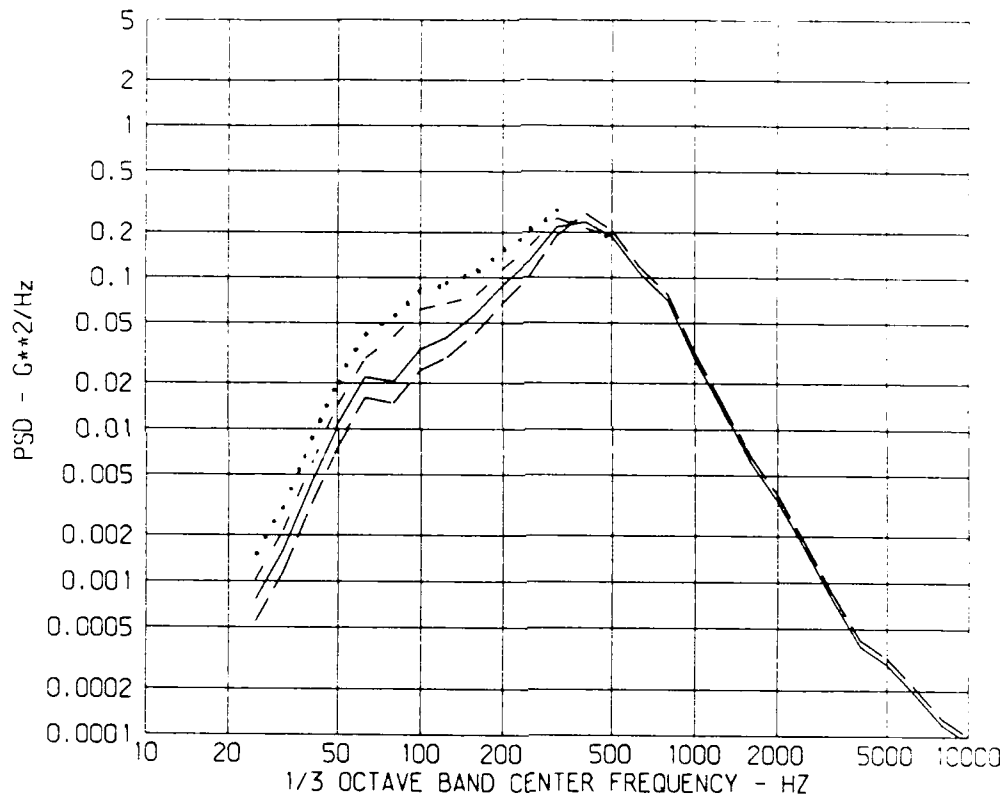


Figure 7. Effect of Panel Damping Loss Factor on 95th Percentile Vibroacoustic Response

Figure 8 shows the vibroacoustic effect of variations of the IM panel size of 29"x16", 29"x33", 29"x82", and 57"x82". Referring to the IM panel sketch in figure 2, it is seen that 29"x82" corresponds to the selected size of the panel. The smaller size choices would require placing stiffeners on the lower +Y panel to break it up into subpanels and the larger size choice would require combining the lower +Y panel with the IM upper +Y panel. The results presented in figure 8 show that panel size has very little effect on the vibroacoustic response except at the frequencies well below the spectrum peak.



Panel Size: 29"x16"....., 29"x33"-----, 29"x82"———, 57"x82"———

Figure 8. Effect of Panel Size on 95th Percentile Vibroacoustic Response

VAPEPS EXTRAPOLATION TO DEFINE RANDOM VIBRATION SPECIFICATION

The VAPEPS theoretical prediction (SEMOD) for the TOPEX instrument module (IM) in Figure 4 would result in a design and test random vibration specification of approximately $0.5 \text{ g}^2/\text{Hz}$ when the traditional JPL 4dB margin is placed on the flight levels. Because this specification would be high compared to other JPL spacecraft programs and compared to the TOPEX component test heritages, it was decided to calibrate the theoretical SEMOD predictions with empirical test data. The VAPEPS semi-empirical prediction code EXTRAP1 is ideally suited to this purpose.

To calibrate VAPEPS for the honeycomb type structure of the TOPEX IM, Fairchild Space Company (FSC) provided acoustic and vibration data from acoustic tests of Control and Data Handling (C&DH) modules from two previous spacecraft programs which used essentially the same Multimission Modular Spacecraft (MMS) bus as TOPEX. These modules were fabricated from one inch honeycomb as is the TOPEX IM. The C&DH module from the GRO spacecraft had equipment loading of 0.11 lb/in^2 and was tested at an overall SPL of 142 dB. The C&DH module from the MMS spacecraft had equipment loading of 0.08 lb/in^2 and was tested at an overall SPL of 149 dB. The TOPEX IM is being designed for equipment loading of 0.07 lb/in^2 and will be qualified to an overall SPL of 146 dB.

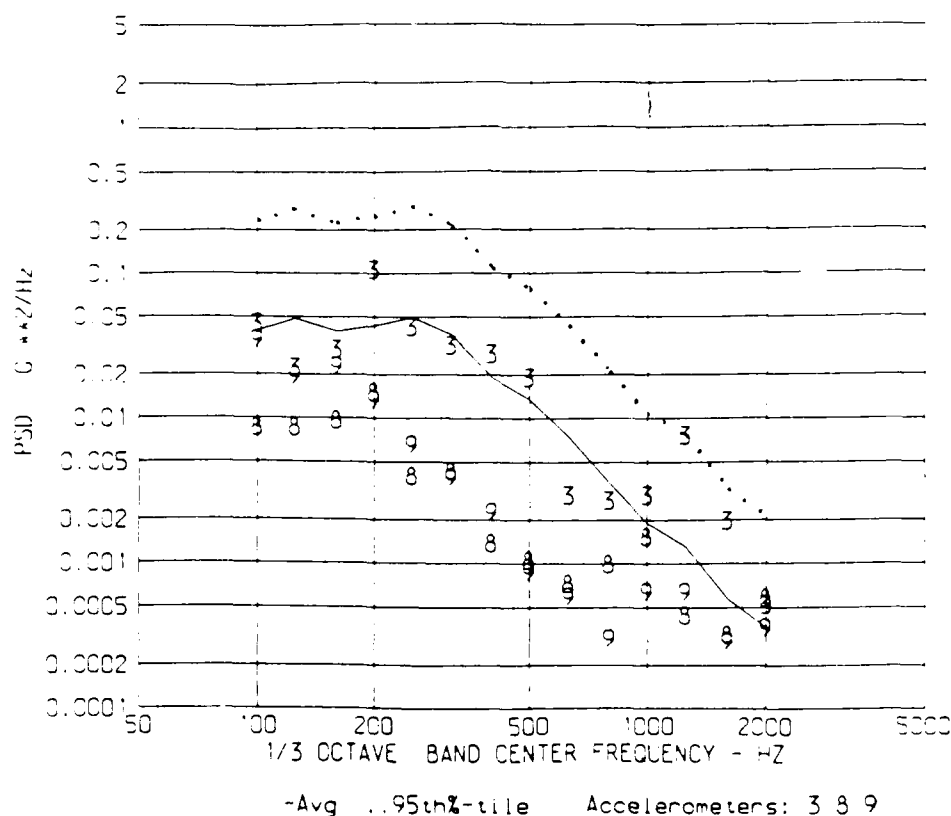


Figure 9. Comparison of VAPEPS Theoretical Prediction with Random Vibration Data from Acoustic Test of C&DH Module from GRO Spacecraft

Figure 9 shows a comparison of the VAPEPS theoretical SEMOD prediction with the random vibration data from the acoustic test of the C&DH module from the GRO spacecraft. The average ratio of the prediction to the data is approximately a factor of two for the GRO module. For the C&DH module from the MMS spacecraft, the corresponding average ratio of theory to data was more like a factor of ten, but this ratio was subsequently reduced by a factor of two to account for possible nonlinearities due to the 149 dB SPL. The comparisons of theory and data from the GRO and MMS spacecraft programs were given equal weight in the semi-empirical prediction of the TOPEX IM random vibration specification.

The VAPEPS semi-empirical prediction technique EXTRAP1 compares the predictions of a theoretical SEMOD model with empirical data for a baseline configuration and uses SEMOD to extrapolate the differences between the theory and data for the baseline to a new configuration for which a prediction is desired. EXTRAP1 thus makes good use of both the theory and data. The results of applying EXTRAP1 to the TOPEX IM using the GRO and MMS C&DH modules as baselines is shown in Figure 10. In concurrence with the VAPEPS EXTRAP1 analysis, FSC set the IM 95th percentile flight levels at a maximum value of $0.08 \text{ G}^2/\text{Hz}$, and JPL has defined a design and test specification for IM instruments with a maximum value of $0.2 \text{ G}^2/\text{Hz}$ as shown in Figure 10.

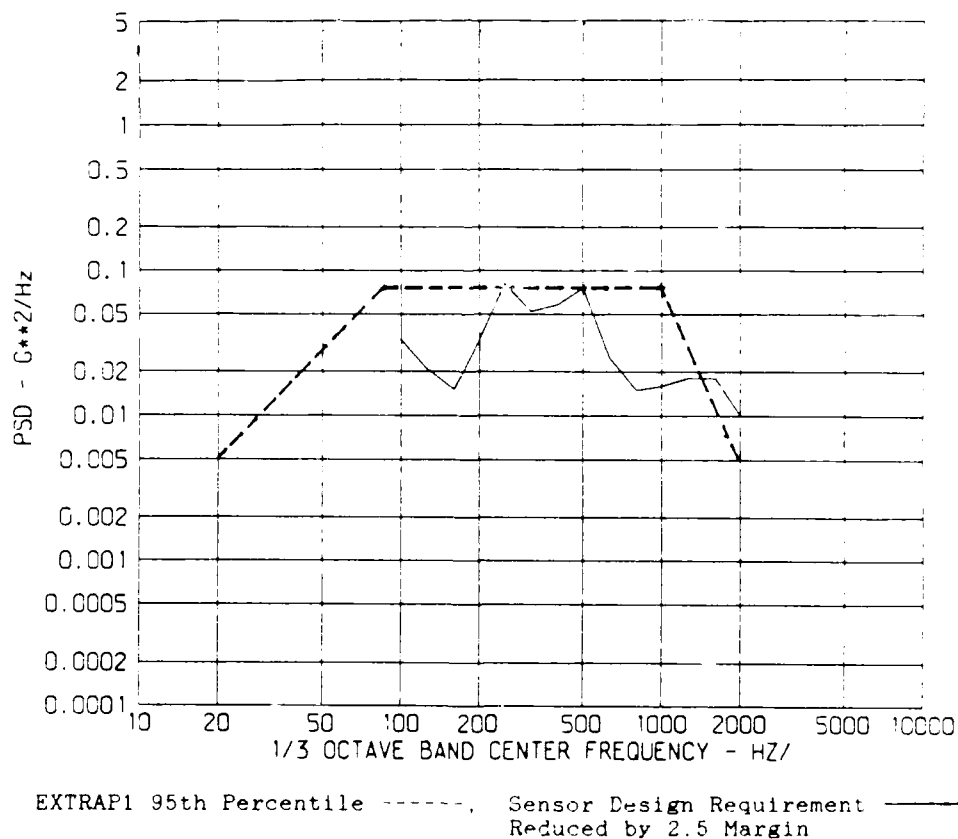


Figure 10. Comparison of VAPEPS Semi-empirical Prediction with JPL Random Vibration Design and Test Requirement for TOPEX Sensors

CONCEPTUAL DESIGN OF DUAL CONTROL RANDOM VIBRATION TEST

Some of the TOPEX spacecraft components have pronounced structural resonances which will be strongly excited by the random vibration test input specified in figure 10. The cognizant engineers for these components want to "notch" the random vibration input at these resonances because they feel that random vibration tests typically subject their components too much higher loads than do the flight environments. Of course, these engineers are right, because the unrealistically high mounting impedance in random vibration tests results in over testing, even when the test and flight levels are comparable. The question is: how and how much to notch? The VAPEPS computer code has been used to predict the TOPEX instrument module acceleration levels and to specify the random vibration test levels of components mounted on the panels. The VAPEPS code may also be used to predict the limit loads used to notch these random vibration tests in the high frequency regime.

There is an extensive body of literature, much of it in the Shock and Vibration Bulletins, concerned with random vibration overtesting because of the incorrect mounting point impedance of shakers. The random vibration notching approach which we are investigating for possible application in the TOPEX program was set forth in three early papers [3, 4, and 5]. In 1960 Morrow [3] described the concept, which we shall call "dual control", of using both motion and force feedback to control shaker impedance. In 1966 Ratz [4] conducted a simple test which demonstrated that a shaker controller could be built to implement this impedance simulation concept. In 1968 Murfin [5] showed that the specification and control of the maximum motion and force is a convenient way to implement impedance simulation. These techniques have been investigated extensively by researchers at Sandia Laboratories, see for example [6] by Smallwood. Recently, Piersol and his colleagues at Astron Research Inc. [7] have been working for the Air Force to develop a recommended approach to this problem.

Impedance and Dual Control Relations

The impedance relations which govern the complex frequency response of a component subjected to sinusoidal or random vibration follow from Thevenin's and Norton's equivalent circuit theorems given in equations (1) and (2) respectively:

$$V = V_o - F/Z_o \quad (1)$$

$$F = F_o - V*Z_o \quad (2)$$

where: V is the interface velocity, F is the interface force, V_o is the source free velocity, F_o is the source blocked force, and Z_o is the source impedance.

From equations (1) and (2), it follows that the source impedance Z_o is equal to the ratio of the blocked force F_o and free velocity V_o :

$$Z_o = F_o / V_o \quad . \quad (3)$$

Similarly, the impedance of the load Z is equal to the ratio of the interface force F and velocity V :

$$Z = F / V \quad . \quad (4)$$

The derivation and combination of the forgoing impedance equations in relation to vibration testing is described in [6], where the respective impedances are defined as the ratios of force to acceleration and called "apparent weights".

Herein, we choose to combine equations (1) and (2) in a form that does not involve the source and load impedances:

$$1 = A/A_o + F/F_o \quad (5)$$

where the interface and free accelerations, A and A_o , have been used instead of the corresponding velocities. It is understood that each term in equation (5) is in general complex and a function of frequency. If the interface acceleration A and force F in a component vibration test were controlled in accord with equation (5), the component would respond at every frequency as in flight; therefore we denote the implementation of equation (5) as "exact dual control". Equation (5) offers the advantage that it does not contain the source and load impedances, with which vibration test engineers are largely unfamiliar. However, equation (5) is theoretically equivalent to other exact impedance control relations described in the literature [6 and 7]. In applying equation (5) to dual specification and control of vibration tests, it is convenient to interpret A_o and F_o as the specified limit acceleration and force which will in general be larger than the free acceleration and blocked force in order to envelope combined source and load resonances, spatial variations, flight-to-flight variations, and other uncertainties.

Conventional random vibration tests are conducted by controlling only the interface acceleration A to the specified acceleration A_o ; that is the second term on the right hand side of equation (5) is ignored.

A simplified form of dual control, which is well suited to implementation with existing random vibration spectrum equalizers, is what may be called "dual extremal control":

$$A \leq A_o \quad \text{and} \quad F \leq F_o. \quad (6)$$

This extremal dual control technique was described very explicitly by Murfin in [5]. (However, Murfin calculated the force limit F_o from the load impedance, equation (4), rather than from the source impedance, equation (3).)

Resonance Frequency Notching

Figure 11 illustrates the use of three control techniques: conventional acceleration control, exact dual control, and extremal dual control. In a conventional vibration test, the shaker acceleration is maintained at the specified acceleration and the force between the shaker and component may become unrealistically large at resonances of the component as illustrated by the dashed curve in figure 11. In exact dual control, as in typical flight mounting configurations, the interface acceleration "notches" at the resonance frequencies and the force increases so that the ratio of interface force to acceleration is as in the conventional test as shown by the solid curve in figure 12. In extremal dual control, the interface force is limited to the same maximum value as in exact dual control and the acceleration notches to the same value as in exact control as shown by the dash-dot-dash curve in figure 11. In [7] research vibration tests were conducted using off-line iterative shaker control techniques corresponding to the three techniques described herein and the results generally confirmed the notching effects illustrated in figure 11.

Implementation of Extremal Dual Control Random Vibration Test

The on-line implementation of an exact dual control random vibration test would be difficult at present. Random vibration spectral equalizers currently in use are not capable of computing the auto and cross spectra of the measured acceleration and force and of comparing these quantities with the appropriate specified acceleration and force as required by equation 5.

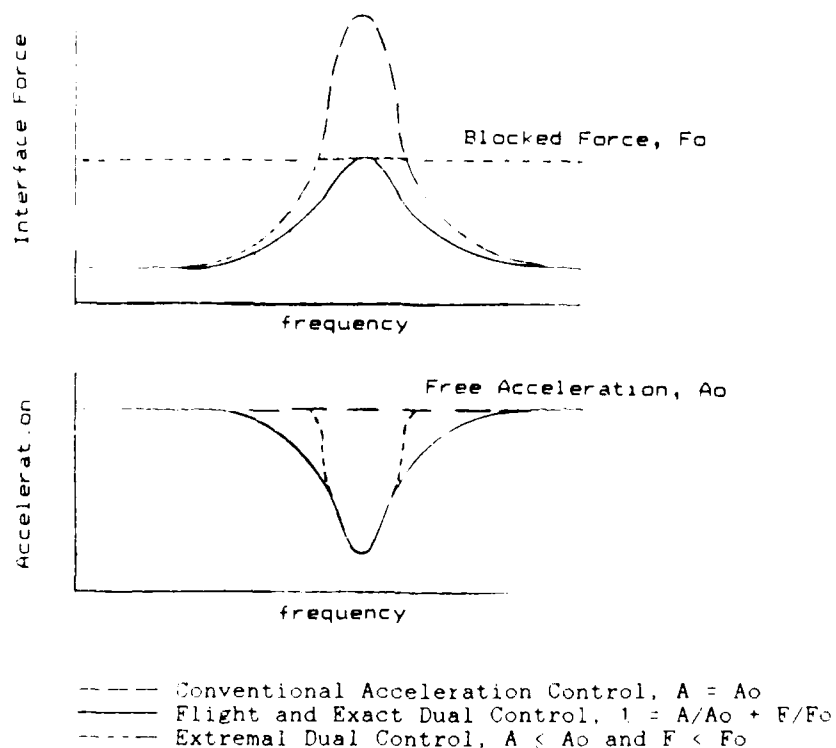


Figure 11. Resonance Frequency Notching

Figure 12 shows the block diagram of a suggested method for on-line implementation of the extremal dual control random vibration test with a conventional random vibration spectrum equalizer. This is the method under consideration for real time notching of random vibration tests of selected TOPEX components. Conventional random vibration equalizers, in the extremal control mode, compute the temporal rms values in narrow frequency bands (typically 5 or 10 Hz) of a number of acceleration measurements and control the shaker in each narrow frequency band by comparing the maximum of these measurements to the specified acceleration spectrum. This type of equalizer can be used to implement extremal dual control random vibration notching in real time, if the frequency spectrum of the force feedback signal is shaped for comparison with the acceleration specification. (Most of the vibration test equalizers will accept only one specified spectrum for random vibration tests.) The required shaping of the force feedback signal may be accomplished by passing the force time history through a one-third octave band spectrum shaping network before the signal is presented to the equalizer as shown in figure 12. (One-third octave band shaping networks are typically available for the purpose of shaping acoustic test spectra.) The appropriate frequency shaping function is:

$$(A_o(f)/F_o(f)) \times (S_{v/g} / S_{v/lb}) \quad (7)$$

where A_o and F_o are the specified limit acceleration and force spectra and $S_{v/g}$ and $S_{v/lb}$ are the accelerometer and force measurement calibration sensitivities. It should be emphasized that the use of a one-third octave band shaping network to filter the broad band force measurement will not negate the ability of the equalizer to notch in 5 or 10 Hz bands.

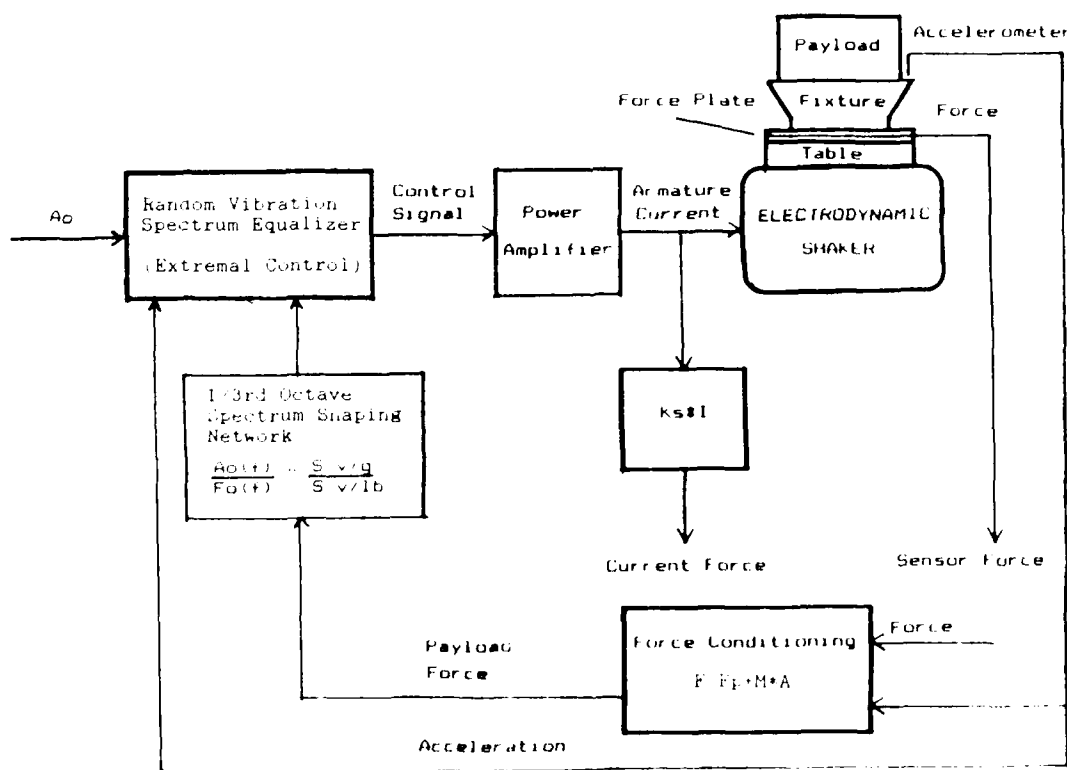


Figure 12. Block Diagram for On-line Implementation of Extremal Dual Control Random Vibration Test

Both the exact and extremal dual control techniques require a measurement of the force F delivered to the component by the shaker and a specification of a limit force F_0 . The force may be measured in one of several ways. If the component is comparable in weight to the shaker armature, the shaker current may provide an adequate measure of the force [7]. Alternately, the shaker force may be measured by a force plate attached to the shaker table. In either of these cases, it may be necessary to correct the gross force measurement as shown in figure 12 by subtracting the force consumed by the mass M between the force sensor and test component, i.e. the armature and/or the test fixture. In some instances rather than correcting the measured force, it may be convenient to specify a gross force limit F_0 which bounds the measured gross force:

$$F_0 = F_0 + M \cdot A_0 \quad (8)$$

where A_0 is the specified limit acceleration taken in phase with the limit force F_0 . A third and preferred way to measure force is to instrument the test component with strain gauges or load cells, as will be done for several of the TOPEX program components.

There is little data to aid in specifying the appropriate force limit, but several approaches are available for investigation. At JPL a "mass-acceleration curve" [8] is often used to estimate the limit loads for test components. Use of the mass-acceleration curve to set the limit loads would be similar to the technique used by Murfin [5]. However, the mass-acceleration curve is usually very conservative and is often replaced by the results of a low frequency transient coupled loads analysis later in spacecraft programs. Both the mass-acceleration curve and coupled loads analysis are generally limited to frequencies below 50 to 100 Hz. At the high frequencies, the limit forces may be calculated using infinite system structural impedance analyses [9] which are identical to those used by the VAPEPS computer code to predict structural vibration transmission. Some extrapolation of these approaches will be required in the mid-frequency range. It is planned to investigate all of these techniques for generating the random vibration test limit forces for the TOPEX program components.

ACKNOWLEDGEMENTS

The work described in this paper was performed by the Jet Propulsion Laboratory, California Institute of Technology, and was sponsored by the National Aeronautics and Space Administration and the United States Air Force.

The authors wish to express their gratitude to Jim Fortenberry of JPL and Paul Larkin of FSC for their technical guidance and cooperation on the TOPEX project and to Melissa Slay and Gloria Badilla for their technical assistance on the application of VAPEPS. We would also like to thank Allan Piersol and his associates at Astron Research and Engineering, where the first listed author first worked on the dual control problem, for their valuable contributions to this work. Sheldon Rubin of Aerospace Corporation first suggested the extremal dual control approach and David Boatman of JPL

helped figure out how to implement the approach with a current random vibration test spectrum equalizer. The support of Don Wong of Aerospace Corporation in both the VAPEPS and dual control areas is deeply appreciated.

REFERENCES

1. R. Stewart, L. L. Fu, and M. Lefebvre, "Science Opportunities From the TOPEX/Poseidon Mission", JPL Publication 86-18, July 15, 1986.
2. "Vibroacoustic Payload Environment Prediction System (VAPEPS) Workshop Notes", Jet Propulsion Laboratory and Lockheed Missiles and Space Company, August, 1988.
3. C. T. Morrow, "Application of the Mechanical Impedance Concept to Shock and Vibration Testing", TRW Space Technology Laboratories, Los Angeles, CA, March 1960.
4. A. G. Ratz, "An Impedance-Compensated Random Equalizer", Proceedings of the IES 1966 Annual Technical Meeting, pp. 353-357, San Diego, April 1966.
5. W. B. Murfin, "Dual Specification in Vibration Testing", Shock and Vibration Bulletin, No. 38, Part 1, pp. 109-113, August 1968.
6. D. O. Smallwood, "The Application of Unloaded (Free) Motion Measurements and Mechanical Impedance to Vibration Testing", Proceedings of IES 1976 Annual Technical Meeting, pp. 71-82, Philadelphia, April 1976.
7. Astron Research and Engineering, "Vibration Test Procedures for Orbiter Sidewall-Mounted Payloads: Phase 1 Final Report", USAF Contract F04701-87-C-0010, March 1988.
8. M. Trubert, "Designing Galileo to Upper Bound Loads for Shuttle/Centaur", NASA/OAST Shuttle Payload Dynamic Environments and Loads Prediction Workshop, January 24-26, 1984.
9. Eugen Skudrzyk, Simple and Complex Vibratory Systems, pp. 263-280, The Pennsylvania State University Press, University Park and London, 1968.

STATISTICAL ENERGY ANALYSIS MODELING OF NON-STRUCTURAL MASS ON LIGHTWEIGHT EQUIPMENT PANELS USING THE VAPEPS PROGRAM

Melissa L. Slay
Jet Propulsion Laboratory
California Institute of Technology
Pasadena, CA 91109

The random vibration environment of equipment mounted on a panel can be predicted analytically using the VAPEPS (VibroAcoustic Payload Environment Prediction System) program. This program uses Statistical Energy Analysis (SEA) to calculate average structural responses to acoustic loads. However, SEA theory is not specifically geared for the analysis of equipment components, and the standard method of modeling these components (as non-structural panel mass) has led to overly conservative predictions. This paper discusses some of the reasons this problem occurs, and presents an alternative modeling technique. Comparisons of these two modeling methods are then shown against actual test data for several flight projects.

INTRODUCTION

Establishing random vibration design and test requirements for panel-mounted equipment on aerospace structures first requires knowledge of the response of the equipment panel itself to high frequency acoustic loads. This response then establishes the random vibration environment of the mounted equipment at the panel interface. The panel response can be determined analytically by the VAPEPS (VibroAcoustic Payload Environment Prediction System) program, which incorporates Statistical Energy Analysis (SEA) to predict structural responses to acoustic excitation. The SEA technique utilizes energy balance equations (energy into an element equals the energy out of the element) to arrive at a spatially averaged response of the element over a specific frequency bandwidth. Elements are defined by their average physical properties, which means that a layered panel or a panel with ribs must be modeled as a homogeneous plate with equivalent properties. A factor can then be added to the predicted average response to account for the spatial variation across the panel.

Components mounted on a panel are not easily modeled as SEA elements, since SEA elements typically have characteristic dimensions that are large compared to the acoustic wavelengths of interest. Candidate methods of modeling the equipment are (1) to assume that the

components are non-structural and share some fraction of the response of the unloaded panel; and (2) to assume that the components change the structural properties (stiffening, damping) of the panel and incorporate these changes when defining the equivalent panel element.

NON-STRUCTURAL MASS ASSUMPTIONS

The usual method of accounting for the equipment mounted on a panel assumes that the equipment is non-structural. This means that the equipment is assumed to have no stiffening effect on its supporting structure, will store energy as a rigid body only, and will not dissipate energy. When the SEA model is built using the VAPEPS program, the non-structural mass (equipment mass) is specified in the panel parameters. It will have no effect in the SEA power balance calculations. Instead, it will be used as part of a scale factor to attenuate the panel response, given by:

$$(a_{\text{loaded panel}})^2 = \frac{m_{\text{structural}}}{m_{\text{structural}} + m_{\text{non-structural}}} (a_{\text{unloaded panel}})^2$$

where: a = acceleration
m = mass

This equation, which is based on the idea of energy sharing between the panel and equipment, works well for lightly loaded panels. In cases where the panel equipment loading becomes large, empirical data show that the non-structural mass assumptions become invalid.

INCORPORATING EQUIPMENT MASS STRUCTURALLY

One method of working around the non-structural mass limitations is to assume a portion of the equipment mass is an extra layer of the plate, and calculate structural parameters for an equivalent, homogeneous plate. Equivalent structural parameters are often calculated for built-up plates (such as honeycomb panels with face sheets or ribbed panels) so that a SEA prediction can be made. This is done by matching bending stiffness ("EI"), mass, critical frequency, and longitudinal wave speed to obtain an equivalent thickness, mass density, Young's modulus, and surface mass density. The VAPEPS program has a runstream that performs these calculations based on the user-defined layers of the panel. For the models described later in this paper, we defined the equipment mass layer by smearing a portion (half) of the total equipment mass into a very thin (.001 inch) homogeneous plate layer with the same surface area as the equipment panel and no stiffness. This definition was based on intuition alone, and used only as a rough estimate of the actual structural characteristics of equipment loads.

VAPEPS MODEL VERIFICATION ACOUSTIC TEST

A recent acoustic test was run at the Jet Propulsion Laboratory (JPL) to measure the responses of a panel under different mass loadings. The panel tested was a former flight spare for the Delta Star UVIE Instrument Pallet, and was configured in the following ways:

Configuration 1: loaded with 20 times the pallet mass (230 lbs)
Configuration 2: loaded with 10 times the pallet mass (115 lbs)
Configuration 3: loaded with 5 times the pallet mass (58 lbs)
Configuration 4: unloaded

The loads were simulated by steel blocks, located as shown in Figure 1. These blocks were bolted to the panel through spacers which eliminate some of the stiffening effect of the mass (as opposed to the blocks being bolted directly to the panel). The panel was suspended in the JPL reverberant acoustic chamber and tested at five noise levels: 137 dB overall (OA), 143 dB OA, 146 dB OA, 149 dB OA, and again at 137 dB OA. Thus far, the data from 16 accelerometers during the runs at 146 dB OA have been analyzed and converted to one-third octave band acceleration spectral densities. These accelerometers were located normal to the pallet as shown in Figures 1 and 2. The one-third octave band responses from the 16 accelerometers were averaged for each configuration and compared. Figure 3 shows that there is little difference between the responses for the three loaded configurations across the frequency spectrum, and all four configurations tend to converge above 500 Hz. This same trend was also observed when only the four accelerometers mounted at the bases of the masses were averaged and compared.

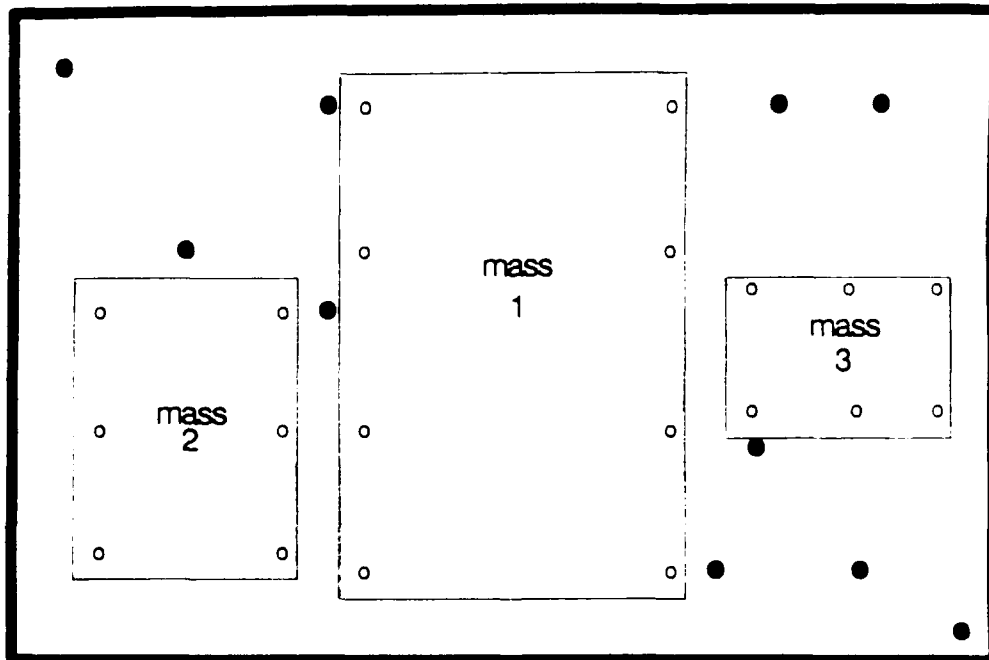


Figure 1. Delta Star Pallet (side 1) Mass Simulator and Accelerometer Locations (● = accelerometer location)

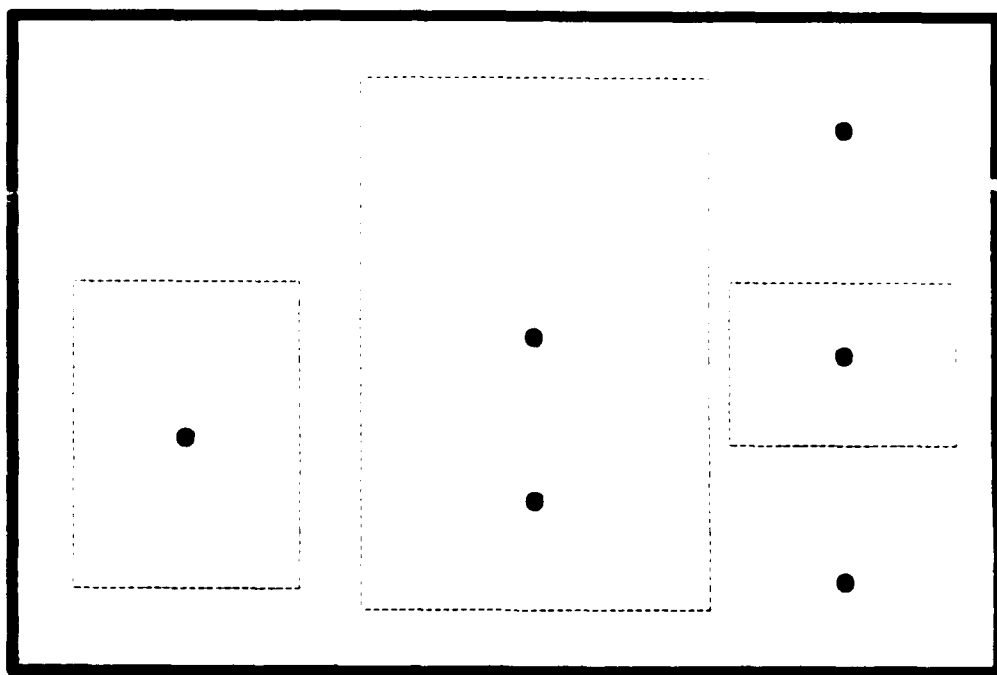


Figure 2. Delta Star Pallet (side 2) Accelerometer Locations (● = accelerometer location)

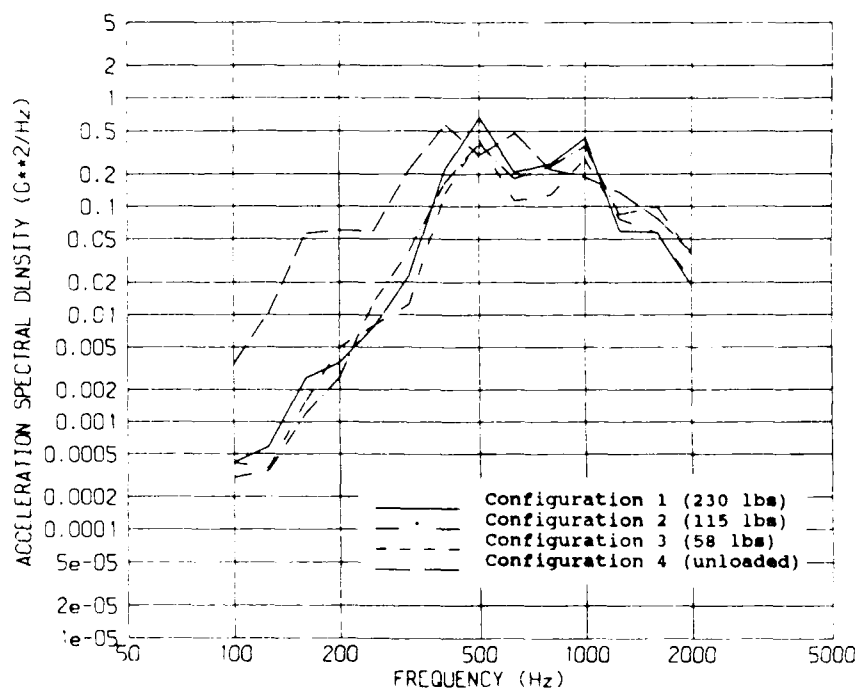


Figure 3. Delta Star Pallet Responses, Developmental Acoustic Tests

Responses from a previous protoflight acoustic test of the same panel loaded with actual equipment were then compared to the panel responses from the Configuration 2 developmental test, since the actual equipment had approximately the same weight (110 lbs) as the steel blocks used in Configuration 2. The average of seven accelerometers mounted on the pallet (as shown in Figure 4) during the protoflight test were used for the comparison shown in Figure 5. The response of the panel loaded with actual equipment remains much lower than the unloaded panel's response (Configuration 4) throughout the frequency range, unlike the response of the panel loaded with steel blocks. This discrepancy is believed to be caused by some basic differences in the structural characteristics between actual equipment and mass simulators. These structural characteristics are compared with each other and with the VAPEPS non-structural mass assumptions below:

	<u>Actual Equipment</u>	<u>Mass Simulator</u>	<u>VAPEPS Assumption</u>
Stiffens supporting structure	sometimes	sometimes	no
Stores energy as a rigid body	no	yes	yes
Stores energy as an elastic body	yes	no	no
Dissipates energy	yes	very little	no

This shows that actual equipment can store and dissipate energy while mass simulators cannot, which could cause the response differences in Figure 5.

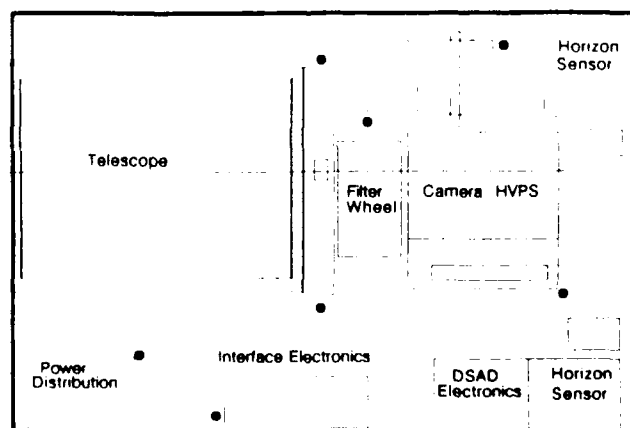


Figure 4. Delta Star UVIE Instrument Pallet Accelerometer Locations (● = accelerometer location)

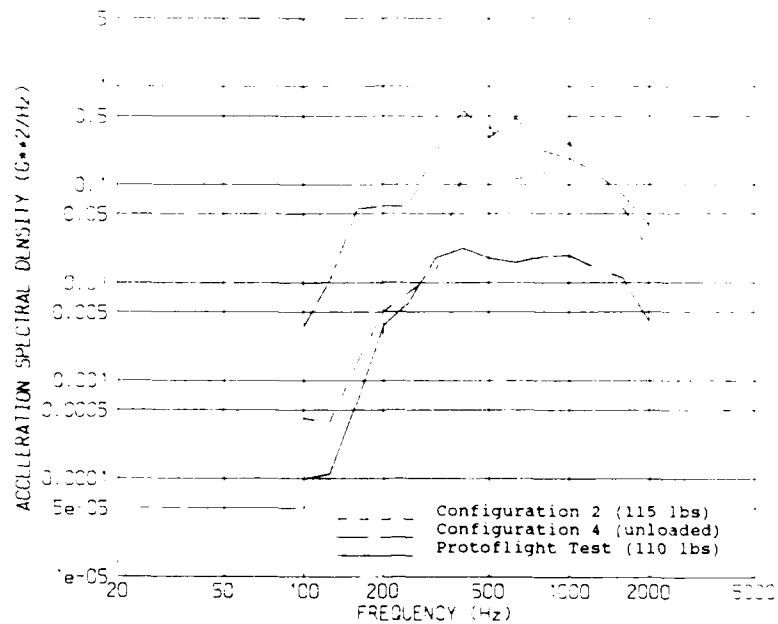


Figure 5. Delta Star Pallet Responses (Developmental and Acoustic Tests)

Figure 6 compares the VAPEPS SEA predictions with the acoustic test data (shown in Figure 5). The prediction of the unloaded panel response agrees reasonably well with the data in frequencies above 630 Hz, which is the low frequency cut-off due to the panel's small modal density. However, the prediction of the panel loaded with non-structural mass shows a large over-prediction in frequencies below 1000 Hz, which is not seen in the unloaded case.

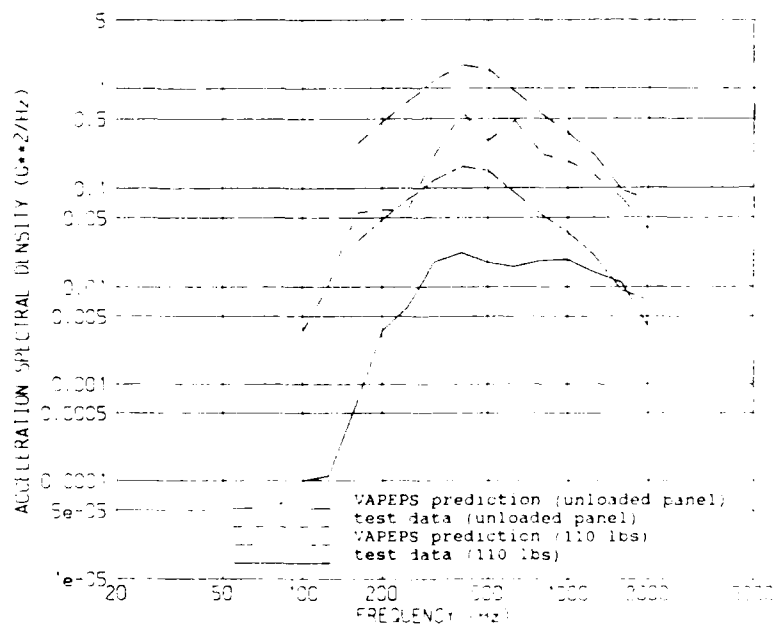


Figure 6. Delta Star Pallet Responses (Developmental and Acoustic Tests) and VAPEPS Predictions

VAPEPS MODEL COMPARISONS

Several flight projects from JPL, Fairchild Space Company, and GE Astro Space Division (ASD) were used for modeling comparisons of the two previously discussed techniques of accounting for equipment mass. Overall, the predictions using the non-structural mass method were consistently high in low frequencies, but became closer to the actual response above about 1000 Hz. The predictions using the half structural/half non-structural mass method usually agreed well in low frequencies, but over-predicted more than the first method above about 1000 Hz. This is because the second method forces the panel's critical frequency to be calculated as higher than it actually is. Modeling methods that kept the critical frequency constant were attempted but with very poor results.

The models used were simplified flat plate/acoustic space models, and were not refined against the test data. Also, corrections were not made to account for the effects of the equipment components on the panel structural damping, since they are not fully known.

Delta Star UVIE Instrument Pallet - JPL

This pallet, previously shown in Figure 4, is made of 40 inch x 24 inch aluminum face sheets with an aluminum honeycomb core, and was loaded with equipment weighing approximately 110 lbs. The two VAPEPS predictions are shown in Figure 7 compared with the average of the data from the seven accelerometers normal to the pallet.

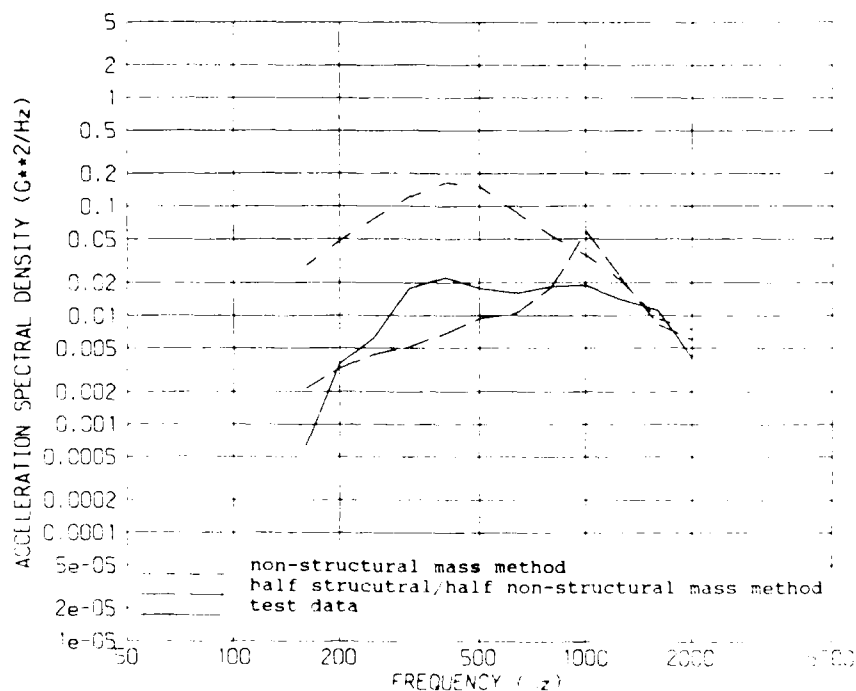


Figure 7. Delta Star Pallet Responses and Predictions

Multiple Mission Spacecraft Communications and Data Handling (MMS CADH) Module - Fairchild

This spacecraft consists of five panels that form a box with one open side. The equipment is mounted primarily on the base panel, which is made of 47 inch x 47 inch aluminum face sheets with an aluminum honeycomb core and loaded with approximately 180 lbs of equipment. The two VAPEPS predictions are shown in Figure 8 compared with the average of data from four normal accelerometers from three separate, identical acoustic tests.

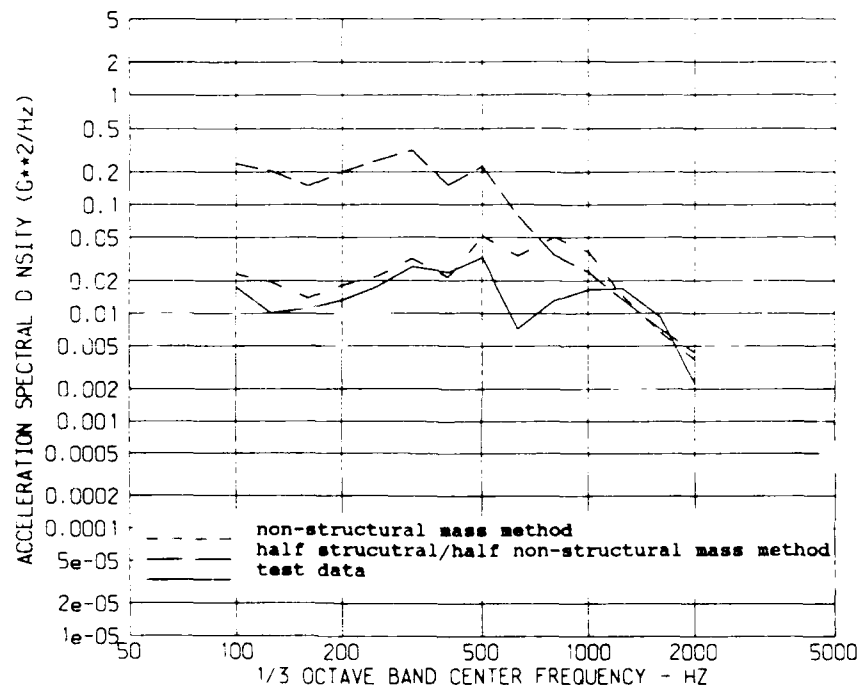


Figure 8. MMS CADH Response and Predictions

Multiple Mission Spacecraft Modular Power Subsystem (MMS MPS)-Fairchild

This spacecraft is identical to the MMS CADH module, except that its base plate is loaded with 400 lbs of equipment. The two VAPEPS predictions are shown in Figure 9 compared with the average of data from five normal accelerometers from three separate, identical acoustic tests.

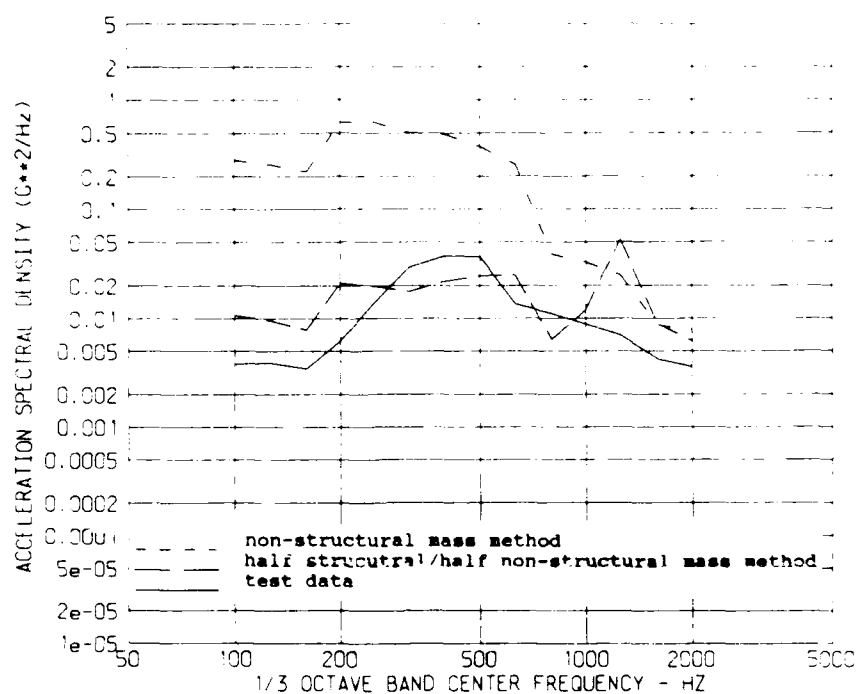


Figure 9. MMS MPS Response and Predictions

SATCOM-K - GE ASD

This satellite structure consists of eight panels forming a box shape. Three of these panels were used in this analysis, all of which were made of aluminum face sheets with an aluminum honeycomb core.

Antenna Panel

This panel is 83.5 inches x 60.5 inches and loaded with 155 lbs of equipment. The two VAPEPS predictions are shown in Figure 10 compared with the average of data from 12 normal accelerometers.

Northwest Panel

This panel is 51.2 inches x 38.2 inches and loaded with 89 lbs of equipment. The two VAPEPS predictions are shown in Figure 11 compared with the average of data from five normal accelerometers.

Northeast Panel

This panel is also 51.2 inches x 38.2 inches, but is loaded with 100 lbs of equipment. The two VAPEPS predictions are shown in Figure 12 compared with the average of data from six normal accelerometers.

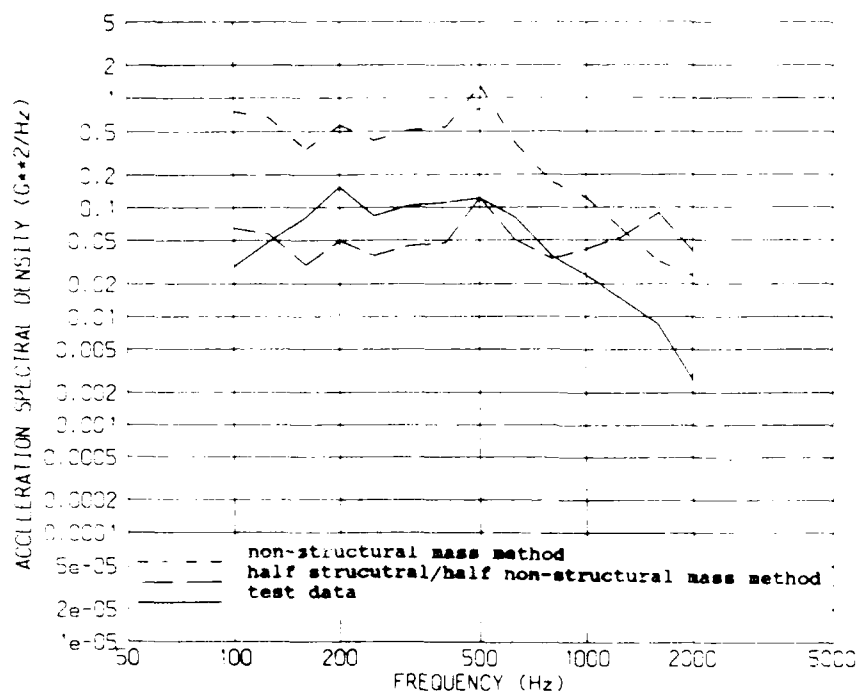


Figure 10. SATCOM-K Antenna Panel Response and Predictions

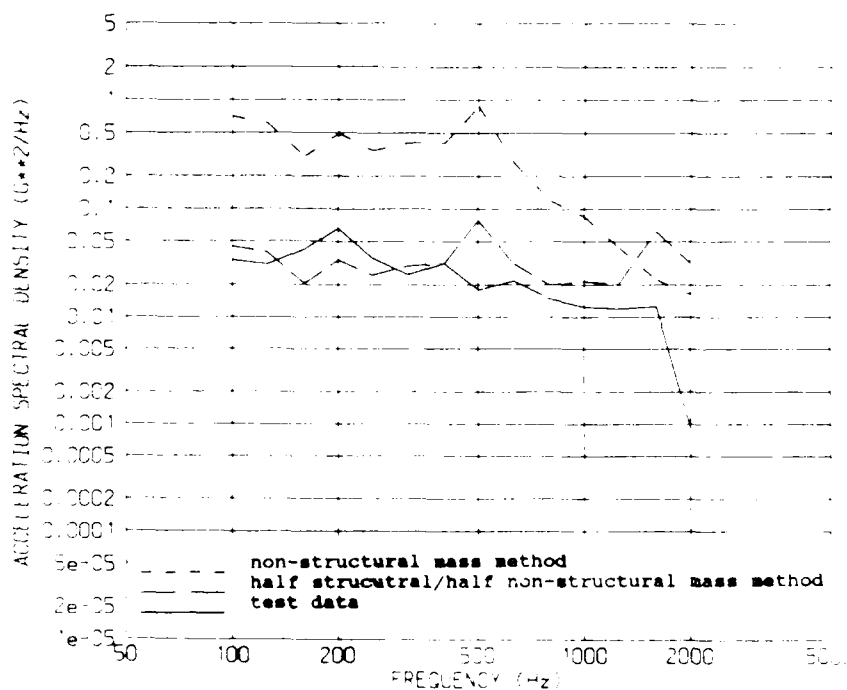


Figure 11. SATCOM-K Northwest Panel Response and Predictions

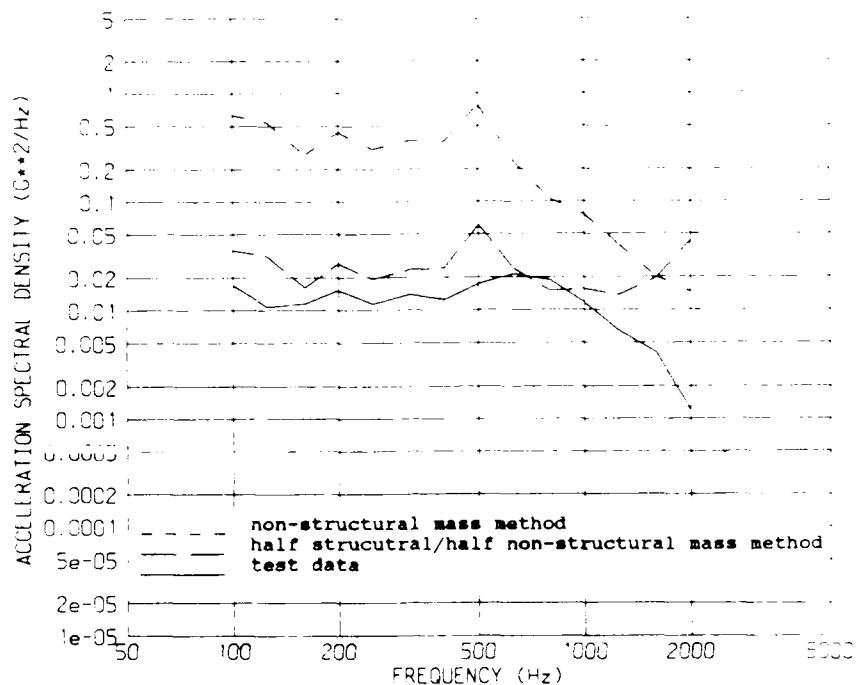


Figure 12. SATCOM-K Northeast Panel Response and Predictions

SUMMARY

This analysis has shown that the SEA non-structural mass assumptions do not adequately describe large mass loadings on lightweight equipment panels. Therefore, building a SEA model of this type of panel requires that special techniques be used to account for the equipment mass. As seen here, assuming that a portion of the equipment is actually part of the panel structure yields better results.

The amount of mass that should be considered structural is not uniquely defined. If test data from a similar baseline structure are available, then the baseline SEA model should be refined against the data, and a VAPEPS extrapolation prediction should be made. Otherwise, judgement based on the trends shown here or previous modeling experience will have to be used. In either method, consideration needs to be given to what type of mass loading is on the panel, since panels mounted with mass simulators have been shown to have higher responses than panels mounted with actual equipment. The method in which the equipment components are mounted should also be considered, since a panel with a box bolted at several locations around its perimeter will be stiffer than a panel with a box bolted at only four corners.

FUTURE WORK

Although assuming half of the equipment component mass loaded on a panel is structural in nature has shown adequate results, there are still several areas that should be examined in detail. First, further acoustic testing should be performed with actual equipment in different configurations. This should include different types of equipment with different mountings to simulate a flight-like panel as much as possible. Then the results from this test could be compared to those from the test discussed previously in this paper. Second, accurate damping measurements should be made so that actual damping values can be obtained. Third, additional methods of modeling equipment components should be investigated and compared with data. The best method or methods of those investigated should be refined and then incorporated into the VAPEPS program. This would eliminate the guesswork currently involved with this type of modeling, and give the program user a more consistent analysis method.

ACKNOWLEDGEMENTS

The work described in this paper was performed by the Jet Propulsion Laboratory, California Institute of Technology, and was sponsored by the National Aeronautics and Space Administration and the United Air Force Space Division.

The author wishes to express her gratitude to Dennis Kern and Terry Scharton of JPL for their technical assistance, and David Boatman, also of JPL, for his direction of the developmental acoustic tests. Also, the following individuals performed a large amount of data reduction for this paper: Juan Fernandez and Sue Rice of JPL, and Dan Rodina, formerly of JPL.

The author would also like to thank David Chu and Carl Voorhees of G. E. Astro Space, Princeton, New Jersey; and Paul Larkin of Fairchild Space Company, Germantown, Maryland for supplying to JPL some of the test data used in this paper.

REFERENCES

1. Robert E. Barrett, "Techniques for Predicting Localized Vibratory Environments of Rocket Vehicles," NASA TN D-1836, October 1963.
2. Leo L. Beranek, Noise and Vibration Control, McGraw-Hill Book Company, New York, 1971.
3. Gideon Maidanek, "Response of Ribbed Panels to Reverberant Acoustic Fields," Journal of the Acoustical Society of America, Vol. 34, No. 6, June 1962.
4. "VibroAcoustic Payload Environment Prediction System (VAPEPS) Workshop Notes," Jet Propulsion Laboratory and Lockheed Missiles and Space Company, August, 1988.

STRESS ESTIMATION AND STATISTICAL ENERGY ANALYSIS OF THE MAGELLAN SPACECRAFT SOLAR ARRAY USING THE VAPEPS PROGRAM

Gloria A. Badilla¹ and Valerie C. Thomas
Jet Propulsion Laboratory
California Institute of Technology
Pasadena, CA 91109

Large, lightweight aerospace structures may experience significant acoustically induced stresses during launch vehicle liftoff and ascent. A technique for estimating the magnitude of such stresses is included in the VAPEPS (Vibroacoustic Payload Environment Prediction System) Program. The technique may help to identify structural design deficiencies and is particularly useful when a finite element analysis has not been performed or when insufficient acceleration and strain measurements from an acoustic test are available. The VAPEPS stress analysis is also easier and less expensive to perform than a finite element analysis. This paper describes the application of the VAPEPS stress estimation technique to a large spacecraft solar array panel and compares the analytical results with measured test data.

INTRODUCTION

The Jet Propulsion Laboratory, under the sponsorship of NASA and the United States Air Force Space Division, has the responsibility to maintain the VAPEPS Statistical Energy Analysis (SEA) computer program and to independently validate new prediction methodology. Lockheed Missiles & Space Company, the VAPEPS software developer, has incorporated routines for estimating the acoustically induced stresses in simple panel and cylindrical structures [1]. IMSC has also performed an empirical validation of the method using a large right-circular cylinder and a simulated solar panel as a test specimen [2]. An analysis of a Magellan spacecraft solar array, described in this paper, has been performed by JPL to provide an independent verification of the VAPEPS stress prediction method.

Magellan, which is being managed by NASA/JPL, is scheduled for launch aboard the Shuttle in April 1989. Its mission is to perform extensive radar mapping of the planet Venus. The Magellan solar arrays were chosen as good

¹Gloria A. Badilla is an employee of Syscon Corporation, under contract to the Jet Propulsion Laboratory.

models for validating the VAPEPS stress estimation technique for several reasons. The arrays are large (100 in. x 100 in.), lightweight panels, representative of the types of structures for which the technique was specifically developed. Also, an extensive, well documented test program was performed on the solar arrays. Numerous acceleration and strain gage measurements were made during assembly level acoustic testing of test article solar arrays.

The VAPEPS stress estimation method is based on a derived ratio of the spatial averaged, mean square stress to the spatial averaged, mean square displacement of the structure. The approach described in this paper is to first use the VAPEPS program to develop a SEA model of the solar panel and to compare the predicted acceleration response to data measured during an assembly level acoustic test of the array. The measured and analytically predicted acceleration responses are then used to estimate the space averaged, mean square stresses in the array. Results are compared to calculated stresses from measured strains and some conclusions about the VAPEPS approach to stress estimation are discussed.

VAPEPS SEA AND STRESS ESTIMATION TECHNIQUES

VAPEPS SEA Prediction

The VAPEPS method for predicting the theoretical vibration response of a structure to a known acoustic excitation is based on SEA. This method works well in the high frequency regime and can be combined with finite element analyses which tend to become computationally intensive at the higher frequencies of interest. The implementation of SEA incorporated in the VAPEPS program is described in a set of reference manuals [3]. Briefly, the assumptions upon which the method is based can be summarized as follows:

1. Excitation forces are random, steady-state and uncorrelated.
2. Coupling between different SEA elements (mode sets) within the system being modeled is linear and uniform within a frequency band. Coupling is also assumed to be conservative in that no coupling damping is included.
3. The energy is uniformly distributed among the modes of a given frequency band (equipartition of energy).

Given these assumptions, steady state energy balance equations can be written which relate the average energy in a SEA element to its average response. For a large plate-like structure (such as a solar array) VAPEPS only computes the energy of the bending modes. These modes tend to dominate the vibroacoustic response of most lightweight aerospace structures. The output from a VAPEPS SEA prediction consists of spatial-averaged, mean square accelerations, in one-third octave bands, for each element in the model. Since these results are averages over time, space and frequency, the accuracy of the boundary conditions and geometric and material properties of the structure is less significant than it would be for a finite element analysis.

VAPEPS Stress Prediction

In addition to the basic SEA assumptions of equipartition of energy and the secondary importance of boundary conditions, the stress estimation technique requires other assumptions regarding the dynamic behavior of the structure. The VAPEPS equations relating the spatial-averaged mean square in-plane stresses to the spatial-averaged mean square displacements (or accelerations) in a structure are based on the generalized plane stress theory of linear elasticity [4]. Fig. 1 illustrates a simple plate element under plane stress conditions and shows the normal and shear stresses that are calculated by VAPEPS. In this case, the thickness of the plate must be small compared to its other two dimensions and the out-of-plane components of the stress tensor (τ_{xz} , τ_{yz} , σ_z , etc.) are negligible or zero. Simply supported boundary conditions are also assumed to make the mathematical expressions tractable.

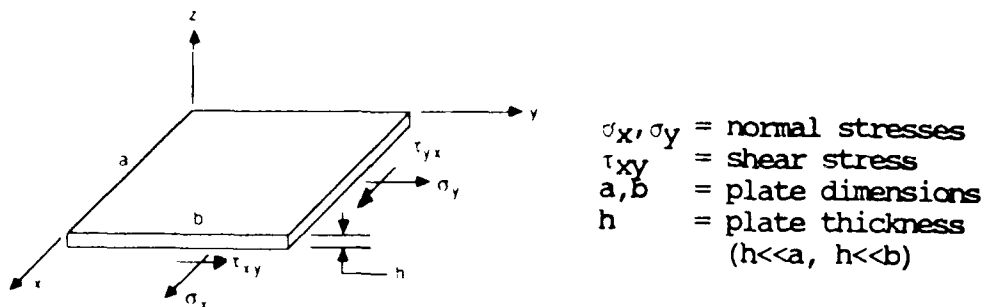


Figure 1. Flat Plate in State of Plane Stress

The VAPEPS procedure requires either empirical or predicted mean square acceleration responses to calculate the spatial-averaged mean square in-plane stresses for each mode. The modal stresses are then summed over each one-third octave frequency band. The overall root mean square stresses are just the square root of the sums of the modal stresses. Details of the analytic procedure are set forth in Reference [2]. The process has been automated for flat plates and cylindrical shells in the VAPEPS software and is transparent to the user. The only inputs that are required are the physical properties of the structure and one-third octave band mean square accelerations.

The VAPEPS developer emphasizes that this technique should only be used to estimate the order of magnitude of stresses in a structure to identify cases which may require more detailed dynamic analysis. Additional correction factors may be needed to scale the average predicted stresses to account for spatial variances.

EXPERIMENTAL INVESTIGATION

The Magellan solar arrays, shown in Fig. 2, are approximately 100 inches in width by 100 inches in length. Each array consists of an aluminum honeycomb core, 1/2 inch thick, with 0.009 inch aluminum face sheets. For strengthening, a strongback, which is a U-shaped aluminum bracket, runs down the length of the panel in the center.

The panels were instrumented with accelerometers and strain gages

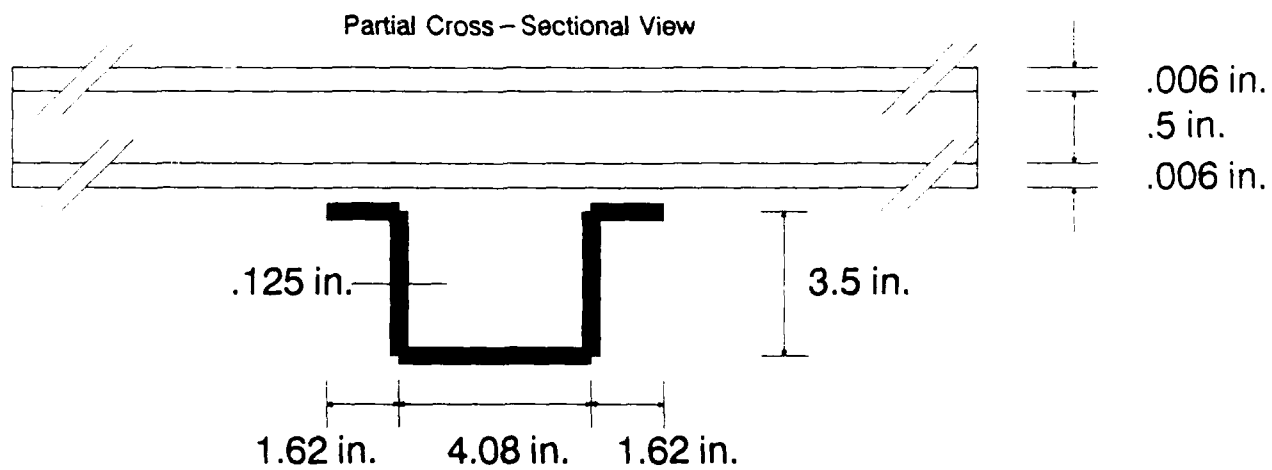
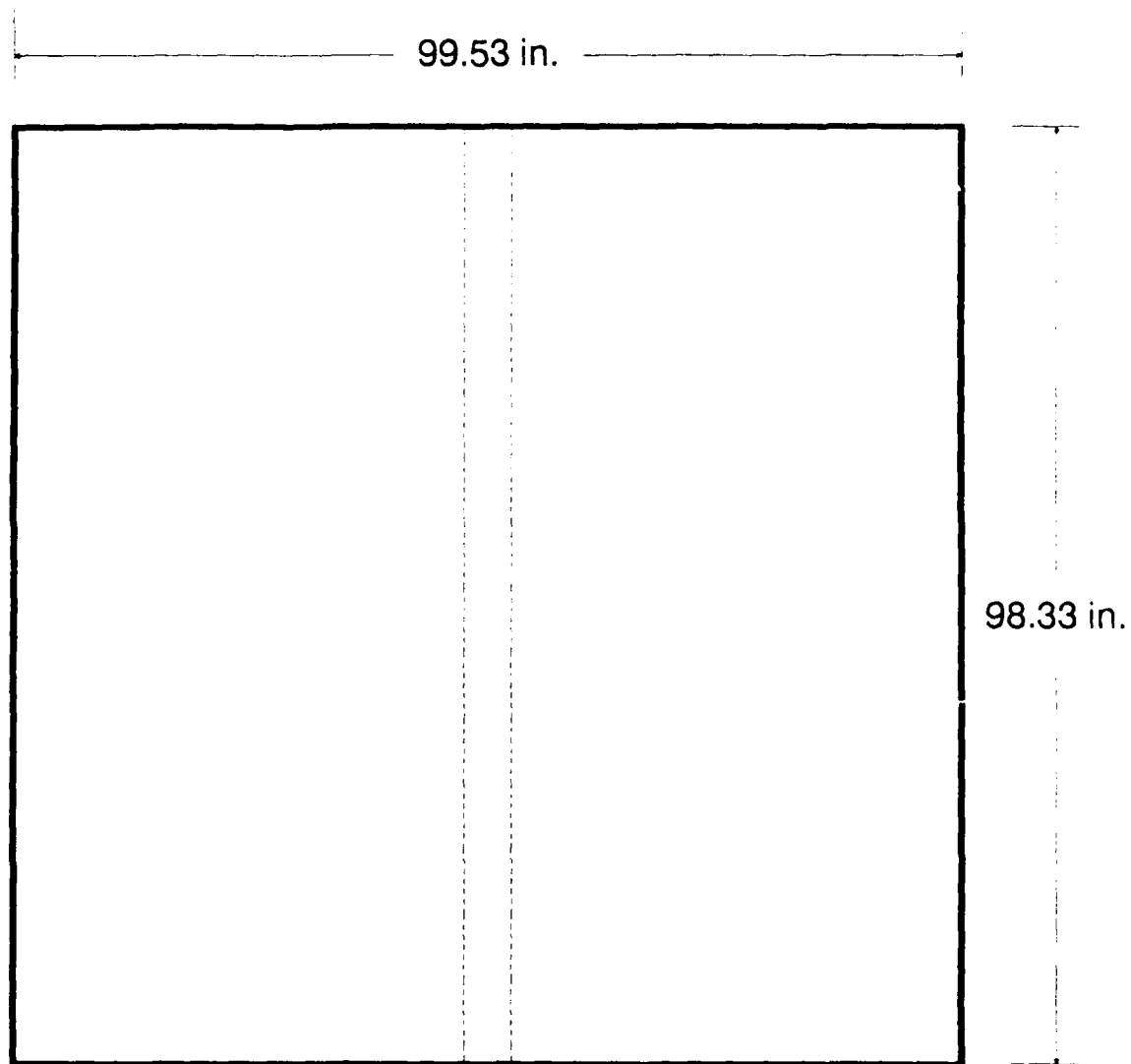
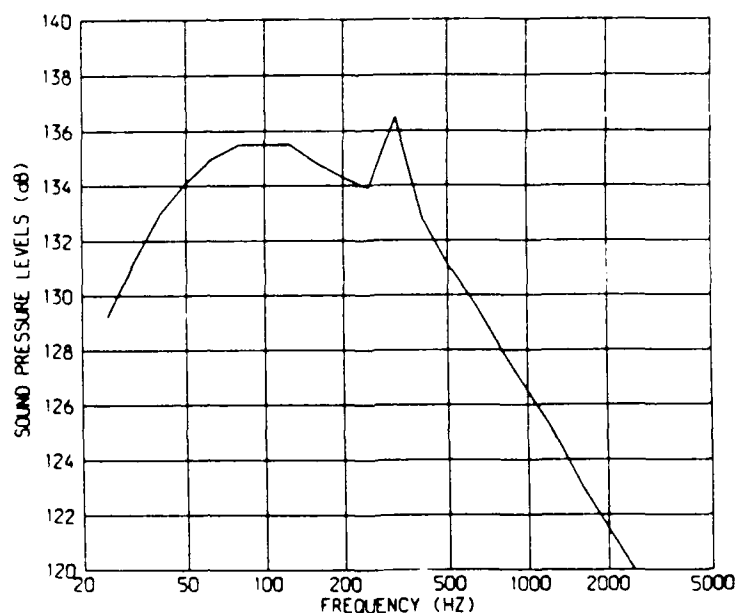


Figure 2. Magellan Solar Array Structure

during the Assembly Qualification Test. Actual flight hardware was not used. Test article solar arrays with mass simulated electrical and thermal subsystems were employed. Fig. 3 is a plot of the average microphone sound pressure levels recorded during the test. Figures 4 through 6 show the test configuration and instrumentation locations. Data from 54 response accelerometers, located on the solar array and support structure, were recorded during the test. Fourteen accelerometers mounted normal to the solar arrays were judged valid for comparison with the VAPEPS acoustic response prediction (4y, 5y, 8y, 9y, 10y, 11y, 12y, 14y, 15y, 18y, 19y, 20y, 22y, and 23y). The average of these accelerometers was used as an input for the VAPEPS stress prediction calculation. Five strain gage rosettes were used for the stress verification.

The test data were recorded on analog tape and then digitally processed. Microphone time histories were converted to one-third octave band pressure spectral densities in units of dBs (re 2×10^{-5} N/m²). Accelerometer data were digitized into one-third octave band acceleration spectral densities in units of G's squared per Hertz. Strain gage data were reduced to one-third octave band strain spectral densities in units of micro-inches/inch squared per Hertz. Stresses in the X and Y directions were then calculated from the measured strains. The stresses were calculated in two ways. The first calculation assumed uncorrelated strains, (all cross product terms were neglected); the second method assumed correlated strains, (cross product terms were included).



OVERALL SOUND PRESSURE LEVELS - 146 dB

Figure 3. Solar Array Assembly Qualification Test
Acoustic Excitation Input

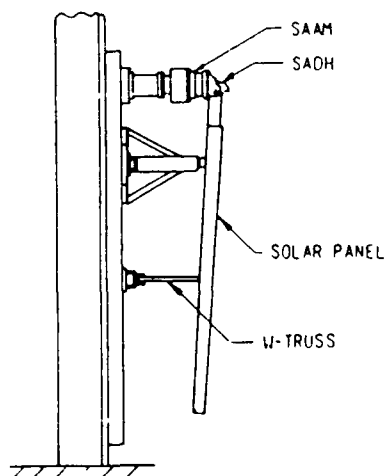


Figure 4. Configuration
for the Solar Array
Assembly Level Test

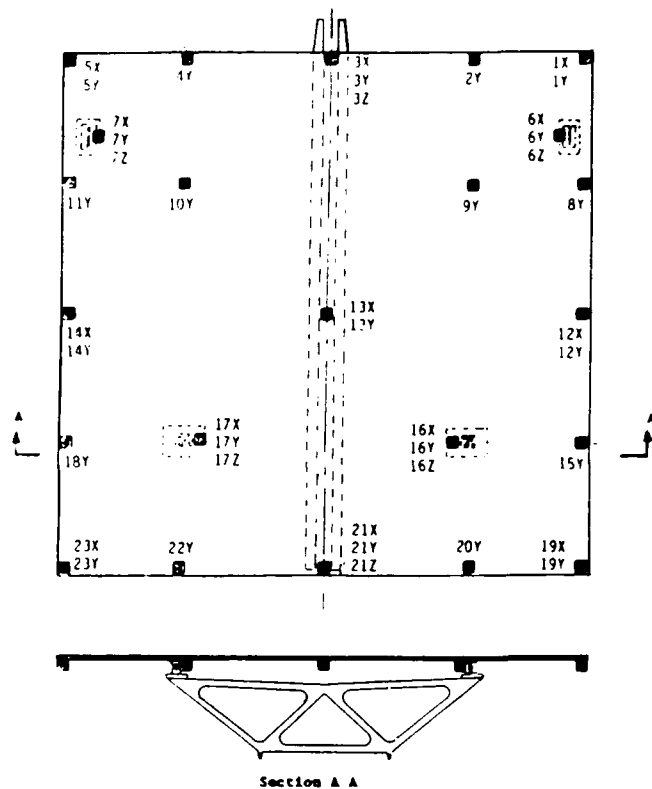


Figure 5. Accelerometer
Locations for the Solar Array
Assembly Level Test

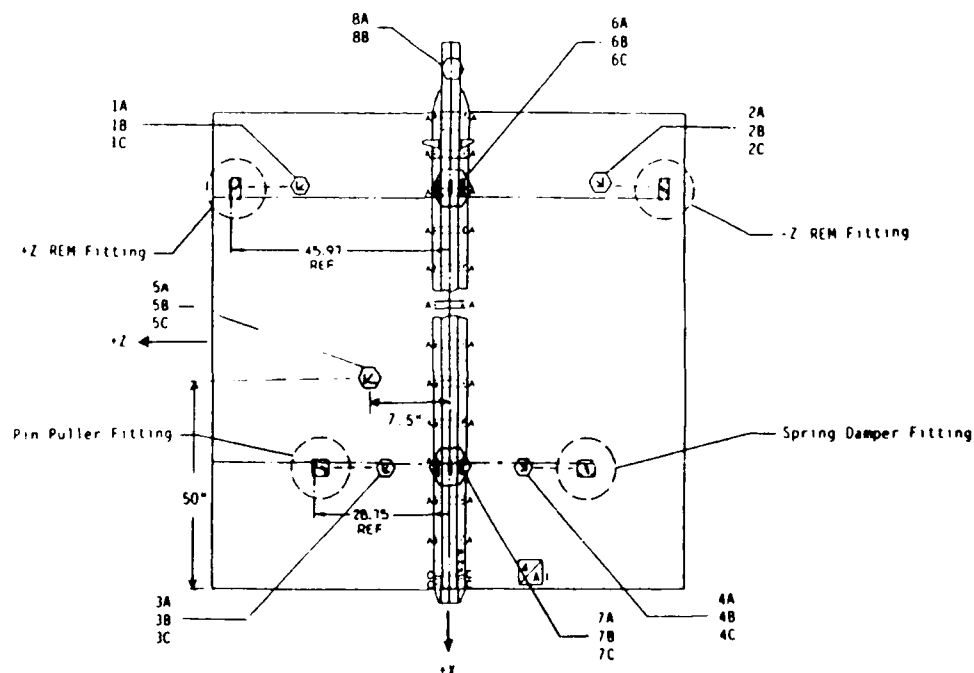


Figure 6. Strain Gage Locations
for the Solar Array Assembly Level Test

ANALYTICAL PREDICTIONS

Equivalent Panel Generation

The VAPEPS software includes a routine (RUN=EQPL) that calculates parameters for an equivalent isotropic, homogeneous, panel given the properties of the actual panel. The actual panel can include stiffeners and multi-layers of different materials. The bending wavespeed of the original panel is kept constant for the equivalent parameters calculated for the SEA prediction.

Two separate SEA models of the solar array were developed. The two models reflect the differences in structural behavior at low and high frequencies. These differences are due to the stiffening effects of the strongback. For the low frequency range (below approximately 100 Hertz), the strongback stiffens the panel. The strongback is incorporated as support beams in the calculation of the equivalent panel parameters. At higher frequencies (above 100 Hertz), the strongback does not affect the stiffness of the structure since the bending wave lengths are small in comparison to the size of the panel. Above 100 Hertz, the 2 halves of the panel vibrate independently. The core and face sheets are the only structure that is involved in this frequency range. The strongback is not included in the equivalent panel calculations used in the high frequency model, but is included in the SEA prediction as non-structural mass.

SEA Prediction

Two SEA models were created using these two sets of equivalent parameters for the high and low frequency ranges. In both cases, there were two SEA elements, an external acoustic space element and a skin element. Both SEA models allowed for excitation and radiation on both sides of the panel. The input excitation was the same for both models and is shown on Figure 3. The damping loss factor (DLF) was set equal to 0.1 which corresponds to a fraction of critical damping of 0.05. A pivot frequency (PIVOTFRQ) of 250 Hertz was used, which is recommended by the VAPEPS developer based on their experience and historical data. This decreases the damping as a function of $1/\text{frequency}$ with damping being 0.1 at 250 Hertz.

The full panel was modeled in the low frequencies. Solar cells, wiring, etc. were added as non-structural mass (ASMS). Since the strongback was already incorporated into the model during the equivalent panel calculation, no edge discontinuities were included for the strongback. Only the full perimeter of the array was used for edge discontinuities (PATA).

VAPEPS uses coupling-loss factors that are based on the assumption that the panel is baffled. The panels are unbaffled in this example. This affects the coupling-loss factor calculations below the coincidence frequency [5]. The coupling-loss factors were therefore adjusted to allow for an unbaffled panel. The calculated coupling-loss factors below coincidence for the simply-supported panel were multiplied by the ratio of the center frequency to the coincidence frequency. At coincidence, the coupling-loss factor was divided by two. These new loss factors were used for the prediction for the low frequency model. Coincidence for this model was at 221 Hertz.

The high frequency model considered only half of the panel because the two symmetrical halves were expected to vibrate independently above 100

Hertz. One-half of the strongback was included as additional non-structural mass. The perimeter of the half panel was used for the PATA value. Adjustments similar to the low frequency model were made to the coupling-loss factors. Coincidence for this model is at 600 Hertz.

Stress Prediction

Two stress predictions were performed. The first prediction used the acceleration response data from the Solar Array Assembly Qualification Test. The second prediction used the acceleration response predicted by VAPEPS. An equivalent homogeneous isotropic thickness was calculated for a solid panel by maintaining the moment of inertia of the honeycomb panel. The surface mass density was the sum of the mass densities for each panel layer plus the surface mass densities of the solar cells and wiring. The modulus of elasticity used was that of aluminum. The methods of calculating these parameters are similar to those used by Lockheed when they performed their verifications [2].

The stress prediction routine calculates the actual modal frequencies for the panel. Some frequency bands above the panel first resonance may not contain any modes. The prediction will show zeros for the calculated stresses within the bands that contain no modes. This mainly occurs in the lower frequency bands where bandwidths are smaller.

COMPARISON OF ANALYTICAL AND EXPERIMENTAL RESULTS

SEA Prediction

The results of the VAPEPS SEA predictions of the acceleration response of the panels are presented as one prediction (Fig. 7). This is a combination of the high frequency and low frequency models. The two predictions were combined at 100 Hertz.

The predicted results are slightly conservative across the spectrum except below 50 Hertz and above 600 Hertz. The over prediction below 50 Hertz is due to the lack of modes available for a good statistical calculation. SEA predictions are not valid where the number of modes is small; this model is considered invalid below 50 Hertz. The discrepancy above 600 Hertz, where the response is under predicted by as much as 7 dB, is believed to be caused by the following:

1. Non-linearities in the panel response which were noted during modal surveys. These non-linearities were attributed to the slop in the interface fittings used to support the panels during testing.
2. The accelerometers used to determine the spatial averaged response of the panel were located mostly near its edges, corners or areas where high responses were predicted from a finite element analysis. The measured data may therefore not be representative of the true rms acceleration. The measured accelerometer data are enveloped by the 95th percentile prediction.

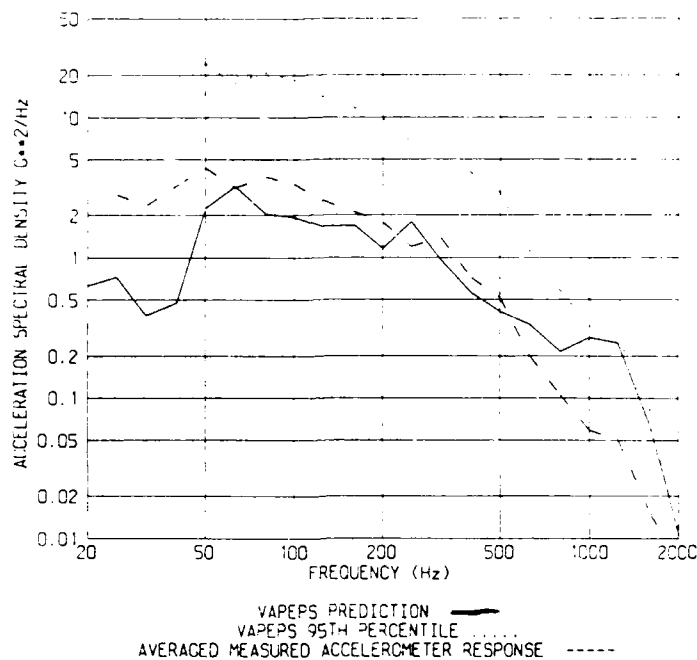


Figure 7. Comparison of Measured Response Data
and VAPEPS SEA Prediction
from Magellan Solar Array Assembly Level Acoustic Test

Stress Prediction

Both measured accelerations and accelerations predicted using VAPEPS were used as inputs to the stress model. Figures 8a-8d are a comparison of the predicted stresses to the calculated stresses from the measured strains. Shown are the comparisons of the stress predictions in the X and Y directions using the accelerations from the VAPEPS SEA prediction and the average of the measured accelerations from the Solar Array Assembly Level Test. Two sets of calculated stresses from the measured strains are presented on each plot. They are the extreme cases for the data analysis. The upper curve is the correlated case and the lower curve is the uncorrelated case. As expected, the stress prediction using predicted accelerations is conservative in the low frequencies since the accelerations were conservative. The stress levels predicted using measured accelerations compared better to measured stresses, although they were also conservative in the lower frequency bands. Again, this could be partly due to the effects of non-linearities in the support frame attach points. Also, the five strain gage rosettes were located in the center of the panel and may not be representative of the true spatial average. This could be the explanation for the discrepancies between the predicted stresses to the calculated stresses from the measured strains. Table 1 is a listing of the overall stress levels in PSI rms. The overall stresses for the two predictions using the different acceleration inputs, and the calculated stresses from measured strains from the correlated and the uncorrelated data

reductions are listed for both the X and Y direction.

Table 1
Comparison of Overall Predicted Stress Levels
to Overall Calculated Stresses from Measured Strains
in PSI rms

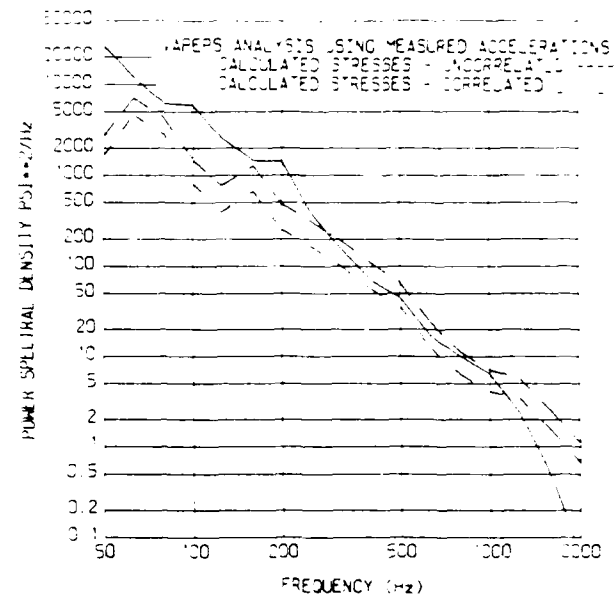
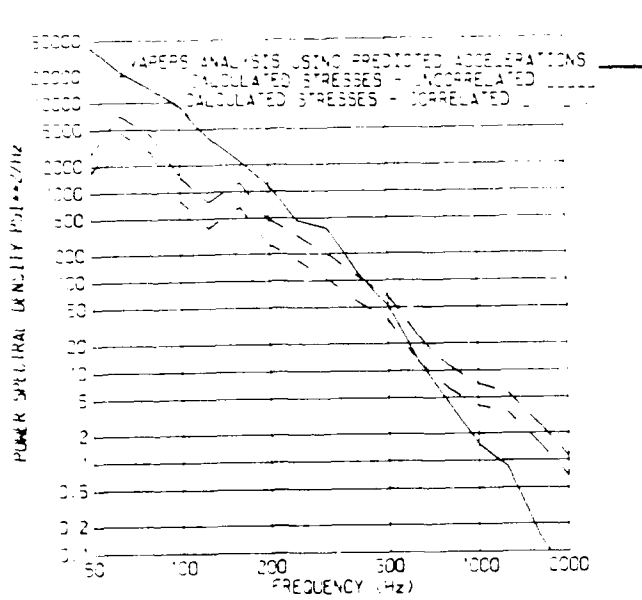
	Direction	
	X	Y
Predictions		
using VAPEPS predicted accelerations	1.59×10^3	1.45×10^3
using measured accelerations	1.34×10^3	1.33×10^3
Calculated stresses from measured strains		
correlated	7.77×10^2	9.15×10^2
uncorrelated	6.00×10^2	7.62×10^2

CONCLUSIONS/RECOMMENDATIONS

The stresses calculated using VAPEPS are within approximately a factor of two of the calculated stresses from measured strains within the solar panel. A thorough understanding of the assumptions used in SEA and the VAPEPS stress routine is necessary to be certain that models are developed which adequately represent the actual system. Large variances in structural parameters such as damping, non-structural mass, boundary conditions, and frequency dependent characteristics can significantly affect the response of the structure. If these effects are not accounted for in the prediction, the results will not be valid. The low frequencies are most affected by these structural parameters.

For the most accurate prediction of overall stresses, it is recommended that a stress prediction be performed with actual measured acceleration data. Should this not be available, using the responses calculated from a

X DIRECTION



Y DIRECTION

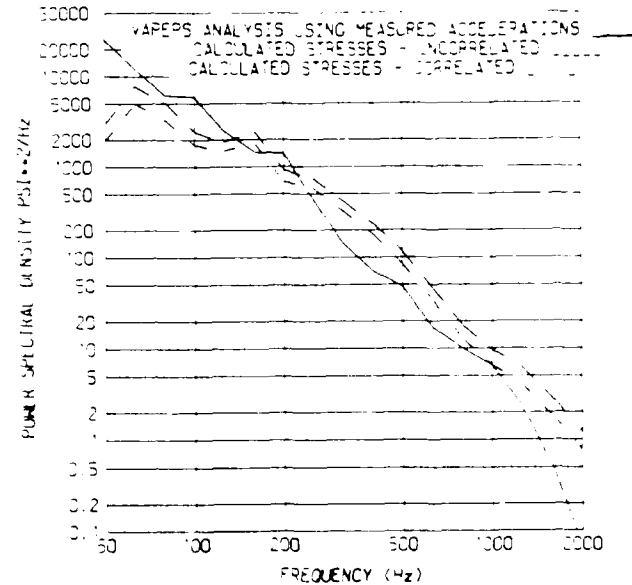
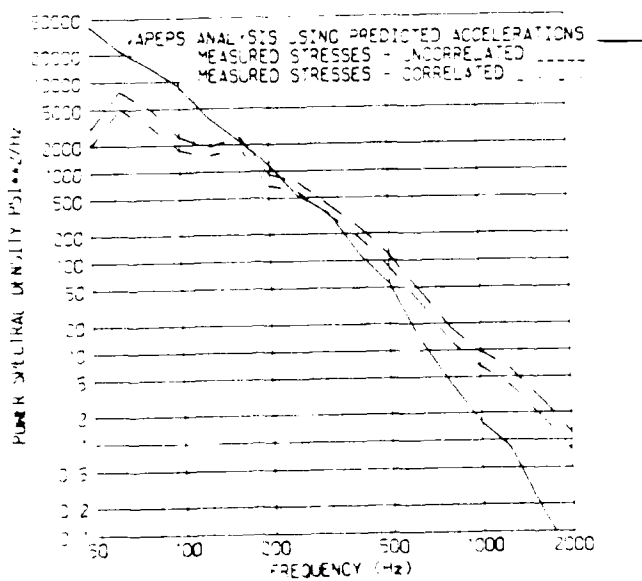


Figure 8a-d. Comparison of VAPEPS Stress Predictions to Calculated Stresses from Measured Strains From Magellan Solar Array Assembly Level Acoustic Test

VAPEPS model which has a high confidence level of accuracy is appropriate. VAPEPS has the capabilities to do predictions by extrapolation. This method uses information from previous flights or tests that are stored within the VAPEPS Global Database, or a database at a local site. This method predicts acoustic responses which have a high confidence level of accuracy.

The stresses predicted by VAPEPS for the Magellan Solar Arrays are adequate to show whether further analysis is required. The predicted stresses from VAPEPS give a slightly conservative approximation to the overall stresses. For all predictions, it is recommended that a FEA analysis be performed to the first few modes. This is a good supplement to the SEA prediction which is not accurate in the low frequency regime where there are not many modes.

ACKNOWLEDGEMENTS

The work described in this paper was performed for the Jet Propulsion Laboratory, California Institute of Technology, and was sponsored by the United States Air Force Space Division through an agreement with the National Aeronautics and Space Administration. The authors would like to thank Dr. Terry D. Scharton and Mr. Dennis L. Kern of the Jet Propulsion Laboratory for their technical advice and for the stimulating and informative discussions of these models.

REFERENCES

1. Y. A. Lee, W. Henricks and D. Park, "VibroAcoustic Payload Environment Prediction System (VAPEPS) Volume I: VAPEPS Improvement and Verification," NASA CR 177905, Sept. 1985.
2. Y. A. Lee, D. Crowe and W. Henricks, "VAPEPS Improvement with Stress Estimation and Progressive Wave Excitation," NASA CR 180783, June 1987.
3. "Vibroacoustic Payload Environment Prediction System," Volumes I-V, NASA CR 166823, Lockheed Missiles & Space Company, Sunnyvale, CA, Dec. 1982.
4. L. D. Landau and E. M. Lifshitz, Theory of Elasticity, 2nd Edition, Pergamon Press, New York, 1970.
5. William K. Blake, Mechanics of Flow-Induced Sound and Vibration, Vol. 1, Academic Press, New York, 1986. pg.332

BIBLIOGRAPHY

1. R. H. Lyon, Statistical Energy Analysis of Dynamical Systems, MIT Press, Cambridge, MA, 1975.
2. William T. Thomson, Theory of Vibration with Applications, 2nd Edition, Prentice-Hall, Inc., New Jersey, 1981.

DYNAMIC MEASUREMENT

AN AUTOMATED VIBRATION TRANSDUCER CALIBRATION SYSTEM USING ADVANCED FFT TECHNIQUES

Torben Licht
Brüel & Kjær Instruments, Inc.
Nærum, Hovegade 18
Denmark
and
Ernst Schonthal
Brüel & Kjær Instruments, Inc.
185 Forest Street
Marlborough, MA 01752

ABSTRACT

The 2 Channel FFT Analyzer makes it possible to calibrate a vibration transducer, at a large number of points over a wide frequency range, in one single measurement. The ability to control the 2 Channel FFT Analyzer by a personnel computer forms the basis for an Automated Vibration Transducer Calibration System. An overview of considerations, requirements and consequences will be discussed.

INTRODUCTION

For the Calibration Laboratory there is a number of obvious benefits by having the calibration process automated.

1. High, consistent accuracy
2. Reduced operator dependency
3. Faster calibration
4. Consistent philosophy
5. Database management capability

To obtain these benefits the first decision to be made is the choice of a suitable calibration method.

CALIBRATION OF TRANSDUCERS

Principles of Back-to-Back Calibration by Substitution

The traditional back-to-back calibration technique is based on the principle illustrated in Fig. 1. The Device Under Test (DUT) is mounted in a back-to-back manner with a Standard Reference Accelerometer, and the combination is mounted on a suitable vibration source. The input acceleration to each accelerometer is identical and consequently, the ratio of their sensitivities is simply the ratio of their outputs.

Traditionally, the accelerometers are excited at a single frequency, and their outputs are measured (after suitable pre-amplification) by using a high quality electronic voltmeter, the accuracy of which is known. This method produces good results. However, it produces a measure of the sensitivity at a single frequency. Therefore, attaining a comprehensive knowledge of an accelerometer's characteristics can be rather time consuming.

Back to Back Calibration Calibration by Comparison

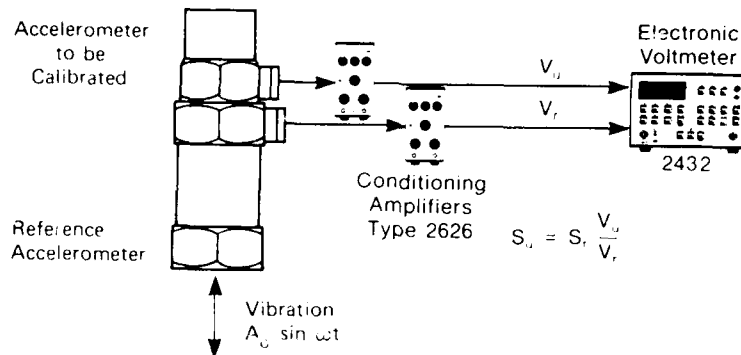


Fig. 1. Principle of the back-to-back calibration technique

Back-To-Back Calibration Using FFT Analysis

The advent of the dual-channel analyzer (with built-in broad-band random noise generator) enables relatively fast frequency response function (magnitude and phase) measurement. Consequently, the sensitivities of two accelerometers can be compared by using a Dual-Channel Signal Analyzer to measure the ratio of their outputs. By feeding the output from the standard reference accelerometer to the channel A input, and the output from the test accelerometer (DUT) to the channel B input, the relative sensitivity of the DUT can be presented on the analyzer's display screen as a frequency response function (magnitude and phase).

Calibration by substitution

In practice, it has proved advantageous, with regard to accuracy, to employ the FFT-based back-to-back calibration method, using the calibration by substitution technique, which eliminates channel mismatch and gain errors.

The calibration by substitution technique, which is based on the principle shown in Fig. 2, involves making two measurements. The reference measurement, in which a working standard accelerometer is calibrated against a standard reference accelerometer, is stored. Then the DUT is calibrated against the working standard, producing a frequency response function measurement, which is compared to the stored measurement. The working standard remains fixed to the exciter head. The standard reference accelerometer and the DUT are individually compared to the working standard. The charge sensitivity of the unknown accelerometer is then calculated as follows:

$$\frac{S_u(f)}{S_s(f)} \times \frac{S_r(f)}{S_r(f)} = \frac{H_u(f)}{H_r(f)} \text{ or } S_u(f) = S_r(f) \times \frac{H_u(f)}{H_r(f)}$$

where $S_u(f)$ is the charge sensitivity of the test accelerometer

$S_r(f)$ is the charge sensitivity of the standard reference accelerometer

$S_s(f)$ is the charge sensitivity of the working standard accelerometer for the measurement

$H_u(f)$ is the frequency response function for the test accelerometer relative to the working standard accelerometer

$H_r(f)$ is the frequency response function for the standard reference accelerometer relative to the working standard accelerometer

The ratio $H_u(f)/H_r(f)$ can be found directly from the equalized frequency response function. This is a post-processing function of the analyzer, which calculates the complex ratio between the measured and stored frequency response functions.

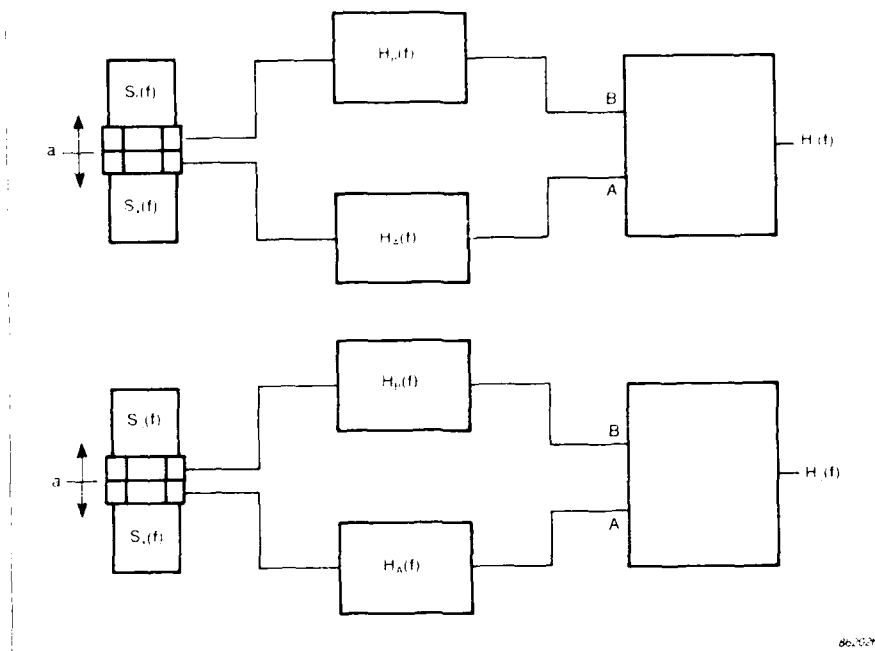


Fig. 2. Principle of the back-to-back calibration by substitution technique

CALIBRATION SYSTEM

The calibration system shown in Fig. 3 has been designed to achieve the goals listed in the introduction.

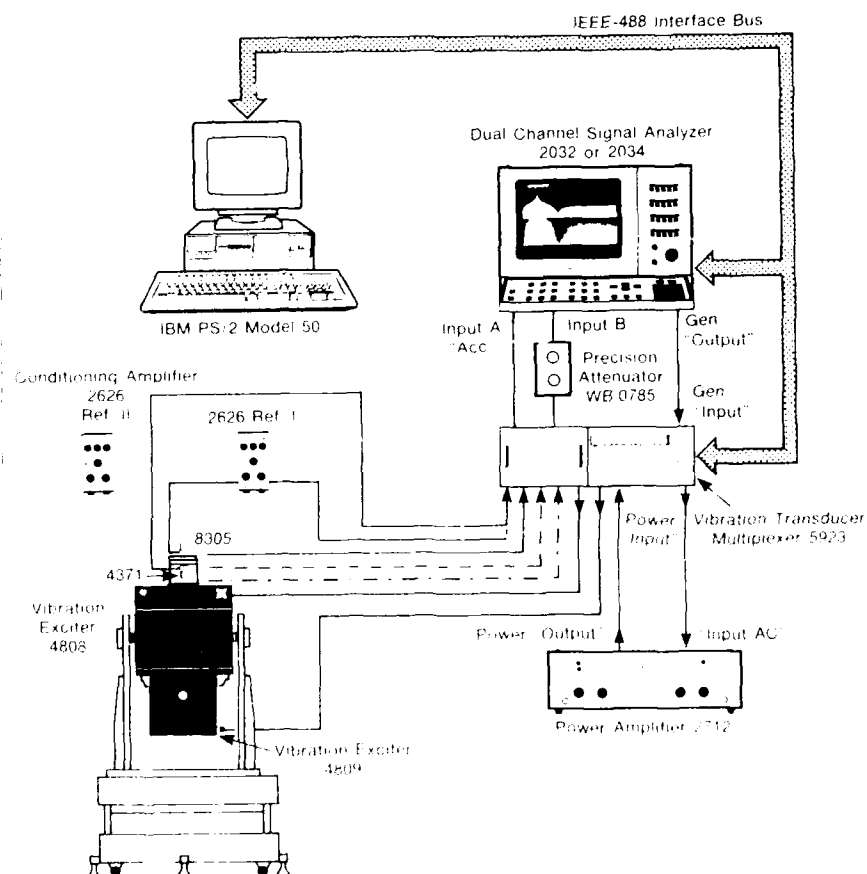


Fig. 3. Calibration System instrumentation setup

High, consistent accuracy

To achieve this major goal a number of precautions has been taken.

1. The above mentioned calibration by substitution method using random-noise excitation is used. This gives a full frequency response function (800 - 1600 lines) in about the same time as one or two points with traditional methods. The substitution removes the dependence on gain of all the instruments but one- a precision attenuator.

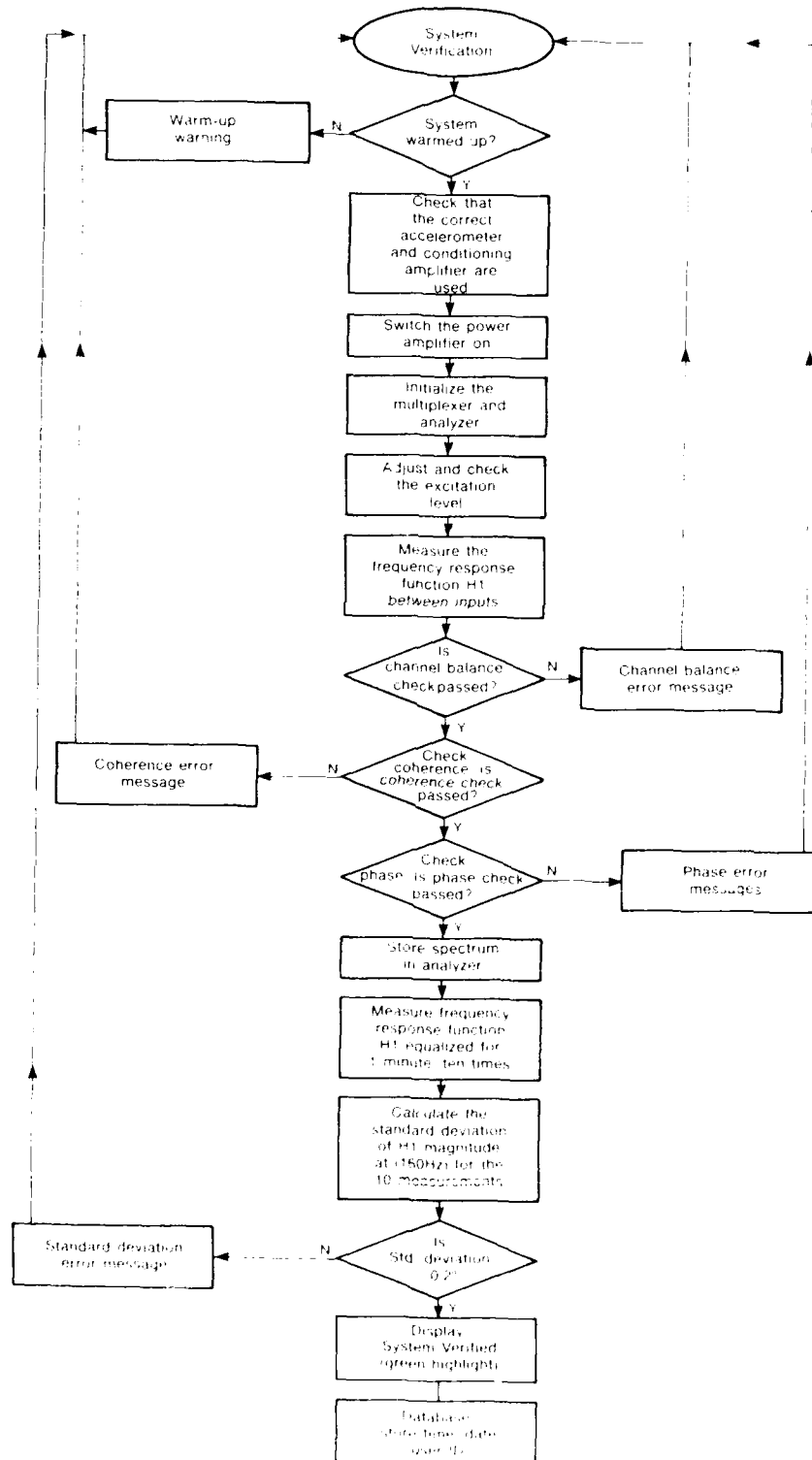


Fig 4 Flow chart for the System Verification program

2. Verification

To obtain VALID calibrations (i.e. data which can be stored in the database. A printout clearly marked NOT VALID can however always be made) three conditions must be fulfilled:

a. The system must be warmed up (1/2 hour)

b. A System Verification must have been performed.

This consists of 10 consecutive one minute measurements on a reference standard transducer. The standard deviation of the measured sensitivities of the reference frequency must meet strict tolerances (e.g. less than 0,2%). A flow chart is shown in Fig. 4.

c. A Standard Verification must have been performed.

This is a comparison of two reference standard accelerometers at the reference frequency. If they do not compare as specified within strict tolerances (e.g. 0,5%) changes are that one of them has changed for whatever reason.

3. Coherence is measured during verifications (to very strict tolerances) and during calibration to guarantee that the signal to noise level is sufficiently high, that no spurious signals are present and that the transducer is reasonably linear.
4. Corrections taking into account the frequency dependence of the reference standard sensitivity and the different mounting conditions can be made automatically.

Reduced Operator Dependence

The operator is relieved from all the operations which could be computer-controlled i.e.

- Retrieval of test specifications
- Analyzer set-up
- Input selection
- Attenuator selection/bypass
- Level adjustment
- Report preparation and writing
- File Keeping

Furthermore, the computer prompts all necessary operations and checks most manual settings.

Therefore the operator can concentrate on some of the crucial operations in vibration transducer testing:

- Inspection of transducer mounting surfaces
- Inspection of transducer connectors
- Proper mounting
- Proper cable connection and mounting
- Proper labelling

FASTER CALIBRATION

The time to perform one calibration can be divided in four parts:

1. Find test specifications.

The system uses a very rapid and easy to use menu system to select the test specifications for a given type of transducer. Figs. 5 and 6 shows the Main Menu with entry to Product Data and the Generic Product Data file for an accelerometer. It is a matter of a few seconds to select the transducer. Compared to classical retrieval of manuals and records at least a factor of 10 is gained.

2. Inspection and mounting

This is still manual operations with a duration of one to two minutes. There are no reason to believe that this will ever be made by robots except for dedicated production lines.

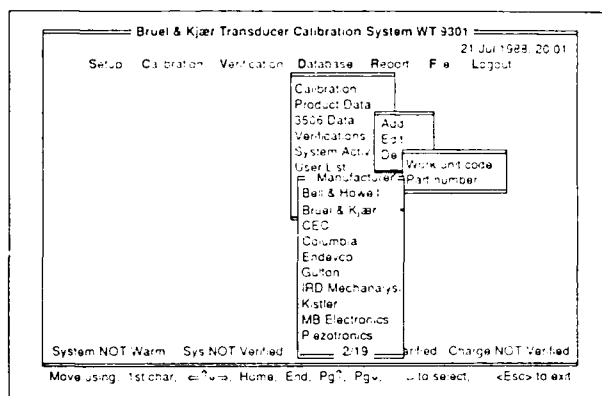


Fig. 5. The Main Menu

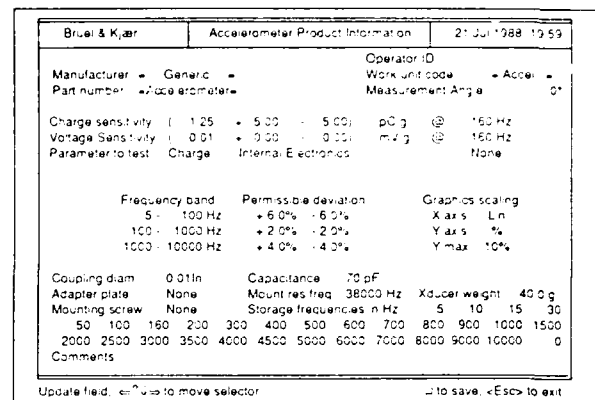


Fig. 6. Generic Product Data file for an accelerometer

3. Calibration Measurements

A calibration giving 1550 measurement points is performed in 2-3 minutes.

The duration is mainly determined by the averaging over 64 spectra at low frequencies. This is a fundamental limitation (Bandwidth \times Time) which cannot be circumvented by any method. The time to do the same measurements manually would probably be at least 100 times longer (but maybe fewer points were acceptable).

4. Report preparation and writing

Only the serial number of the transducer has to be typed in, after which the calibration report can be downloaded into a print spooler in a few seconds, and the system is ready for the next measurement using spare time to print the report simultaneously.

Again this would take 10 to 100 times longer, if not more, to do manually, even on a pre-printed chart.

From the above it can be seen that the total time is reduced at least by a factor of 10, and that further reduction possibilities are limited.

CONSISTENT PHILOSOPHY

In many calibrations a certain amount of personal judgement are used to determine whether a transducer can be accepted or not.

By entering acceptance/rejection criteria in the computer database no personal judgement and differences in judgement from day to day or from person to person will alter the decisions.

This provides a consistent philosophy.

DATABASE MANAGEMENT CAPABILITY

The database contains the following information:

- Reference Standard Transducer specifications
- Transducer test specifications
- System Users, their pass words and security level
- System activity - entries, verifications and calibrations

Calibration Results

A number of possibilities to sort or select these data are provided to permit easy access to view or print out the content of the database.

Backup and filing functions are provided and a restructuring function permits optimum use of the available hard-disc memory.

CONCLUSION

Automation of vibration transducer calibration is a reliable way to make the calibration laboratory fulfil the primary goals of high consistent accuracy, large throughput, consistent philosophy and good filing practices.

REFERENCES

- [1] ROBERT HAGGER & GINGER CORLEY: "*Automating the Calibration Process*", National Conference of Standards Laboratories 1988
- [2] BARRETT C. CRANER: "*Software Evaluation in the Laboratory - an overview*" National Conference of Standards Laboratories, 1988
- [3] LICHT, T.R. & ANDERSEN, E.: "*Trends in Accelerometer Calibration*", Brüel & Kjær Technical Review 2, 1987

DYNAMIC CRITERIA

AVIONICS ENVIRONMENTAL RELIABILITY

Amarshi A. Bhungalia and George Kurylowich

Environmental Reliability Group
Environmental Control Branch
Vehicle Subsystems Division
Flight Dynamics Laboratory

ABSTRACT

This paper presents progress in developing and demonstrating an analytical method for evaluating avionics Printed Circuit Board (PCB) and Line Replaceable Unit (LRU) stress levels and life available prior to failure. The prediction capability provides vibrational stress assessment based on finite element modeling of the electronic components, associated avionic boards and LRU's. The analytical method is applicable to vibration environments that are encountered in the service of military aircraft/spacecraft. The objective of the effort is to provide an analytical capability to be used by government procurement agencies to evaluate the avionic designs of avionic suites to be used by the United States Department of Defense (DOD). The experimental validation effort conducted by the contractor is presented and discussed. Progress to validate the structural prediction models through governmental in-house efforts are also presented and discussed herein.

INTRODUCTION

Studies conducted from the early 1970's through the middle 1980's have shown that military avionic equipment accounts for 20 - 40% of all maintenance actions (See References 1 & 2). In the past, assessment and verification of hardware reliability was generally achieved through testing, both in the laboratory and in operations. Today, the emphasis is on striving for greater reliability during the design stage by better defining the environment, and also by developing an assessment tool so that the design of the system can be evaluated prior to procurement (See References 1 through 7).

This paper presents the development of a technology to be transitioned to the avionic procurement community. The objective of this transition is to improve avionic reliability early in the DOD procurement design process through innovative applications of computer aided engineering (CAE). The computerized resource described herein permits the reliability of individual components on the printed circuit board, or the LRU to be quickly evaluated. In addition, it is necessary that an effort be conducted to demonstrate that this computerized capability provides estimates of stress and Mean Time Between Failure (MTBF) that are within acceptable limits to the CAE user. The initial

steps in validation of these computerized capabilities by performing correlations of analysis with experimental data is given in this paper.

PROGRAM PLAN

The Environmental Control Branch (AFWAL/FIEE) of the Vehicle Equipment Division of the Flight Dynamics Laboratory (AFWAL/FI) initiated a program in 1985 which consisted of three contractual efforts which were to: (1) Develop a computer-aided engineering program to analyze electronic designs for vibration environments during the Preliminary Design Review (PDR) and Critical Design Review (CDR); (2) Develop a reliability life model or algorithm for avionics, based on analysis of existing avionic vibration fatigue data; and (3) Parallel the above reliability life model effort by developing an algorithm reflecting thermal cycling environmental stress-related impacts when imposed on the avionics. The effort related to the vibrational aspects of this effort have been completed and are discussed herein. Efforts relating to the thermal cyclic effort are not completed; thus, discussion related to thermal analysis is not presented in this paper.

VIBRATION STRESS ANALYSIS OF AVIONICS

Studies were conducted by Rome Air Development Center (RADC), NY, and the Naval Avionics Center (NAC), IN, to select a finite element analysis program appropriate for modeling avionic packages. Several finite element programs reflecting the advancements made by 1983 in adapting finite element computerized analyses towards electronic component/board/enclosure geometrical/analytical considerations were considered. In light of the above and additional studies conducted, the candidate capability selected and purchased by AFWAL/FIEE was a finite element capability identified for use in analysis of electronic packages as the "Numerical Integrated Elements for System Analysis (NISA)" computer code (See References 8 & 9).

AFWAL/FIEE then began developing a preprocessor to NISA in the effort described in the Program Plan given above. This preprocessor was designed to permit entry of relatively easy-to-obtain descriptive information about the PCB or LRU to be analyzed. The information that is input consists of board dimensions and structural characteristics, component locations, type of component, and all other related data needed. After the information is entered, the preprocessor constructs the appropriate finite element representation to be used by the NISA analysis. The finite element mesh size, arrangement, mass and stiffness lumping is accomplished using engineering rules embedded within the preprocessor (See References 10 & 11).

A part of the computerized preprocessor development was to include "default" or typical component "Size/Geometrical/Structural" characteristics for users who are not familiar with industry Electronic/Fabrication/Integrity standards. These "default" electronic components and their characteristics are provided in Figure 1. Details as to lead wire definition is depicted in Figure 2 of the components considered. The effect of wire dimension ($diam_{+}$) as well as the effect of wire bending effects are also reflected in the Fatigue Relationship curve shown in Figure 2.

Now, correlations of analyses versus tests were performed by the contractor of this effort. The Lockheed Company, CA, which developed these computerized predictive capabilities, selected a flight control avionic LRU used in the Air Launched Cruise Missile (ALCM) and Ground Launched Cruise Missile (GLCM) as a test specimen. Multiple axis-vibration tests were performed on the unit (See Figure 3). The results of this test are shown in Figure 4 (Also, see References 10 & 11); of importance, the finite element analysis provided good correlation with test data and the peak values agreed within 15 percent between test and analysis.

IN-HOUSE VALIDATION OF THE VIBRATIONAL CAPABILITY

Upon receipt of the preprocessor software in late 1986, an in-house effort was initiated to validate the NISA capability. The first effort undertaken was to correlate the finite element model against exact solutions provided by Steinberg (See Reference 3). In addition, this effort included use of the NASA Structural Analysis (NASTRAN) computer program for purposes of correlations with the results from the NISA program, and the results are shown in Figures 5 through 11. The purpose of the NASTRAN correlation effort was that this capability is accepted by structural analytical technologists in government and industry as a standard. It is seen that the correlation for vibrational frequency f_n , the vertical axis in these figures, is excellent between the exact theoretical solution, and the NISA and NASTRAN results for the first 5 modes of excitation.

Reference is now made to Figure 5 as the example on how the exact solutions for each mode of frequency excitation f_n were obtained. The first mode solution is defined in the upper left corner of this figure for one fixed edge. Modes 2 through 5 were obtained by multiplying the result for mode 1 by adjustment factors given in Reference 12 as a function of the mode excited and as a function of the number of free edges, supported edges, and fixed edges restraining the board. This procedure was applied for all modes above the first for the results shown in Figures 5 through 11. As indicated above, the correlation of the NISA and NASA results with the exact solution is excellent.

An in-house effort was conducted using the test specimens, as geometrically constrained by boundary conditions shown in the upper left hand corners of Figures 12 through 17. These boards were tested while mounted in a rig that constrained their edges. The rig was then mounted on a shaker and excited through frequencies from 10 to 2000 Cycles Per Second (CPS). Ten small mass accelerometers were mounted on the boards with one accelerometer mounted on the rig restraining the test specimens. The test data was measured and stored on magnetic tape. Data reduction was performed following the test to produce time histories of excited modes at the locations of the accelerometers.

Figures 12 through 17 identify the boards as being either composite or steel. Those test specimens given as composite consisted of copper/fiberglass/copper layers; that is, the copper outer layers were .003 in. thick while the middle fiberglass layer was .06 in. thick. The steel boards were .063 inches in thickness.

Each board tested had an electronic component located at each of the ten crosses shown on the boards depicted in each of the figures. The components consisted of capacitors, integrated circuits (IC), diodes, transistors, and relays. These components were representative of the component data base stored in the preprocessor (Also see Figure 1). The electronic components, as well as the accelerometers attached to the board, were represented as point masses attached to the board modeled in the NISA analysis performed. The components mounted onto the board were not representative of any electronic circuit; that is, there was no wiring attaching the components into a circuit and none of the components were powered or heated by any external source.

As seen in Figures 12 through 17, the correlation of the NISA analysis with test data was excellent in so far as the frequency was concerned relative to the modes excited.

FURTHER VIBRATIONAL RELIABILITY LIFE MODEL CONSIDERATIONS

An extensive open and private literature search was performed to collect data related to fatigue failures in electronic components, lead wires, and solder joints. The fatigue data was identified as being dependent upon the type of mounting used, such as surface mounted or poked through, and whether a multi-pin DIP had side brazed leads or bent leads. The types of component fatigue data identified are delineated in Table 1.

The focus of the technical efforts in this study used the identification and validation of simplified methods for stress analysis of components mounted on PCBs. This approach, while technically attractive, could not be fully validated since the current state of the art is such that direct measurement of stress/strain in component leadwires is difficult. Despite quantity and quality problems with the fatigue data collected, it was observed that this study should be focused upon leadwire and solder joints. A data base was formulated for the default mechanical properties of each component, mounting geometry, series of curves and charts that have the stresses and fatigue lives previously calculated for each component.

As part of this effort, studies were conducted to develop a simplified finite model for accurately predicting fatigue life of the electronic components. A PCB can be populated with many electronic components, and modeling each and every component with each and every pin could be time-intensive, because of the resultant size of the finite element model. The approach used to solve this problem was as follows: (1) Guidance provided in References 10 and 11 showed that under vibration stress, the outermost pins on a component fail first provided all the pins/solder joints are of equal strength; (2) The outermost pins at four corners were modeled in the NISA and preprocessor separately, and second, third, and fourth pins were lumped and modeled at the location of the third pin; and (3) The outermost pins were assumed to experience the most stresses and pins closer to the center of the critical component were assumed to experience the least impact. This approach resulted in smaller finite element models in the preprocessor, and savings in computer time. The validation of the analyses through correlation with test data still

needs to be performed.

The collected vibration fatigue data indicated that there was a threshold size for most component types. Components smaller than the threshold value were considered to not fail before a component larger than the threshold, provided everything else was equal. Using this criteria, critical threshold sizes were established. The established critical component sizes for vibrational fatigue are summarized in Table 1. This approach permitted the analysis to be focused on the critical components rather than in modeling everything. This saved computing time while not sacrificing accuracy.

CONCLUDING REMARKS

Presented herein is the progress achieved in developing and demonstrating an analytical development, based upon finite element modeling, for predicting avionic equipment stress/strain characteristics and the life available in the equipment prior to failure.

The first effort initiated was to correlate the analysis with exact solutions provided for the first mode of vibratory excitation by Steinberg (See Reference 3) and which was extended to the higher modes by Leissa (See Reference 12). Included in this effort is correlation of the analytical method with NASTRAN, a finite element method long accepted by structural engineers as a standard. The results are shown in Figures 5 through 12. The correlation of the exact solution with the results from this predictive method and also NASTRAN are excellent. The conclusion reached was that the analytical method developed produced good results when applied to homogeneous plates, or boards, that are free-edged, edge supported, or fixed edged as the boundary condition. This correlation relates only to the natural frequency excitation related to the first five modes of excitation. Correlations of board displacement and/or stress/strain characteristics as compared to the NISA and/or NASTRAN predictions still need to be shown.

A test was conducted using a composite board and a steel board with 10 electronic components mounted on the board. The results of the tests as correlated with the frequency prediction of the analysis are shown in Figures 13 through 17. Again, the correlation of the results from the test with analysis is excellent. The conclusions reached are that the analytical method developed can be applied to composite avionic boards and that good results can be expected when the electronic components are relatively small so as to be represented as a point mass, as was the modeling used in the case here.

Further efforts are needed, and are planned as part of the effort to validate that this computerized capability provides good results for: (1) Board displacement (the results shown in Figures 5 through 17 do not include displacement as a function of frequency); (2) The electronic component models as provided by the default representations shown in Figure 1; (3) The prediction of stress/strain/life when an actual component differs significantly from the default representation of the component as given in Figure 1; (4) The life prediction because of the variations in component weight, lead wire diameter, board thickness etc., due to tolerance errors

induced by the manufacturing process followed in producing the components and boards; and (5) The prediction of stress/strain/life as a result of the simplifying assumptions made to decrease computation time.

To conclude, a prediction capability has been developed that permits rapid assessment of vibrational stresses and Mean Time Between Failure (MTBF) of avionic equipment and LRU's. The capability is computerized, user friendly, and depicts the equipment being analyzed in color graphics, prior to analysis, to provide a check reducing the probabilities of erroneous geometric and electronic component characteristic inputs by the user. The purpose of the effort is to provide an analytical capability for government procurement agencies to evaluate the avionic designs of avionic suites. The correlation of this predictive capability with test data conducted so far is very encouraging. Please contact the primary author of this paper for further details for becoming a user of this capability.

1. ANON., "United States Air Force Reliability and Maintainability (RM 2000) Action Plan", 1 February 1985.
2. Dantowitz, A., Hirschberger G., and Praviolo, D., "Analysis of Aeronautical Equipment Environmental Failures", AFFDL-TR-71-52, 1971.
3. Steinberg, D. S., "Vibration Analysis for Electronic Equipment", John Wiley & Sons, 1973.
4. Sloan, J. L., "Design and Packaging Electronic Equipment", Van Nostrand Reinhold, 1985.
5. Burkhard, A., and Earls, D. L., "Development of a Combined Environment Test for Reliability Assessment of Avionics Systems", NAECON, 1977.
6. Parther, D., and Earls, D. L., "Combined Environment Reliability Test (CERT) for Avionic Systems", The Journal of Environmental Sciences, March/April 1975.
7. Burkhard, A., "Evaluation of Engineering Environmental Testing and Evaluation Technology", The Journal of Environmental Sciences, Vol. XXIX, No. 2, March/April 1986.
8. Southland, J. R., Beatty, V. R., Vitallano, W. J., "Finite Element Analysis of Microelectronic Packages", RADC-TR-82-133, 1982.
9. Kothawala, K. S., Mathers, M. D., Razzaque, A., Ho P., "Numerically Integrated Elements for System Analysis, User's Manual", Engineering Mechanics Research Corporation, 1985.
10. Soovere, J., Dandawate, B. V., Garfinkel, G. A., et al., "Vibration Stress Analysis of Avionics", AFWAL TR-87-323, April 1987.
11. Soovere, J., Dandawate, B. V., et al., "Vibration Reliability Life Model for Avionics", AFWAL-TR-87-348, September 1987.
12. Leissa, W., "Vibration of Plate", National Aeronautics and Space Administration, Washington, D. C., N70-18461, 1969.

HYBRID

No. of Pins = 44

A = 1.300 ; B = 1.595 ; C = 1.600
D = 0.1800 ; E = 0.1000 ; F = 0.1000
G = 0.1800E-01 ; H = 1.100

These are default values.
You can redefine them by using the " USER-DEFINED HYBRID " option.
Will you USE them to define the component?(y/n) >

HYBRID PACKAGES

- 1 22-pin PM2201
- 2 24-pin PM2401
- 3 38-pin PM3801
- 4 36-pin PM3601
- 5 44-pin PM4401
- 6 USER-DEFINED HYBRID
- 7 CRITICAL COMP MENU

DIP

No. of Pins = 40

A = 2.096 ; B = 0.6000 ; C = 0.1350
D = 0.1000 ; E = 0.1850E-01 ; F = 0.5000E-01
G = 0.1850 ; H = 0.1000E-01 ; I = 0.1500

These are default values.
You can redefine them by using the " USER-DEFINED DIP " option.
Will you USE them to define the component?(y/n) >

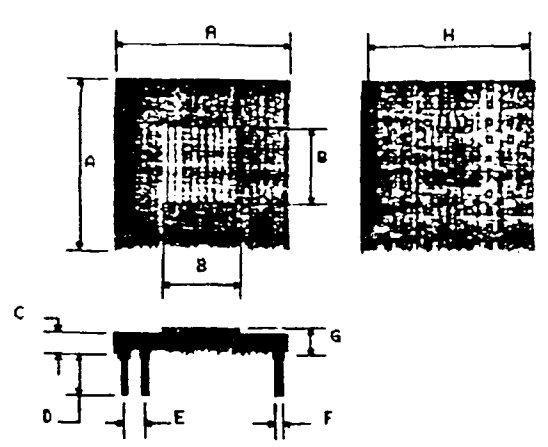
D I P e

- 1 18-pin DIP
- 2 20-pin DIP
- 3 22-pin DIP
- 4 24-pin DIP
- 5 40-pin DIP
- 6 USER-DEFINED DIP
- 7 CRITICAL COMP MENU

HYBRID/DIP

FIGURE 1. ELECTRONIC COMPONENT DATA BASE (GENERALIZED REPRESENTATION) (CONT'D)

PIN ARRAY



PIN ARRAY₆

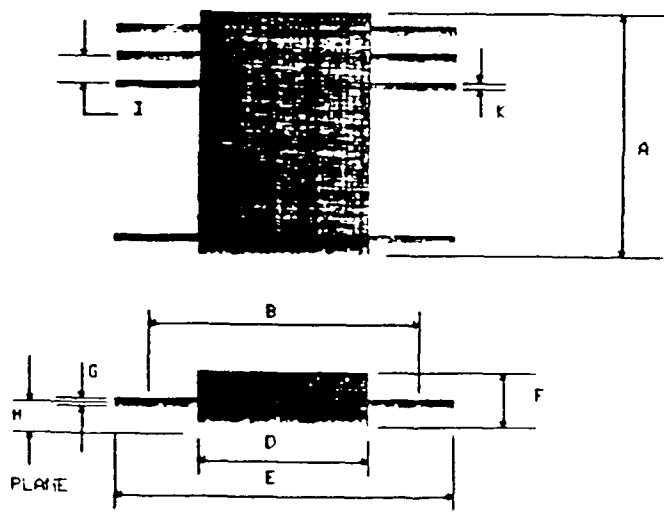
- 1 TWO LAYERS OF PINS
- 2 THREE LAYERS OF PINS
- 3 USER-DEFINED
- 4 CRITICAL COMP. MENU

No. of PINS = 84

A = 1.120 ; B = 0.7000 ; C = 0.9500E-01
D = 0.1900 ; E = 0.1000 ; F = 0.2000E-01
G = 0.1150 ; H = 1.000

These are default values.
You can redefine them by using the " USER-DEFINED " option.
Will you USE them to define the component?(y/n) >

FLAT PACK



FLAT PACK₆

- 1 22-pin
- 2 24-pin
- 3 USER-DEFINED F. PACK
- 4 CRITICAL COMP. MENU

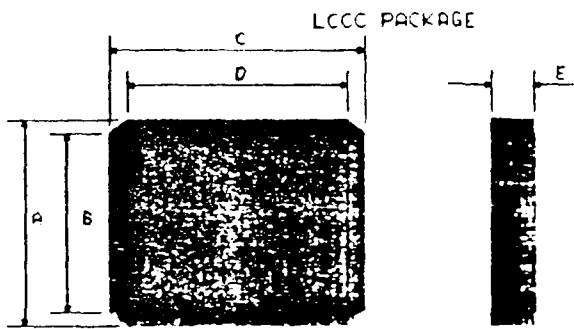
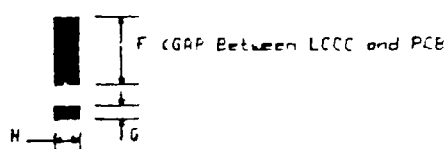
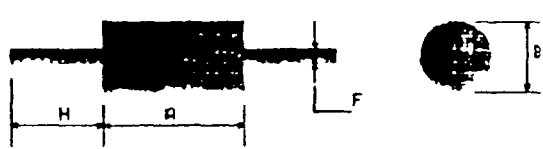
No. of Pins = 24

A = 0.6400 ; B = 0.5000 ; C = 0.0000E+00
D = 0.4000 ; E = 1.160 ; F = 0.9000E-01
G = 0.6000E-02 ; H = 0.1000 ; I = 0.5000E-01
K = 0.1900E-01

These are default values.
You can redefine them by using the " USER-DEFINED F. PACK " option.
Will you USE them to define the component?(y/n) >

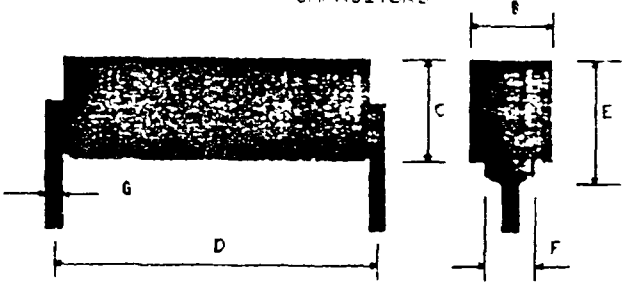
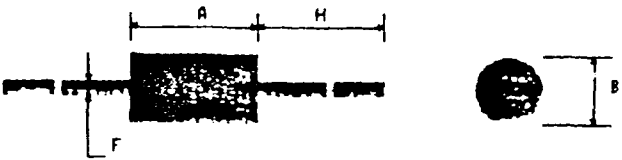
PIN ARRAY/FLAT PACK

FIGURE 1. ELECTRONIC COMPONENT DATA BASE (GENERALIZED REPRESENTATION) (CONT'D)

<div style="text-align: center; margin-bottom: 20px;">  <p>LCCC PACKAGE</p> </div> <div style="text-align: center; margin-bottom: 20px;">  <p>PIN DATA</p> </div> <div style="margin-top: 20px;"> <p>No. of Terminals = 84</p> <p>A = 1.165 ; B = 1.065 ; C = 1.165</p> <p>D = 1.065 ; E = 0.1200 ; F = 0.6000E-01</p> <p>G = 0.1000E-01 ; H = 0.5000E-01</p> <p>These are default values.</p> <p>You can redefine them by using the " USER-DEFINED LCCC " option.</p> <p>Will you USE them to define the component?(y/n) ></p> </div>	<div style="text-align: center; margin-bottom: 10px;"> <p>L C C C s</p> </div> <ol style="list-style-type: none"> 1 20-terminals 2 28-terminals 3 44-terminals 4 52-terminals 5 68-terminals 6 84-terminals 7 USER-DEFINED LCCC 8 CRITICAL COMP. MENU
<div style="text-align: center; margin-bottom: 20px;">  <p>RESISTOR</p> </div> <div style="margin-top: 20px;"> <p>MIL-R-55182 Config.</p> <p>A = 0.4370 ; B = 0.1650</p> <p>D (span between leads) = 0.5000</p> <p>F = 0.2700E-01 ; H = 1.625</p> <p>These are default values.</p> <p>You can redefine them by using the " USER-DEFINED RESIST. " option.</p> <p>Will you USE them to define the component?(y/n) ></p> </div>	<div style="text-align: center; margin-bottom: 10px;"> <p>MIL-R-55182 Config.</p> </div> <ol style="list-style-type: none"> 1 Style RNC50 2 Style RNC55 3 Style RNC60 4 Style RNC65 5 RESISTOR MENU

LCCC PACKAGE/RESISTOR

FIGURE 1. ELECTRONIC COMPONENT DATA BASE (GENERALIZED REPRESENTATION) (CONT'D)

CAPACITORS	
 <p>Configuration 1</p>  <p>Configuration 2</p>	<p>Configuration 2</p> <ol style="list-style-type: none"> 1 Mil. style CKP11 2 Mil. style CKP12 3 Mil. style CKP13 4 Mil. style CKP14 5 CAPACITOR MENU
<p>Configuration = 2</p> <p>A = 0.5200 ; B = 0.2650</p> <p>D (span between leads) = 0.7000</p> <p>F = 0.2700E-01 ; H = 1.500</p> <p>These are default values.</p> <p>You can redefine them by using the "USER-DEFINED CAPACITOR" option.</p> <p>Will you USE them to define the component?(y/n) ></p>	

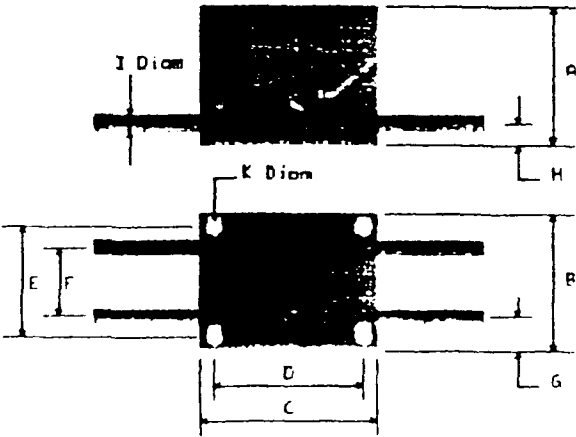
REACTOR	
	<p>TRANSFORMERS</p> <ol style="list-style-type: none"> 1 985910-1 2 USER-DEFINED TRANSF. 3 CRITICAL COMP. MENU
<p>Multiple Reactor</p> <p>A = 1.100 ; B = 1.220 ; C = 1.350</p> <p>D = 1.000 ; E = 1.000 ; F = 0.6000</p> <p>G = 0.2000 ; H = 0.1500 ; I = 0.4300E-01 ; K = 0.1020</p> <p>These are default values.</p> <p>You can redefine them by using the "USER-DEFINED TRANSF." option.</p> <p>Will you USE them to define the component?(y/n) ></p>	

FIGURE 1. ELECTRONIC COMPONENT DATA BASE (GENERALIZED REPRESENTATION)

FATIGUE RELATIONSHIP

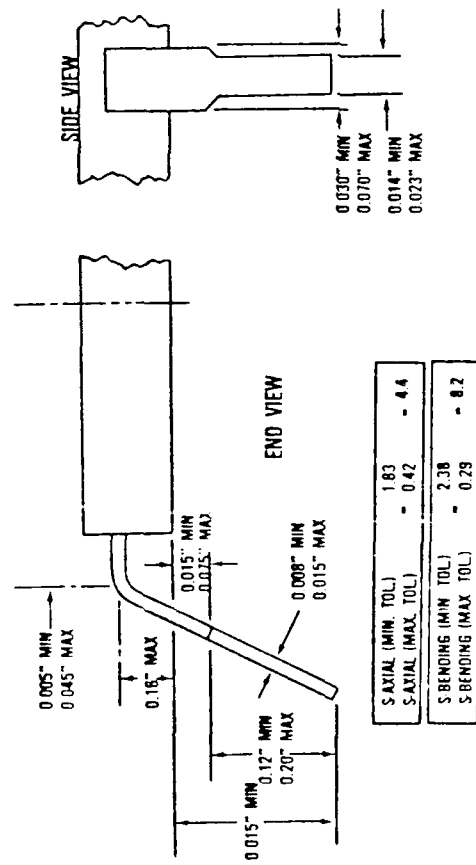
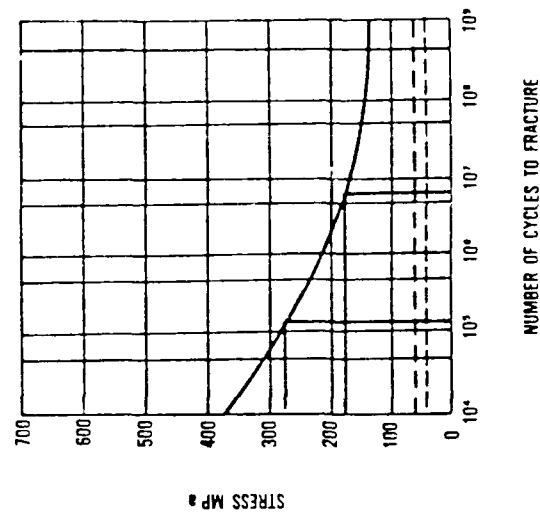


FIGURE 2. LEAD WIRE AND RELATIONAL FATIGUE/FRACTURE EFFECT

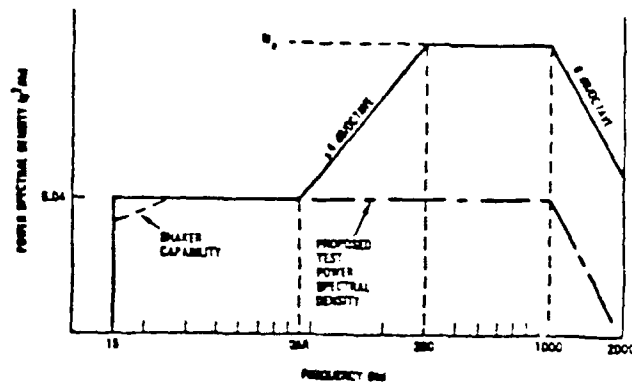


FIGURE 3. SPECIFIED TEST ACCELERATION POWER SPECTRAL DENSITY

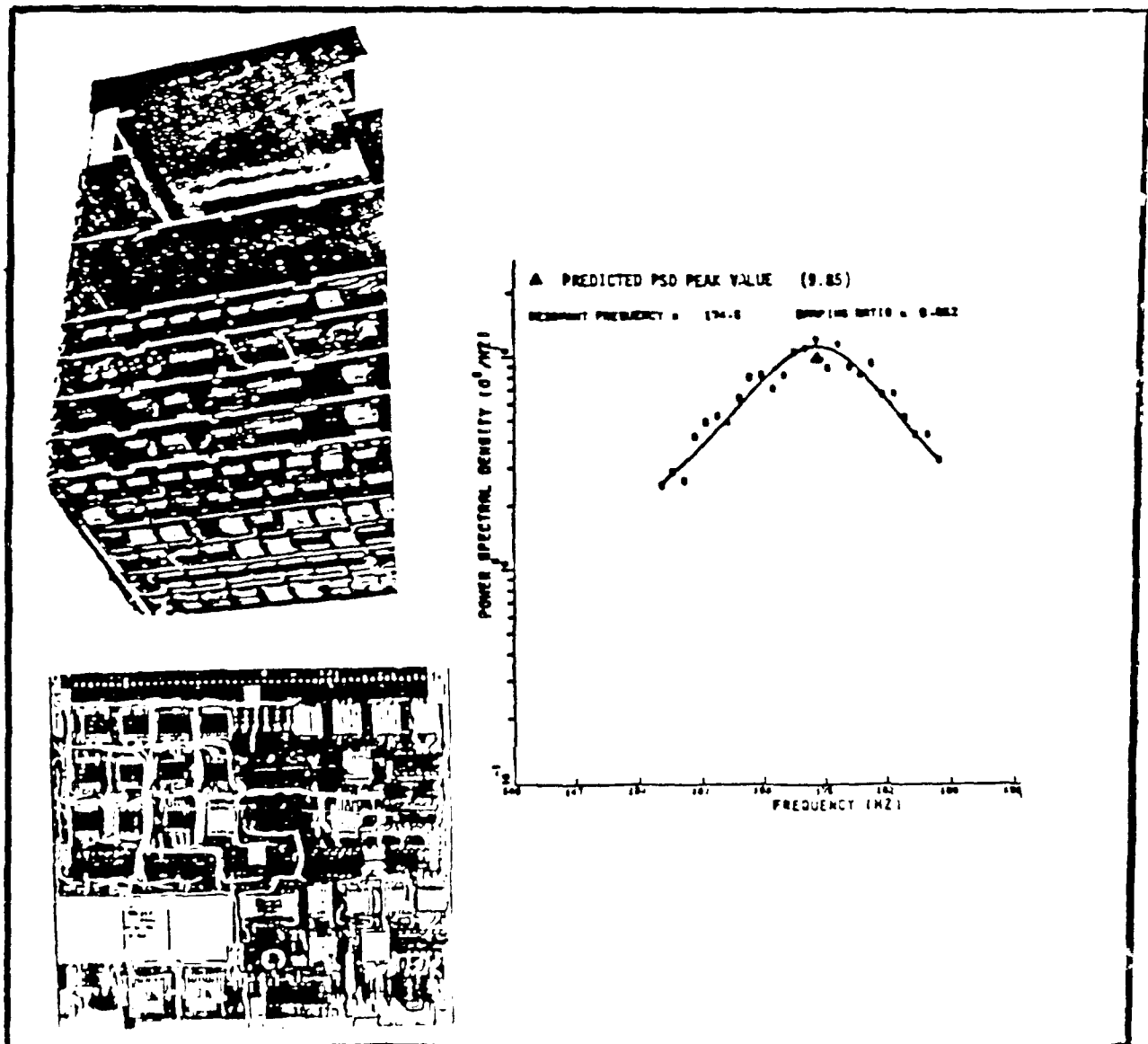


FIGURE 4. CORRELATION OF ANALYSIS AND TEST

Free edge Supported edge Fixed edge

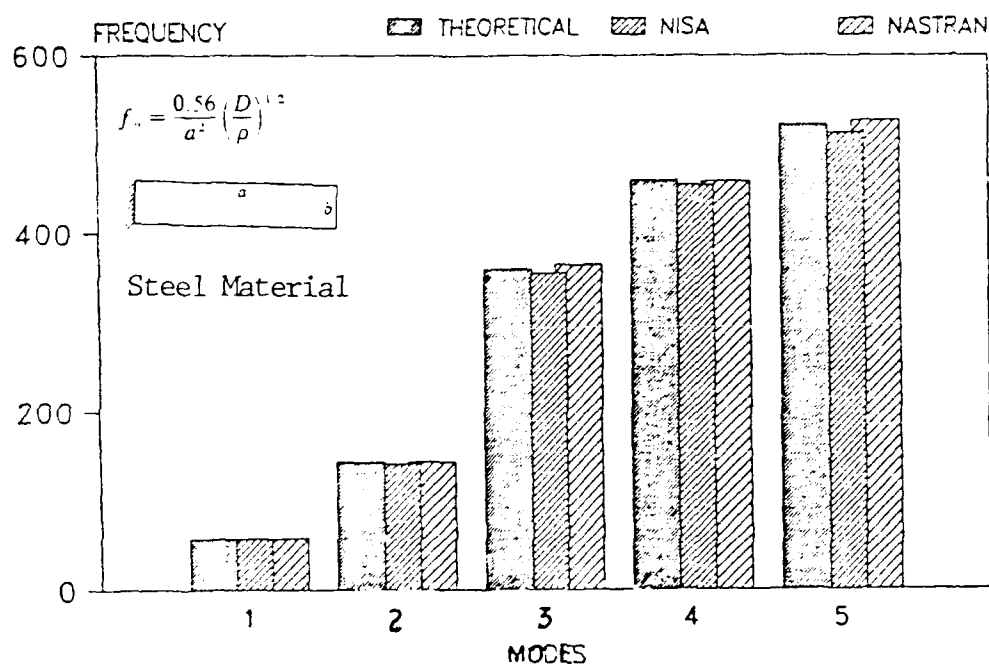


FIGURE 5. FREQUENCY CORRELATION BOARD 1

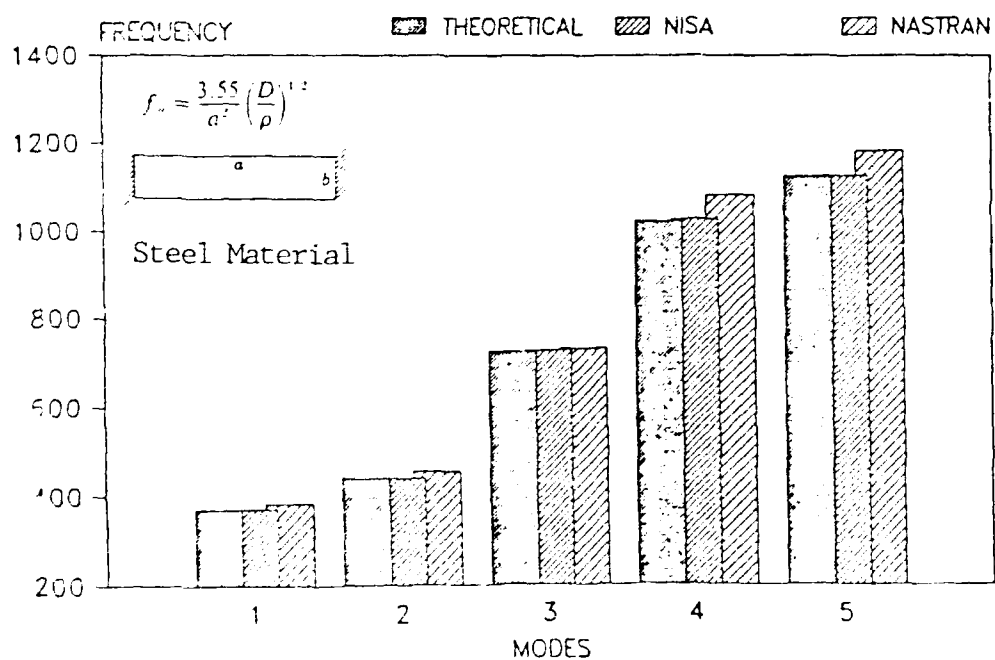


FIGURE 6. FREQUENCY CORRELATION BOARD 2

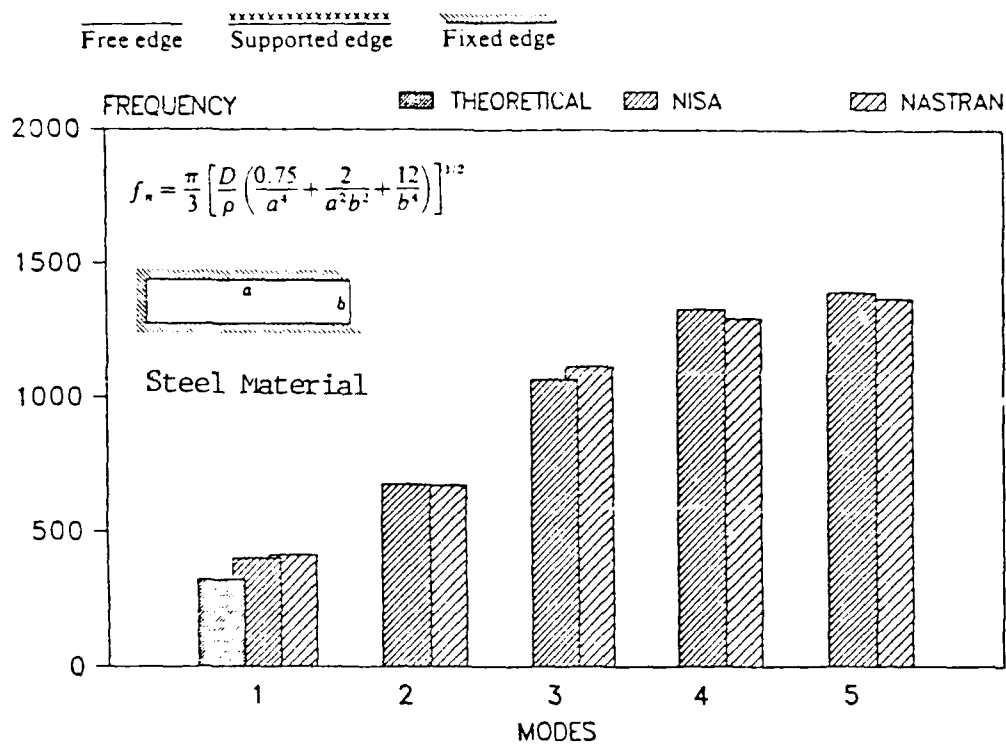


FIGURE 7. FREQUENCY CORRELATION BOARD 3

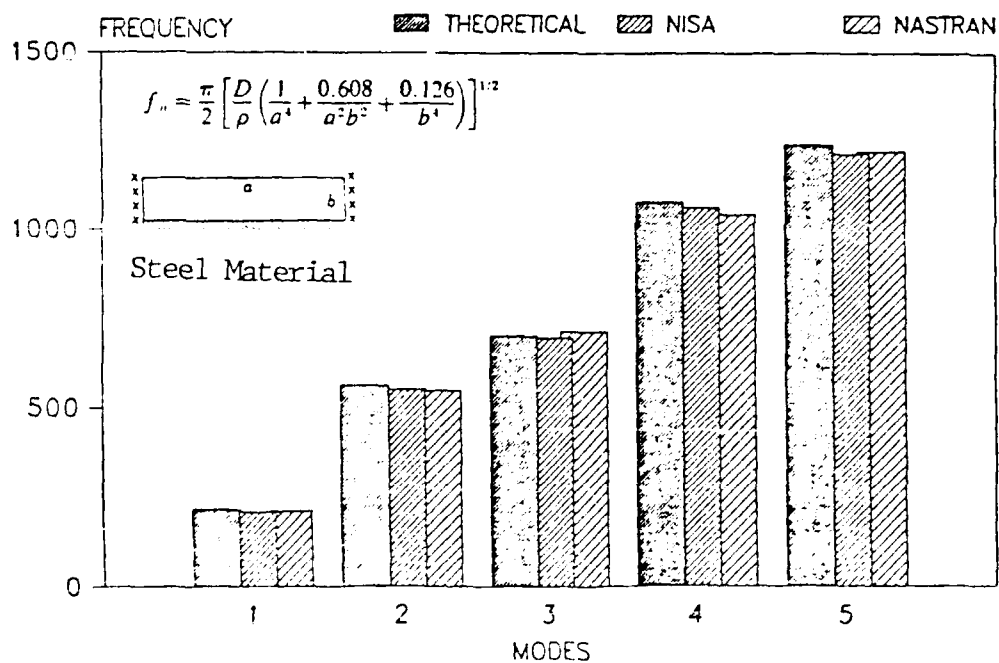


FIGURE 8. FREQUENCY CORRELATION BOARD 4

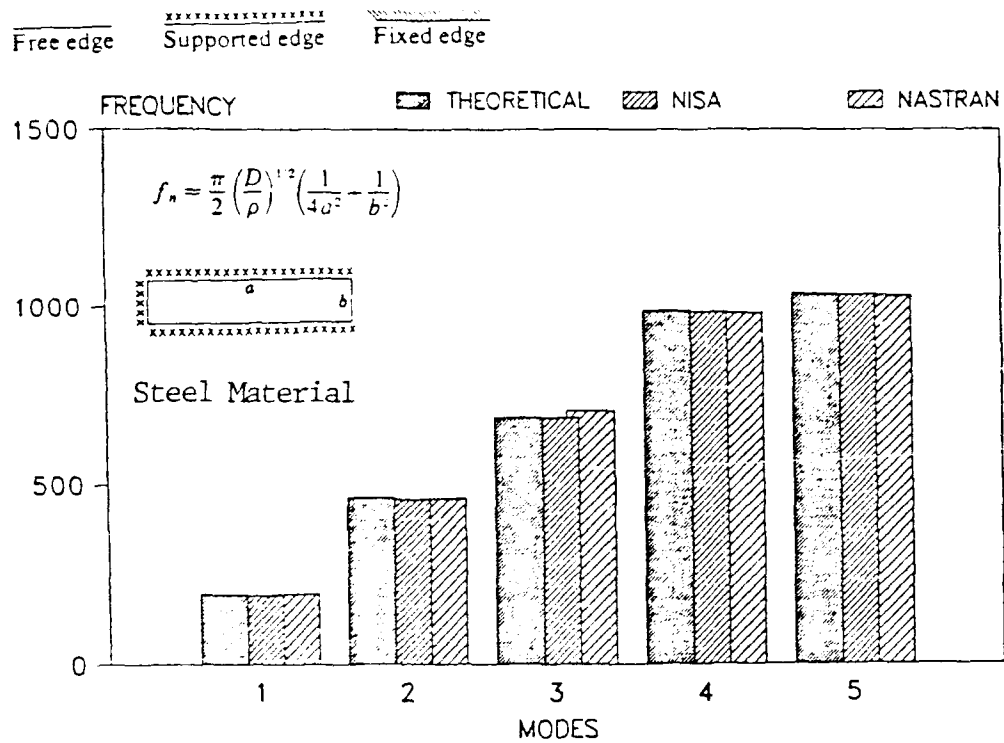


FIGURE 9. FREQUENCY CORRELATION BOARD 5

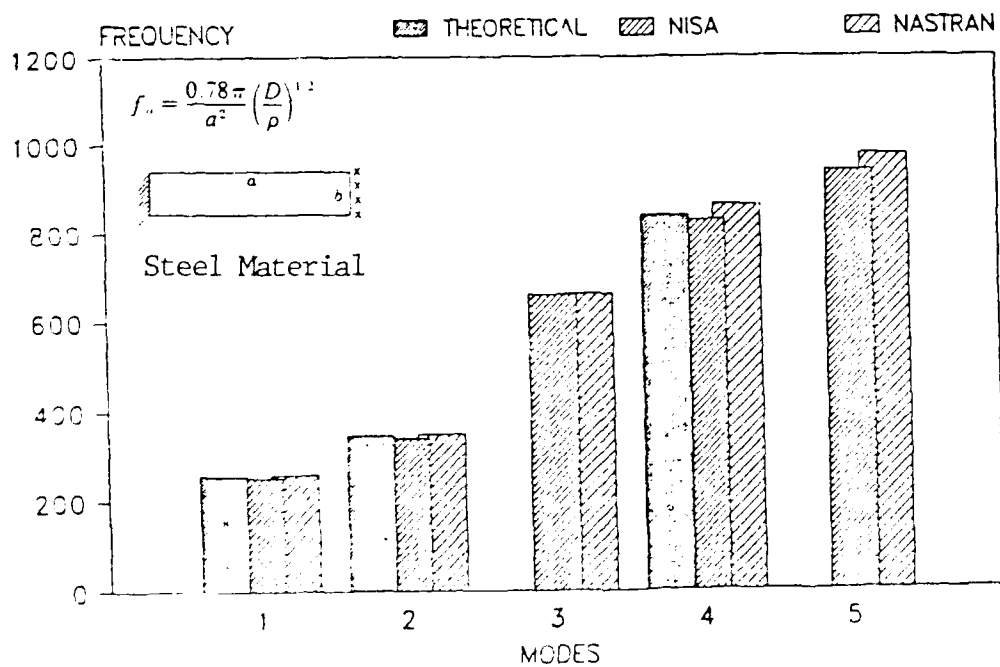


FIGURE 10. FREQUENCY CORRELATION BOARD 6

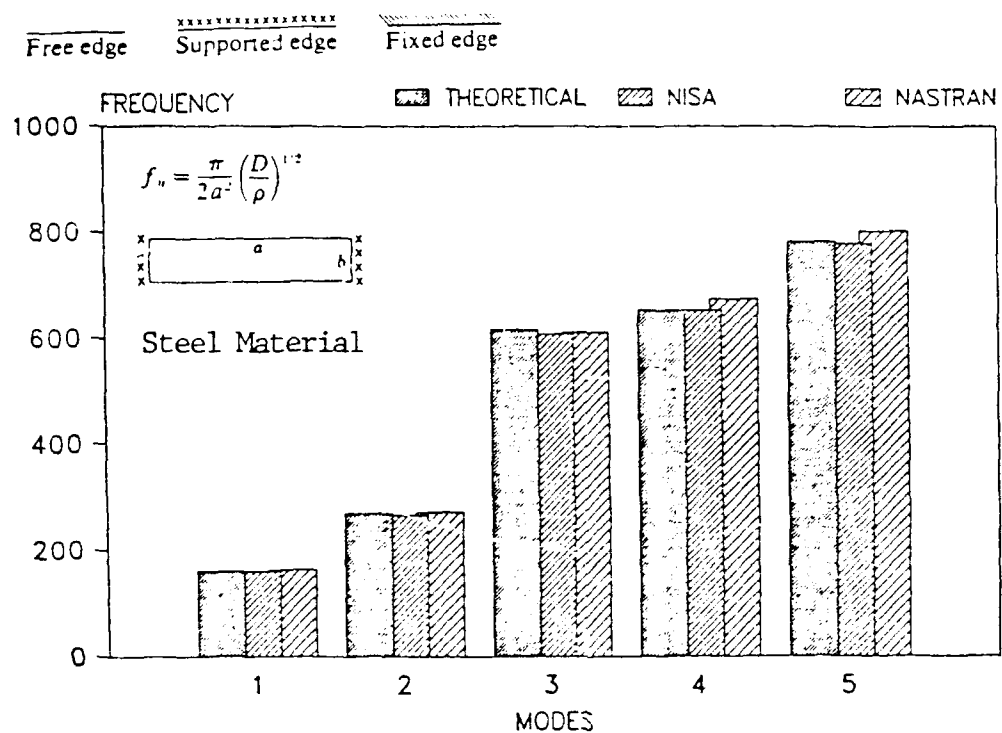


FIGURE 11. FREQUENCY CORRELATION BOARD 7

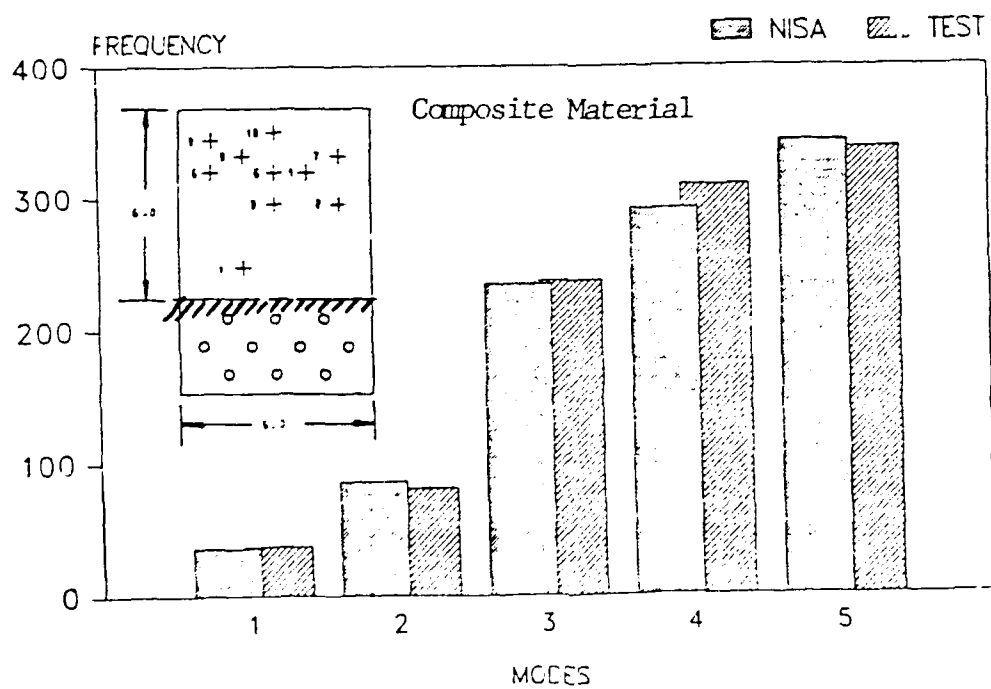


FIGURE 12. FREQUENCY CORRELATION BOARD 8

Fixed edge

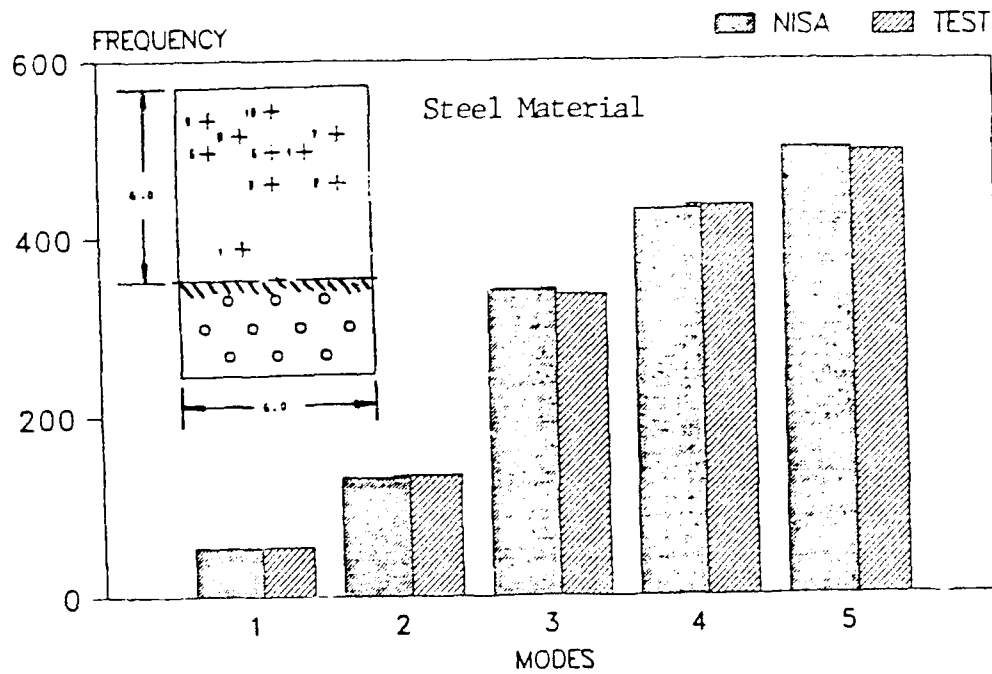


FIGURE 13. FREQUENCY CORRELATION BOARD 9

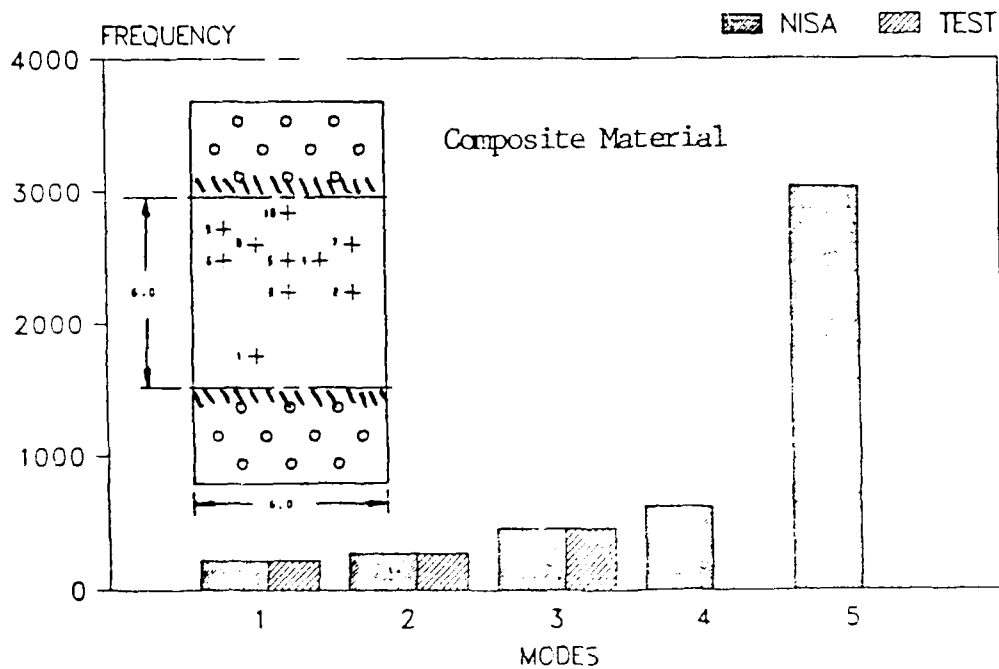


FIGURE 14. FREQUENCY CORRELATION BOARD 10

Fixed edge

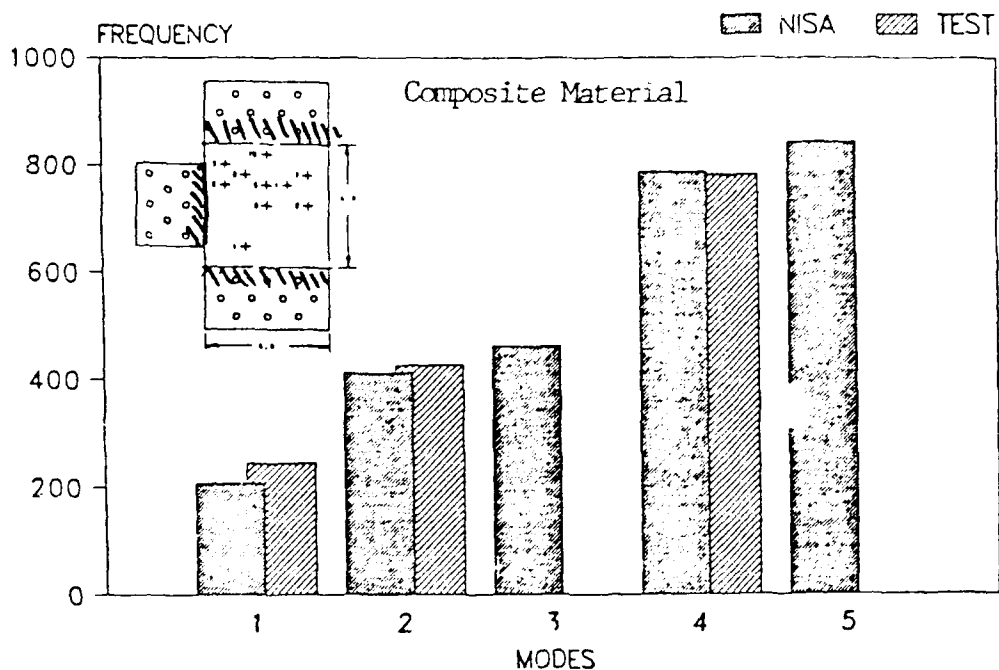


FIGURE 15. FREQUENCY CORRELATION BOARD 11

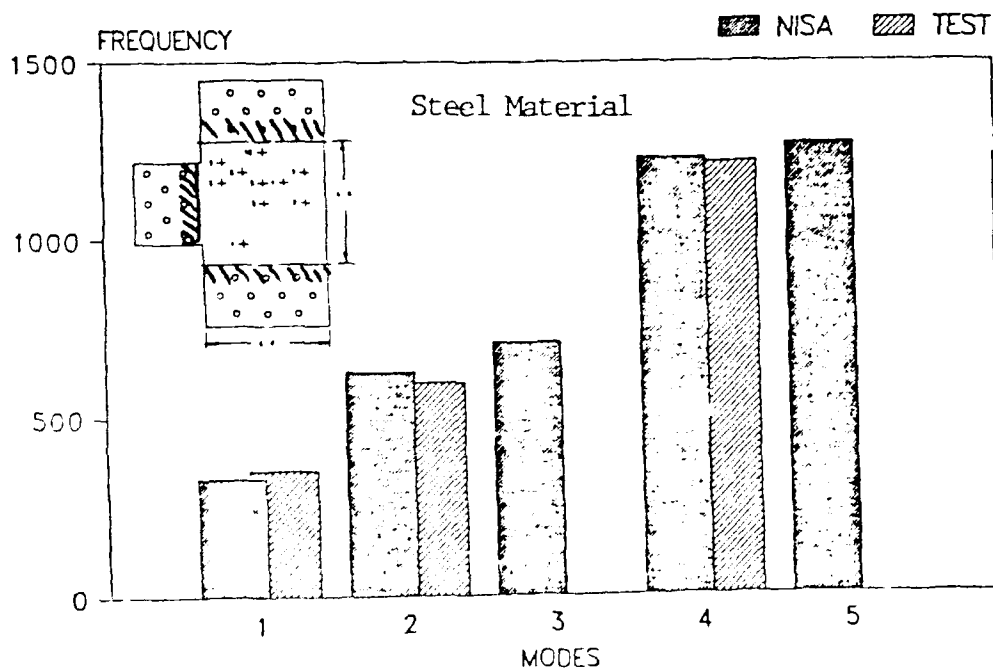


FIGURE 16. FREQUENCY CORRELATION BOARD 12

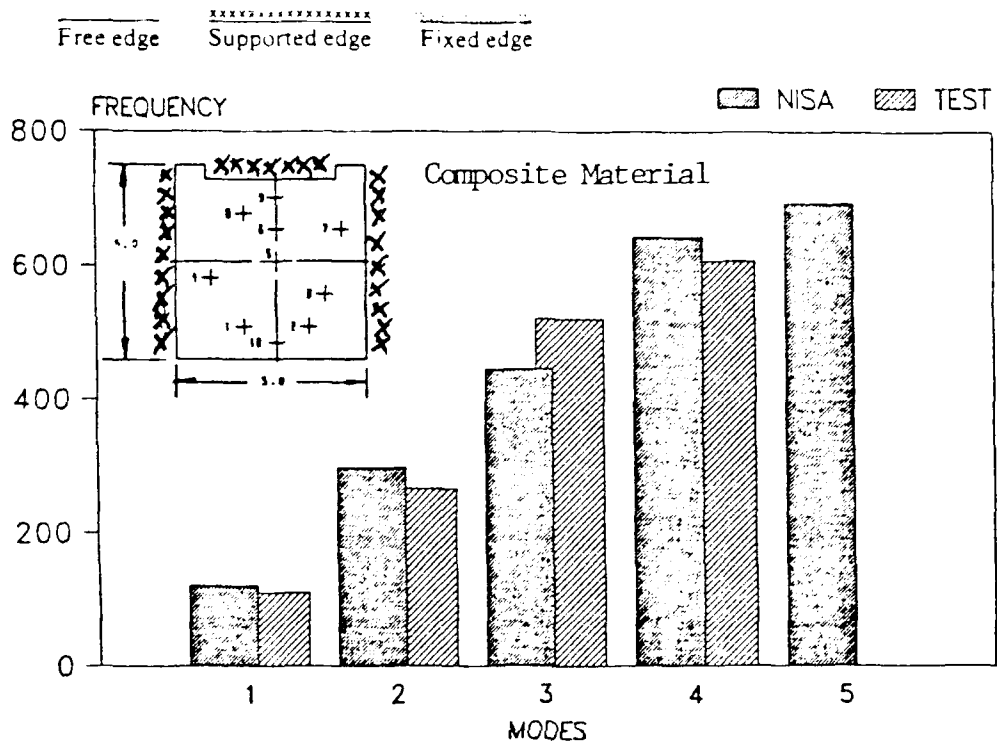


FIGURE 17. FREQUENCY CORRELATION BOARD 13

ELECTRONIC COMPONENTS	FATIGUE DATA CATEGORY	LEAD WIRE MATERIAL
1. LEADLESS CHIP CARRIER - SURFACE MOUNT	2	SOLDER
2. LEADLESS CHIP CARRIER - J OR L WIRE	0	KOVAR, SOMETIMES COPPER
3. STANDARD DIP - POKE-THROUGH	3	KOVAR
4. STANDARD DIP - SURFACE MOUNT	1	KOVAR
5. SIDE BRAZE DIP - POKE-THROUGH	3	KOVAR
6. SIDE BRAZE DIP - SURFACE MOUNT	0	KOVAR
7. FLAT PACK (OR HYBRID) - POKE-THROUGH	3	KOVAR
8. FLAT PACK (OR HYBRID) - SURFACE MOUNT	3	KOVAR
9. PIN GRID ARRAY - POKE-THROUGH	0	KOVAR
10. FLAT PACK ARRAY - 4 SIDE LEADS - SURFACE MOUNT	0	KOVAR
11. AXIAL LEADED DEVICES (RESISTORS, ETC.) - POKE-THROUGH	3	COPPER, KOVAR, NICKLE, SILVER AND DUMET
12. AXIAL LEADED DEVICES - SURFACE MOUNT	3	SAME AS #11
13. BLOCK DEVICES (TRANSFORMERS, ETC.) - POKE-THROUGH	3	COLD ROLLED COPPER WIRE
14. BLOCK DEVICES - SURFACE MOUNT	3	SAME AS #13
15. VERTICAL COMPONENTS (CR-06, ETC.) - POKE-THROUGH	3	SAME AS #13

A. COMPONENT FATIGUE DATA

FATIGUE DATA CATEGORY
 3 - GOOD DATA
 2 - SOME DATA
 1 - SOME QUESTIONABLE DATA
 0 - NO DATA TO DATE

COMPONENT	CRITICAL LENGTH INCHES
DIPS - POKE-THROUGH AND SMT	1
HYBRIDS - POKE-THROUGH	1
PIN ARRAY - POKE-THROUGH	1
FLAT PACKS - LONG LEADS	1
SHORT LEADS	3/4
LEADLESS CHIP CARRIERS	5/8
RESISTORS - SMALL DIAMETER CASE	1
RESISTORS AND TANTALUM	3/4
CAPACITORS - LARGE DIAMETER CASE	3/4
TRANSFORMERS	3/4
VERTICAL COMPONENTS	MOUNTING HEIGHT IS CRITICAL

B. CRITICAL COMPONENT SIZES FOR VIBRATION FATIGUE

TABLE 1. ELECTRONIC COMPONENT FATIGUE DATA CONSIDERATIONS (CONT'D)

ID	ELECTRONIC COMPONENT	MOUNTING
A	DIP - SIDE BRAZED LEADS	POKE THROUGH
B	DIP - STANDARD LEAD WIRES	POKE THROUGH
C	DIP - SIDE BRAZED LEADS	SURFACE
D	DIP - STANDARD LEAD WIRES	SURFACE
E	PIN GRID ARRAY	POKE THROUGH
F	LEADLESS CERAMIC CHIP CARRIERS	SURFACE
G	FLAT-PACK	SURFACE
H	HYBRIDS - FLAT PACK CASE	POKE THROUGH
I	HYBRIDS - FLAT PACK CASE	SURFACE
J	CKR 05 AND 08 CAPACITORS	POKE THROUGH
K	AXIALLY LEADED COMPONENTS (RESISTORS, CAPACITORS)	POKE THROUGH
L	AXIALLY LEADED COMPONENTS (RESISTORS, CAPACITORS)	SURFACE
M	BLOCK ENCAPSULATED COMPONENTS (TRANSFORMERS, INDUCTORS)	POKE THROUGH
N	BLOCK ENCAPSULATED COMPONENTS (TRANSFORMERS, INDUCTORS)	SURFACE
O	LEADLESS RESISTORS AND CAPACITORS	SURFACE

C. SUMMARY OF ELECTRONIC COMPONENTS

TABLE 1. ELECTRONIC COMPONENT FATIGUE DATA CONSIDERATIONS (CONT'D)

MODAL APPLICATIONS

STRUCTURAL VERIFICATION USING MODAL FREQUENCY TESTING: A NONDESTRUCTIVE EVALUATION

Thomas F. Drouillard and David N. Ikle
Rockwell International Corporation
Rocky Flats Plant
P.O. Box 464
Golden, CO 80402

Douglas K. Gustaveson
Lawrence Livermore National Laboratory
P.O. Box 808
Livermore, CA 94550

An investigation was carried out to study the application of modal frequency testing as a nondestructive method for structural verification and bond characterization of a dissimilar-metal structure joined by solid-state bonding. Important to the success of this investigation were the contributions from three disciplines: nondestructive evaluation, experimental modal analysis, and statistical analysis. This interdisciplinary effort resulted in a unique concept of structural verification -- the use of modal frequency testing to determine the geometrical consistency of precision parts and to characterize the condition of the silver solid-state bonds in a beryllium/stainless steel structure during its manufacture. Two methods of data analysis will be presented: one is an overlay of frequency response measurements to observe macro effects, and the other is principal component analysis of modal parameters to distinguish micro effects. The sensitivity of modal testing to small changes in the mass of a structure will also be discussed.

INTRODUCTION

The search for a nondestructive test method to evaluate bonded structures and measure bond strength has been ongoing for nearly four decades. No non-destructive method has yet been found that can determine the strength of a bond. If the geometry of the structure permits, ultrasonic testing can be used to distinguish areas of unbond where there is physical separation. However, it cannot reliably distinguish bond conditions that may vary from tight contact between interface surfaces to a fully metallurgically bonded interface. Consequently, bond testing generally consists of a proof loading test with some fraction of the samples tested to destruction. For structures with large bonded areas it is common practice to remove and destructively test many small tensile coupons. In some cases pressure testing is used to apply more realistic stresses to the structure, for example, to create both tensile and bending stresses in a pressure vessel or pipe joint.

It has been well known for a long time that when struck with a hammer the sound of a structure changes if a crack or other similar flaw is present. This means that the natural frequencies of the structure have been altered, generally

to lower frequencies. Tang and Huang [1] reported that such a phenomenon has been used for monitoring a variety of engineering structures. Tracy et al. [2] cite a number of studies since the early 1970's in the use of modal analysis as a nondestructive testing technique to detect structural damage. They used modal analysis techniques to investigate the effects of impact damage on the dynamic properties of advanced composite materials. In the present investigation the use of a modal analysis technique is applied to the nondestructive evaluation of a dissimilar-metal structure during its manufacture.

The scope of the investigation encompasses three major disciplines: non-destructive evaluation, experimental modal analysis, and statistical analysis. The results of this interdisciplinary investigation are presented in this paper. Discussed are the rationale for applying modal frequency testing to the study of a bonded structure; the development of the test parameters and selection of instrumentation; and the test fixture and procedure used to achieve reproducibility in repeated measurements of a given part and consistency in measurements from part to part. Also presented are two methods of analyzing modal test data. One is a composite overlay method in which the frequency response function (FRF) of a test part is overlayed on that of a nominal part in order to visualize shifts in individual frequency peaks. This reveals consistency in nominal parts and identifies parts that grossly differ from nominal. The second and more sensitive method uses a modal analysis technique to identify frequency and damping values which are then statistically analyzed by a method based on principal components to distinguish small differences between parts.

MODAL ANALYSIS TECHNIQUE

The objective of the modal analysis procedure is to accurately identify modal parameters from measured frequency response functions in order to properly characterize the dynamic behavior of a mechanical structure. This becomes increasingly important when the analysis is used as a means of nondestructive evaluation to distinguish structural differences introduced during the manufacture of high precision parts.

To estimate modal parameters from frequency response measurements a number of computational algorithms have been developed. A theoretical development of these parameter estimation, or curve fitting, techniques is given by Brown et al. [3]. To compare the dynamic behavior of one part with another it is imperative to use an estimation technique that is consistent and repeatable, so that changes observed during the analysis process can be attributed to variations between manufactured parts and not analysis aberrations. The analysis method selected for this study calculates modal parameters directly using the partial-fraction-expansion (PFE) formulation of the frequency response function. A complete description of the PFE method is given by Gustaveson [4]. The method does not rely on polynomials for the computation of modal parameters which often cause numerical instabilities and a divergence of the complete analysis (due to the excessive order required of the polynomial). Instead, the modal parameters are computed using a technique based upon the minimization of the least-squares-error of a set of nonlinear PFE equations (in the frequency domain) utilizing empirical frequency response data. Evaluating the equations in this manner provides a significant advantage with regard to numerical stability and increased accuracy of the modal parameters.

Residual energy, due to modes that lie outside of the measurement frequency range, is compensated for in terms of residual parameters in the mathematical model rather than arbitrarily over-specifying the actual number of modes in the analysis model. Analysis techniques that require over-specification, in order

to deal with residual energy, produce computational or fictitious modes as well as physical modes. It becomes necessary for the operator to sort out and distinguish which modes are computational and which modes are real, thus giving rise to the possibility of error. These so-called computational modes are an inherent by-product of the polynomial-based curve fitting techniques. The PFE method instills a high degree of confidence in the modal parameters it produces by avoiding the instabilities of polynomials and by eliminating the need to over-specify the analysis model.

The PFE analysis method fulfills the nondestructive evaluation requirements by providing a high degree of accuracy and numerical stability necessary as a prerequisite for a statistical analysis of the modal parameters. The PFE method is also well suited to a production-like application because it requires minimal operator intervention.

TEST SPECIMENS

The test specimen selected for this study was a tube-on-plate geometry comprised of 304 stainless steel with an inserted beryllium ring, joined together by silver solid-state bonding. Additionally, four all-stainless steel parts were made from 304 bar stock. The specimen configuration was approximately 4 inch outside diameter by 3.5 inch inside diameter with a 4.5 inch diameter by 0.5 inch thick base. The overall height was approximately 2.75 inches. Figure 1 is a sketch of the dissimilar-metal test specimen.

The technology of making silver solid-state bonds between beryllium and itself, as well as other metals, is well documented in the literature [5,6,7, 8,9,10]. Therefore, no attempt will be made to discuss the bonding or manufacturing processes used here except to report the parameters used in producing the test specimens.

The surfaces of the component parts to be bonded were coated with pure silver using a hot-hollow cathode deposition process. The thickness of silver coating varied from 2-4 mils with the average thickness in the 2-3 mil range. The component parts were assembled and encapsulated in a thin, form-fitting stainless steel can. The can was evacuated and then sealed. Bonding was accomplished in an autoclave at a pressure of 30 ksi and temperature of 600° C. The can was stripped from the part, after which the part was machined to the configuration shown in Figure 1. Automated machining was used to produce consistency in part geometry. The open end was threaded to accommodate a cap for either tensile or pressure testing. The flange on the base provided a means of attaching the second grip for tensile testing.

For the purposes of this investigation, 56 bonded beryllium/stainless steel (BSS) parts were manufactured with tight controls on material properties and close machining tolerances. However, three of those parts had known gross machining errors, and another three were suspected of having weak bonds. Reduced bond strengths were suspected because the cans bulged during the autoclave bonding process, indicating trapped gas in the cans. Bulging is caused by expansion of gas trapped in the can which may contaminate the silver surfaces and impair bonding. Deliberate attempts to produce weak bonds failed, since those bonds were so weak that the parts fell apart before machining. Thus, the study was designed to evaluate the results of modal testing 50 nominal and 6 potentially anomalous parts.

Four all-stainless steel (SSS) parts were also made. They were machined from 304 bar stock to the same configuration as the BSS parts. Three were

identical and one was slightly different due to a machining error. These parts proved to be of value in our repeatability study and mass variability study. The effects on the frequency response measurements from the geometrically out-of-tolerance SSS and BSS parts were significant enough to warrant broadening the scope of our investigation to include all conditions that affected the frequency response of a part. We studied the anomalies that inadvertently happened during the investigation. There was no attempt to produce controlled machining errors, substitute components with different alloy composition, change the mechanical properties of any component, or further try to make defective bonds.

EXPERIMENTAL

Instrumentation

Transducers consisted of a PCB Piezotronics Model 303A02 accelerometer, fitted with a mounting shoe, and a Model 086C80 instrumented hammer. These were connected to PCB Model 480D06 power units. Measurements were processed in a two-channel Hewlett-Packard Model 3562A Dynamic Signal Analyzer, then transferred to a Hewlett-Packard Series 200/300 computer. Data analysis (curve fitting) was then performed on the frequency response measurements using Dynamic Software Systems "SPRINT" modal analysis software package.

Test Setup

The accelerometer was attached to the part with mounting wax on the bottom surface near the outer edge of the flange. The wax attachment was found to be more satisfactory than small mechanical clamps, which caused additional mass loading and more variability in frequency response measurements. To support the part, both a sponge pad and a cork ring were evaluated with equal success. However, the cork ring was selected because it provided a means to obtain better repeatability in setting up parts in the test fixture. A cutout in the cork ring provided space for the accelerometer. The cork ring, with the part sitting on it, was positioned up to the suspended instrumented hammer with the accelerometer vertically aligned with the hammer head. The axis of the hammer head was visually aligned normal to the part surface. The hammer was suspended as a pendulum in the fixture so that the arc length of its swing could be adjusted and fixed for repeatability. A diagram of the test setup is shown in Figure 2. The fixture provided a quick and easy test setup while maintaining measurement repeatability from part to part. This was confirmed by statistical analysis of the modal parameters. Based on a pooled estimate of the variance using eight replicates on ten BSS parts, the two sigma estimates of measurement error ranged from a minimum of ± 1.38 Hz for the first analyzed mode of vibration to a maximum of ± 17.12 Hz for the last analyzed mode of vibration in the frequency range of 3 kHz to 15.5 kHz.

Test Procedure

One frequency response measurement was made on each part. Each measurement was the average of ten hits of the instrumented hammer just above center on the beryllium ring component. The frequency response measurements contained five modes for BSS parts and six modes for SSS parts in the frequency range of 3 kHz to 15.5 kHz. The point of impact was kept constant for all measurements by virtue of the test fixture. A typical measured FRF with its synthesized FRF (curve fit results) superimposed is shown for BSS Part 4716 in Figure 3. Figure 4 is a numeric printout of the modal parameters derived by the curve fit analysis for BSS Part 4716. Figure 5 is an overlay plot of the measured and synthesized FRFs while Figure 6 is a printout of the modal parameters for a

typical SSS part. The "SPRINT" software program provides the option of plotting the measured FRF, the synthesized FRF, or an overlay plot of both. All FRF plots, both measured and synthesized, are displayed in a log-linear format.

RESULTS AND DISCUSSION

Methods of Data Analysis

Two methods were utilized to analyze modal test data. The first method was to visually examine the plots of measured and synthesized frequency response functions. This method provided a means of seeing shifts in frequency peaks that were indicative of part differences on a macro scale. The second method was a statistical analysis of modal parameters which is sensitive to differences between parts on a micro scale. The statistical method was used to analyze only frequency and damping values; amplitude and phase data were considered to contain no useful information relative to our study. The frequency response pattern is summarized by two independent measures which can be used to distinguish anomalous parts from nominal parts. A detailed discussion of this second method is presented later under Statistical Analysis of Modal Parameters.

With regard to the first method mentioned above, visual examination of FRF plots of nominal parts showed they were consistent enough to prompt overlaying one upon another to look for shifts in modal peaks to indicate something different in a given part. Subsequently, this technique was improved by overlaying the synthesized FRFs which provided better accuracy and readability. The frequencies of each mode were averaged for the fifty nominal parts, and BSS Part 4716 was selected as being representative of that average pattern. Part 4716, shown in Figure 3, was then used as a reference with which to compare measurements on other parts. This composite overlay method proved to be useful in detecting macro differences in parts, particularly machining errors.

Material Properties

The affect of a change in material properties (i.e., that affect of a change in the mass, stiffness, and/or damping) is best displayed by comparing the FRF plots of a BSS part (Figure 3) and a SSS part (Figure 5). Figures 4 and 6 list the modal parameters for these two parts. The insertion of the beryllium ring caused a significant change in the FRF. Although not specifically studied here, it is obvious that modal frequency testing is sensitive to changes in material properties. This implies that the test could be useful in verifying the proper selection of the correct material or alloy and, for example, that the structure has been given the proper heat treatment. A composite of fifteen synthesized FRFs, shown in Figure 7, provides a graphic indication of the consistency of nominal BSS parts. The small variation in frequency of each mode is believed to be caused by a slight difference in the weight of each part due to allowable machining tolerances and the result of different thicknesses of silver coatings in the bond joints.

Mass Variability

The four all-stainless steel parts were identical in all respects except one, SSS Part #3 had a machining error. The top lip above the threaded end was 0.030 inches longer than the other three parts. This geometrical difference (causing a change in mass of approximately 2.5 grams) is quite noticeable in a composite overlay of the four measured FRFs shown in Figure 8. There is a slight shift to a lower frequency of mode 1 and significant shift to lower

frequencies of modes 2 and 5 due to the added mass for Part #3 with the longer lip. Modes 3, 4, and 6 remain unaffected. This precipitated a study of the affect of mass variability using narrow strips of lead tape to change the mass of the top lip of SSS Part #1, approximately 1 gram per layer. After each layer was applied, a frequency response measurement was made. Figure 9 is a composite overlay of the synthesized FRFs for the original part and after each layer of lead tape was applied. There is a decrease in frequency of modes 1, 2, and 5 with each successive layer of lead tape. There is no significant affect on modes 3, 4, and 6. The effect on the frequency response by changing the weight locally with lead tape is the same as that produced by SSS Part #3 with the machining error. This study shows there is a linear relationship between frequency and weight for mode 1 as shown graphically in Figure 10.

A similar mass variability study was performed on beryllium/stainless steel Parts 4634, 4702, and 4714. Strips of lead tape were added to the top lip, above the threaded portion of the stainless steel component. Frequency response measurements and weights were taken after each successive layer of tape was applied. A composite overlay of the synthesized FRFs for BSS Part 4714 is shown in Figure 11. Modes 1, 2, and 4 show a decrease in frequency with an increase in weight. Modes 3 and 5 are unaffected. Figure 12 is a plot showing a linear relationship of frequency versus weight of mode 1 for BSS Part 4714.

Three beryllium/stainless steel parts had various machining errors that caused a change in their masses. These included BSS Part 4570 with a circumferential tool gouge that removed about 2.3 grams of metal on the inside surface, about midway on the upper stainless steel component; BSS Part 4602 with a flange 0.034 inches undersize, resulting in a reduction of weight of approximately 16 grams; and BSS Part 4657 with the outside diameter 0.036 inches undersize, except for the threaded portion, causing a reduction in weight of about 50 grams. The measured FRF of each of these improperly machined parts is shown relative to that of Reference Part 4716 in Figures 13, 14, and 15. In all three cases there is clearly a shift in a number of frequency peaks. The tool gouge in Part 4570 caused a decrease of 2.3 grams in a total weight of 1580 grams, representing a material loss of about 0.146%. SSS Part #3 with the 0.030 inch longer lip had an increase of 2.5 grams in a 1775 gram part, representing a material difference of 0.141%. In both cases modal frequency testing was sensitive enough to detect these relatively small changes in weight. Weight differences of this magnitude are shown to be of a macro scale that are readily detected by the shift in one or more frequency peaks by the composite overlay method of analysis.

Bond Condition

Using the composite overlay method to evaluate the FRFs from the bulged can parts, two appeared to be normal (BSS Parts 4634 and 4702) and one suspect (BSS Part 4714). The measured FRFs of the two normal appearing parts are represented by BSS Part 4702 in Figure 16. Figure 17 is the measured FRF of suspect Part 4714, showing a slight increase in frequency of modes 1, 3, 4, and 5. BSS Parts 4702 and 4714 were subsequently tensile tested to failure. Part 4702 failed in the silver-beryllium bond just above the flange at 42,960 pounds load. Part 4714 failed in the same location at 45,000 pounds. Part 4634 was not tested. Typical failure of nominal parts occurs in beryllium at about 60,000 pounds. Failure loads of the two bulged can parts were approximately 25% below normal, however, the change in joint condition that caused this amount of reduction in bond strength is not clearly apparent in the FRFs by using the overlay analysis method. It is interesting to note that the machinist reported that Part 4714 sounded different during the machining operation.

Statistical Analysis of Modal Parameters

The objective of the statistical analysis was to develop a sensitive quantitative procedure for discriminating between nominal and anomalous beryllium/stainless steel parts on the basis of their modal parameters. This is commonly accomplished in the case of a single discrimination criterion by assuming that it is normally distributed and computing the mean (m) and standard deviation (s) from a sample of nominal parts. A prediction interval is then constructed equal to $(m - ks, m + ks)$, where k is a function of the sample size and the desired confidence level. A part is classified as nominal if its value is within the prediction interval and anomalous if its value is outside this "normal range." However, this method is not appropriate in the case of multiple classification variables that are significantly correlated, since the actual confidence level associated with a set of dependent prediction intervals is not equal to that of the individual intervals. The result will generally be a loss of sensitivity, in that many anomalous parts are likely to be incorrectly classified as nominal.

The solution is to utilize statistical methods for the analysis of multivariate data [11]. In particular, principal component analysis permits the reduction of measurements on many correlated variables to values of a smaller number of independent measures that contain most of the original information. By a least squares technique, linear combinations of the original variables are estimated which produce standardized principal component scores that are independent standard normal deviates (i.e., they follow a normal distribution with mean 0 and standard deviation 1). The estimated coefficients of each linear combination are multiplied by the original variables and the products are summed to produce the principal component scores. For simplicity of interpretation, the variables are first standardized by subtracting the mean and dividing by the standard deviation of the sample data. The number of principal components to be retained is determined by how much of the variance in the original data is desired to be explained.

The modal parameters from the 50 nominal BSS parts studied here were analyzed using the principal component procedure of the SAS statistical software system [12]. Preliminary analysis of modal parameters indicated that damping values would not be useful for classification purposes, but that principal components based on the five modal frequencies would be, due to their high degree of intercorrelation. The final results are summarized in Table 1, where the standardized principal component coefficients are listed for the first two components, or factors, which explain approximately 92% of the variance in the frequencies. The statistical interpretation of the two sets of coefficients is that the first principal component (Factor1) is roughly the unweighted mean of all five modal test frequencies, while the second component (Factor2) is roughly the mean of frequencies 2 and 4, minus the mean of frequencies 3 and 5. Factor1 explains 67% of the variance in the frequencies and reflects simply an up or down shift in all the frequencies. Factor2 explains an additional 25% of the variance and describes a more subtle shift in the differences between the last four modes. At this time, it is not clear what underlying physical mechanism is reflected in Factor2.

Since the standardized principal component scores are independent standard normal deviates, they may be compared directly to tables of the standard normal distribution. Thus, at roughly the 99% level of confidence, parts with scores greater than 2.5 in absolute value for either Factor1 or Factor2 may be considered to be potentially anomalous. In addition, an overall probability may be associated with each part, since the sum of the squares of two independent standard normal variates follows a chi-square distribution with 2 degrees of freedom.

The standardized scoring coefficients estimated from the 50 nominal BSS parts were used to compute the first two principal component scores for all 56 BSS parts, including the three with machining errors (Parts 4602, 4657, and 4570) and the three bulged can parts with suspected weak bonds (Parts 4634, 4702, and 4714). Table 2 summarizes the results for the 15 parts with the smallest overall probabilities. Clearly, Parts 4602 and 4657 are substantially different in both dimensions from all the other parts, while Part 4570 is somewhat less so. On the other hand, amongst the three parts with suspected weak bonds, Part 4714 has a score on Factor1 which places it outside the expected range of scores for nominal parts, while Parts 4634 and 4702 were in the nominal range of scores. This supports the suspicion from the composite overlay analysis that only Part 4714 is anomalous due to poor bonding. The principal component scores are displayed graphically in Figure 18, where Factor1 scores are plotted against Factor2 scores for the 50 base, or nominal, parts and the six test, or anomalous, parts. In Figure 19 the same principal component scores are plotted, excluding the three extreme parts with known machining errors. Figures 20 and 21 illustrate an alternative graphical representation useful for monitoring production processes for trends, where the principal component scores are plotted according to the manufacturing sequence of the parts. The pattern for Factor1 exemplifies a controlled process with only random variation, while that for Factor2 clearly reflects a shift in the process about halfway through the production run.

The effect of mass variation is illustrated in Figures 22 and 23, where the principal component scores are plotted against weight for BSS Parts 4634, 4702, and 4714. Separate simple linear regression lines are fit through the data for each part. Regression analysis indicates that the fit for each line is extremely good, and that the regression lines are parallel. The all-stainless steel parts were not analyzed by principal components, since the multivariate structure of their frequency response functions was presumed to be different from that of the BSS parts, and there was no sample of nominal parts with which to estimate the scoring coefficients.

Multivariate statistical analysis of modal parameters has been found to be extremely useful in summarizing the correlated data produced by modal frequency testing. Further research needs to be done using controlled experimentation to systematically relate physical features of parts to specific changes in the principal components.

CONCLUSIONS

The success of this investigation is attributed to the contributions from three disciplines: nondestructive evaluation, experimental modal analysis, and statistical analysis. It was found that modal frequency testing offers a unique nondestructive method for structural verification. It provides a means by which to verify consistency and uniformity in the manufacture of high precision parts. Modal frequency testing can be used to confirm consistency and reveal variability due to differences in material properties, mass differences due primarily to machining errors, and variations in bond condition. It has been shown that modal testing distinguishes dimensionally out-of-tolerance parts caused by machining errors as well as changes in material properties which cause a change in mass or stiffness of the structure. The partial-fraction-expansion (PFE) analysis method of computing modal parameters provided the high degree of accuracy and numerical stability necessary to perform a statistical analysis of the modal parameters. The PFE method also was found to be well suited for use in a production-like application because it requires a minimal amount of operator intervention. Two methods of analysis were presented by which modal parameters were evaluated.

One is the composite overlay method which provides a graphic means for visually detecting macro differences. In this method the frequency response function of a representative nominal part is selected as a reference to which all subsequent FRF measurements are compared. The second method is principal component analysis of modal parameters which distinguishes micro differences and yields valid estimates of the statistical significance of those observed differences. Both methods clearly revealed machining errors with weight differences as small as 0.14%. Also, both methods showed the bonds in one suspect part to be anomalous and in two other suspect parts to be normal. However, the bond strengths in two of the three parts that were destructively tensile tested failed approximately 25% below normal. We feel that these substandard bond conditions are at the threshold of detectability and that there is a correlation between bond strength and modal frequency response. Further research is indicated to resolve this relationship.

DISCLAIMER

No specific intent is made to endorse any one manufacturer's equipment or software. The authors cite specific instrumentation and software simply because they have successfully used them for the described work.

REFERENCES

1. Z. Q. Tang and T. C. Huang, "Modal Analysis of a Cylindrical Shell with a Longitudinal Crack," Modal Testing and Model Refinement, Edited by D. F. H. Chu, AMD-Vol. 59, pp. 77-84, American Society of Mechanical Engineers, New York, 1983
2. J. J. Tracy, D. J. Dimas, and G. C. Pardoen, "The Effect of Impact Damage on the Dynamic Properties of Laminated Composite Plates," Fifth International Conference on Composite Materials, ICCM-V, Edited by W. C. Harrigan, Jr., J. Strife, and A. K. Dhingra, pp. 111-125, The Metallurgical Society, Warrendale, Pennsylvania, 1985
3. D. L. Brown, R. J. Allemang, R. Zimmerman, and M. Mergeay, "Parameter Estimation Techniques for Modal Analysis," SAE Paper No. 790221, SAE Transactions, Vol. 88, pp. 828-846, 1979
4. D. K. Gustavson, "Direct Parameter Identification from Frequency Response Measurements," Proceedings of the 5th International Modal Analysis Conference, Volume II, pp. 1352-1356, Union College, Schenectady, New York, 1987
5. S. R. Maloof and J. B. Cohen, "Brazing of Beryllium for High-Temperature Service," Welding Journal, Vol. 40, No. 3, pp. 118s-122s, March 1961
6. A. T. D'Annessa, "Diffusion Bonding Beryllium, Molybdenum and Tungsten," Metal Progress, Vol. 91, No. 2, pp. 71-74, February 1967
7. J. L. Knowles and T. H. Hazlett, "High-Strength Low-Temperature Bonding of Beryllium and Other Metals," Welding Journal, Vol. 49, No. 7, pp. 301s-310s, July 1970
8. G. S. Ignatovskaya and M. A. Komarov, "Welding of Beryllium to Titanium and Steel," Welding Production, Vol. 20, No. 1, pp. 30-32, January 1973

9. M. O'Brien, C. R. Rice, and D. L. Olson, "High Strength Diffusion Welding of Silver Coated Base Metals," Welding Journal, Vol. 55, No.1, pp. 25-27, January 1976
10. C. R. Heiple, "Silver Solid-State Bonding: A Review and Assessment," RFP-3867, Rockwell International Corporation, Rocky Flats Plant, Golden, Colorado, July 7, 1986
11. T. W. Anderson, An Introduction to Multivariate Statistical Analysis, John Wiley and Sons, New York, 1984
12. SAS Institute Inc., SAS User's Guide: Statistics, Version 5 Edition, Cary, North Carolina, 1985

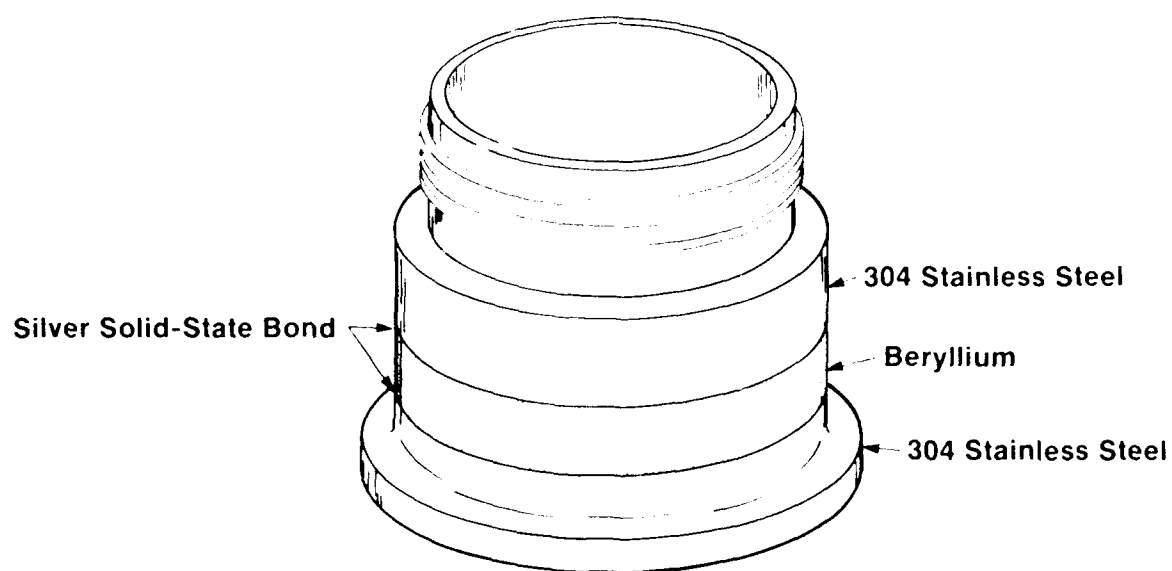


Fig. 1 Sketch of silver solid-state bonded beryllium/stainless steel test specimen

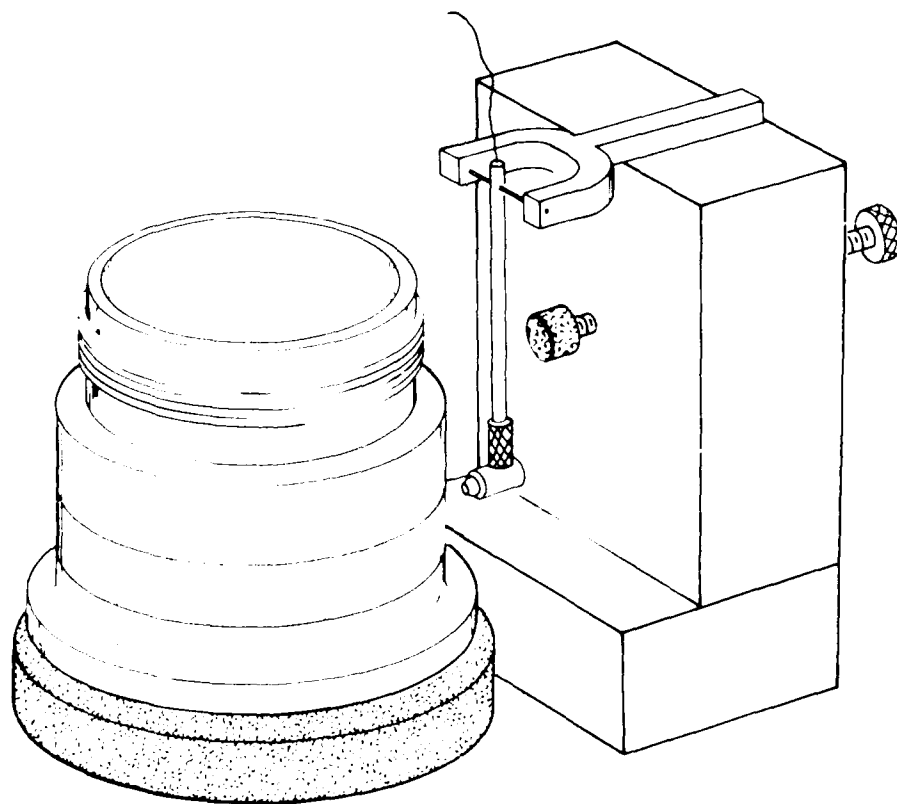


Fig. 2 Sketch of test setup showing test fixture and part sitting on cork ring

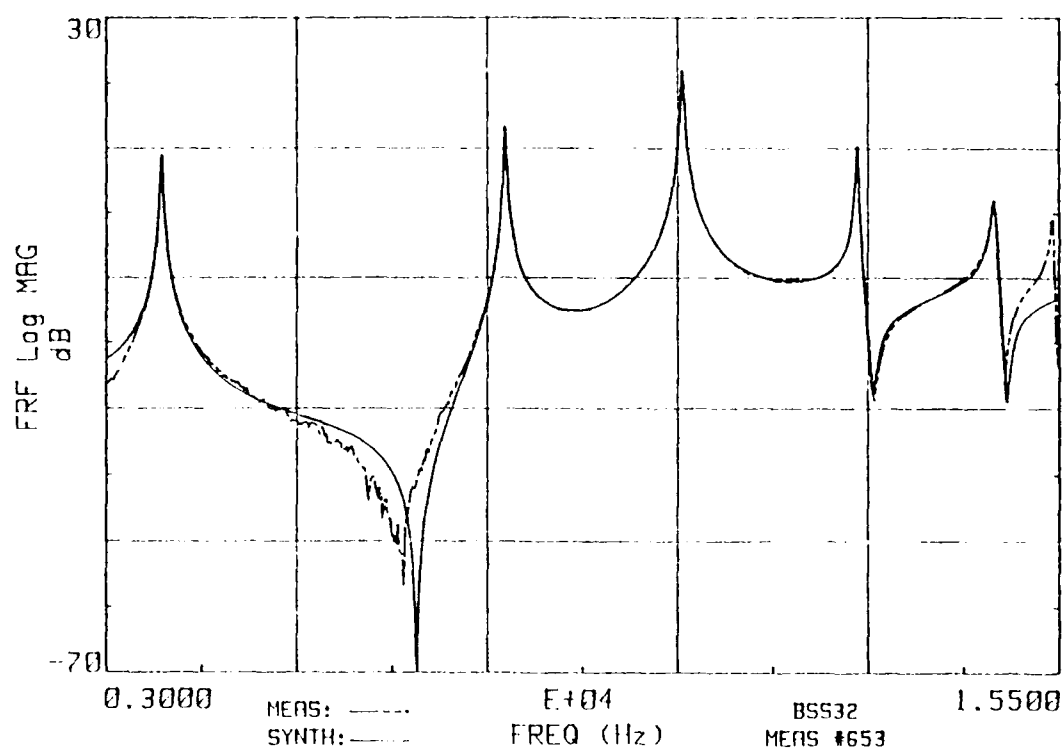


Fig. 3 Measured and synthesized FRFs of BSS Reference Part 4716

***** MODAL PARAMETERS *****				
Project: BSS32			Meas: #653	
D.O.F.s: 1X/1X			Units: g's/lbf	
MODE (#)	FREQ (Hz)	DAMPING (%)	AMPLITUDE	PHASE (Deg)
1	3729.158	0.375	5.0934E+002	0.48
2	8235.083	0.168	7.8168E+002	-0.37
3	10564.438	0.161	2.6574E+003	175.97
4	12860.430	0.111	5.7560E+002	-5.08
5	14657.780	0.208	4.6232E+002	-15.66
6	0.000	0.000	0.0000E+000	0.00
7	0.000	0.000	0.0000E+000	0.00
8	0.000	0.000	0.0000E+000	0.00
9	0.000	0.000	0.0000E+000	0.00
10	0.000	0.000	0.0000E+000	0.00

Fig. 4 Printout of modal parameters of BSS Reference Part 4716

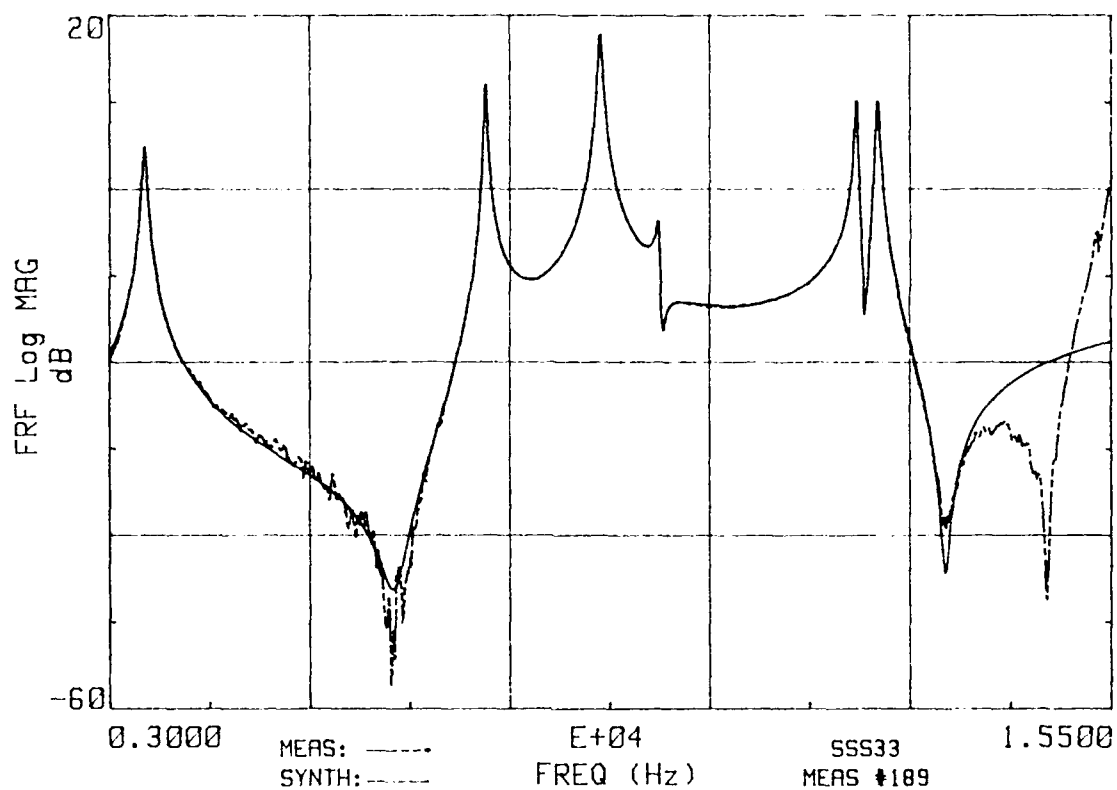


Fig. 5 Measured and synthesized FRFs of SSS Part #1

***** MODAL PARAMETERS *****				
Project: SSS33			Meas: #189	
D.O.F.s: 1X/1X			Units: g's/lbf	
MODE (#)	FREQ (Hz)	DAMPING (%)	AMPLITUDE	PHASE (Deg)
1	3439.152	0.804	6.0084E+002	-2.84
2	7696.416	0.204	8.4791E+002	-1.15
3	9133.233	0.274	2.5189E+003	176.73
4	9864.400	0.236	1.4540E+002	-2.24
5	12337.632	0.130	6.9158E+002	-0.38
6	12599.928	0.165	8.7588E+002	-5.35
7	0.000	0.000	0.0000E+000	0.00
8	0.000	0.000	0.0000E+000	0.00
9	0.000	0.000	0.0000E+000	0.00
10	0.000	0.000	0.0000E+000	0.00

Fig. 6 Printout of modal parameters of SSS Part #1

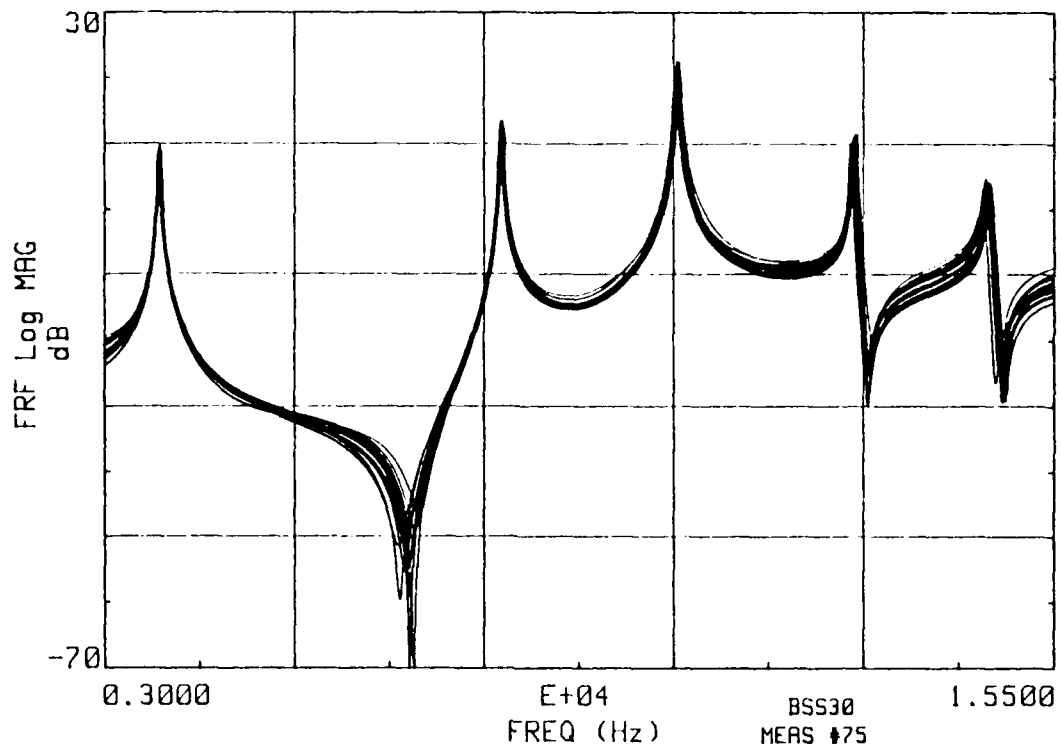


Fig. 7 Composite overlay of 15 synthesized FRFs of BSS parts

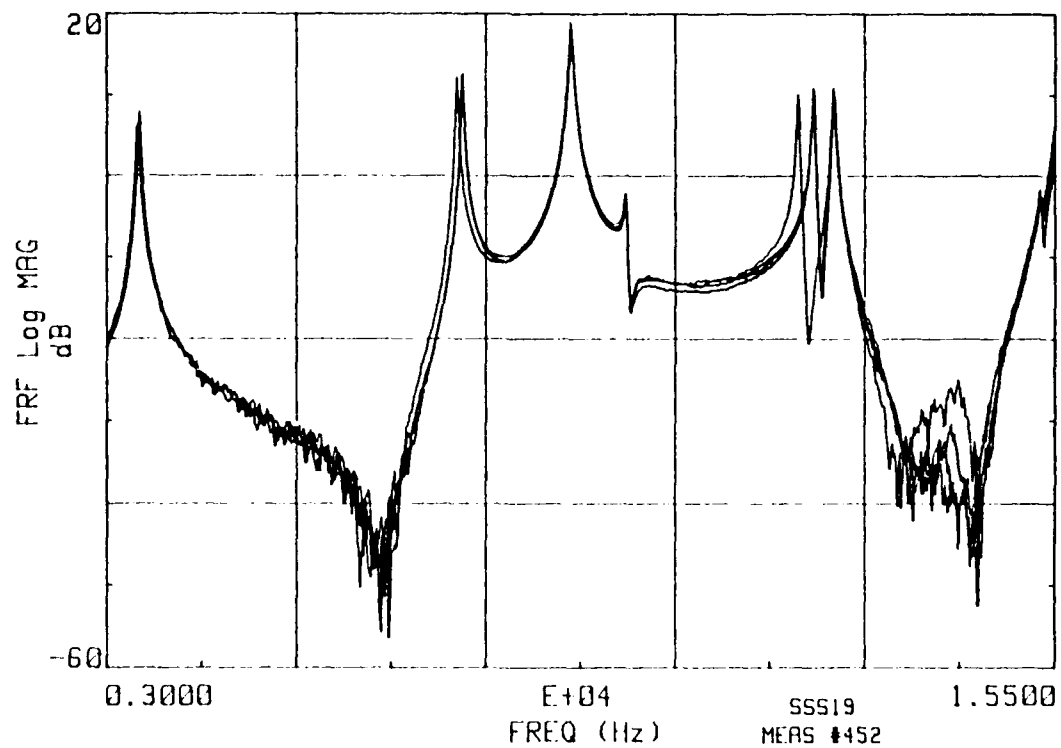


Fig. 8 Composite overlay of measured FRFs of three good SSS parts and one SSS part with machining error

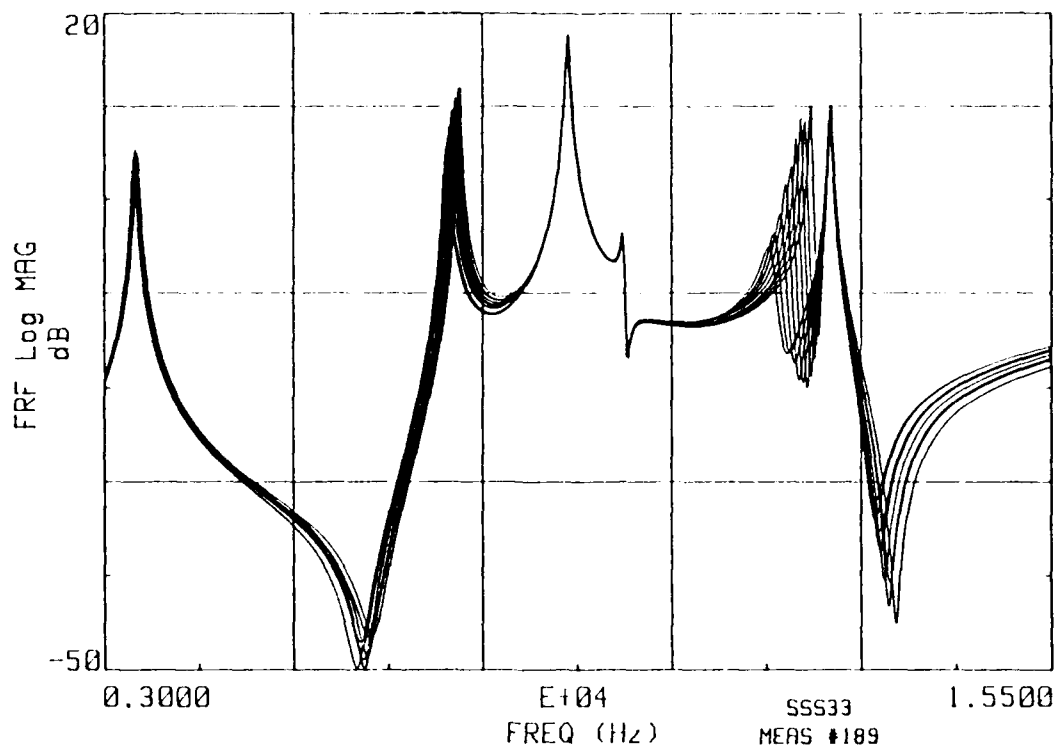


Fig. 9 Composite overlay of synthesized FRFs of SSS Part #1 for mass variability study

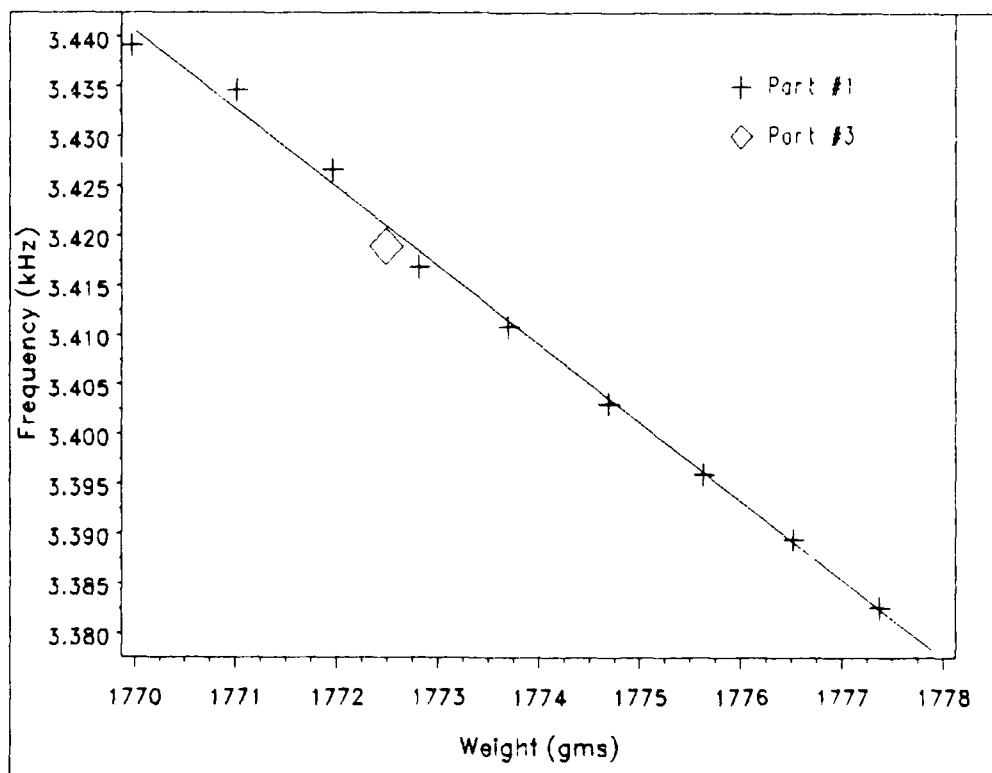


Fig. 10 First modal frequency vs. weight for mass variability study of the top lip of SSS Parts #1 and #3

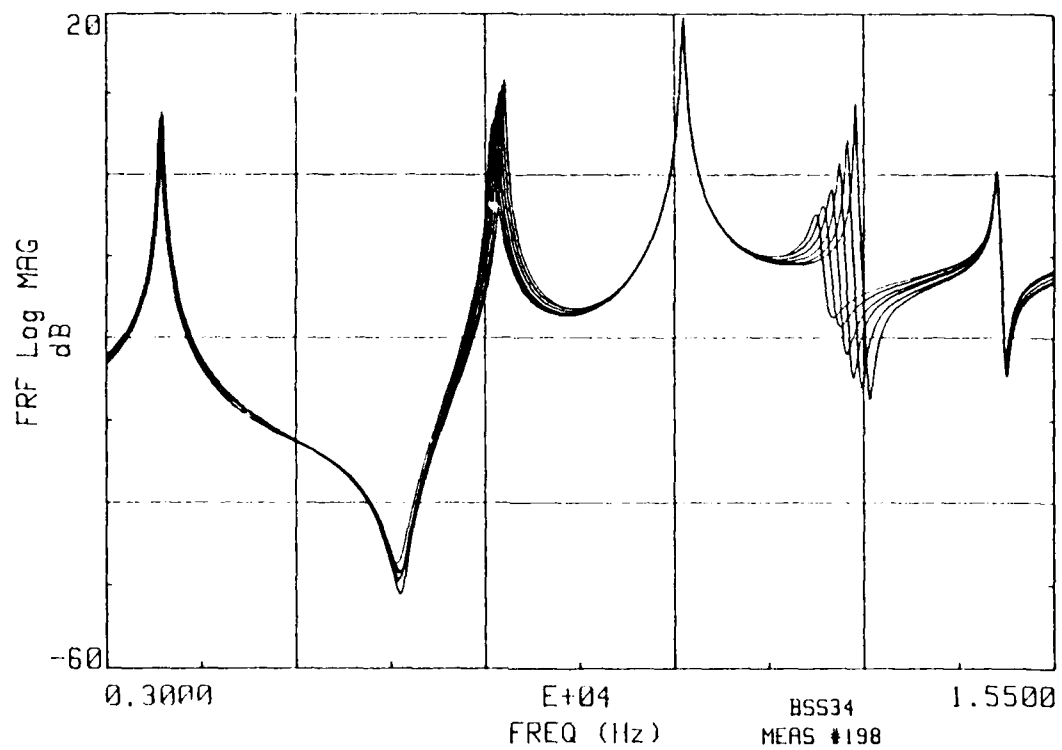


Fig. 11 Composite overlay of synthesized FRFs of BSS Part 4714 for mass variability study of top lip

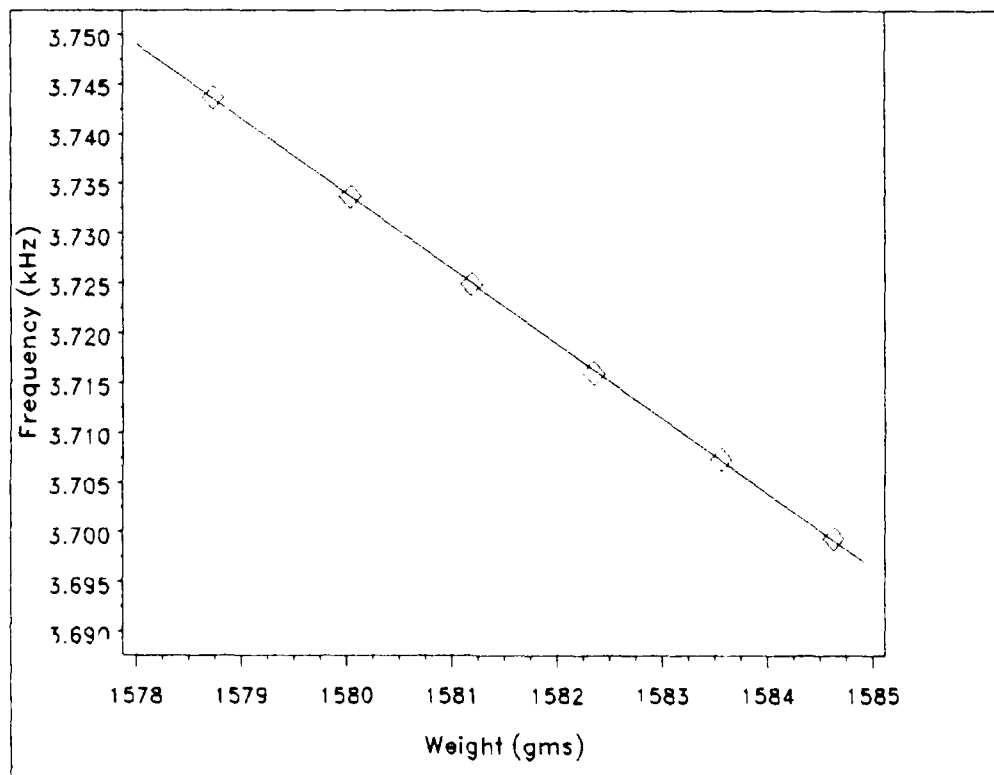


Fig. 12 First modal frequency vs. weight for mass variability study of the top lip of BSS Part 4714

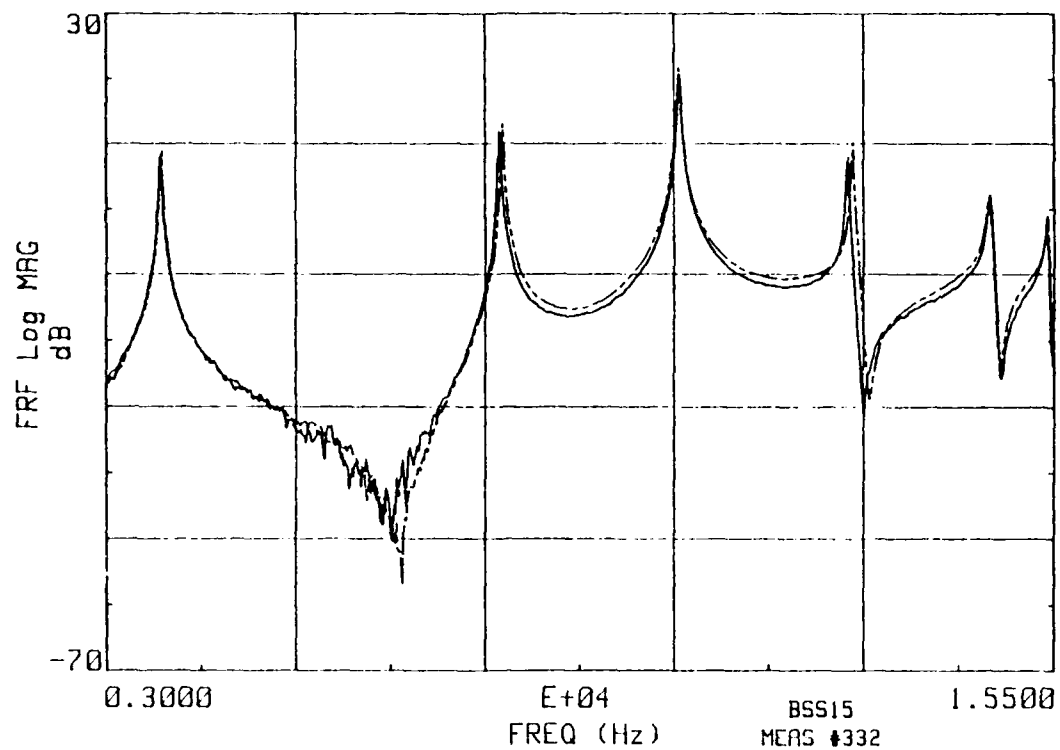


Fig. 13 Comparison of measured FRFs of BSS Part 4570 with tool gouge on inside surface (solid line) to BSS Reference Part 4716 (dotted line)

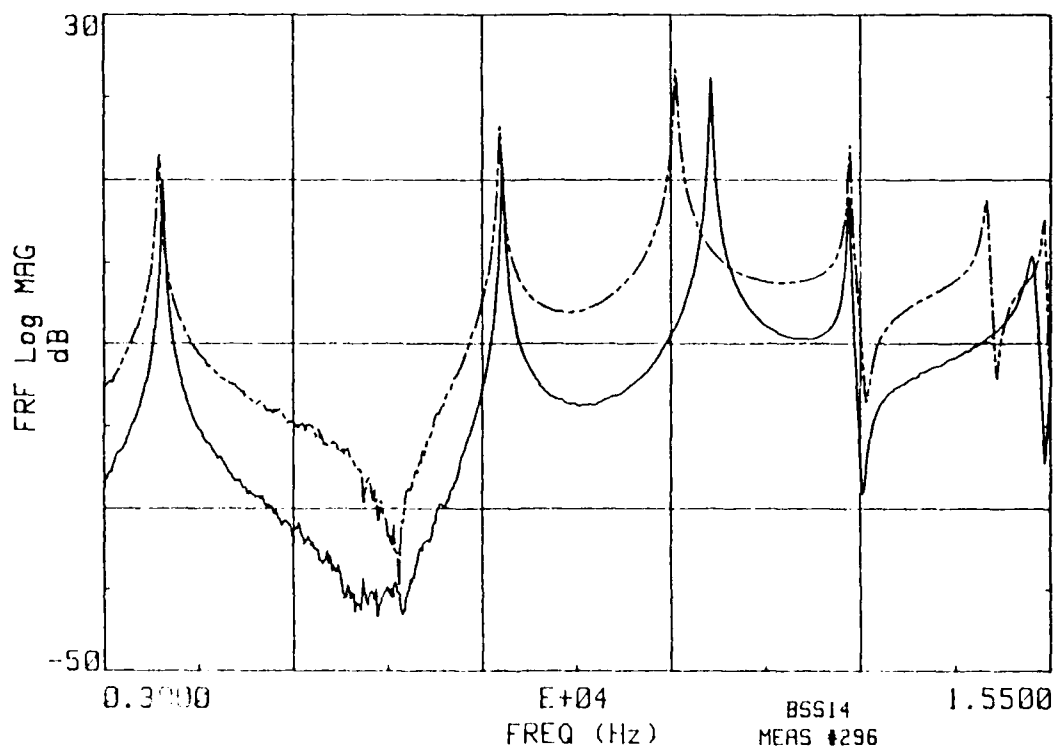


Fig. 14 Comparison of measured FRFs of BSS Part 4602 with undersize flange (solid line) to BSS Reference Part 4716 (dotted line)

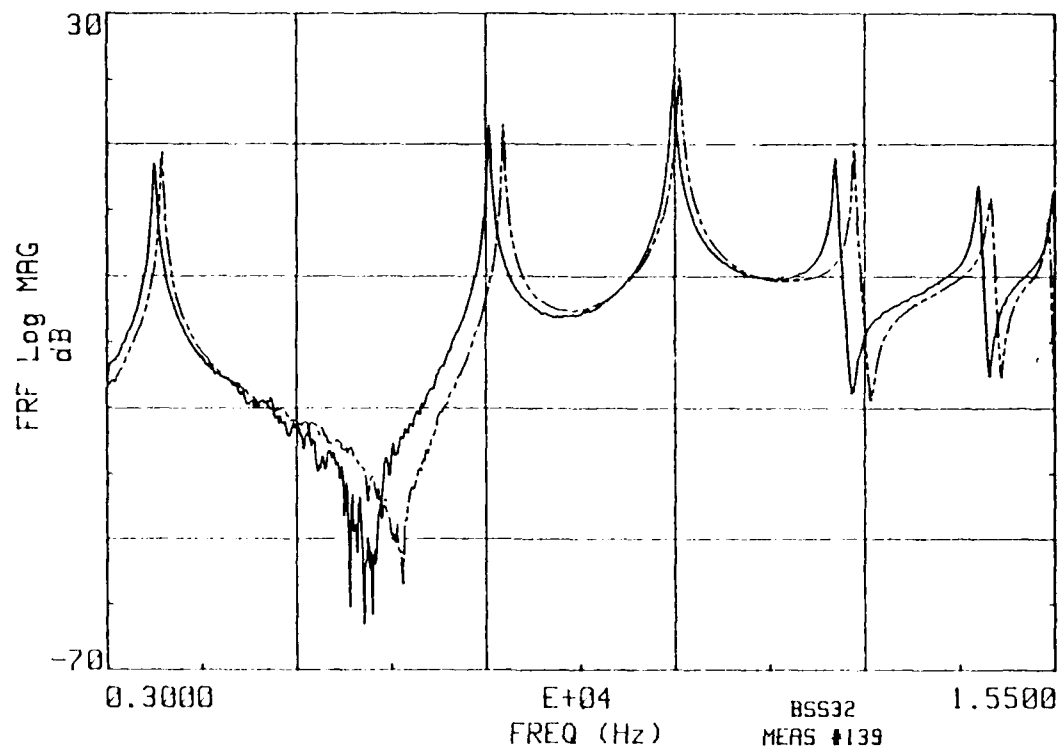


Fig. 15 Comparison of measured FRFs of BSS Part 4657 with undersize outside diameter (solid line) to Reference Part 4716 (dotted line)

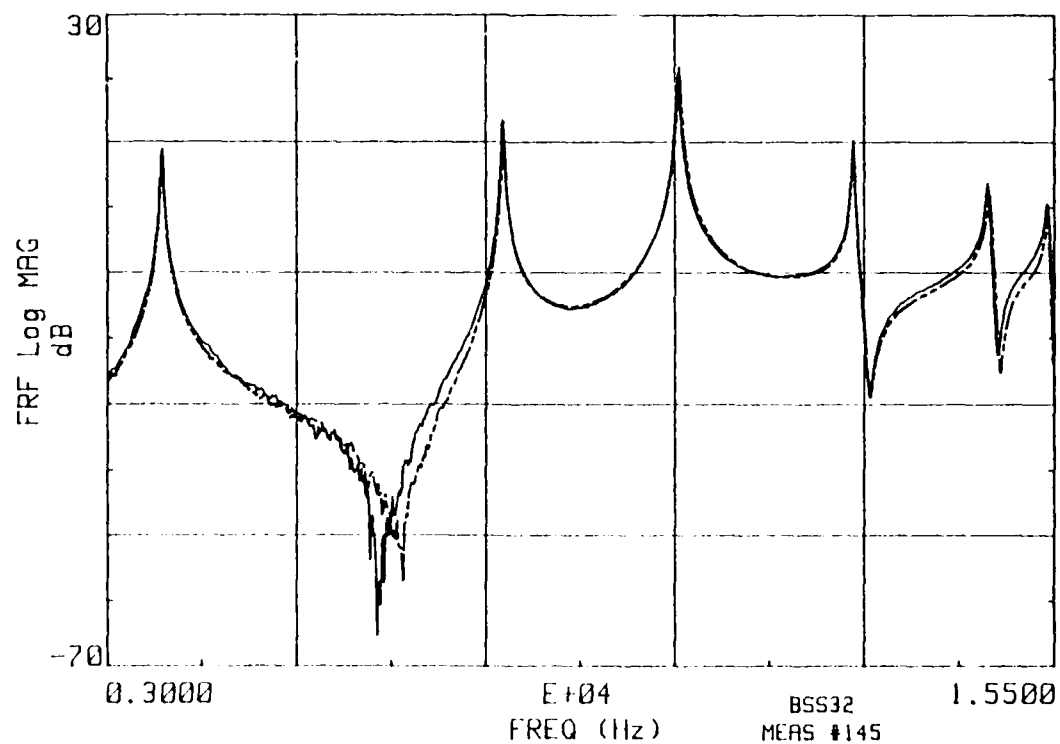


Fig. 16 Comparison of measured FRFs of bulged can Part 4702 (solid line) to BSS Reference Part 4716 (dotted line) showing no apparent differences in frequency peaks

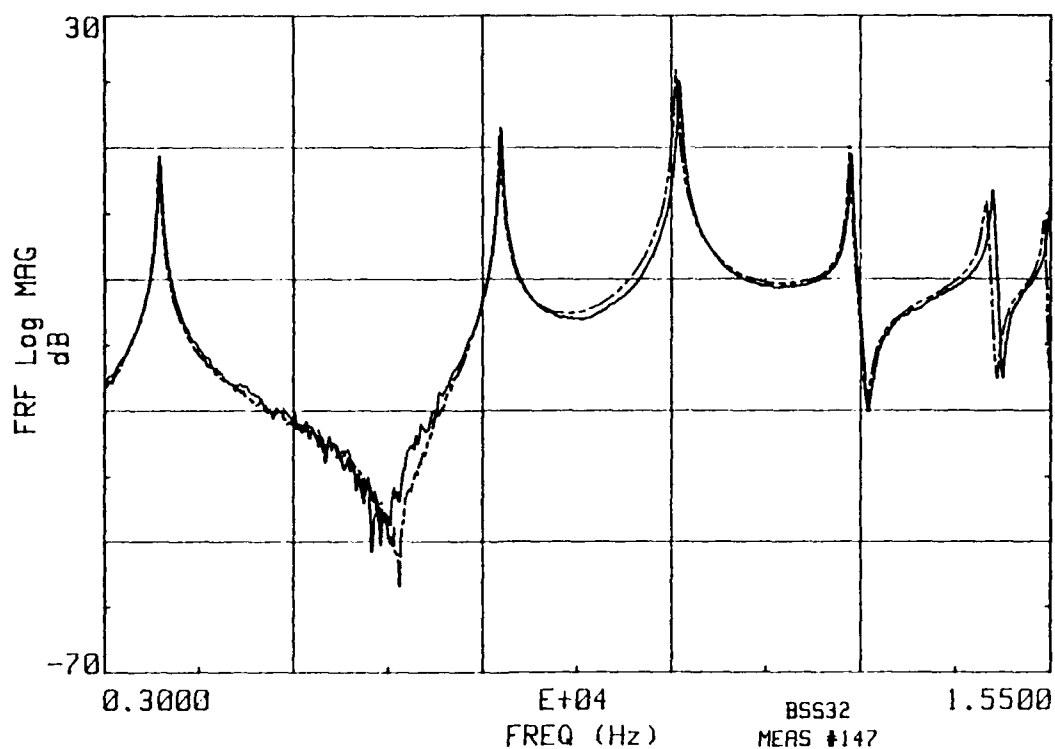


Fig. 17 Comparison of measured FRFs of bulged can Part 4714 (solid line) to Reference Part 4716 (dotted line) showing shifts in modes 1, 3, 4, and 5

Table 1 Standardized principal component scoring coefficients for first two components and each modal frequency

	FACTOR1	FACTOR2
MODE 1	0.28	-0.00
MODE 2	0.26	0.34
MODE 3	0.24	-0.40
MODE 4	0.20	0.55
MODE 5	0.22	-0.47

Table 2 Principal component scores and overall probabilities for the 15 most extreme of the 56 BSS parts

PART	FACTOR1	FACTOR2	CHISQR	PROB
4602	13.57	-16.89	469.84	0.0000
4657	-16.28	-11.51	397.78	0.0000
4570	-2.80	-4.33	26.65	0.0000
4740	2.21	2.36	10.52	0.0051
4748	-2.85	0.00	8.13	0.0170
4714	2.65	-0.95	7.96	0.0186
4711	2.27	-1.41	7.19	0.0273
4728	0.92	2.10	5.27	0.0716
4701	-2.27	0.24	5.23	0.0728
4749	1.07	1.83	4.53	0.1036
4705	-0.89	-1.80	4.06	0.1308
4683	1.02	-1.67	3.87	0.1439
4723	-0.56	-1.86	3.79	0.1500
4693	1.63	-0.92	3.50	0.1735
4732	-0.14	1.74	3.07	0.2144

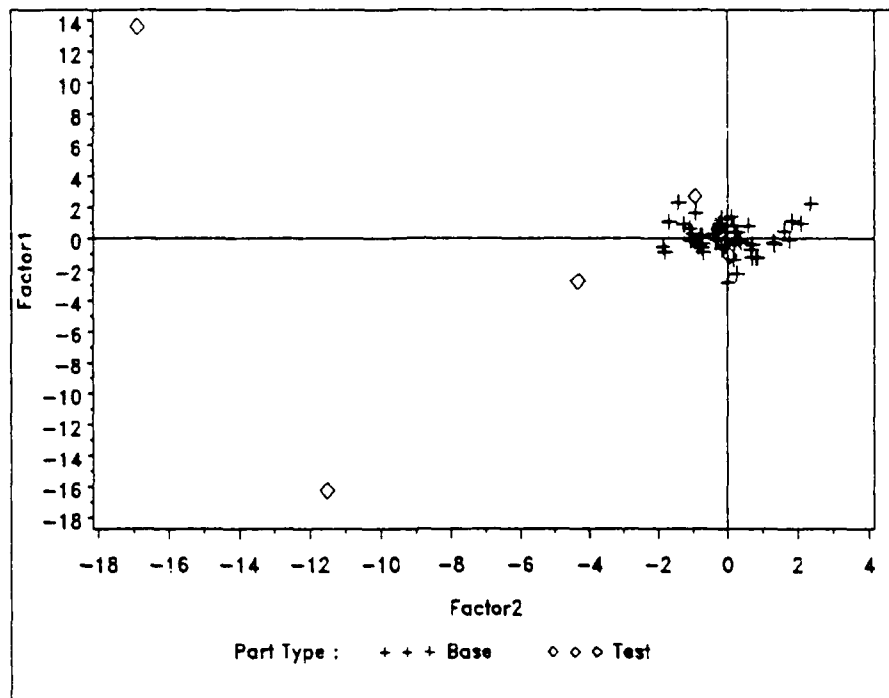


Fig. 18 Principal component scores for 50 Base and 6 Test parts

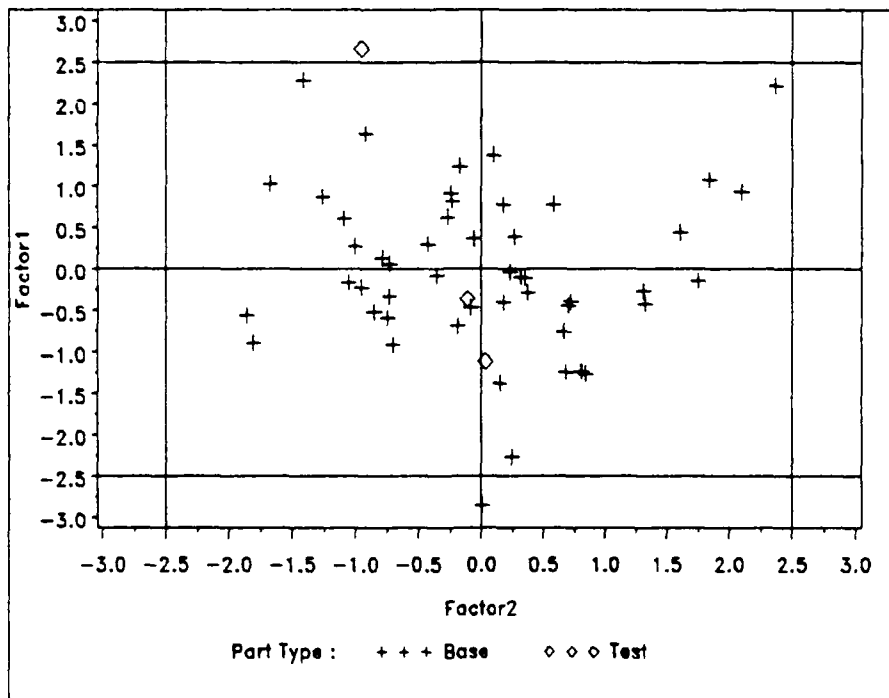


Fig. 19 Principal component scores for 50 Base and 3 suspect bond parts with 99% confidence prediction limits

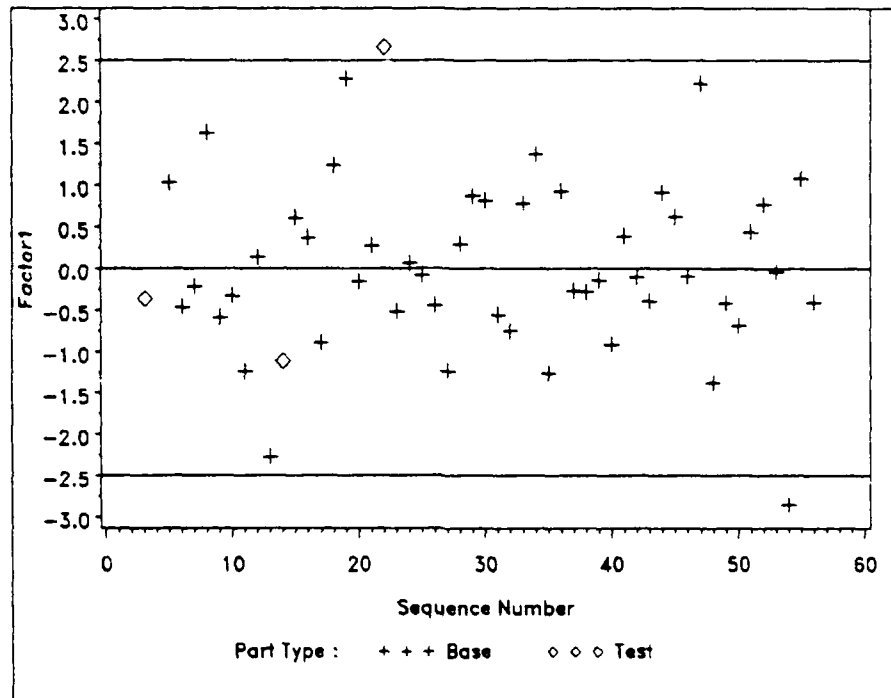


Fig. 20 First principal component score vs. manufacturing sequence for 50 Base and 3 Test parts with 99% confidence prediction limits

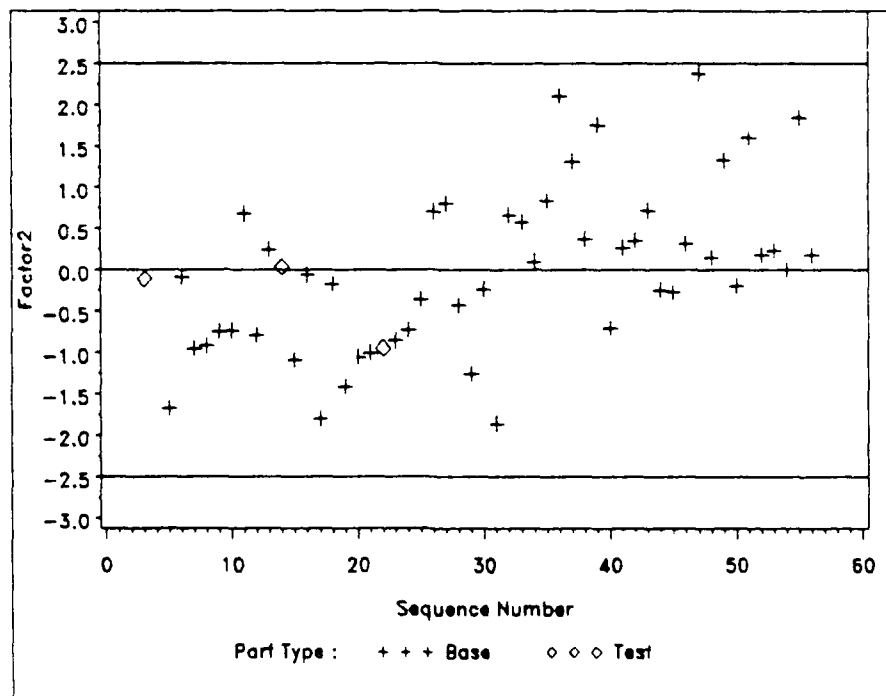


Fig. 21 Second principal component score vs. manufacturing sequence for 50 Base and 3 Test parts with 99% confidence prediction limits.

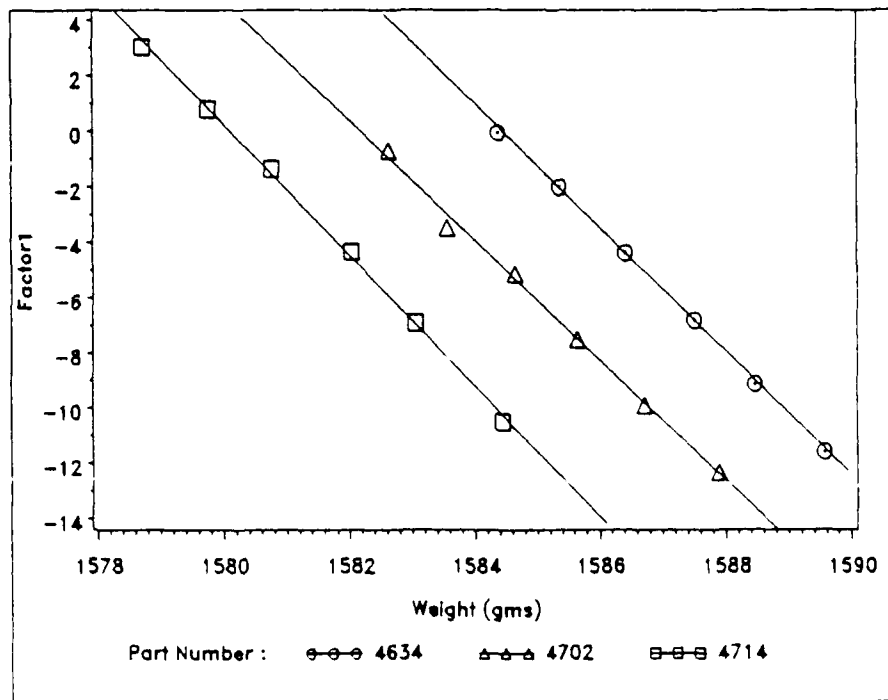


Fig. 22 First principal component score vs. weight for three BSS Test parts with simple linear regression lines

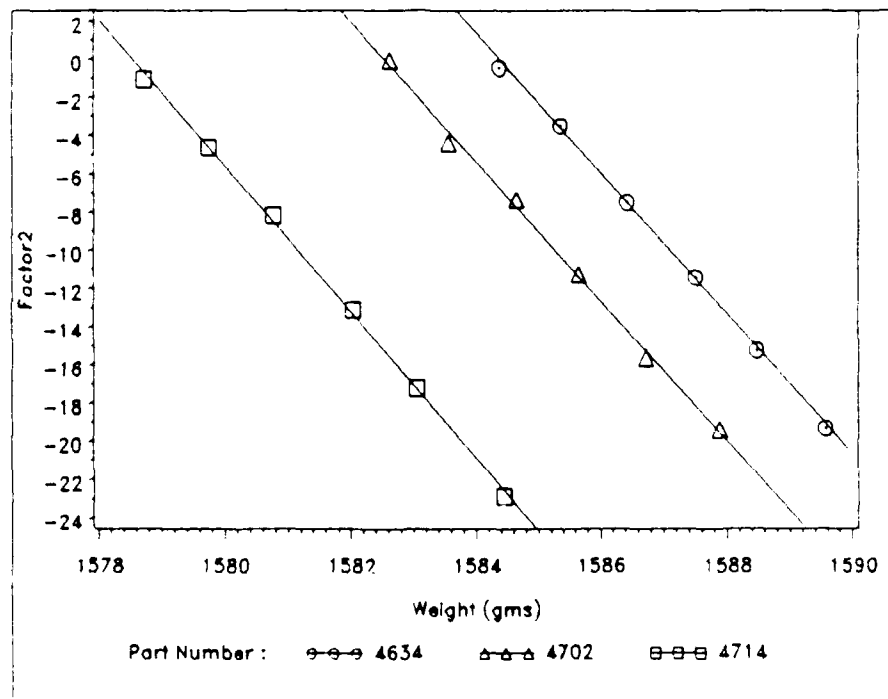


Fig. 23 Second principal component score vs. weight for three BSS Test parts with simple linear regression lines

MODEL VALIDATION USING SUBSTRUCTURE MODAL-TESTING, APPLIED TO A LARGE AND VERY FLEXIBLE WIND TURBINE

**Thomas G. Carne, James P. Lauffer,
Anthony J. Gomez, Thomas D. Ashwill
Sandia National Laboratories, Albuquerque, NM 87185**

The Sandia 34-Meter Test Bed Turbine is a vertical-axis wind turbine, thirty-four meters in diameter, designed to provide a test-bed for research in aerodynamics, structures and control. In order to design a large wind turbine, knowledge of the modal frequencies and mode shapes is essential for predicting structural response. During the design, analytical or finite element models are utilized for estimates of these modal parameters. However, when hardware becomes available, modal testing can be used to verify or update the models. The concept of substructure modal testing was developed for the Sandia 34-Meter Test Bed in order to more fully evaluate the accuracy of the finite element model. Instead of performing only one test on the entire turbine, separate tests and analyses were performed on major substructures of the turbine, including three separate blade sections, the tower supported by the guy cables, and the entire turbine. The results were then compared to analytical predictions from the finite element models of the substructures and the entire turbine.

INTRODUCTION

In the design of a large flexible wind turbine, knowledge of the modal frequencies and mode shapes is essential for predicting structural response and fatigue life. During the design process, analytical models must be depended upon for estimates of the modal parameters. When the turbine hardware becomes available for testing, the actual modal parameters can be experimentally determined. These measured data can be used to update the analytical predictions or modify the model.

The analytical model is a critical design tool because it is used to predict fatigue life, evaluate operational constraints (wind speed and rotation speed), and guide redesign if needed. The model can also include the gyroscopic effects of a rotating turbine [1]. Consequently, verification of the model with test data is very important, and this is ordinarily performed after the turbine is assembled. Typically, results of a modal test on the entire turbine are compared with predictions from the model. If the agreement is acceptable, then the verified model can be used with assurance of reasonable accuracy. However, if there are some discrepancies between the test results and the analytical predictions, then determining where the model is inadequate and improving it can be a most difficult problem.

The concept of verification through substructure modal testing can be used to alleviate this problem. With this concept the structure is divided into

substructures, usually major portions of the structure, and then each of these substructures are individually tested and their models verified. If possible, some substructures can be further assembled; these combined substructures tested; and their models verified. Using this technique, any inadequacies in the models are discovered at the substructure level. If all the substructures have verified models and if there still are any discrepancies between the test data and analytical results for the entire turbine, then the problem can be isolated to the modeling of the joints which connect the substructures.

The 34-Meter Test Bed is rated at 500 kW at 37.5 rpm and has a thirty-four meter diameter rotor and a total height of fifty meters. The entire rotor, including the central column and the two slender curved blades, rotates on bearings. The top of the rotor is supported by guy cables through a bearing. Figure 1 is a photograph of the completely assembled turbine. Each blade consists of five different blade sections with different chords and airfoils. These sections are constructed from extruded 6063-T6 aluminum, and cold bent to the appropriate radius of curvature. Figure 2 shows a diagram of the assembled blade with the five sections indicated. The center blade section has a seventeen meter radius and a 0.91 meter chord and is approximately 17.5 meters long. The center section is connected on both ends to intermediate sections which have a thirty meter radius and a 1.07 meter chord, and are approximately six meters in length. Lastly, there are top and bottom sections which are straight with a 1.22 meter chord and approximately eleven meters long. Reference [2] describes the design and fabrication of the turbine in more detail.

For the Test Bed Turbine we have tested three different blade substructures, the column substructure supported by the guy cables and base, and finally the entire turbine. The blade substructures include both the center section and an intermediate section. These two sections were then joined and tested as a unit, creating a combined blade section over twenty-five meters long with one joint between the sections. These tests are described in the following Experimental Techniques section. The Results section contains a discussion of the analytical predictions as compared to the experimental results.

EXPERIMENTAL TECHNIQUES

To measure the modal frequencies and mode shapes of the various substructures, we have used the frequency response function (FRF) approach. In this approach one first measures the response of the structure as a function of frequency due to a force input at a driving point. Using a set of these FRFs, which represent the responses at all the points of interest on the structure, one can estimate the modal frequencies and mode shapes of the modes within the frequency range of the measurements. The type of input force can be fairly general, that is, it can be sinusoidal, random, or transient in nature, as long as it has sufficient frequency content over the frequency range of interest. Given the force input to the structure, the FRF can be measured with good accuracy provided that proper experimental techniques are utilized [3,4]. Once the FRFs are measured, there are many techniques that can be used to estimate the modal parameters [3-5]. The specific experimental techniques used for the individual substructures will be described in this section.

Blade Section Tests

For any modal test in which one wants to compare the results with analytical calculations, a key element is matching the boundary conditions in

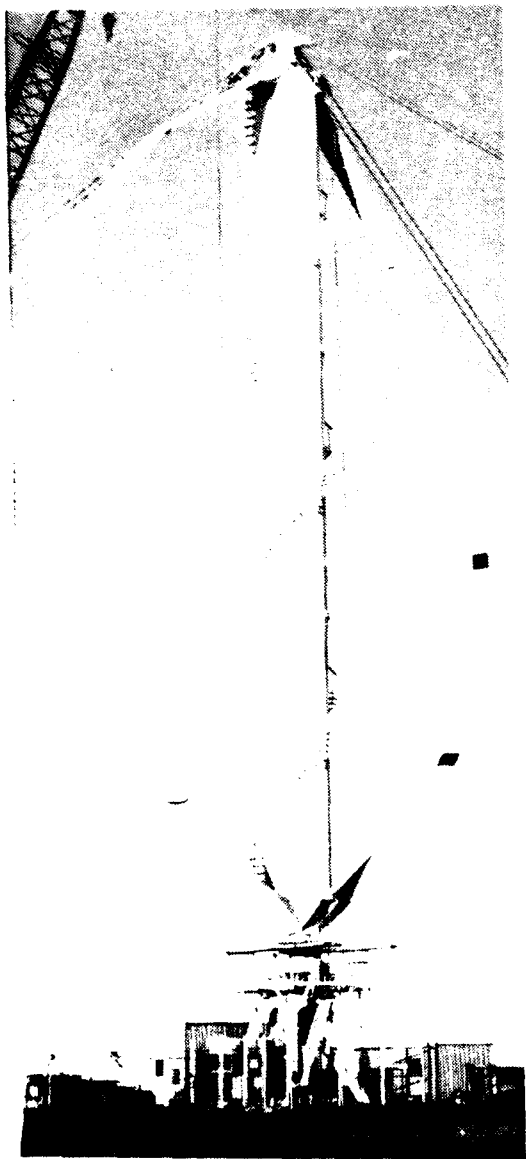


Figure 1. Sandia 34-Meter Test Bed

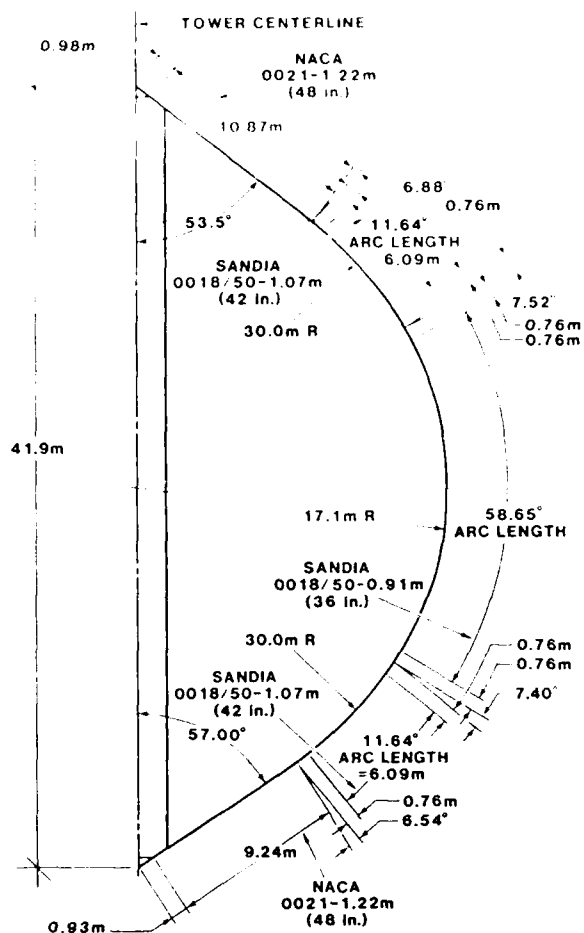


Figure 2. Diagram of Blade Sections

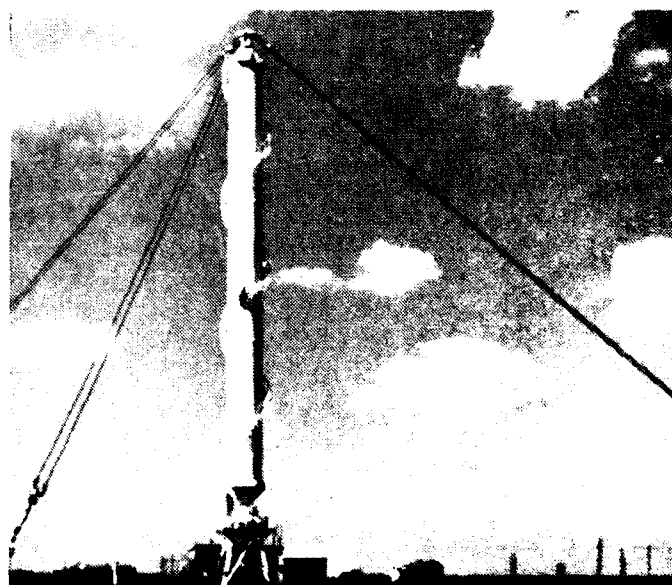


Figure 3. Tower Supported by Guy Cables

the test with that in the model. For the tests on the blade sections, this was the principal difficulty. For all three of the blade tests the sections were supported very softly with elastic cords to simulate free boundary conditions. Free boundary conditions are used in the experiment because they could be approximated in the laboratory, and are quite easy to include in the finite element model. As a rule of thumb, to simulate the free boundary conditions one would like the frequencies of the rigid-body modes of the structure on its support system to be less than ten percent of the frequency of the first elastic mode. Ideally, if one had truly free boundary condition, then the rigid-body modes would all be at zero Hz.

The blade sections basically have two different types of modes, flatwise bending and edgewise bending. The flatwise modes involve bending normal to the chord of the blade (the flatwise or the soft direction) and consequently are much lower in frequency than the edgewise modes which involve bending in the same direction as the chord (edgewise or the stiff direction). See Figures 1 and 2 for details of the blades. By hanging the blade sections in a pendulum fashion so that the flatwise direction was normal to the pendulum support, we created a very soft or low-frequency support in the flatwise direction. In the edgewise direction the softness of the elastic straps was sufficiently low so that the highest edgewise rigid-body mode was well below the elastic edgewise modes. For example in the case of the center section, the first flatwise mode was at 2.17 Hz while the highest pendulum-type rigid-body mode was at 0.30 Hz. While this is higher than suggested by our rule of thumb, the effect of the support was further minimized by supporting the blade at the nodes of the first mode, so that the support had a negligible effect on the elastic mode frequency.

To measure the FRFs for the blade, a transient force was input with a rubber-tipped sledge hammer, instrumented with a force transducer. Two sets of FRFs were measured using flatwise and edgewise excitation to insure that all the modes of interest were excited. Tri-axial measurements were made along both the leading and trailing edges of the sections using high output accelerometers.

Tower Test

The tower test was different from the blade tests in that we wanted to include the uncertain boundary conditions which the turbine base provide for the tower. This test was performed in the field on the erected tower supported at the top by the guy cables and the bottom by the turbine base. Figure 3 shows a photograph of the tower alone without the blades attached. The tower was instrumented with accelerometers normal to its axis along its length.

As in the blade test, a transient input force was used to excite the structure. However, in this case the transient was provided by suddenly cutting a steel cable tensioned to 45,000 N (10,000 lbs). The cable was attached near the middle of the tower, and then tensioned to the preload by a winch at the ground level. By suddenly cutting the cable, a step force is input to the structure. This force can be measured using a load cell in series with the cable. With this as the input, FRFs can be measured using techniques developed in [6]. This particular force input has a very desirable feature in that its frequency content is inversely proportional to frequency. This creates most of the energy at the very low frequencies and will excite the low frequency modes of the tower quite well.

Using this step force input (called step-relaxation), and the response accelerometers on the tower, a complete set of FRFs were measured. The mode

shapes and frequencies for the tower were extracted from the FRF data, and these will be discussed in the Results section.

Turbine Test

Figure 4 displays front, top, and side views of the mode shapes for the entire turbine as computed using the finite element model. One can see that the mode shapes become fairly complex, although they typically involve only in-plane motion or out-of-plane motion, where the plane is defined by the undeformed blades and tower. These mode shapes are for the parked turbine; for the rotating turbine the shapes vary with the rotation speed and couple with each other, [1].

For the modal test of the entire turbine, we used two different excitation techniques, step-relaxation, as discussed above for the tower, and wind excitation. This results in two separate modal tests. The wind excitation technique [7] was developed because there is a difficulty in performing step-relaxation testing of a wind turbine. This is due to the fact that the vibratory response induced by the wind on the blades may be large when compared to the response from the step input. The vibratory response due to the wind is uncorrelated with the step-relaxation force and has the same effect as noise on the response signal. This results in noisy estimates of the FRFs. Because modal parameters can not be accurately extracted from noisy FRFs, and because windless days could not be guaranteed, we performed a modal test of the turbine using wind as the excitation force. However, there was sufficient time when the winds were low, so a normal step-relaxation test could also be conducted.

Performing a modal test with wind excitation is similar to performing a step-relaxation test with some important differences. One significant difference is that the forces acting on the structure are not measured. We assume that these forces are random, broadband, and have sufficient energy content over the entire frequency range of interest. Additionally, we assume the the wind forces acting on the turbine do not have any holes or peaks in the frequency domain. Because the force can not be directly measured, we cannot calculate FRFs as is normally done in a modal test; instead, we measure auto- and cross-spectra between the response acceleration signals. From these spectra, using techniques developed in [7,8], the modal parameters including the modal frequencies, mode shapes, and modal damping can be extracted.

Table 1 shows results from these two tests with both the modal frequencies and damping factors listed for the two excitation techniques. The mode numbers of the first column refer to the numbering of Figure 4. The modal parameters extracted using the wind or step-relaxation testing are virtually identical, except for the first rotor twist mode (1.51 Hz for wind and 1.35 Hz for step-relaxation). This difference can be attributed to the brakes which were applied during the tests. During the step relaxation test, large torques were applied to the braking system when pulling on the blades. This excited a nonlinear response in the friction brakes which was not excited in the low torque wind excitation test. One can also observe that the damping in this mode is much higher for the step-relaxation test than for the wind test. This indicates that substantial energy has been dissipated through the sliding friction of the brakes. Further discussion and results of these tests can be found in Reference [8].

RESULTS

The principal results are comparisons of the modal frequencies between the tests and the analyses for each of the substructures and the entire turbine.

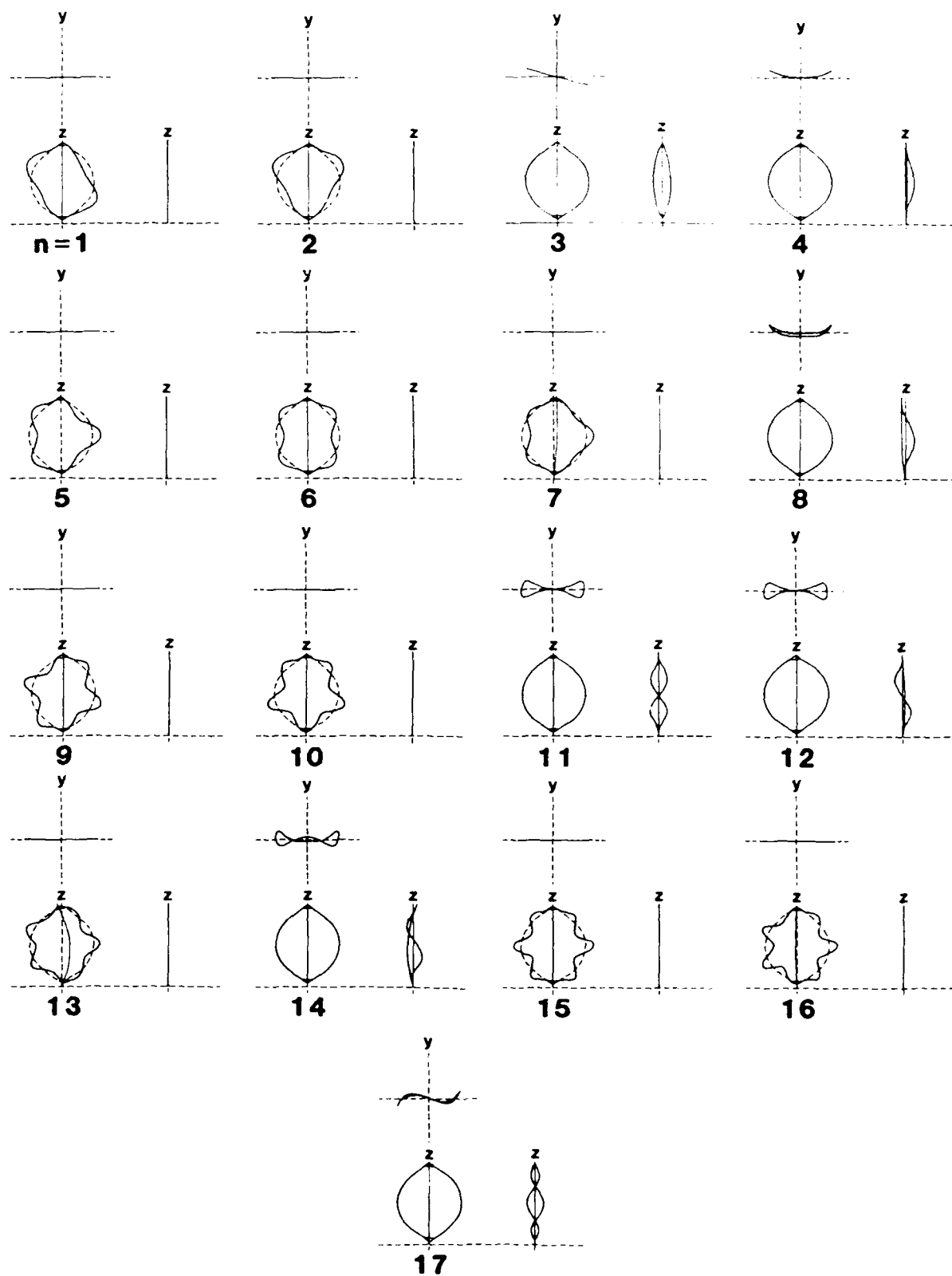


Figure 4. Mode Shapes of the Turbine from the Finite Element Model

Table 1. Modal Frequency and Damping Ratios

<u>Mode #</u>	<u>Wind</u>		<u>Step-Relaxation</u>		<u>Description</u>
	<u>Frequency</u> (Hz)	<u>Damping</u> (% critical)	<u>Frequency</u> (Hz)	<u>Damping</u> (% critical)	
1&2	1.06	2.0	1.04	1.8	1st Flatwise (Combined Mode)
3	1.51	1.1	1.35	10.0	1st Rotor Twist
4	1.81	0.2	1.81	0.2	1st Blade Edgewise
5	2.06	1.1	2.06	1.3	2nd Flatwise Anti-Symmetric
6	2.16	1.7	2.16	1.2	2nd Flatwise Symmetric
7	2.50	0.4	2.49	0.4	1st Tower In-Plane
8	2.61	0.3	2.60	0.2	1st Tower Out-of-Plane
9&10	3.49	0.7	3.45	0.9	3rd Flatwise (Combined Mode)
11	3.59	0.1	3.59	0.1	2nd Rotor Twist
12	4.06	0.2	-	-	2nd Blade Edgewise
13	4.69	0.4	-	-	2nd Tower In-Plane
14	5.28	0.4	-	-	3rd Blade Edgewise
15	5.08	0.5	-	-	4th Flatwise Symmetric
16	5.33	0.4	-	-	4th Flatwise Antisymmetric

If there is close agreement between the two results, then one can have high confidence in the accuracy of the model. Some qualitative comparisons of mode shapes are also presented, but in general, the mode shapes were quite similar between the tests and the analysis. For the substructure tests only a few modes were measured as compared to the turbine test, since the lowest modes of each substructures should capture the fundamental dynamics of that structural unit.

Center Blade Section

Table 2 presents the results for the center blade section, see Figure 2. Three flatwise and two edgewise modes are included from both the test and the analysis. The differences are quite small for the lower modes, but increase somewhat for the higher modes. Overall, one would conclude that the model for the center section is quite accurate.

Intermediate Blade Section

Table 3 presents the results for the intermediate blade section. The correlation between the analysis and test results is not nearly as good as it was for the center blade section. Of the five modes, the three flatwise modes have excellent agreement while the edgewise mode is different by over one hundred percent and the twisting mode does not even appear in the analysis. Examining the mode shapes for both this test and the center section, one can see that the modes that include twisting are not well predicted by the model, as compared to the pure flatwise or pure edgewise modes. That is not unexpected since the model does not include any rotary inertia about the blade axis. Consequently, if a mode's primary kinetic energy comes from twist about the blade axis, that mode will not be modeled well. Clearly this substructure has a good model for flatwise deformation for all modes up to the third mode; however, it demonstrates the inadequacy of the model for twisting modes about the axis of the blades. As we will see later in the results for the entire turbine, this particular inadequacy does not affect the quality of the overall model, since this twisting deformation is not dominant for the low frequency modes of the entire turbine.

Combined Blade Section

For the substructure consisting of a combination of the center and intermediate sections (over twenty-five meters long), the modal frequencies are quite low starting at about one Hz. These results are shown in Table 4. Here, as with the center section, the agreement is outstanding with very small differences in the frequencies including four flatwise modes and two edgewise modes. This fine agreement also establishes the adequacy of the model of the joint between the blade sections. Figure 5 shows test and analysis results for the three flatwise and the first edgewise modes for this substructure. One can see the shapes are very similar. The edgewise mode does include some twisting, but it does not contribute significantly to the kinetic energy of the mode. Note also that the first edgewise mode has three nodes along its length rather than two as we see for the flatwise modes; this is a result of the curvature in the blade.

Table 2. Modal Frequencies for the Center Blade Section

<u>Mode Shape</u>	<u>Analysis</u> (Hz)	<u>Test</u> (Hz)	<u>Difference</u> (%)
1st Flatwise	2.22	2.17	2
2nd Flatwise	6.31	6.16	2
3rd Flatwise	12.7	12.3	3
1st Edgewise & Twist	15.6	16.4	5
2nd Edgewise	33.5	29.8	12

Table 3. Modal Frequencies for the Intermediate Section

<u>Mode Shape</u>	<u>Analysis</u> (Hz)	<u>Test</u> (Hz)	<u>Difference</u> (%)
1st Flatwise	15.6	15.4	1
2nd Flatwise	44.5	44.4	0
Twisting	-	62.9	-
1st Edgewise with Twisting	146.	71.7	103
3rd Flatwise	89.2	87.6	2

Table 4. Modal Frequencies for the Combined Section

<u>Mode Shape</u>	<u>Analysis</u> (Hz)	<u>Test</u> (Hz)	<u>Difference</u> (%)
1st Flatwise	1.11	1.09	2
2nd Flatwise	3.32	3.14	6
3rd Flatwise	6.83	6.54	4
1st Edgewise	6.88	7.07	3
4th Flatwise	11.4	11.0	4
2nd Edgewise	18.2	18.1	1

Table 5. Modal Frequencies of the Tower with Guys

<u>Mode Shape</u>	<u>Analysis</u> (Hz)	<u>Test</u> (Hz)	<u>Difference</u> (%)
1st Bending	2.60	2.64	2
2nd Bending	4.43	4.81 5.19	8 15

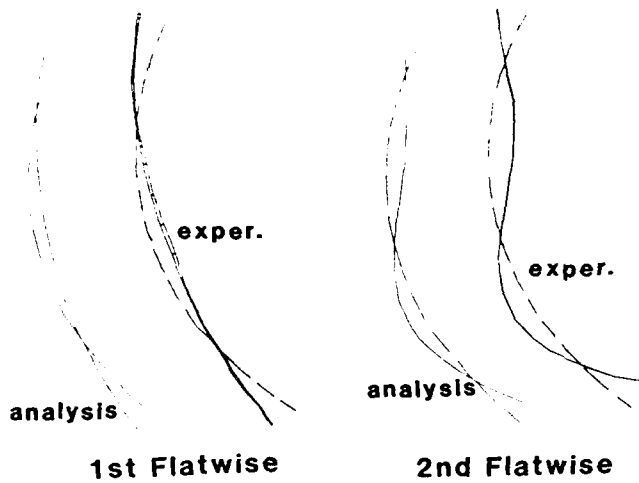


Figure 5. Comparison of Mode Shapes, Analysis and Test, for Combined Blade Section

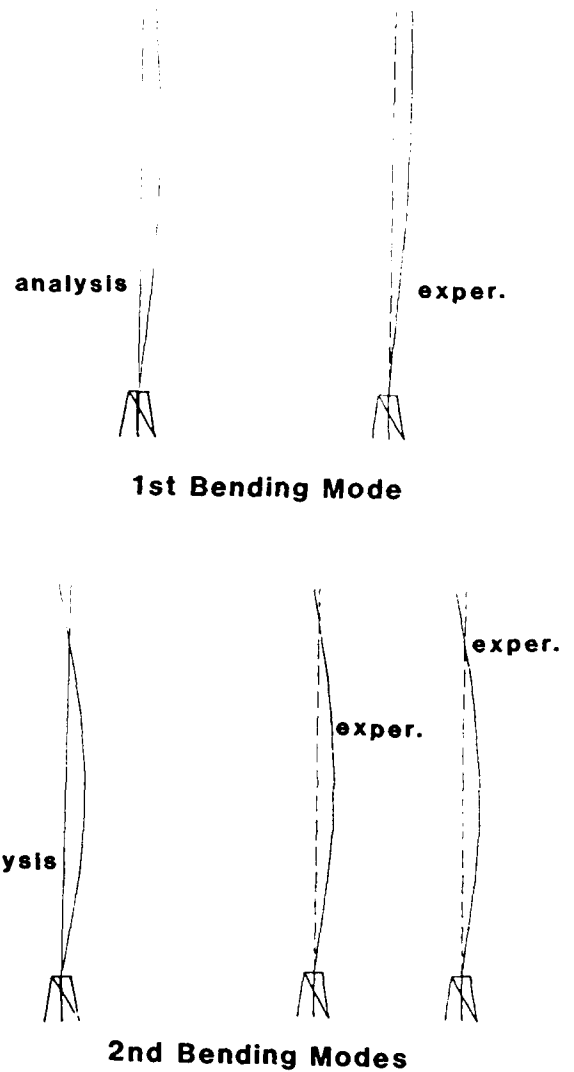


Figure 6. Comparison of Tower Mode Shapes, Analysis and Test

Tower Substructure

Table 5 shows the modal frequency results for the tower supported by the guy cables and the turbine base. Just a few modes were measured as it was felt that they represented the basic dynamics of this structural unit. The first modal frequency has been predicted quite well with only a two percent difference, and the mode shapes agree as depicted in Figure 6. In contrast, there appear to be two second bending modes in the test data, while only one is predicted by the analysis. Both of these modes are higher than the analysis by eight and fifteen percent. The difference between the analysis and the test is apparently due to the dynamics of the guy cables. In the model the cables are treated as massless axial springs, but in fact, they possess mass and have lateral modes in the frequency range of this test. These two "second bending modes" which are measured in the test are actually coupled modes including both the tower and the guy cables. This effect has not been included in the model. The differences are further illustrated by the mode shapes shown in Figure 6. The node points for the two test modes are shifted relative to each other, showing that they are distinct modes.

Entire Turbine

Finally, Table 6 shows the results of the analysis and test for the entire turbine. The test results are the average of the step-relaxation and the wind data, except for the first rotor twist mode where the wind result is used. The agreement is excellent for the ten modes listed, most having less than two percent difference. Only the first blade edgewise mode has a difference greater than three percent. Refer to Figure 4 for a diagram of these mode shapes. Interestingly, the agreement for the entire turbine is as good as that for any of the substructures, apparently showing a forgiveness of the small modelling inadequacies or a cancelling of errors. In any case, the results for

Table 6. Modal Frequencies for the Entire Turbine

<u>Mode Shape</u>	<u>Analysis</u> (Hz)	<u>Test</u> (Hz)	<u>Difference</u> (%)
1st Blade Flatwise	1.05	1.05	0
1st Rotor Twist	1.56	1.51	3
1st Blade Edgewise	1.72	1.81	5
2nd Blade Flat, Anti	2.07	2.06	0
2nd Blade Flat, Symm	2.14	2.16	1
1st Tower In-Plane	2.46	2.50	2
1st Tower Out-of-Plane	2.58	2.61	1
3rd Blade Flat, Anti	3.49	3.47	1
3rd Blade Flat, Symm	3.51	3.47	1
2nd Rotor Twist	3.52	3.59	2

the entire turbine do show that it is not absolutely necessary that every substructure be perfectly modeled in order to have an adequate model for the entire structure. This is due to the fact that certain deformations, which may not be modeled adequately, will be exercised in a substructure test, but are not involved in the low frequency modes of the entire turbine.

CONCLUSIONS

The finite element model of the 34-Meter Test Bed has been validated with modal tests of four substructures (three blade sections and the tower) and the entire turbine. In general, the correlation between tests and analyses were excellent for both the substructures and the turbine. The excellent correlation between model and test for the substructures helped ensure a similar result for the entire turbine. However, the substructure modal testing approach did reveal areas of the substructure models which were inadequate. The models were not accurate for certain deformations exercised in the substructure tests. These inadequacies did not affect the accuracy of the overall turbine model as these deformations were not important for the low frequency turbine modes.

A variety of modal testing techniques were employed to test the different structures, including excitation with transient impacts, step-relaxation, and wind excitation. Free boundary condition were well approximated on the very flexible blade sections by using a combination of a pendulum support with soft elastic straps.

REFERENCES

1. Carne, T. G., Lobitz, D. W., Nord, A. R., Watson, R. A., "Finite Element Analysis and Modal Testing of a Rotating Wind Turbine," The International Journal of Analytical and Experimental Modal Analysis, Vol. 3, No. 1, January 1988, pp. 32-41.
2. Ashwill, T. D., "Structural Design and Fabrication of the Sandia 34-Meter Vertical Axis Wind Turbine," Proceedings of the 1987 ASME-JSME Solar Energy Conference, Honolulu, HA, March 1987.
3. Ewins, D. J., Modal Theory: Theory and Practice, John Wiley & Sons Inc., New York, 1985.
4. Allemang, R. J. and Brown, D. L., "Experimental Modal Analysis," Handbook on Experimental Mechanics, Prentice-Hall, Inc., Englewood Cliffs, NJ, 1987, pp. 659-738.
5. MODAL-PLUS Reference Manual, Version 9, The SDRC Corporation, Milford, Ohio.
6. Lauffer, J. P., Carne, T. G., and Ashwill, T. D., "Modal Testing in the Design Evaluation of Wind Turbines," Proceedings WindPower '87, SERI/CP-217-3315, 1987, pp. 79-87.
7. Carne, T. G., Lauffer, J. P., Gomez, A. J., and Benjannet, H., "Modal testing the EOLE," Seventh ASME Wind Energy Symposium, ASME, New York, 1988, pp. 61-68.

8. Lauffer, J. P., Carne, T. G., and Gomez, A. J., "Modal Survey of the 34-m Test Bed Turbine," Sandia Technical Memo, June 7, 1988.

ANALYTICAL ESTIMATION OF EARTH PENETRATOR* STRUCTURAL RESPONSE AND COMPARISON WITH LABORATORY SHOCK AND MODAL TEST DATA

Robert J. Kipp
Applied Mechanics Division II

Vesta I. Bateman
Vibration Testing Division

Sandia National Laboratories
Albuquerque, NM

ABSTRACT

Analytical techniques for predicting transient structural response of earth penetrating projectiles during severe penetration events are presently being used at Sandia. Such analyses are subject to uncertainties arising from two areas: the prediction of the loads exerted on the penetrator, and the modeling of the detailed structural response of the penetrator to these loads. This paper discusses efforts to validate the accuracy of a structural model through comparison with data from laboratory shock and modal tests of a field test configuration penetrator, and the insight this is providing with respect to penetrator structural modeling.

INTRODUCTION

Applications of transient structural analysis of penetrators include evaluating penetrator capabilities, determining the desirability/feasibility of design modifications, and enabling a "balanced design" to be achieved; that is, a penetrator in which no structure or component has significantly less capability to survive prospective penetration events than other structures/components of the penetrator. The confidence with which penetration analysis can be applied to these endeavors has traditionally been limited by uncertainty in the accuracy of analytical results. The uncertainty arises from two areas: the prediction of the loads exerted on the penetrator, and the modeling of the detailed structural response of the penetrator to these loads. The level of uncertainty is particularly acute for transient lateral load-induced phenomena, such as component lateral acceleration environments and case bending stresses, which are extremely important in the determination of penetrator capability yet most difficult to characterize and quantify.

*This work was performed at Sandia National Laboratories and supported by the U.S. Department of Energy under contract DE-AC04-76DP00789.

Recently, data systems have become available which are enabling the simultaneous acquisition of axial and lateral accelerations and case strains during actual penetration events with a degree of dependability sufficient to allow meaningful comparisons with analytical predictions of structural response, including lateral load-induced phenomena. It is important, however, that the accuracy of analytical structural models be verified independent of the penetration load uncertainty. This can be accomplished through comparison with data from laboratory modal and shock tests which have been performed on field test configuration penetrator units. The internal structures included in these units are rather complex and significantly affect the response of the penetrator to time-dependent loads.

This paper discusses one analytical technique used in penetration analysis, the laboratory shock and modal tests, efforts to reconcile the analytical response predictions with the measured data, and the insight this is providing with respect to penetrator structural modeling and testing.

ANALYTICAL TECHNIQUE

The analytical technique presently being used makes use of two computer codes: GNOME [1], in which cavity expansion load models are used to predict axial and lateral force-time histories on a rigid penetrator, and SHELL SHOCK [2], with which the penetrator is structurally modeled and the transient structural response of the penetrator to the loads predicted by GNOME are determined. The method is uncoupled; that is, the technique can not take into account the effect that deformation of the structure during penetration may have on the forces exerted on it by the geologic target. The significance of this simplification is presently not known, although it is generally believed to be small for axial effects but possibly not small for lateral effects.

The emphasis of this paper is on validation of the accuracy of the SHELL SHOCK structural model of the penetrator. The penetrator is modeled as a perfectly symmetric structure. A schematic of the model is shown in Figure 1. The case is modeled using solids and shells of revolution, while the internals are modeled using solids, beams, and lumped masses. SHELL SHOCK allows asymmetric load application and response calculation without the need of a 3-D model. It also performs eigenvalue/eigenvector extraction to determine modal frequencies and shapes. SHELL SHOCK treats material response in a linear manner except that it permits piecewise linear description of the load/deflection response of beams.

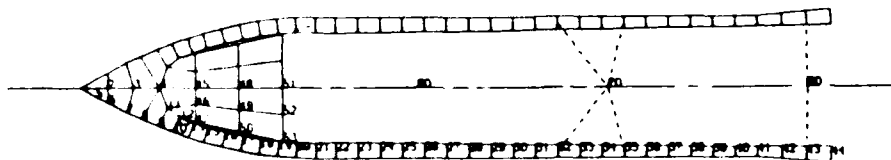


Figure 1. Schematic of SHELL SHOCK Structural Model of Penetrator

The internals of the field test unit penetrator are rather complex, as can be seen in Figure 2, which is a drawing of the penetrator itself. An aspect of this unit which is difficult to analytically model a-priori by presently available means is the frictional interaction between the internal bracing and the case. This interaction can significantly affect lateral stiffness and axial and lateral damping coefficients. The bracing is evident in Figure 2 about 2/3 of the way aft of the nose.



Figure 2. Field Test Configuration Penetrator

EXPERIMENTAL TECHNIQUES

The field test configuration penetrator was subjected to two different forcing functions in the laboratory: a low-level (about 2 klb) point force generated with an instrumented hammer, and a high-level (about 100 klb) point force generated with a Reverse Hopkinson Bar Technique. The penetrator case material is steel (Type 4340) which has a yield strength in excess of 170 ksi; the case was not visibly deformed by any of the tests described in this paper. The intent of the tests described herein is not to simulate a field test penetration environment, whose impulse is much higher, but to characterize the penetrator structural response to known axial and lateral loads and to compare to the response analytically predicted with a computer model.

A modal analysis with low-level force excitation was performed to determine the modal frequencies and the modal shapes. The modal frequencies and corresponding descriptions appear in Table 1. Space and configuration constraints severely limited instrumentation on the internals of the penetrator unit. Consequently, modal information regarding the internals is of less than desired detail. Note also that many of the modes are closely spaced, making experimental differentiation of these modes tenuous.

Table 1. Penetrator Modal Frequencies and Mode Shape Description.

<u>Mode</u>	<u>Frequency (Hz)</u>	<u>Mode Shape Description</u>
1	728	Internal Component bounce mode with bending
2	736	Similar to Mode 1 but rotated 90 degrees
3	856	Internal component bounce mode with case bending
4	888	Similar to Mode 3 but rotated 90 degrees
5	942	First case bending mode about Y axis
6	992	Torsion with case bending
7	1592	Case ovaling, n=2 mid and aft out-of-phase
8	1792	Case ovaling, n=2 mid and aft in phase
9	1800	First system axial mode
10	2048	Second case bending mode
11	2264	Case ovaling, n=2, 3*
12	2264	Case ovaling, n=3, 3
13	2456	First case axial mode
14	2696	Case ovaling, n=2, 4
15	3224	Third case bending mode
16	3360	Case ovaling, n=2, 6
17	3856	Case ovaling, n=3, mid
18	3952	Case ovaling, n=2 fore, n=3 aft

*n=a, b indicates a sinusoidal wavelengths around the penetrator and b nodes along the length.

System modal test results were used to determine a mounting location for strain gages on the inside of the case. It was determined that a location of 18 inches from the rear would provide acceptable strain response for the first axial and first three bending modes. Four gages were installed on the interior of the penetrator case using a fixture [3]. The gages were oriented 90° apart circumferentially.

The penetrator was then subjected to high-level force inputs of about 100 klbs in the axial direction, and about 60 klbs in the lateral direction, applied at the nose. The high-level forces were generated with a Reverse Hopkinson Bar Technique [4]. The Reverse Hopkinson Bar configuration is shown in Figure 3, where it can be seen that a steel bar is accelerated by air pressure toward the penetrator structure. Flat surfaces were provided on the nose of the penetrator for axial and lateral impact so that a one-dimensional elastic wave propagates down the projectile bar and back to the point of impact.

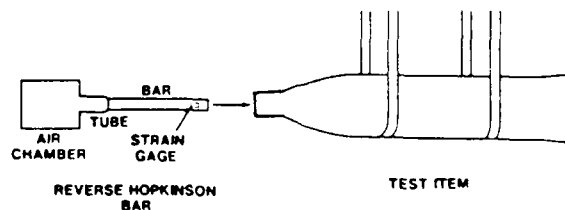


Figure 3. Configuration for Testing a Penetrator with a 1-in.-Dia by 10-in.-Long Hopkinson Bar

The force generated at the interface of the steel bar and the test structure is measured with strain gages installed on the bar 2 inches from the point of impact. Although these strain gages measure the correct amplitude of the elastic wave created by the impact, they record a shorter duration based on their distance from the point of impact. The duration can be easily corrected by adding the time it takes an elastic wave to travel the additional four inches. The corrected pulse durations were used as forcing functions in the analyses.

The steel bar used for these tests is a 1 inch diameter by 10 inch long bar, and the duration of the force generated with this bar impacting a rigid surface is about 100 microseconds. The dimensions of the Hopkinson bar were chosen to generate a trapezoidal pulse of this duration. Reflections in the pulse and imperfect contact between the bar and test specimen tended to distort the desired pulse shape and extend the duration somewhat so that the spectrum for this high-level point force was usable to about 8 kHz. This shape distortion and duration extension were especially noticeable in the lateral force input. The lateral distance across the penetrator nose is less than the length of the impacting bar, so significant reflections were experienced while the bar was in contact with the penetrator. This is illustrated in Figure 4, which compares an uncorrected axial force input with an uncorrected lateral force input.

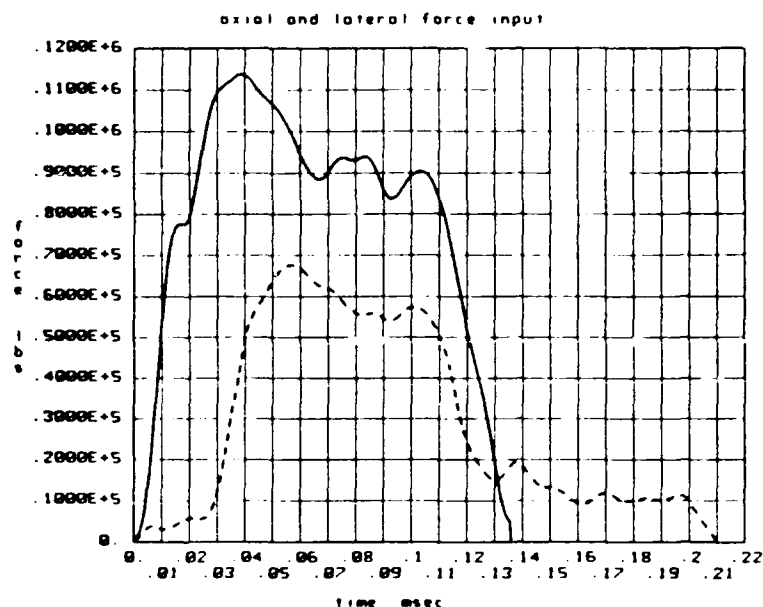


Figure 4. Axial (solid) and lateral (dash) force inputs (uncorrected)

The response was sampled by the data canister installed in the penetrator at 24255 Hz. The axial and bending response to an axial input is shown in Figure 5; the axial and bending response to a lateral input is shown in Figure 6. It is evident from these figures that there is out-of-axis response to the input. Figure 7 shows bending strain in one plane for three different axial input tests, and illustrates a high level of consistency in this out-of-axis response from test to test. The predominant frequencies of the off-axis responses correspond approximately to the first modes (i.e., the bending response to axial input is predominately about 1000 Hz.)

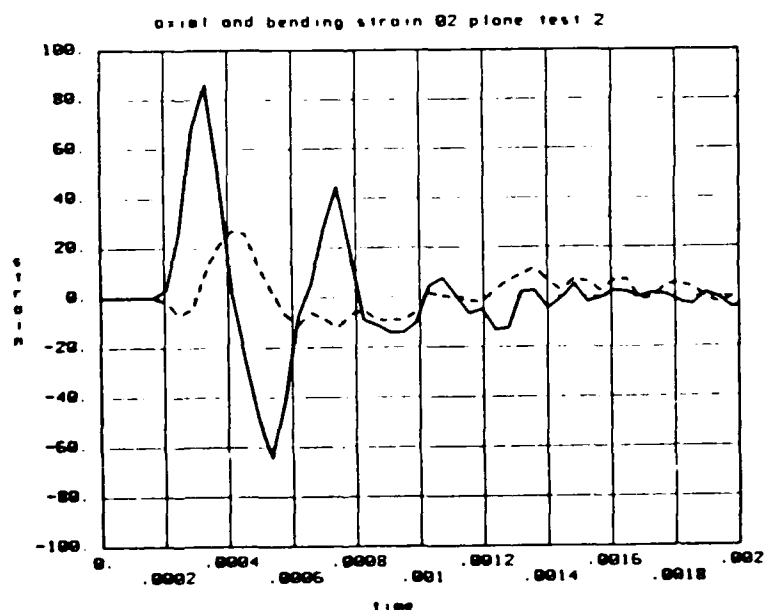


Figure 5. Axial (solid) and bending (dash) strain response to axial input (strain in microstrain, time in seconds).

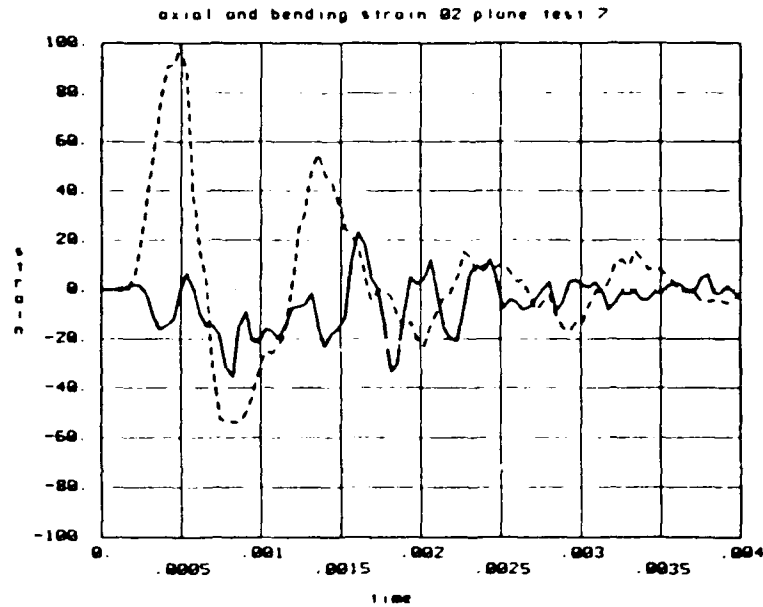


Figure 6. Axial (solid) and bending (dash) strain response to lateral input (microstrain, seconds).

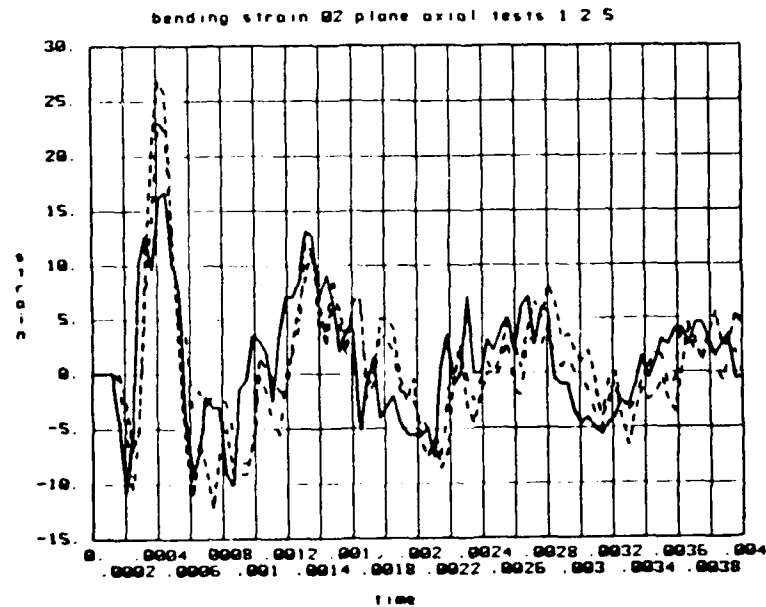


Figure 7. Bending strain (microstrain) for three different axial force inputs (time in seconds).

There are two possible reasons for this out-of-axis response. One, the forcing function is not purely axial or purely lateral. This may occur due to misalignment of the test structure and the Hopkinson bar projectile, but this is difficult to measure quantitatively. The consistency in the off-axis response would suggest that, if misalignment were the cause, it was rather reproducible. Another reason for the out-of-axis response may be asymmetries in the structure which allow coupling of orthogonal modes into any response from excitation in a particular axis.

ANALYTICAL RESULTS AND COMPARISON TO LABORATORY DATA

The original structural model of the penetrator was used to predict axial and lateral modal shapes and frequencies, as well as the case strain response at the strain gage location to the laboratory shock test axial and lateral inputs. Because the analysis treats a symmetric model, it cannot quantify any of the out-of-axis response observed in the tests.

The eigenanalysis predicted a first axial modal frequency for the system of 2473 Hz, which corresponds well with the measured first axial frequency of 2456 Hz. The first axial modal frequency of the empty penetrator case is 2700 Hz.

Figure 8 is a plot showing measured axial strain from one test having axial input and the analytically predicted axial strain using the original structural model. The damping used in the analysis was a stiffness proportional damping, in which the percent critical damping increases linearly with frequency. The original model assumed a stiffness proportional damping coefficient of 5% of critical at 2000 Hz, a commonly used value. Applying the logarithmic damping method to the first cycle of the data indicates a 12% damping value. The frequency content of the data for the first two cycles is predominately the first axial system mode (≈ 2500 Hz), so a stiffness proportional damping value of 12% at 2500 Hz was specified. The resulting better agreement between analysis and data for the first few cycles is shown in Figure 9. Results for the third and higher cycles are of lesser interest since this data is of low magnitude and the out-of-axis response is more significant. Although data from only one axial test was used here, repeated axial tests yielded very consistent results.

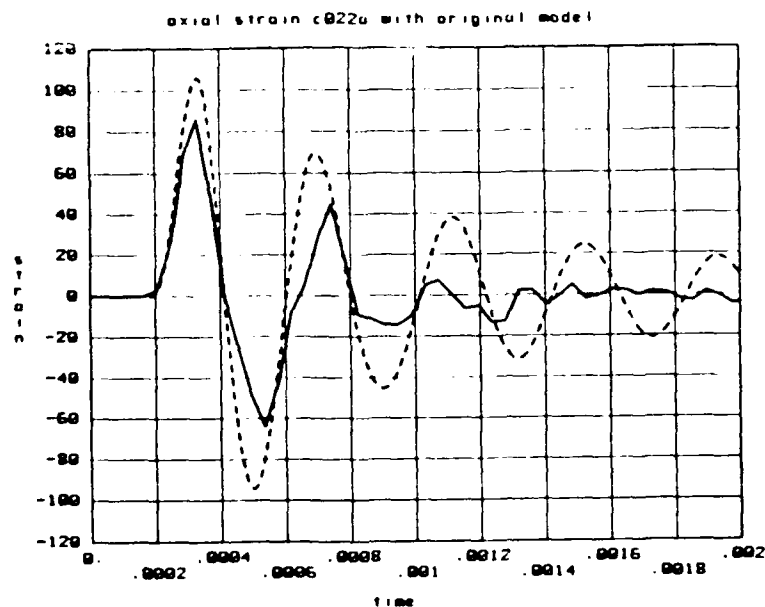


Figure 8. Measured axial strain (solid) and predicted axial strain (dash) for axial input and original model (microstrain and seconds).

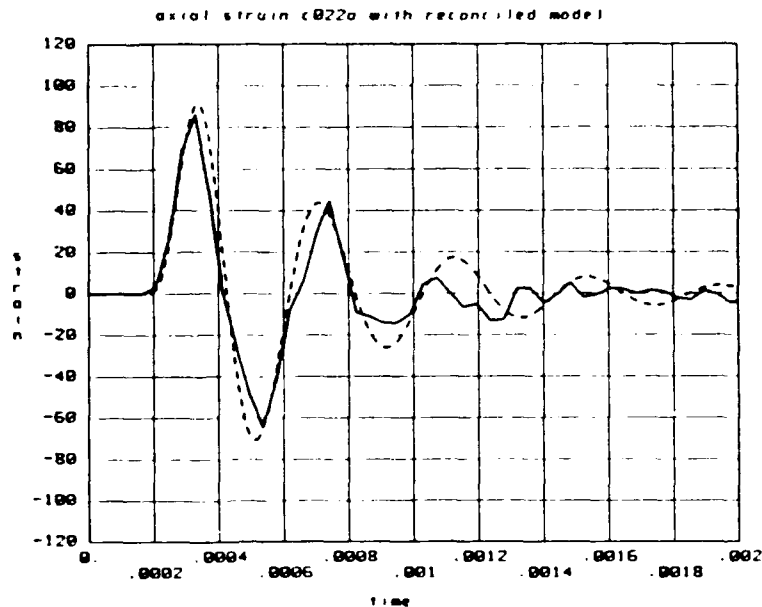


Figure 9. Measured axial strain (solid) and predicted axial strain (dash) for axial input and reconciled model (microstrain and seconds).

The process was repeated for the lateral input test. Eigenanalysis of the original structural model indicated first, second, and third system bending modal frequencies of 874, 1819, and 3437 Hz respectively. The first two bending frequencies were notably less than those measured, 942 and 2048 Hz, while the third was higher than the measured 3224 Hz. The stiffness of the internal lateral bracing was increased in the model until eigenanalysis indicated first bending mode frequency to match the measured closely (948 Hz). The analytical second bending frequency was 1929 Hz, and the third became 3696 Hz. Bending strain data from the lateral Reverse Hopkinson bar test shows that the response is predominantly in the first modal frequency (942 Hz), so the significant inaccuracy in the third lateral mode was judged unimportant. The limited detail of the modal information regarding the internals, mentioned above, precluded further reconciliation of this aspect of the model anyway.

Figure 10 shows the actual bending strain magnitude, along with that predicted by the original (unreconciled) structural model, for the lateral shock input test. (Although the ratio of the peak bending strains of orthogonal gages was reasonably consistent during ringdown, indicating that the bending was reasonably planar, the particular plane of bending during the test was not coplanar with either set of strain gages. The bending strain data must therefore be resolved into magnitude for comparison with the analysis which predicts strain in the plane of bending.) As in the axial analysis, the original lateral model assumed a stiffness proportional damping coefficient of 5% of critical at 2000 Hz. Applying the logarithmic damping method to the first cycle of the lateral data indicates a 6.5% damping value. The frequency content of the lateral data is predominately the first lateral system mode (≈ 1000 Hz), so a stiffness proportional damping value of 12% at 1000 Hz was specified. The resulting better agreement between analysis and data for the first few cycles is shown in Figure 11. Again, results for the third and higher cycles are of lesser interest.

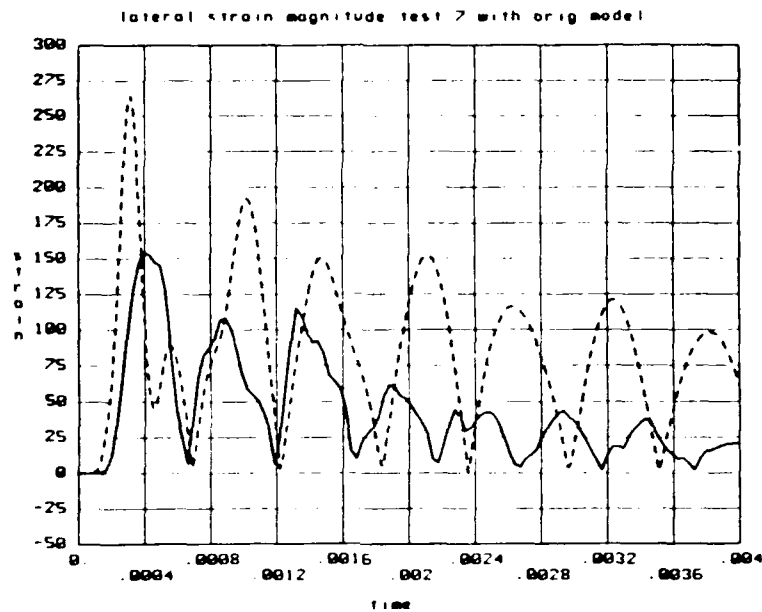


Figure 10. Measured bending strain (solid) and predicted bending strain (dash) for lateral input and original model (microstrain and seconds).

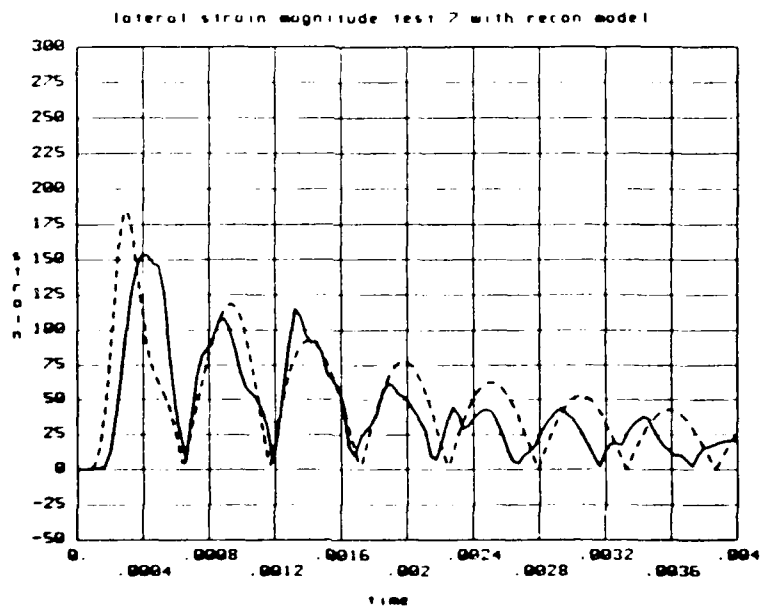


Figure 11. Measured bending strain (solid) and predicted bending strain (dash) for lateral input and reconciled model (microstrain and seconds).

CONCLUSIONS AND SUGGESTIONS FOR FUTURE WORK

This effort has demonstrated the usefulness of laboratory data in improving a structural model of a penetrator in terms of damping and lateral stiffness so that good analytical predictions of strain response to short-time duration axial and lateral point force inputs can be obtained. The use of lateral excitation/bending response data to adjust lateral aspects of a penetrator model is a new technique and proved beneficial since substantial improvement in the lateral response prediction was obtained. Although less uncertainty exists in prediction of axial phenomena than lateral, significant improvement in the axial strain magnitude prediction was facilitated as well by the experimental determination of a damping coefficient more accurate than the one initially assumed.

Numerous factors must be considered when evaluating the applicability of these results to actual earth penetration events and determining direction for future work. Among them are:

1. The high-level force inputs used in the laboratory tests here are 1-2 orders of magnitude less than forces experienced in field penetration events, and the impulse is on the order of 3 orders of magnitude less than field. Penetrators with complex internals will possess some degree of non-linearity, but this is difficult to quantify. A method has been developed and used [5] on an empty penetrator case in which explosive sheet is used to produce force levels comparable to field levels (although the impulse is still much less). The use of this technique on the penetrator used in this study (including internals) would be useful in quantifying the significance of the non-linearities when comparing response to force inputs of greatly different levels.
2. Higher order structural modes did not appear significant in these tests. The higher order modes may have been effectively dampened by the penetrator internals, since in the explosive force tests on an empty penetrator case mentioned above, magnitudes of higher order axial modes were significant. Whether higher modes are significant in actual penetration events will of course depend on the relative rise times and durations of penetration forces compared to these laboratory forces. It appears that, for penetration into relatively homogenous geologic targets at velocities of interest, the axial forces have rise times and durations longer than the bar tests, so the higher axial modes may indeed not be significant. The importance of lateral modes is more difficult to assess at this time, since neither analysis nor intuition conclusively indicates how the rise times and durations of the lateral forces, which are spatially distributed along the length of the penetrator, compare to the lateral force in these tests. Frequency content analysis of well-instrumented field tests can be used to assess this.
3. It may be beneficial to better evaluate the out-of-axis response of penetrator units observed in these tests, as significant bending response was observed during a virtually normal field penetration event in which no bending was expected. This evaluation would initially involve studies of how the addition of off-center masses affect the response of simple beams. Ultimately, lateral Reverse Hopkinson bar

tests at various circumferential orientations on penetrator units, coupled with 3-D finite element structural analysis, could be used to quantify the sensitivity of out-of-axis response to slight structural asymmetries in penetrators.

4. Modal test data were used effectively to adjust aspects of the lateral model. However, modal information regarding the internals more detailed than that acquired here would be required to further improve structural modeling of the internals.

REFERENCES

1. N. T. Davie and M. A. Richgels, GNOME: An Earth Penetrator Code, Sandia Report SAND82-2358, May 1983, unlimited release.
2. J. E. Grant and V. K. Gabrielson, Shell Shock Structural Code, Sandia Report SAND83-8011, March 1984, unlimited release.
3. R. A. May, "Strain Gaging Earth Penetrators to Provide Dynamic Force Data," Proc. 1987 SEM Spring Conference on Experimental Mechanics, Houston, TX, 14-19 June 1987, pp. 108-113.
4. W. K. Bell and N. T. Davie, "Reverse Hopkinson Bar Testing," Proc. 33rd Annual Technical Meeting. Institute of Environmental Sciences, San Jose, CA, 4-8 May 1987.
5. V. I. Bateman, J. L. Cawfield, N. T. Davie, R. J. Kipp, Axial Characterization of the SEPW Penetrator Case, Sandia Report SAND87-2091, February 1988, specified external distribution only.

SHOCK

VERTICAL LAUNCHING SYSTEM MODELING TECHNIQUES FOR SHADOW SIDE EFFECT DURING SHIP SHOCK TRIALS

**Tejbir S. Arora and Michael E. Pearce
Shock Analysis Group
Martin Marietta Aero and Naval Systems
Baltimore, MD 21220**

The USS Mobile Bay (CG 53) Shock Trials were held in May-June, 1987. The charges were exploded alternately on the port side and the starboard side. The vertical response of the Vertical Launching System (VLS) on the side away from charge was higher than the charge side at most locations on the VLS. This phenomenon was recorded during all four shots. This study analytically explains the VLS Shadow Side Effect observed during CG 53 Shock Trials. The methodology and assumptions developed are applicable to future VLS response predictions.

BACKGROUND

USS TICONDEROGA Class ships from CG 52 onwards contain two MK 41 Vertical Launching System (VLS) Launchers each of which contain 61 missiles, each stowed vertically below deck in a sealed canister ready for launch. Each launcher consists of seven eight-cell modules, (six identical standard modules and one system module) plus one five-cell module. The five-cell module has a strikedown system which is elevated to the deck level during replenishment.

The USS Mobile Bay (CG 53) Shock Trials were held in May - June, 1987. There were two MK 41 launchers on the CG 53 as shown in Figure 1. The two launchers were loaded differently in order to obtain the maximum amount of engineering data. The forward launcher was fully loaded with sixty-one missiles or weight simulators and the aft launcher simulated a nearly spent launcher. The explosive charges were set alternately on the port side and the starboard side. During the test, an unanticipated phenomenon was noticed in the VLS response for all four shots. The vertical response of the VLS was significantly lower on the charge side than the shadow side (side furthest away from the charge).

When the charge is exploded in water, the ship is assumed to be at rest. The time it takes the shock wave to travel to the near side of the ship differs from the time it takes to reach the far side. When the shock wave first strikes the ship, it excites the near side which in turn excites the whole ship structure. Further, the velocity of sound is higher for the ship structure than the velocity of sound for the water. So, by the time the shock wave travels accross the hull shape to the far side, the ship structure

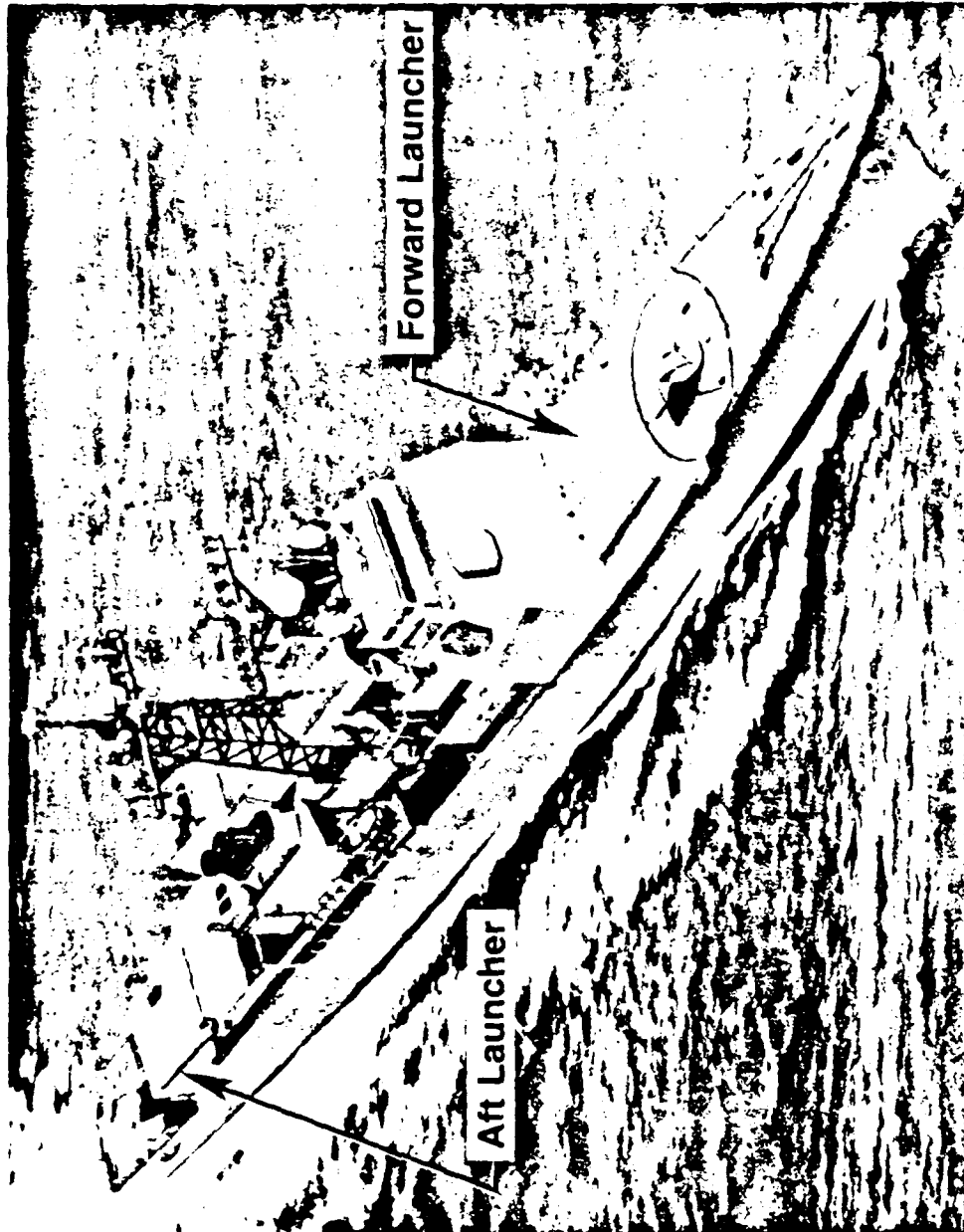


Figure 1a. Launcher location on CG 53

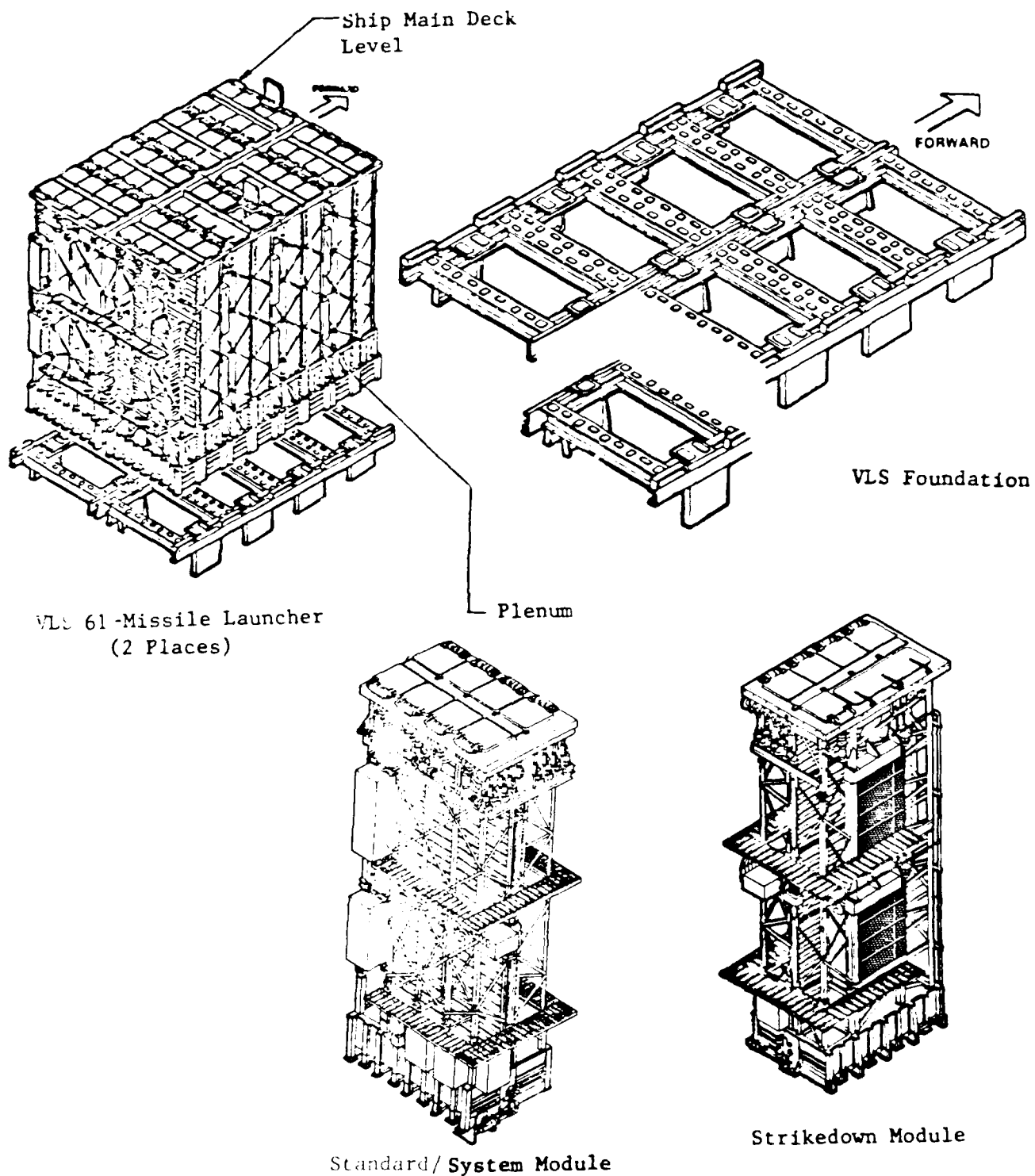


Figure 1b. Vertical Launching System for the USS Mobile Bay

has already been excited by internal forces. Depending on the phasing of the arrival of these two waves, the shock loads can result in higher response of the ship's components on the far side than the charge side. Impact time phasing and amplitude change of the Shock pulse is under study at Martin Marietta Aero and Naval Systems.

This paper concentrates on the launcher response and is not intended to characterize the overall ship response which is the subject of a further study. The purpose of this study was to perform a transient analysis to explain this shadow side effect and to establish a methodology of including this effect on the response predictions for future Shock Trials. The plan for this study was to:

- a) review and evaluate Shock Trials measured data at the launcher/ship interfaces for USS Yorktown (CG 48) and CG 53.

- b) review MK 26 Guided Missile Launching System (GMLS) analyses for USS Kidd (DDG 993) and CG 48 Shock Trials. (The MK 41 VLS in CG 53 occupied the space of the MK 26 GMLS in the comparably structured hull (CG 48 and DDG 993)).

- c) prepare a simplified model for the VLS with a CG 53 foundation model. Perform transient analysis using measured data from the CG 53 Shock Trials (Shots Three & Four).

- d) evaluate the VLS response after replacing the CG 53 foundation model with a DDG 51 subbase model.

Reference [2] compared the analytical predictions with the measured data for the MK 26 GMLS from the CG 48 Shock Trials. It was found that the MK26 analysis vertical response predictions were conservative for the forward launcher and nonconservative for the aft launcher. In addition, measured data showed that the forward launcher vertical response was 10-15 percent higher on the shadow side than the charge side. Whereas the aft launcher measured data did not show any shadow side effect.

The MK26 GMLS pretest analysis [3] was performed using translational and rotational transient input loads at the foundation flat and the ship structure. The transient inputs to the MK26 GMLS were generated using a fluid-structure interaction model. The MK26 analysis for CG 48 also showed higher shadow side vertical response than the charge side vertical response for the forward launcher.

A review of the MK 26 GMLS analysis [4] for the DDG 993 indicated that the vertical response predictions for the forward and aft launchers did not show any shadow side effect.

The MK41 VLS analyses for the CG 53 Shock Trials were conducted using two methods. The Dynamic Design Analysis Method (DDAM) pretest analysis [5] was performed for several loadout configurations. The transient analysis [1] was performed for a heavy loadout to simulate a full up launcher and a light loadout to simulate a nearly spent launcher. The vertical response from both the analyses did not indicate any shadow side effect. The transient analysis was

performed using translational loads only. The loads were applied to the ship structure through a seismic mass rigidly attached to the outer boundary points of the ship structure. The reason that no shadow side effect appeared was that no rotational effects or side to side variations were present in the transient loads.

The MK 41 VLS post Shock Trials correlation analysis was conducted using the transient analysis method [6]. The charge side response predictions showed good correlation to the CG 53 Shock Trials measured data. However, the vertical analytic response for the shadow side was lower than the measured data by 40 percent. The CG 53 Shock Trials measured data was used as input loads to the VLS foundation.

The CG 53 Shock Trials data was reviewed for both Shot Three and Shot Four. At most locations on the MK 41 VLS the charge side response was lower than the shadow side response. Table 1 shows a comparison of the response between charge side and shadow side for the forward and aft launchers. Figure 2 gives the location of instrumentation gages on the plenum top/canister base and the deck level for the forward and the aft launchers. The general trend of CG 53 measured data for the MK41 is shown in figures 3 and 4, and [11]. Shot Four (Starboard Charge) shows a greater shadow side effect than Shot Three (Port side Charge). The VLS plenum top response also varies depending on where the instrumentation gage was located. The vertical acceleration peak g level at the plenum top/canister base for Shot Three and Shot Four measured data are presented in Figure 5.

Table 1. CG 53 Shock Trials Data Review

Forward Launcher Response-Heavy Loadout

	Shot 3	Shot 4
Plenum	CS = SS	CS < SS
Canister/Missile Aft Interface	CS = SS	CS < SS
Component Boxes	CS < SS	CS < SS
Deck	CS < SS	CS < SS

Aft Launcher Response-Light Loadout

Plenum	CS < SS	CS < SS
Canister/Missile Aft Interface	CS > SS	CS < SS
Component Boxes	CS < SS	CS < SS
Deck	CS < SS	CS < SS

Where CS = Charge Side
 SS = Shadow Side
 Shot 3 Port Side
 Shot 4 Starboard Side

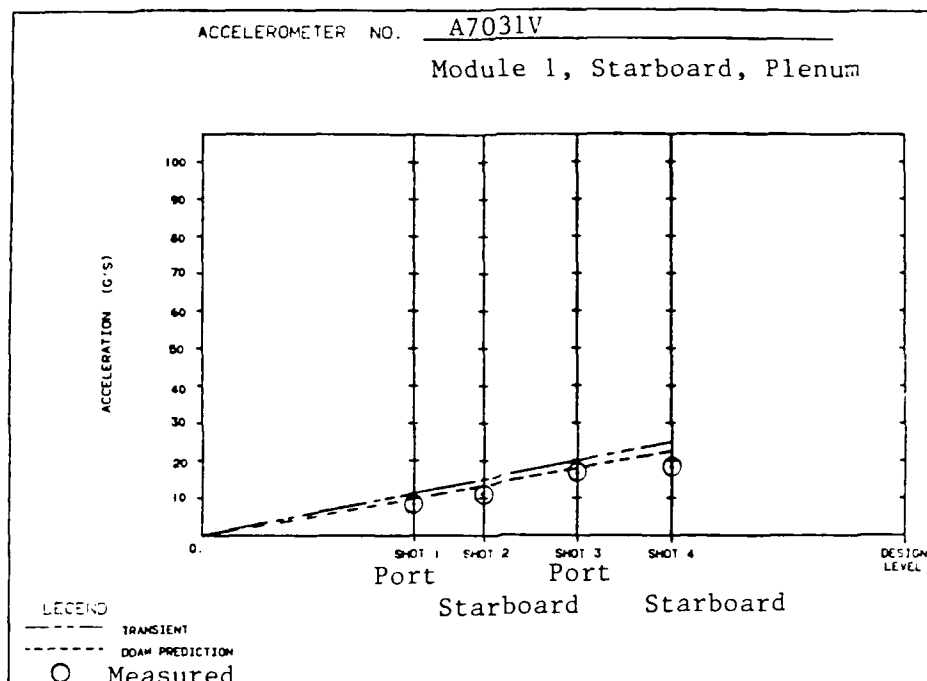


Figure 3. Starboard Side Acceleration Response, Pretest Analysis versus CG 53 Shock Trials Measured.

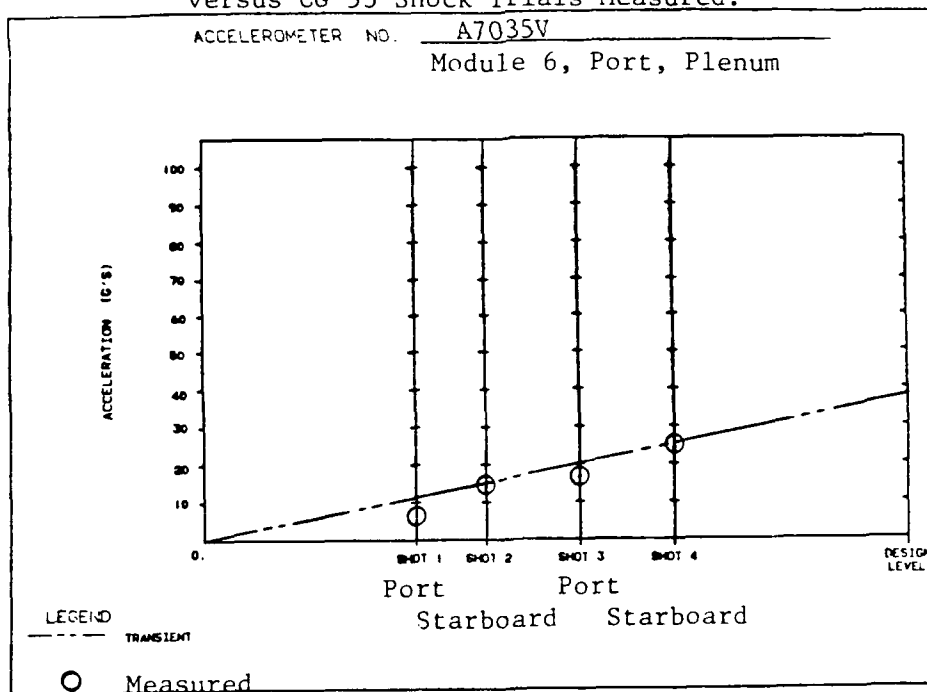


Figure 4. Port Side Acceleration Response, Pretest Analysis versus CG 53 Shock Trials Measured.

TECHNICAL APPROACH

The mathematical models used for this study are similar to those used in [6]. The models were modified to the extent that boundary conditions were re-examined for the VLS foundation/deck to ship interfaces. For the transient analysis, performed in [1] and [6], ship roll effect was neglected. The foundation pedestals were rigidly connected to the foundation triple beams. So, the post test analysis loads [6] were applied at the triple beams and outboard channels.

For the VLS Shadow Side Effect Study, the vertical response was assumed to be decoupled from the fore/aft response. In addition, pitch and yaw responses were neglected. Only a portion of the VLS structure in the fore/aft direction, consisting of two modules across the ship's centerline, was required for analysis. This study started with stick models of two VLS eight-cell modules [13] and a beam foundation model similar to the model used by [8]. Different boundary conditions at the VLS foundation/ship structure interface were examined. Further, for each side of the VLS a detailed module model (Figure 6) was used and a reduced foundation model (Figure 7) was developed for this study. Since only one module on each side of the ship's centerline was modeled for this study. This required the addition of masses to the model at the four corners of the foundation to account for the adjacent modules. Different missile/canister loadout configurations presented are:

- CG 53 Shock Trial heavy loadout with VLS Foundation
- CG 53 Shock Trial light loadout with VLS Foundation
- CG 53 Shock Trial heavy loadout with DDG 51 subbase

The majority of time on this effort was spent selecting the proper boundary conditions. First a baseline model was established. Loadouts representative of the Shock Trials were developed to determine the boundary conditions. Some of the parameters considered were:

i. Boundary Conditions at the Foundation/Ship Structure Interface

The fore-aft (X), pitch (RY), and yaw (RZ) motions of the ship were assumed to be negligible with respect to the vertical (Z) and athwartship (Y) responses, and therefore these degrees of freedom were constrained for the model boundaries. In addition to this, there were two types of model boundary conditions studied: Case 1. The VLS foundation outboard channel and pedestal base (Figure 7) were assumed to be free in the translational degrees of freedom (DOF) Y(2) and Z(3). Translational DOF X(1), and Rotational DOF RX(4), RY(5), and RZ(6) were constrained. Case 2. All boundary conditions for the model were the same as Case 1 except rotational DOF RX(4) was freed.

ii. Canister to Launcher Interface

The interface between the canister and the VLS module is highly nonlinear. When the ship moves upward, the inertia force of the canister is reacted at the plenum top plate. And when the ship moves downward, the inertia force of the canister is reacted at the dogdown structures four feet above the plenum Figure 6 and [8]. Reference [1] conducted a single cell study of a linear versus nonlinear vertical interface between the canister and the VLS launcher. Results of this analysis indicated that the linear interface was approximately similar to the nonlinear interface case. In order to simplify the analysis approach, the following assumptions were made:

- the canister was assumed to be supported at the plenum irrespective of the direction of ship movement. Linear interface elastic springs in the fore and aft (X), athwartship (Y), and vertical (Z) directions were modeled. The spring stiffness $K = 1.0E8$ lb/in was assumed for all translational directions. Rotational RX and RY DOF were free and RZ was modeled with a stiff rotational spring of stiffness $K = 1.0E9$ lb/in.

- the canister was not supported at the dogdowns.

- the canister top to module deck interface was modeled with linear springs ($K = 1.0E8$ lb/in) in the X and Y directions. Canister translational Z, rotational RX, RY, and RZ DOF were assumed to be free.

iii. Dynamic Reduction

MSC/NASTRAN (Version 65B), a finite element structural analysis program, was used to perform direct transient response analysis. The superelement technique used was similar to the one described in [1]. The residual structure was solved using the Generalized Dynamic Reduction (GDR) technique instead of the Guyan reduction technique used in [1]. The GDR technique [9] is considered the most accurate method for dynamic reduction. Also, the model size for this study was small compared to the model used by [1]. So the process of Guyan reduction was eliminated.

There were three phases of operation for superelement analysis with MSC/NASTRAN. The first phase of analysis was to perform eigenvalue solution (SOL 63) for all superelements using the GDR technique. The second phase was to combine all superelement data to form the model for the residual structure and perform direct transient analysis using MSC/NASTRAN SOL 69 [10]. The last phase was the data recovery phase. Acceleration time history data were recovered at various launcher locations.

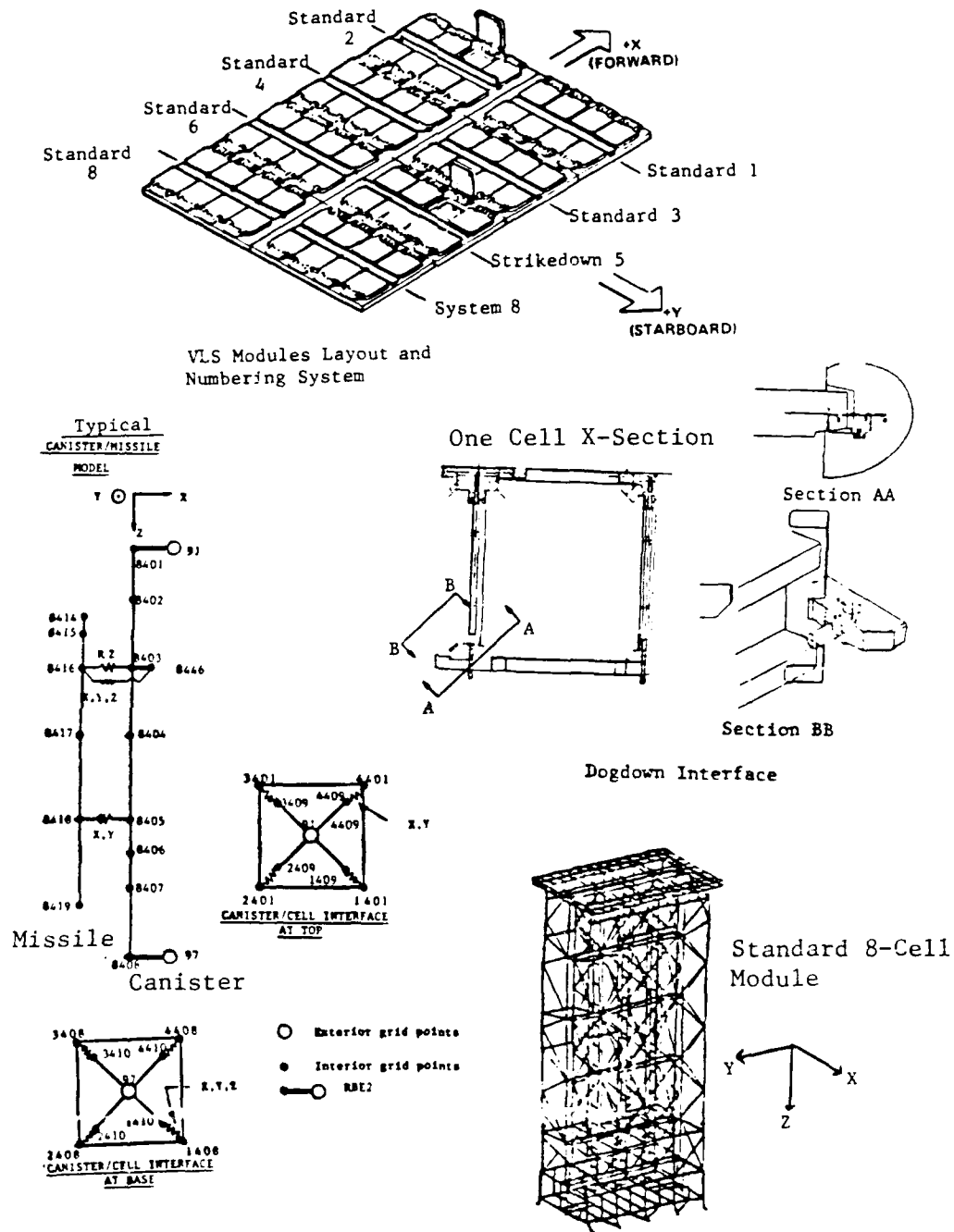
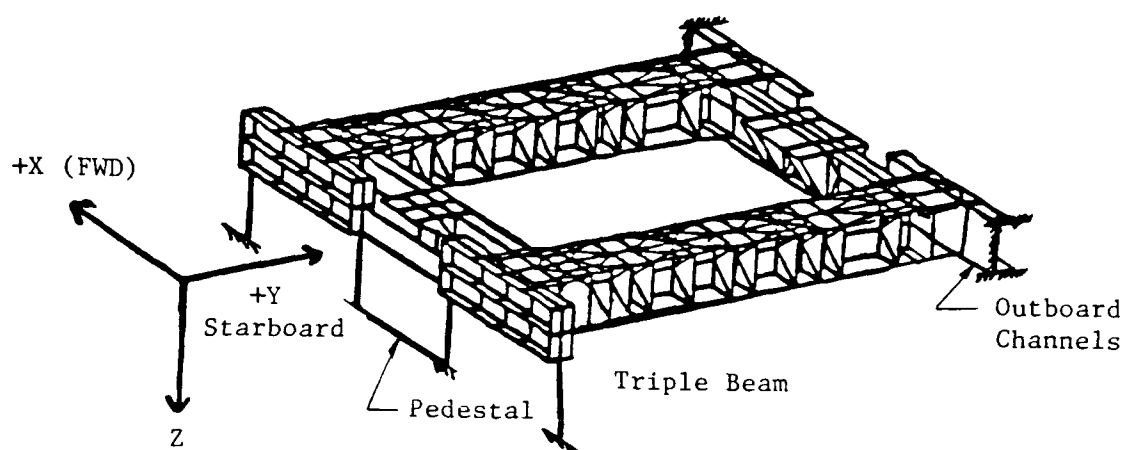
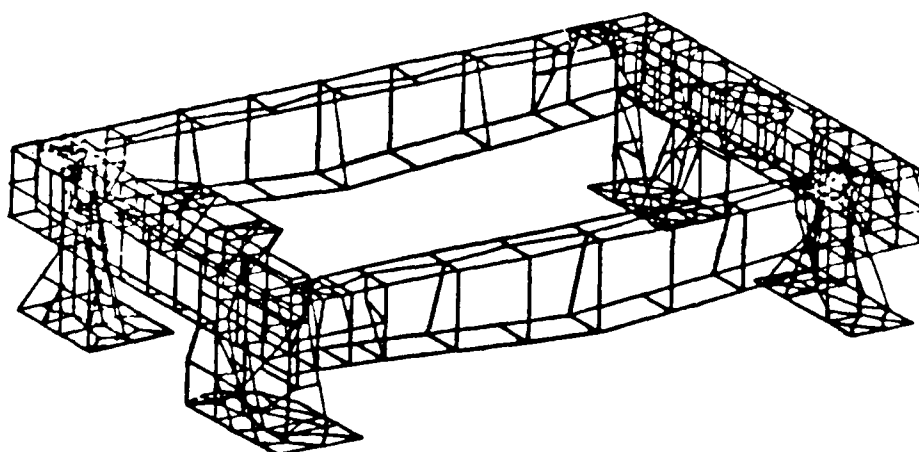


Figure 6. VLS modules and Finite Element Model of standard 8-cell and a typical canister/missile FEM model



VLS Foundation FEM for one module

7(a)



DDG 51 Subbase FEM

7(b)

Figure 7. CG 53 VLS Foundation Finite Element Model (FEM) for one Module and DDG 51 Subbase FEM for one Module

MATHEMATICAL MODELING

As mentioned previously, the finite element models used in this analysis were essentially the same as those used in [6]. Some minor modifications incorporated specifically for the shadow side effect transient analysis were:

- i Canister to module dogdown springs were removed from the module superelement
- ii The aft foundation plate model was reduced to a model for one module only. The inboard pedestals on either end of the module were modeled as bar elements with modified structural properties [13].
- iii The foundation boundary points DOF four (RX) were fixed in Case 1 in order to neglect ship roll motion, and were freed in Case 2 in order to permit ship roll motion.

The Finite Element Models (FEM) of the 8-cell module, canister/missile, foundation and subbase are shown in Figures 6 and 7. Table 2 gives the weights of the major components used for the Shadow Side Transient Analysis.

Table 2 Model Weight Summary

Item	Unit Weight (LBS)
Standard Module	37,135
Foundation For One Module (in CG 53)	7,334
SM2 Missile/MK 13 Canister	3,770
VLASROC Missile/MK 15 Canister	4,020
Tomahawk Weight/MK 14 Canister	5,960
MK 13 Canister and Adapter + Cell Cover	2,220
Subbase For One Module (in DDG 51)	3,949

RESIDUAL STRUCTURE

The residual structure is a collection of all the superelements. It contains boundary degrees of freedom of all the components and the seismic masses to represent the VLS foundation/ship and the VLS deck/ship interfaces. The boundary conditions for the structure are defined through the seismic masses with the enforced loads in MSC/NASTRAN [9]. For Case 1 boundary conditions, the seismic masses were fixed in X, RX, RY, and RZ and freed in Y and Z. For Case 2 boundary conditions, the seismic masses were fixed in X, RY, and RZ and freed in Y, Z, and RX. The seismic masses enable the transient

loads to be enforced on the model.

The Generalized Dynamic Reduction (GDR) method was used to further reduce the number of degrees of freedom. The cut-off frequency specified was 60 HZ. The total number of DOF in the residual structure were approximately six hundred and fifty.

APPLIED LOADS

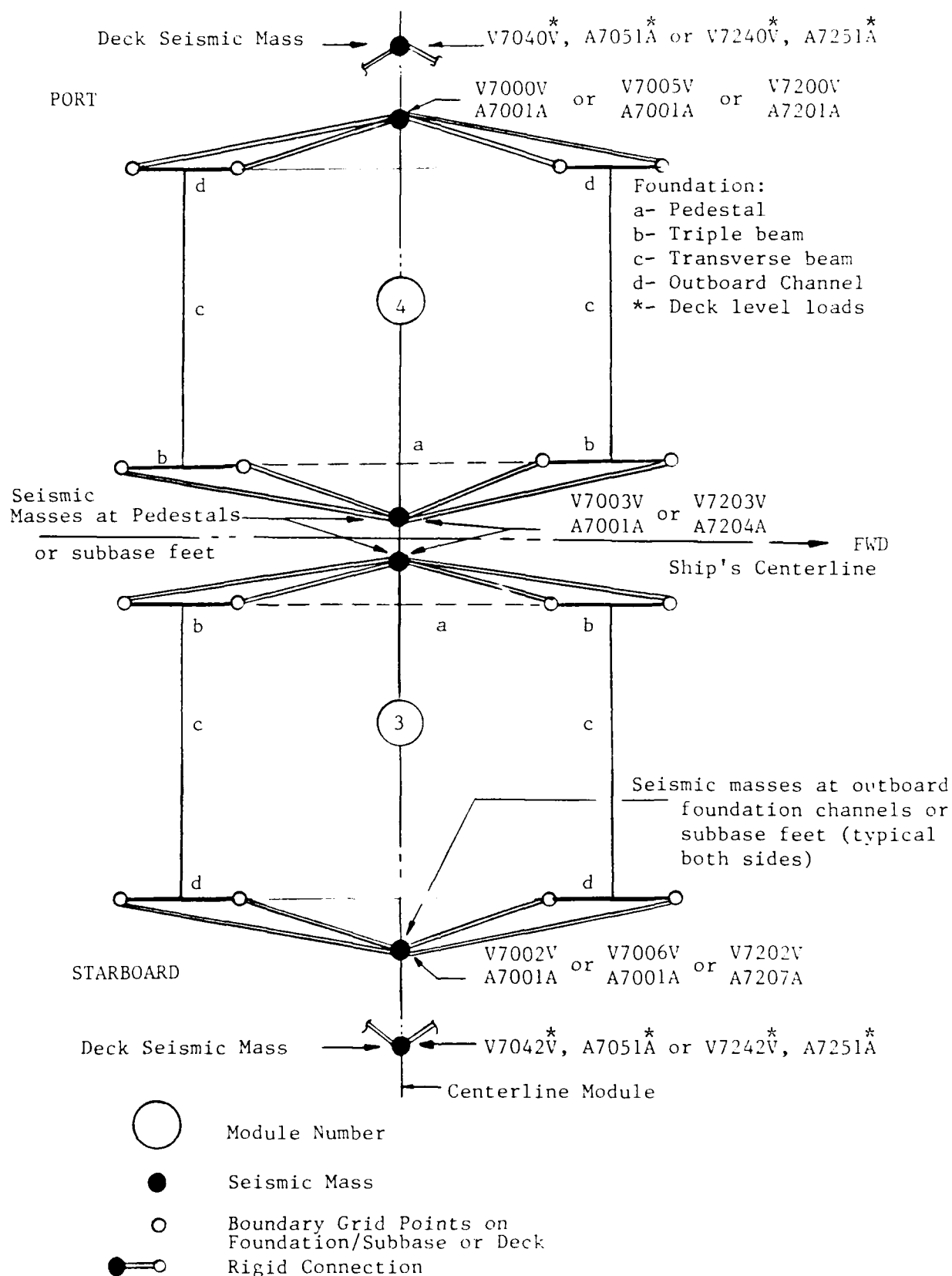
Input loads for the VLS shadow side effect study were obtained from the CG 53 Shock Trials Shot Four data for the forward VLS launcher and Shot Three for the aft VLS launcher. Figure 8 shows the location of seismic masses and channel numbers used as input loads. Figures 9 through 14 show time histories of applied loads for the forward and aft launchers. Scale factors were used to interpolate/extrapolate the measured data for instruments which did not coincide with the locations of seismic masses in the FEM.

TRANSIENT ANALYSIS RESULTS

MSC/NASTRAN SOL 69 [10] was used to perform transient dynamic analysis for this study. There were several models prepared for different loadout configurations [13]. Results are presented for the loadout configurations which were represented in the CG 53 Shock Trials.

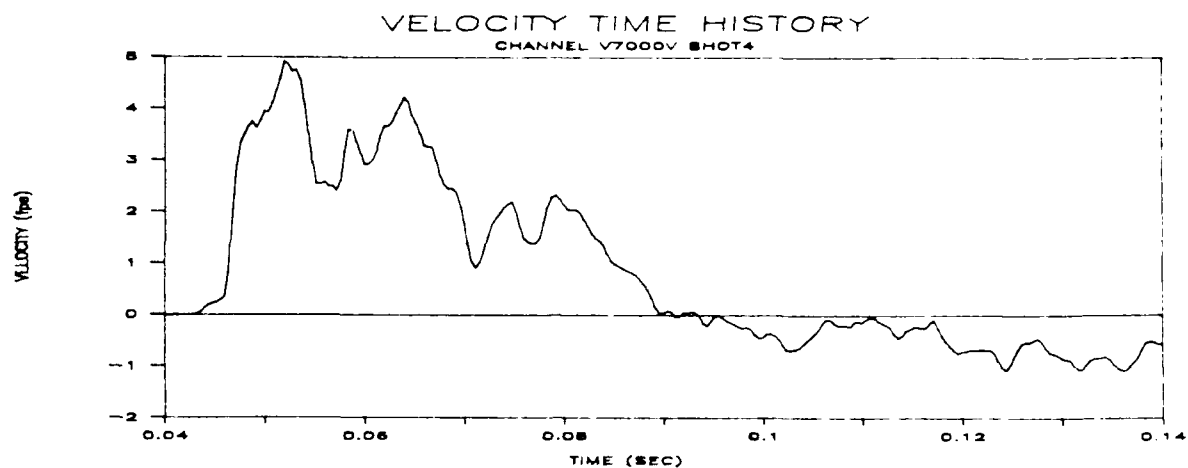
The heavy loadout configuration used input data from Shot Four. The starboard side of the ship was the charge side. This loadout configuration was evaluated for two subcases of loads: (A) using forward channels V7000V and V7002V and (B, using aft channels V7005V and V7006V. The rest of the loads remained the same as shown in Figure 11. Further, this configuration was evaluated for Case 1 and Case 2 boundary conditions. Loading A Results: Figures 15 through 17 show the vertical accelerations at the plenum top/canister base and deck level for the two cases. The response comparison plots show time history and shock spectra correlate better for Case 2 than Case 1. Analysis time history peaks for the shadow side do not match the measured data but, analysis shock spectra are within 10 percent of measured data up to the cut-off frequency of 60 Hz. The response frequency of Case 2 matches the measured data. Loading B Results: Figures 18 through 20 show the accelerations at the plenum top/canister base and deck level for the two cases. The peak acceleration response data shows a shadow side effect for both cases, but the shock spectra comparison between the Shock Trials data and the two cases shows Case 2 to be closer to the measured data.

The light loadout configuration used Shot Three data for the aft launcher. The port side of the ship was the charge side. This configuration was also evaluated for Case 1 and Case 2. Figures 21 through 23 show the accelerations at the plenum top/canister base and deck level for the two cases. The peak acceleration response data show no appreciable shadow side effect for either Case 1 or Case 2. The shock spectra and time history comparison between the

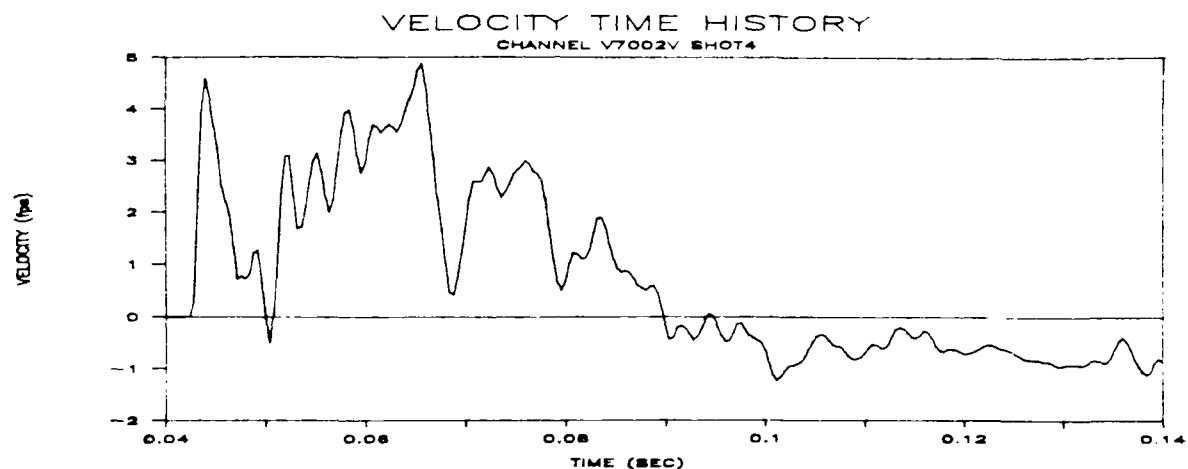


Note:
Channel Numbers 7000-7051 are for forward launcher and 7200-7251 are for aft launchers

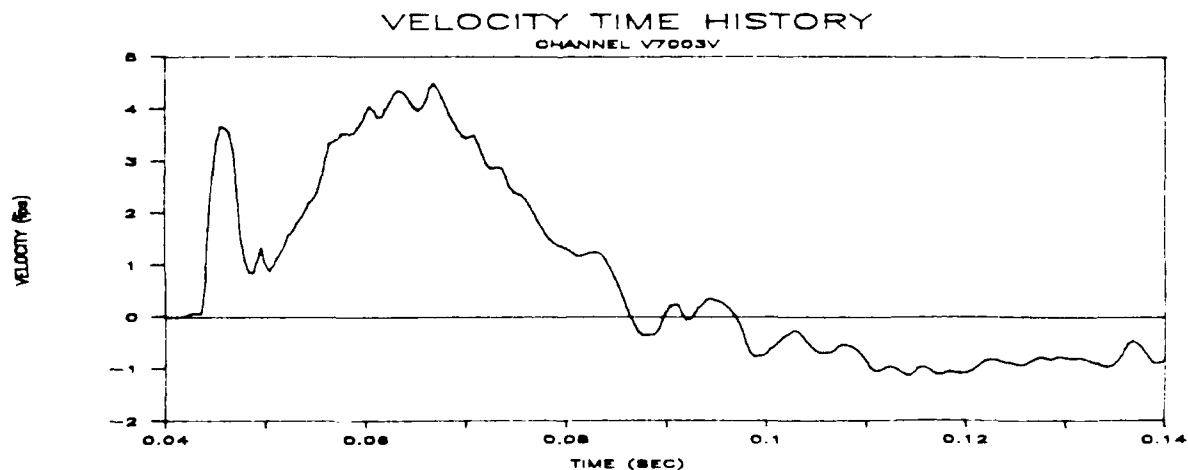
Figure 8. Loads applied at the ship/foundation or subbase and ship/deck interface



9(a)

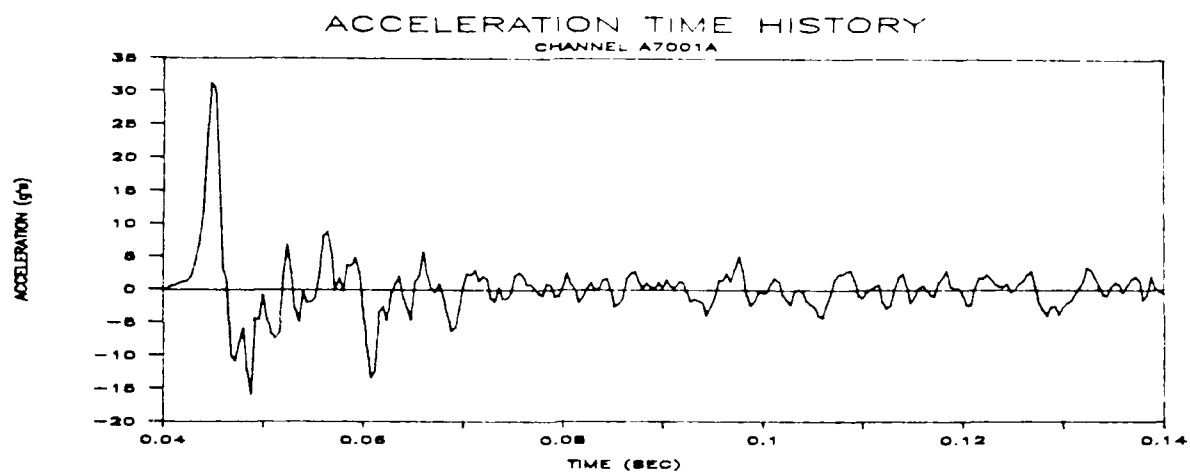


9(b)

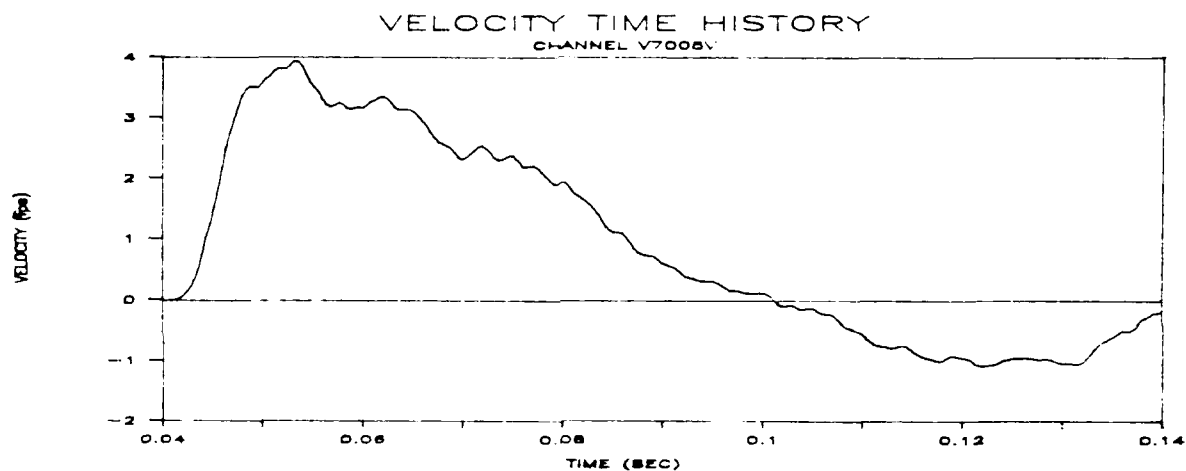


9(c)

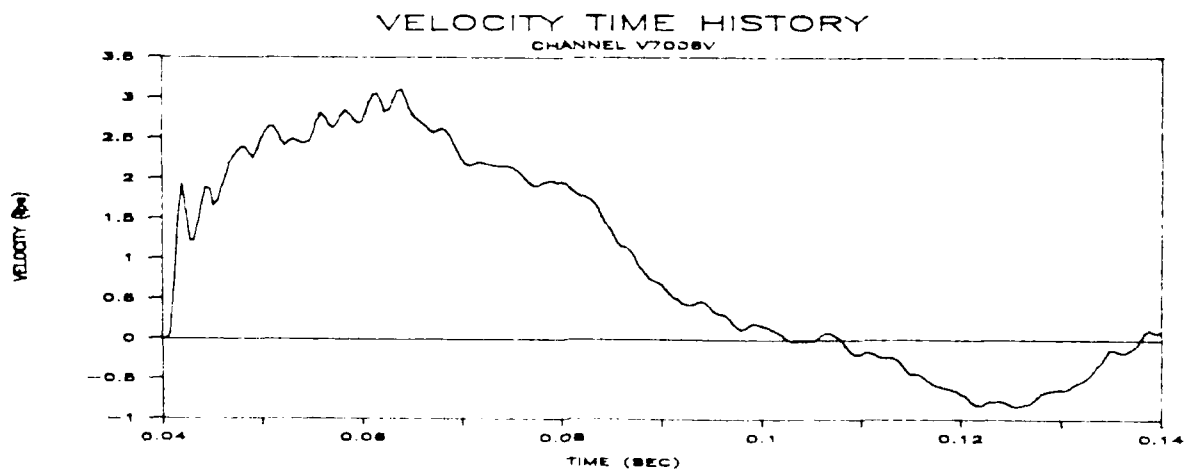
Figure 9. Shock Trials measured time history data, Shot Four forward launcher, used as input loads - vertical velocity (ft/sec)



10(a)



10(b)



10 (c)

Figure 10. Shock Trials measured time history data, Shot Four, forward launcher, used as input loads - vertical velocity(ft/sec), athwartship acceleration(G's)

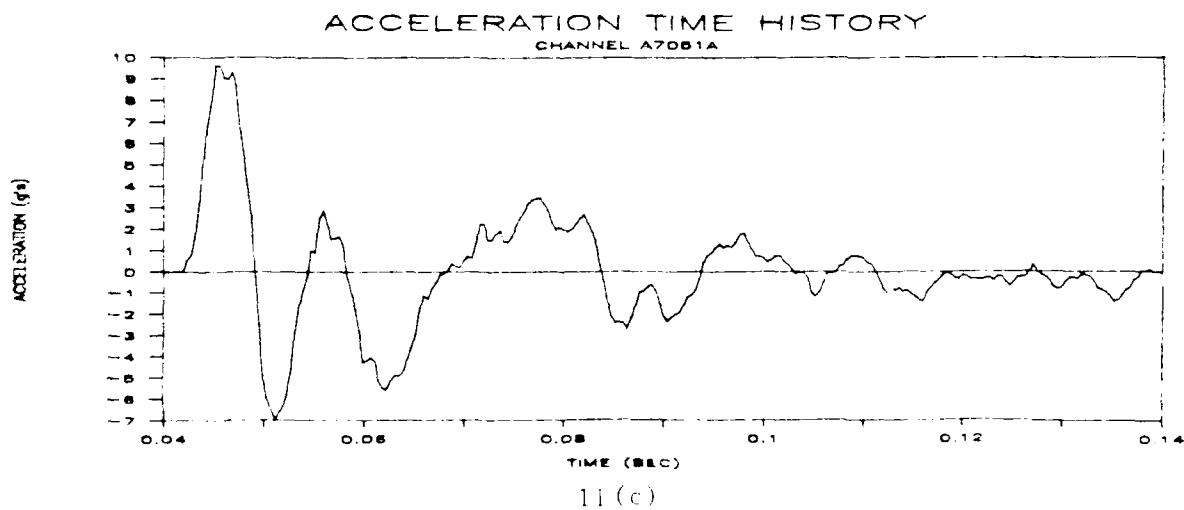
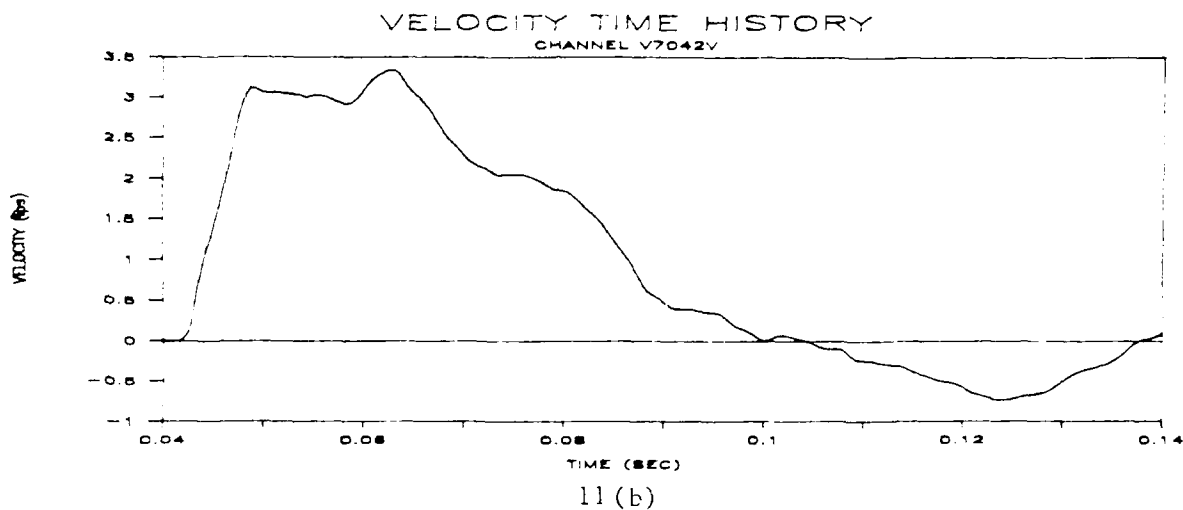
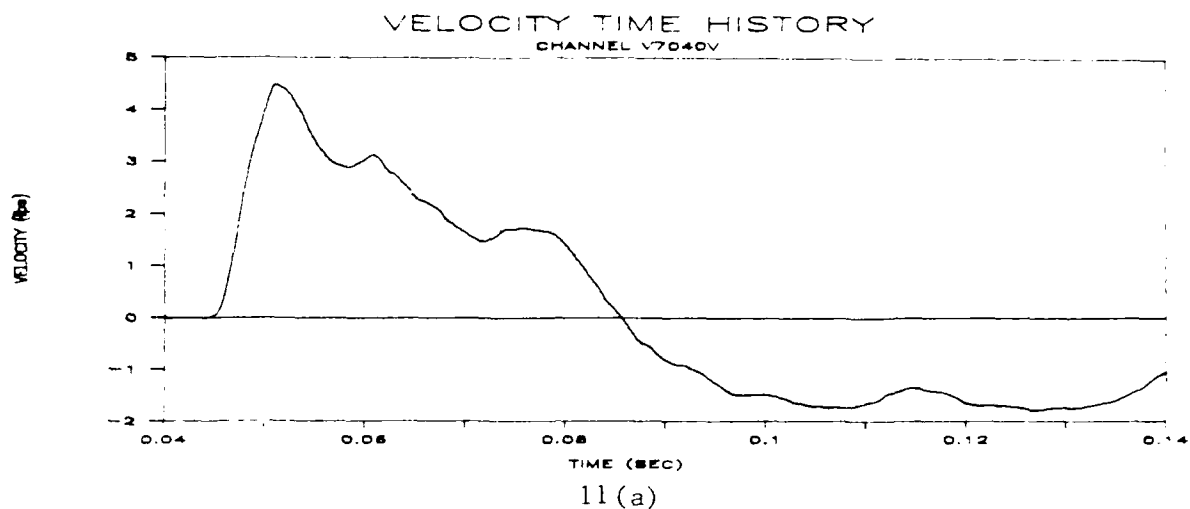


Figure 11. Shock Trials measured time history data, Shot Four, forward launcher, used as input loads - vertical velocity(ft/sec), athwartship acceleration(G's)

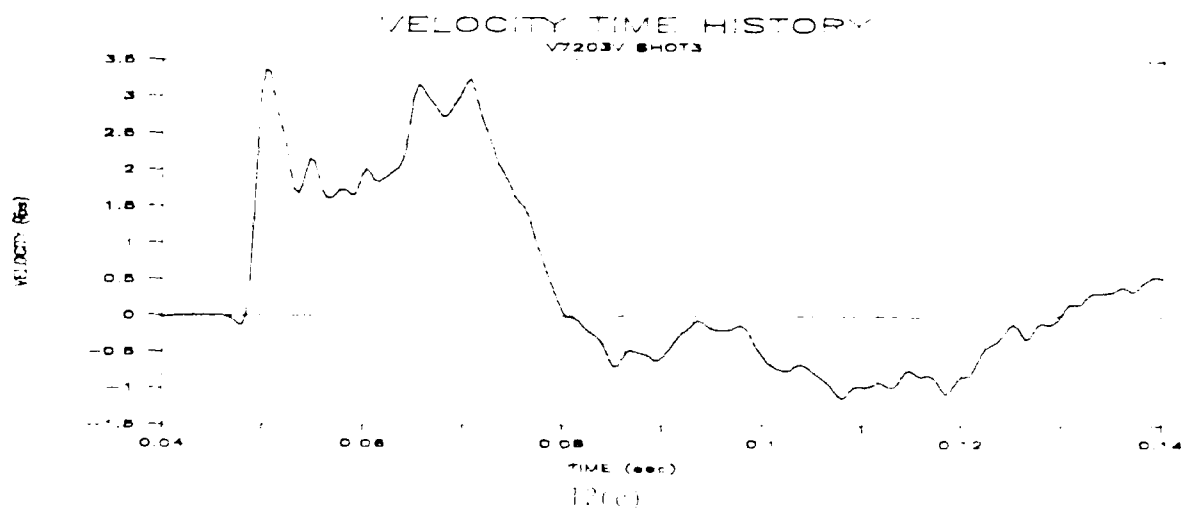
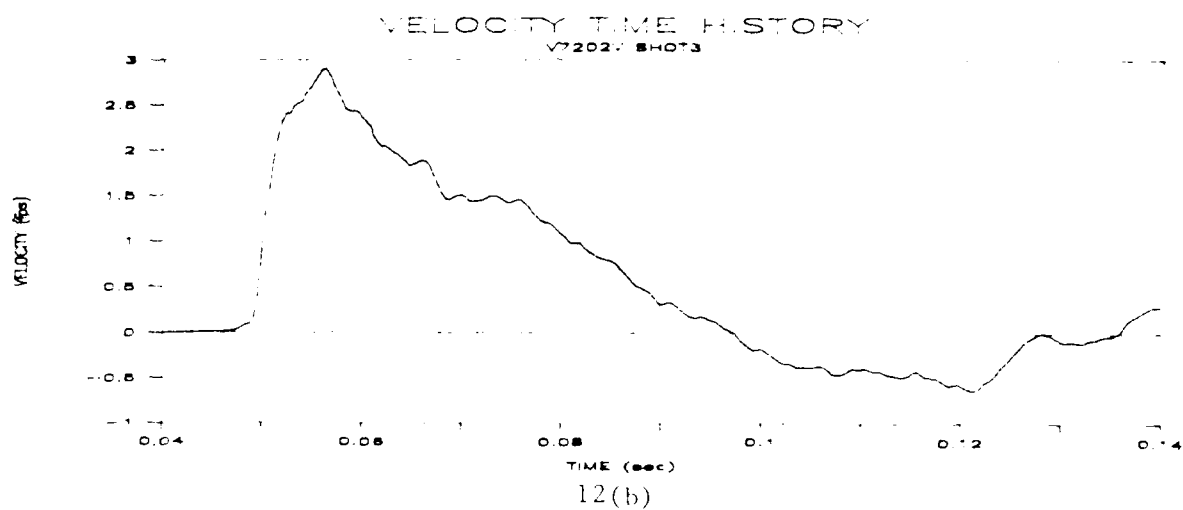
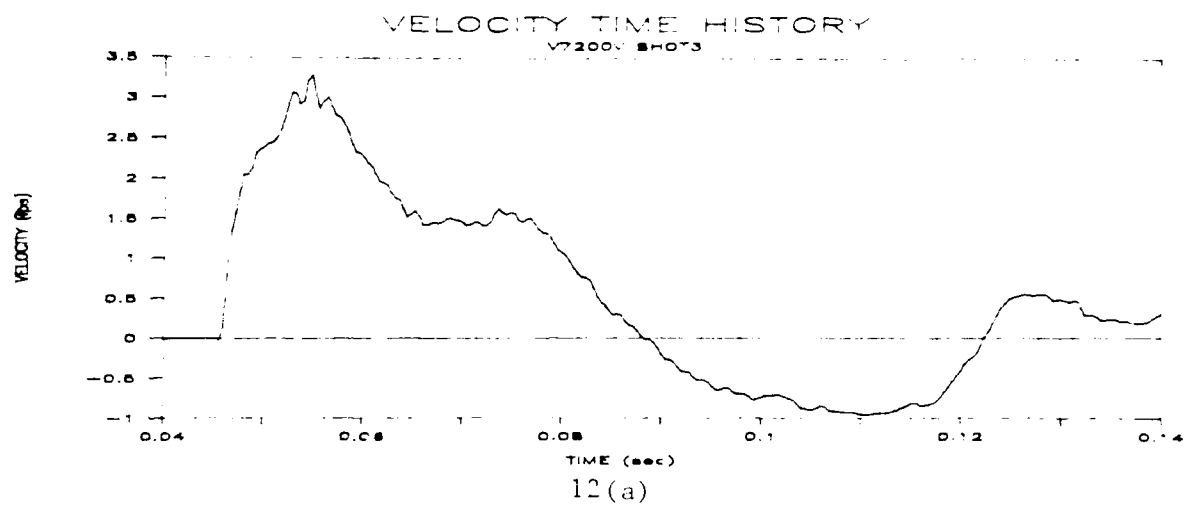


Figure 12. Shock Trials measured time history data, Shot Three aft launcher, used as input loads - vertical velocity (ft/sec)

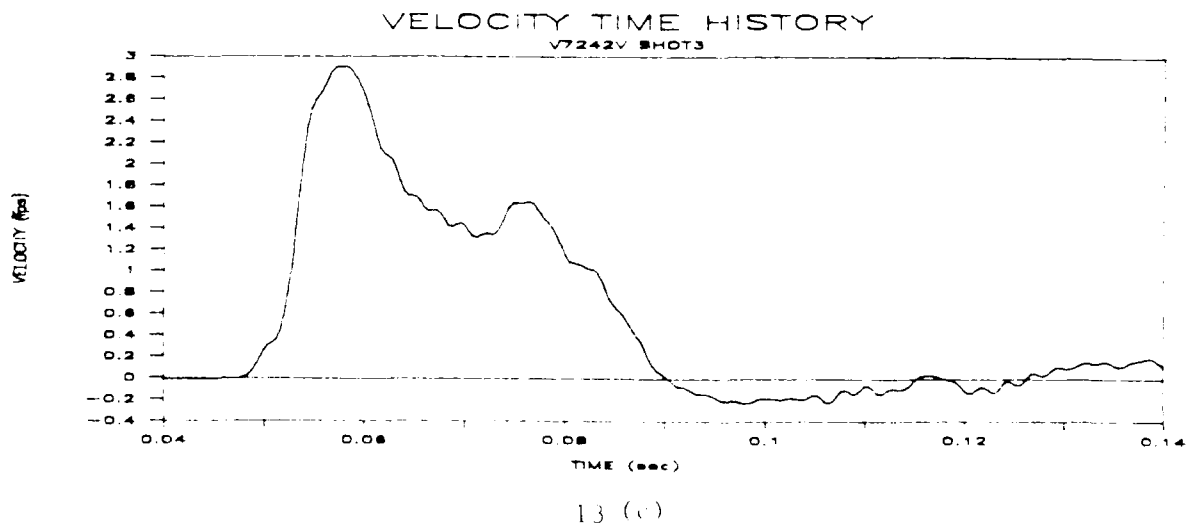
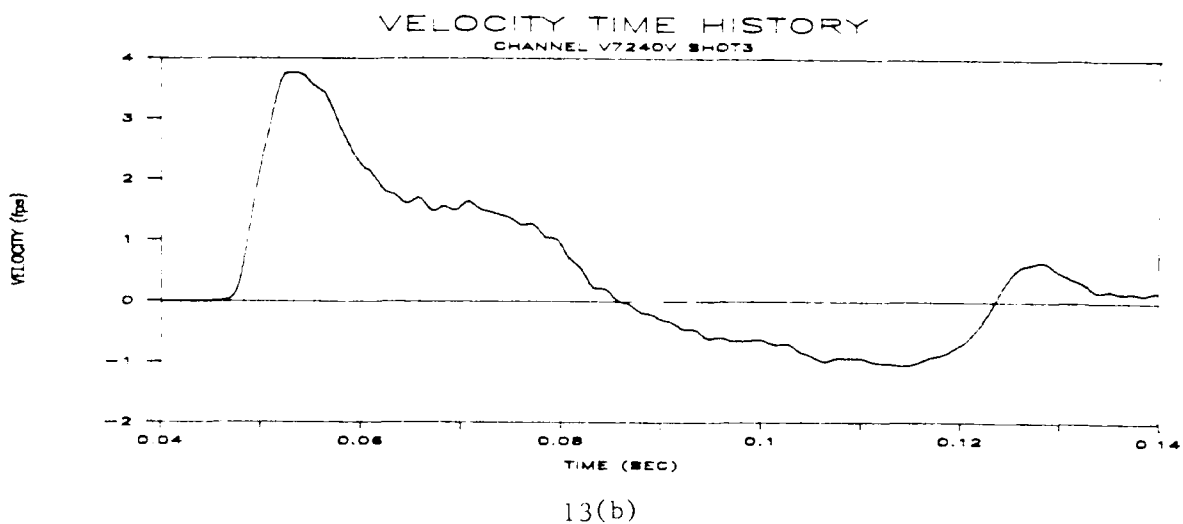
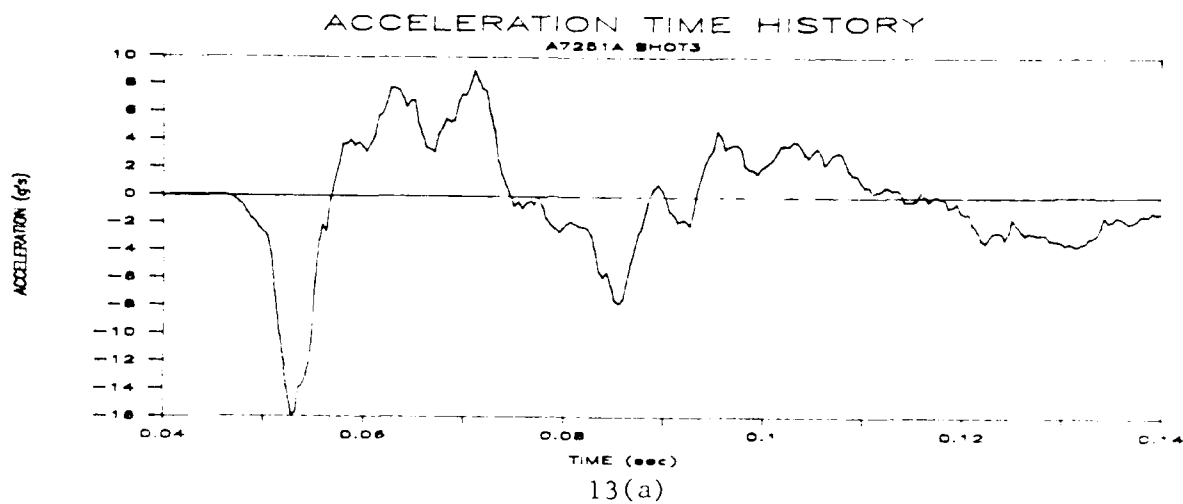


Figure 13. Shock Trials measured time history data, Shot Three, aft launcher, used as input loads - vertical velocity(ft/sec), athwartship acceleration(G's)

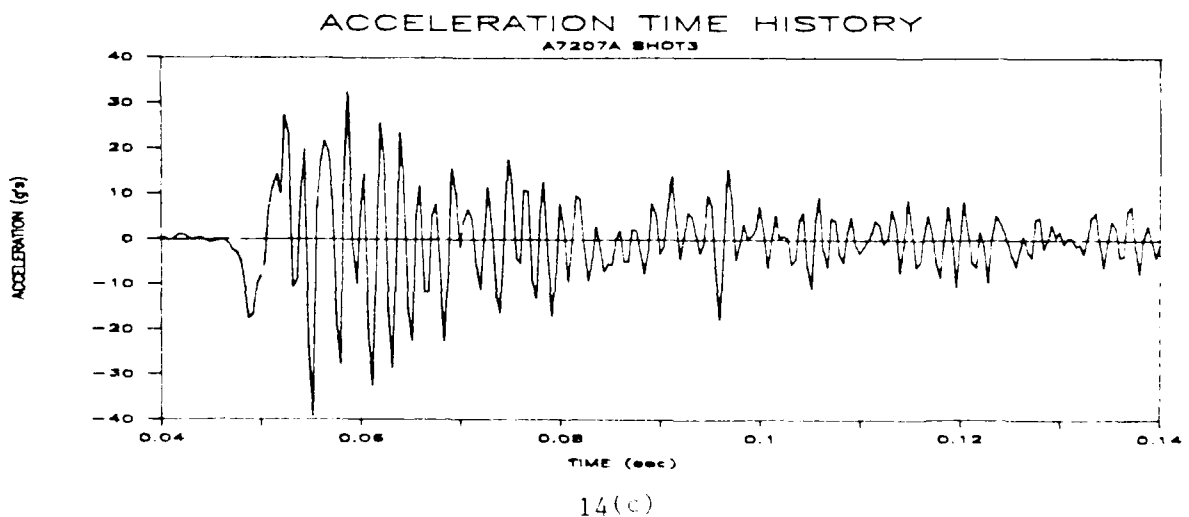
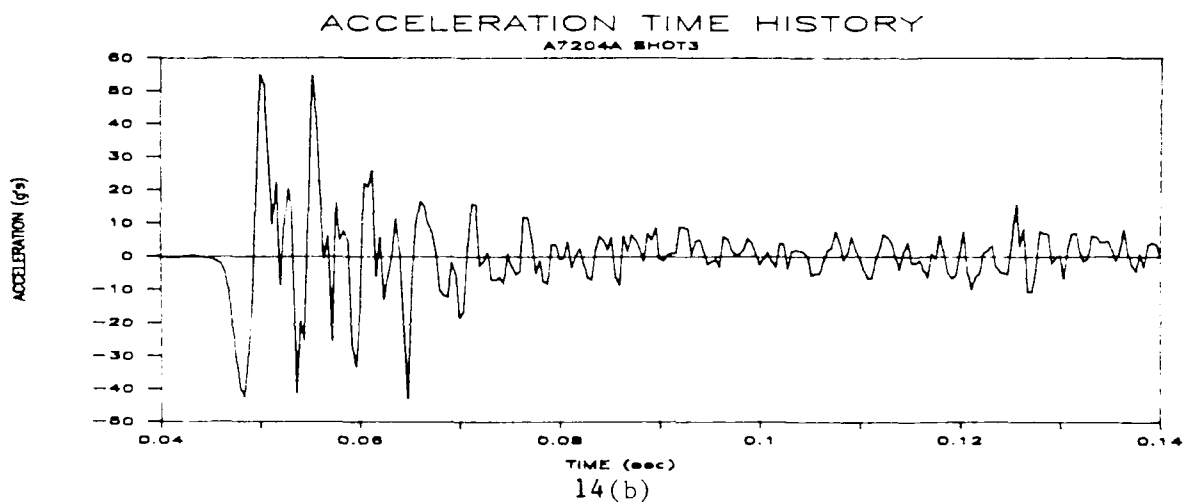
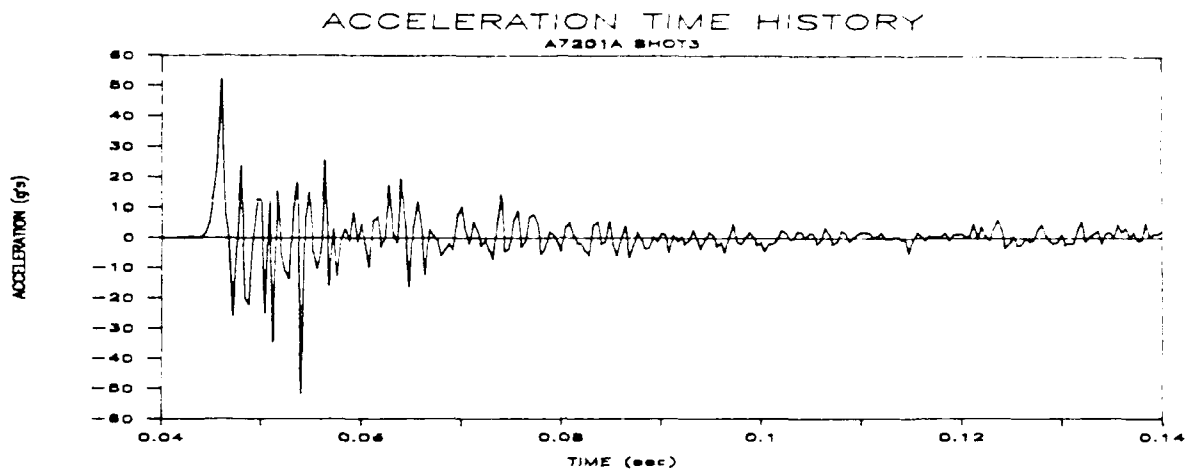


Figure 14. Shock Trials measured time history data, Shot Three, aft launcher, used as input loads - athwartship acceleration(G's)

VERTICAL ACCELERATION (G'S) AT
PLENUM/CANISTER BASE AND DECK LEVEL.

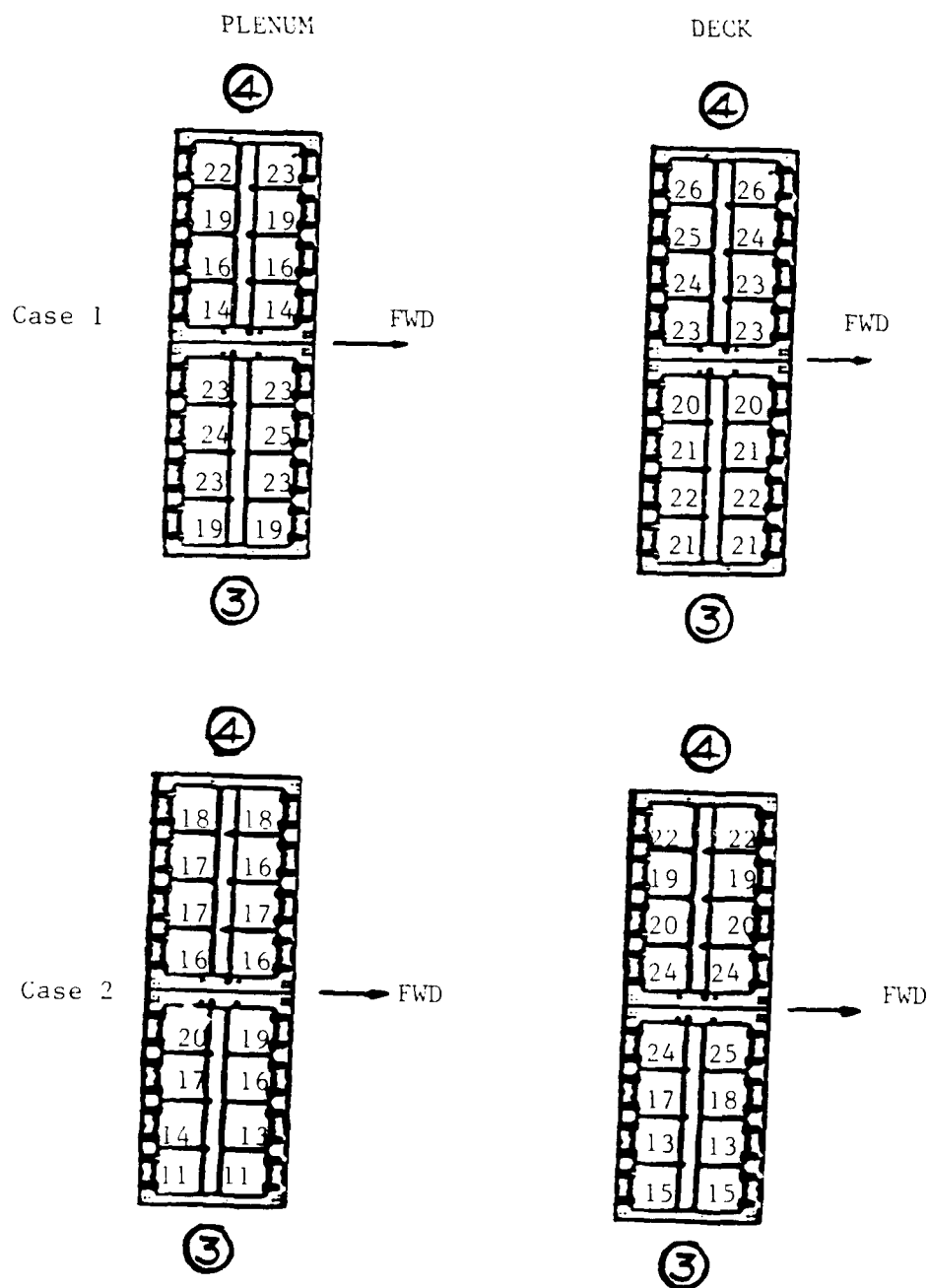


Figure 15 Vertical Accelerations (G's) at Plenum/Canister base and Deck Level Loading A, Heavy Loadout, Forward Launcher

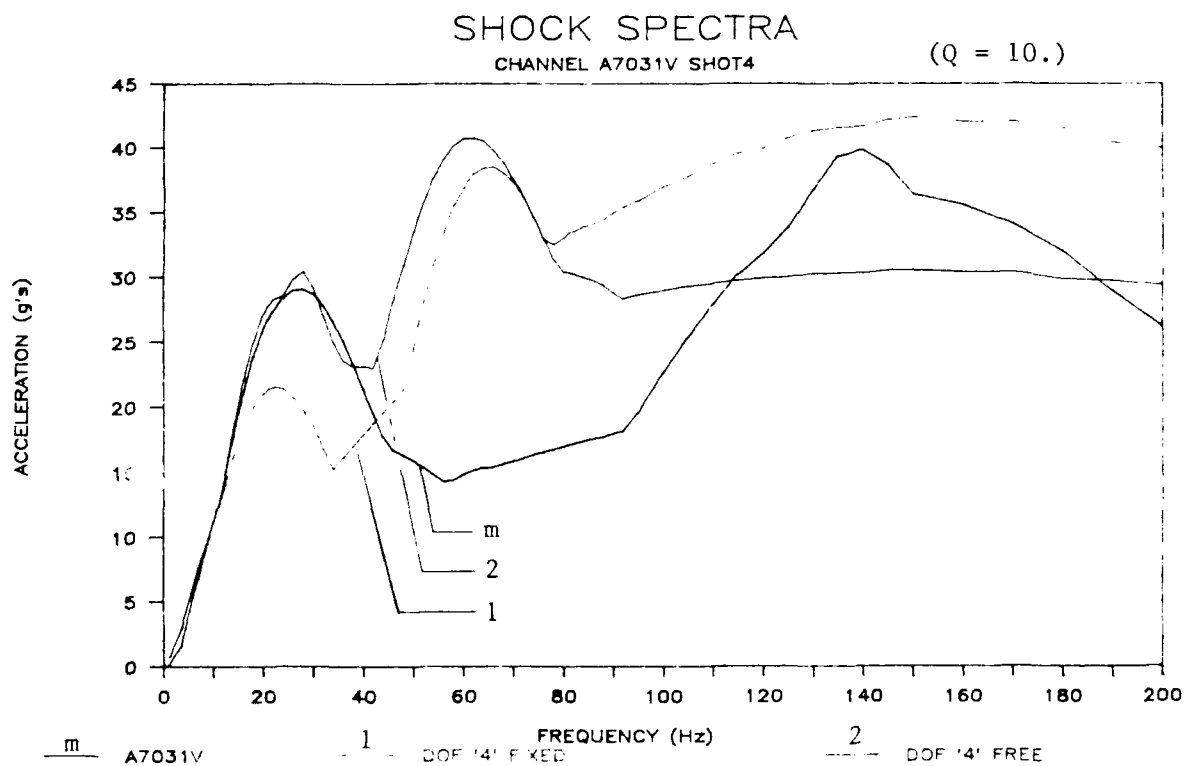
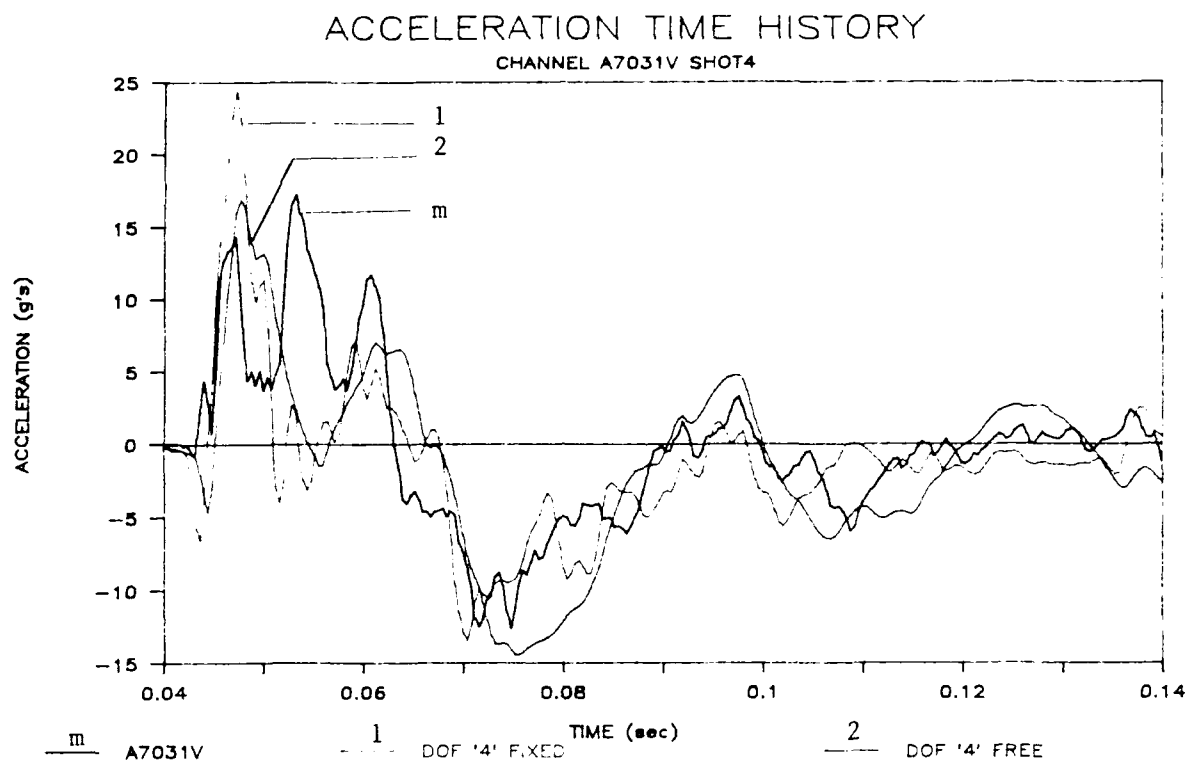


Figure 16. Charge side acceleration response comparison between Shot Four measured vs analytical, Loading A, heavy loadout, forward launcher

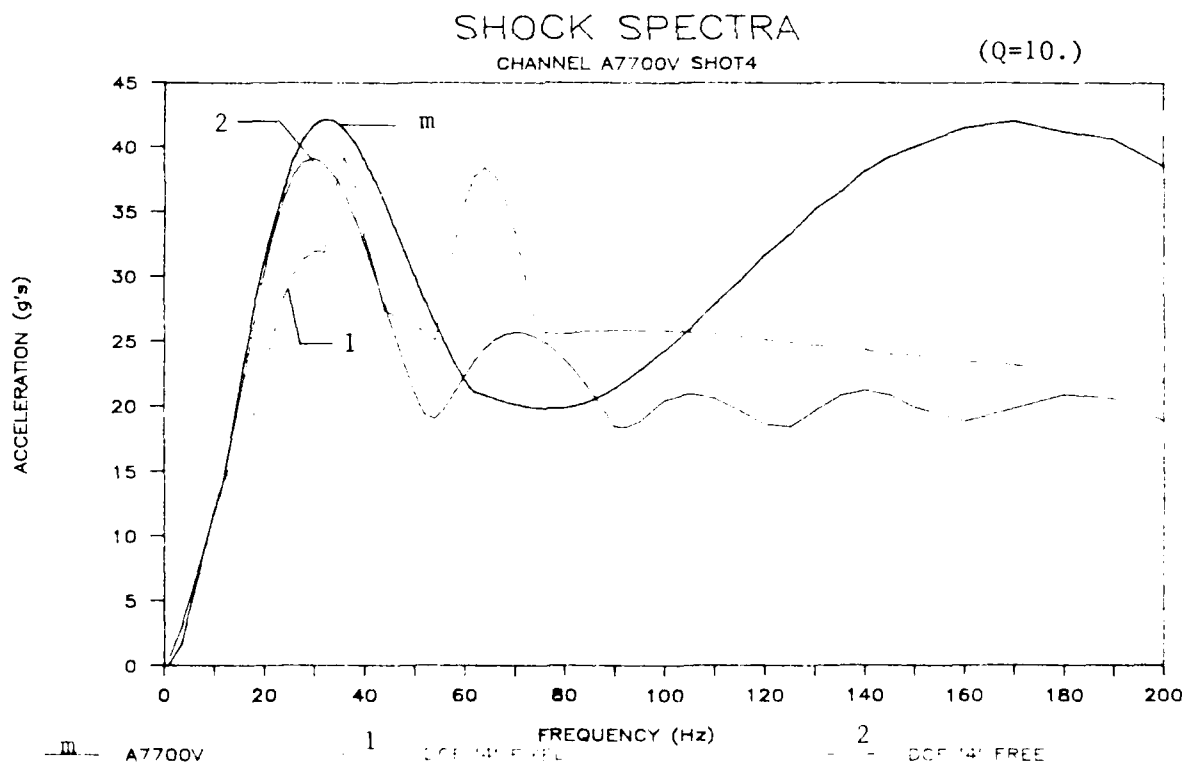
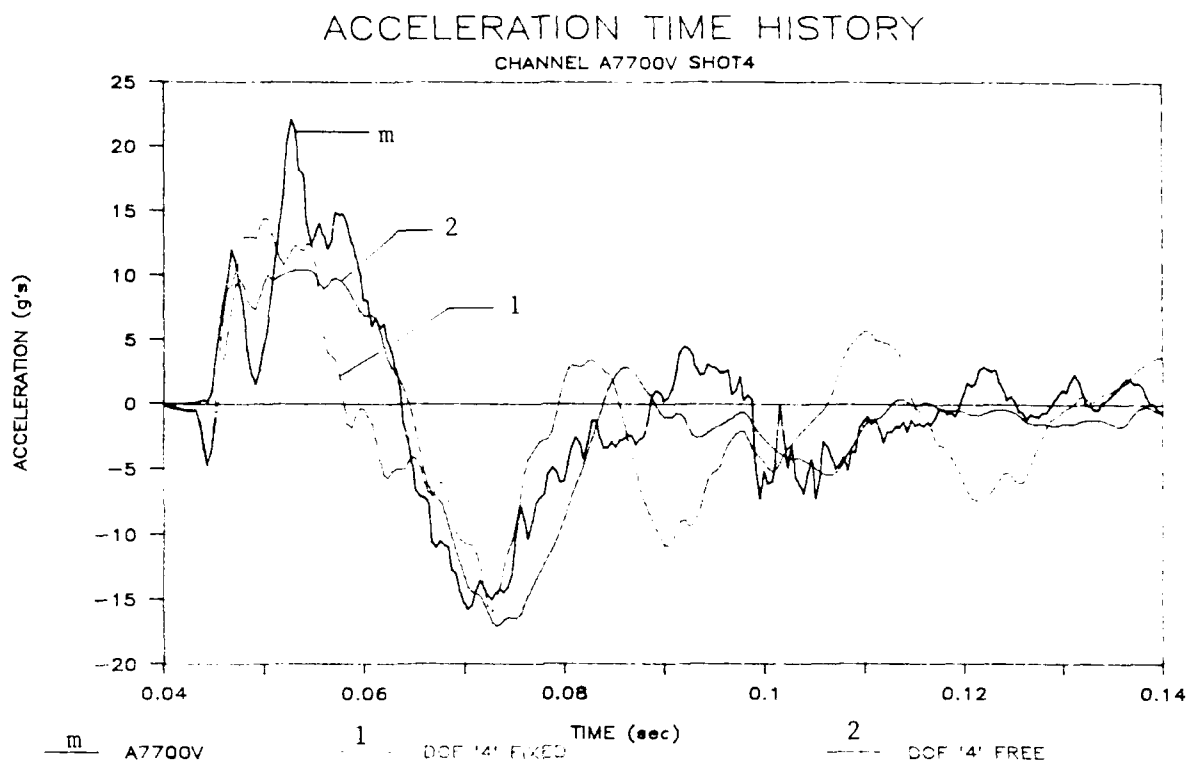


Figure 17. Shadow side acceleration response comparison between Shot Four measured vs analytical, Loading A, heavy loadout, forward launcher

VERTICAL ACCELERATION (G's) AT
PLENUM/CANISTER BASE AND DECK LEVEL

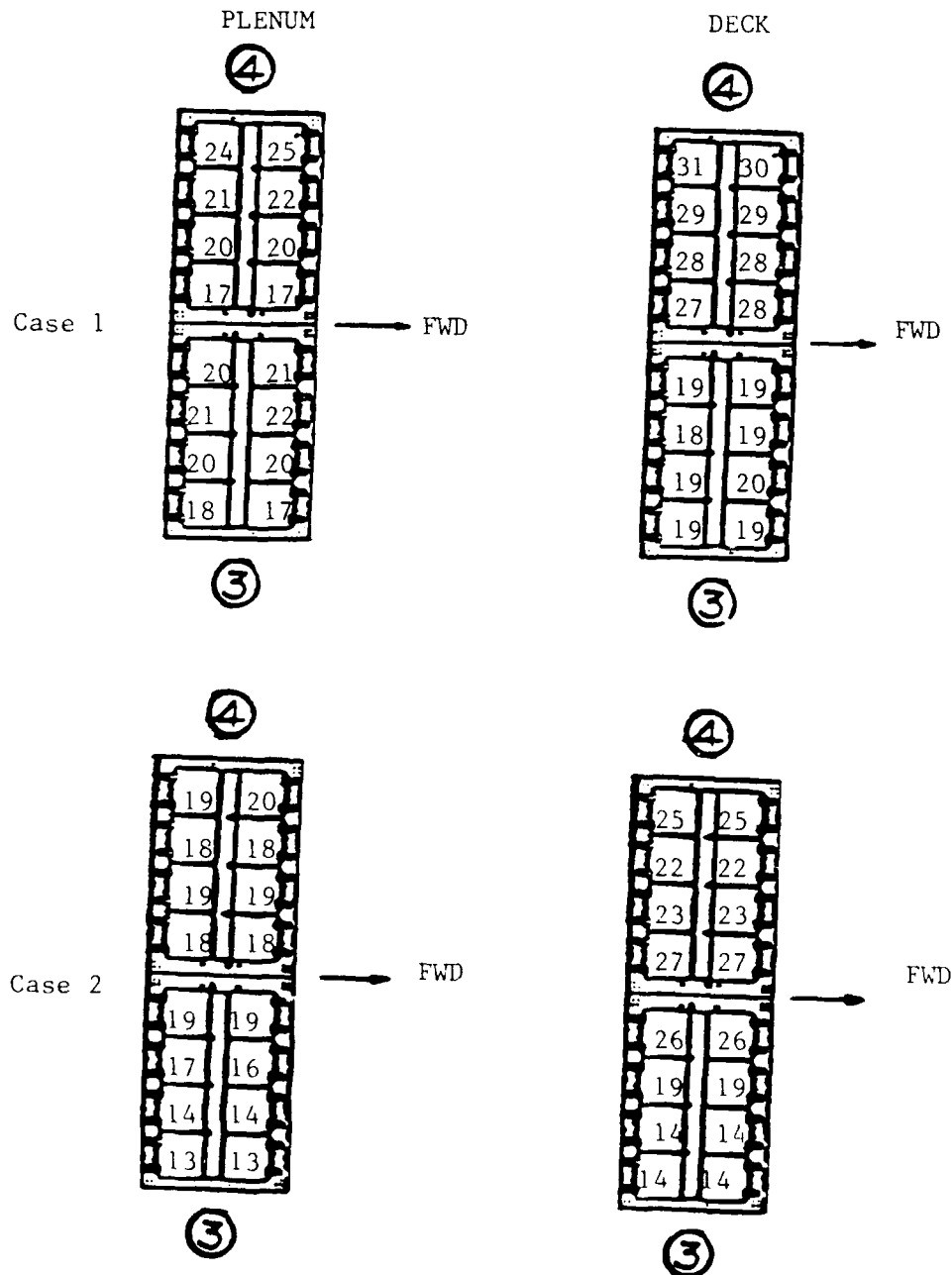


Figure 18. Vertical Accelerations (G's) at Plenum/Canister base and Deck Level, Loading B, Heavy Loadout, Forward Launcher.

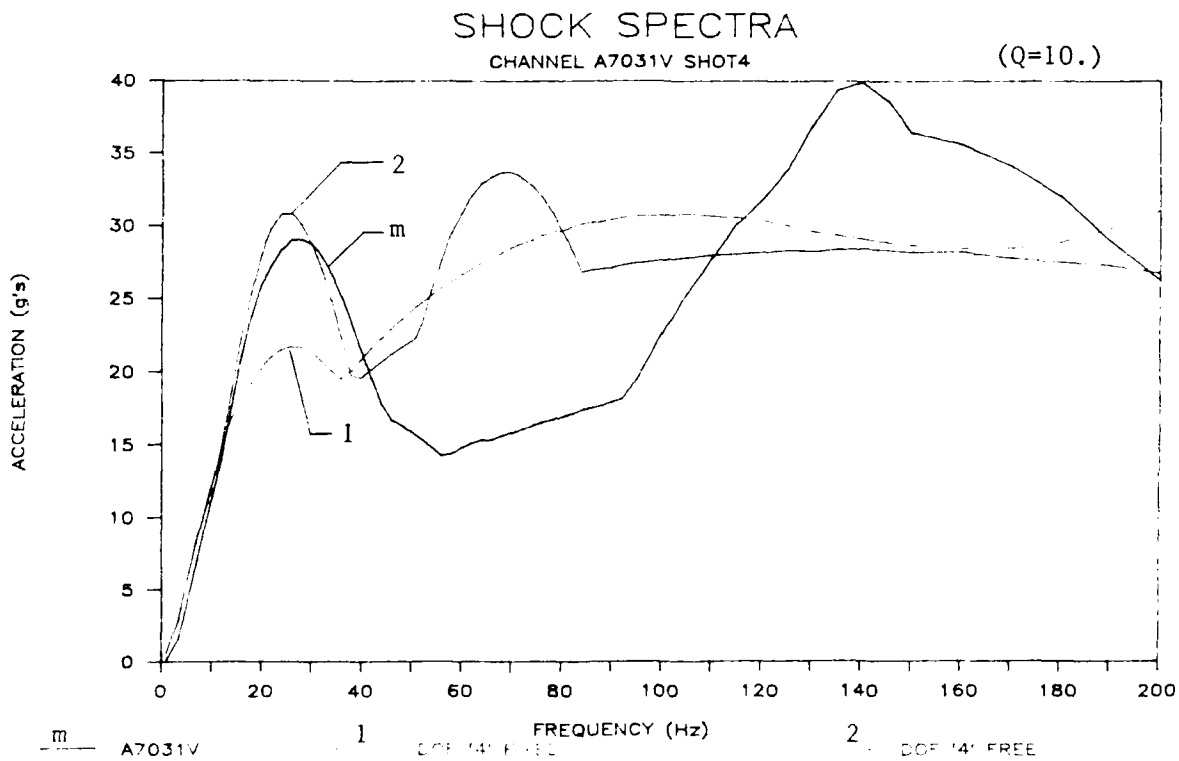
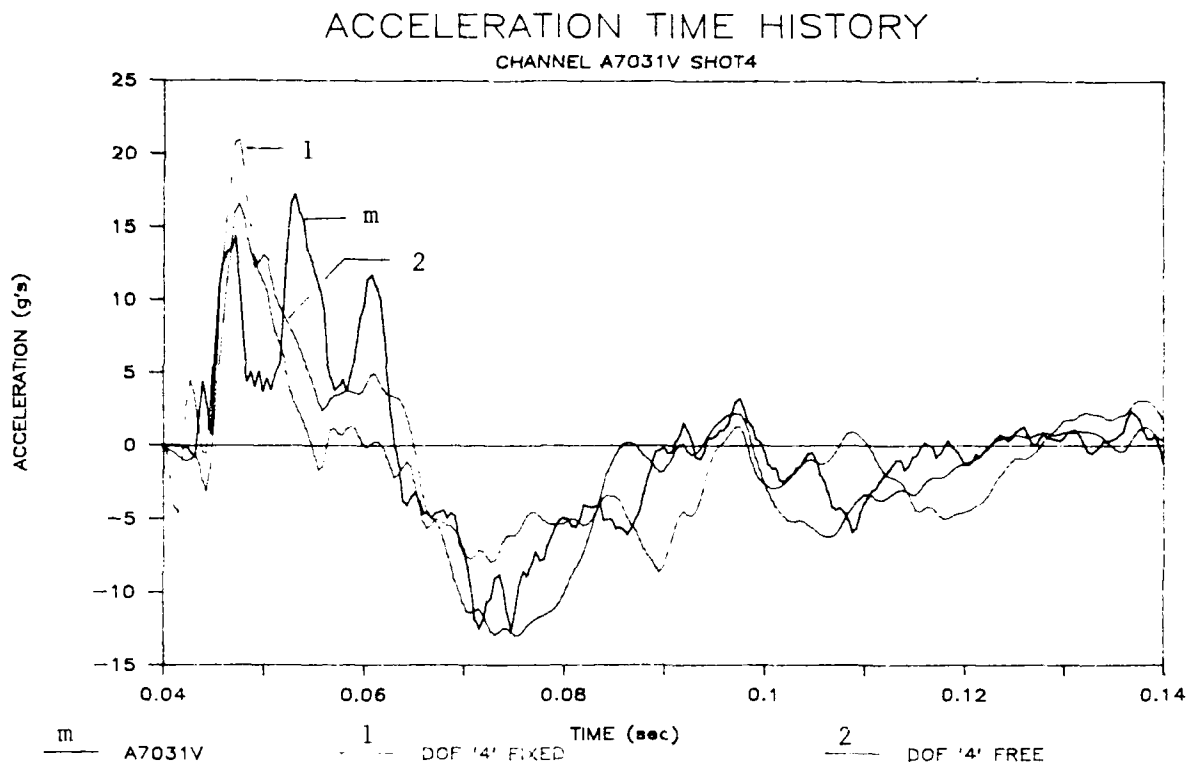


Figure 19. Charge side acceleration response comparison between Shot Four measured vs analytical, Loading B, heavy loadout, forward launcher

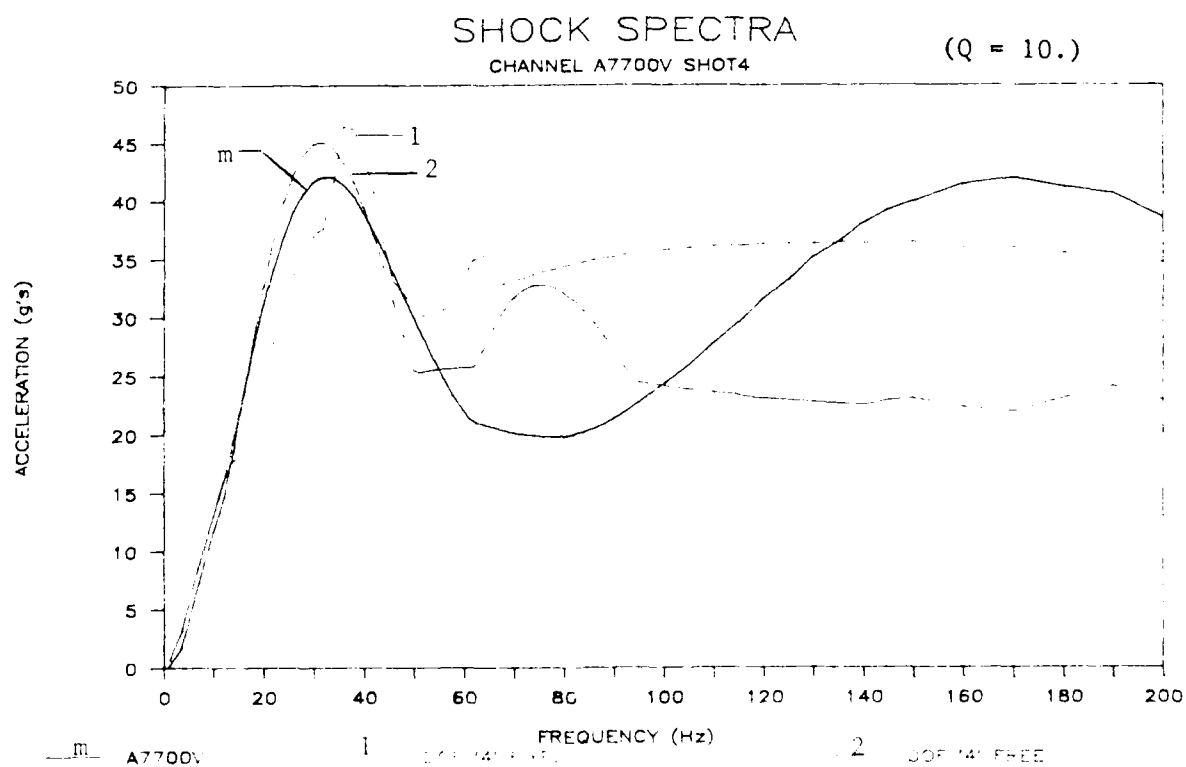
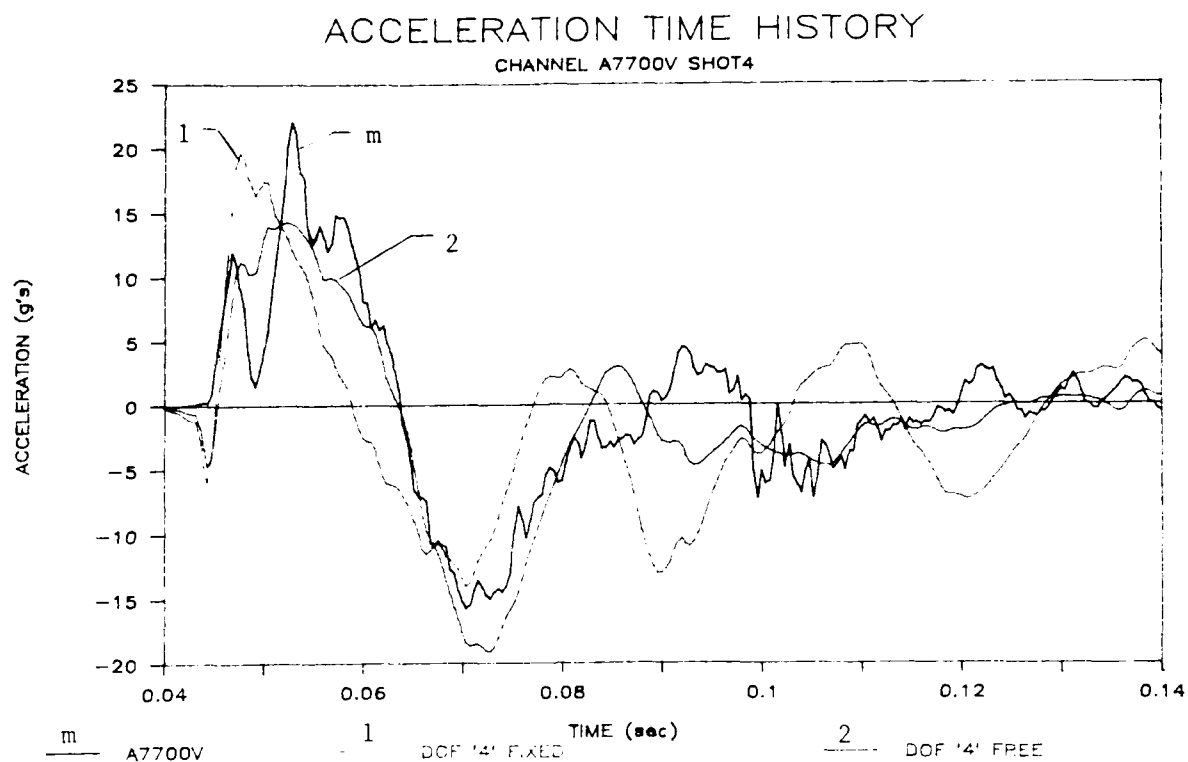


Figure 20. Shadow side acceleration response comparison between Shot Four measured vs analytical, Loading B, heavy loadout, forward launcher

VERTICAL ACCELERATION (G's) AT
PLENUM/CANISTER BASE AND DECK LEVEL

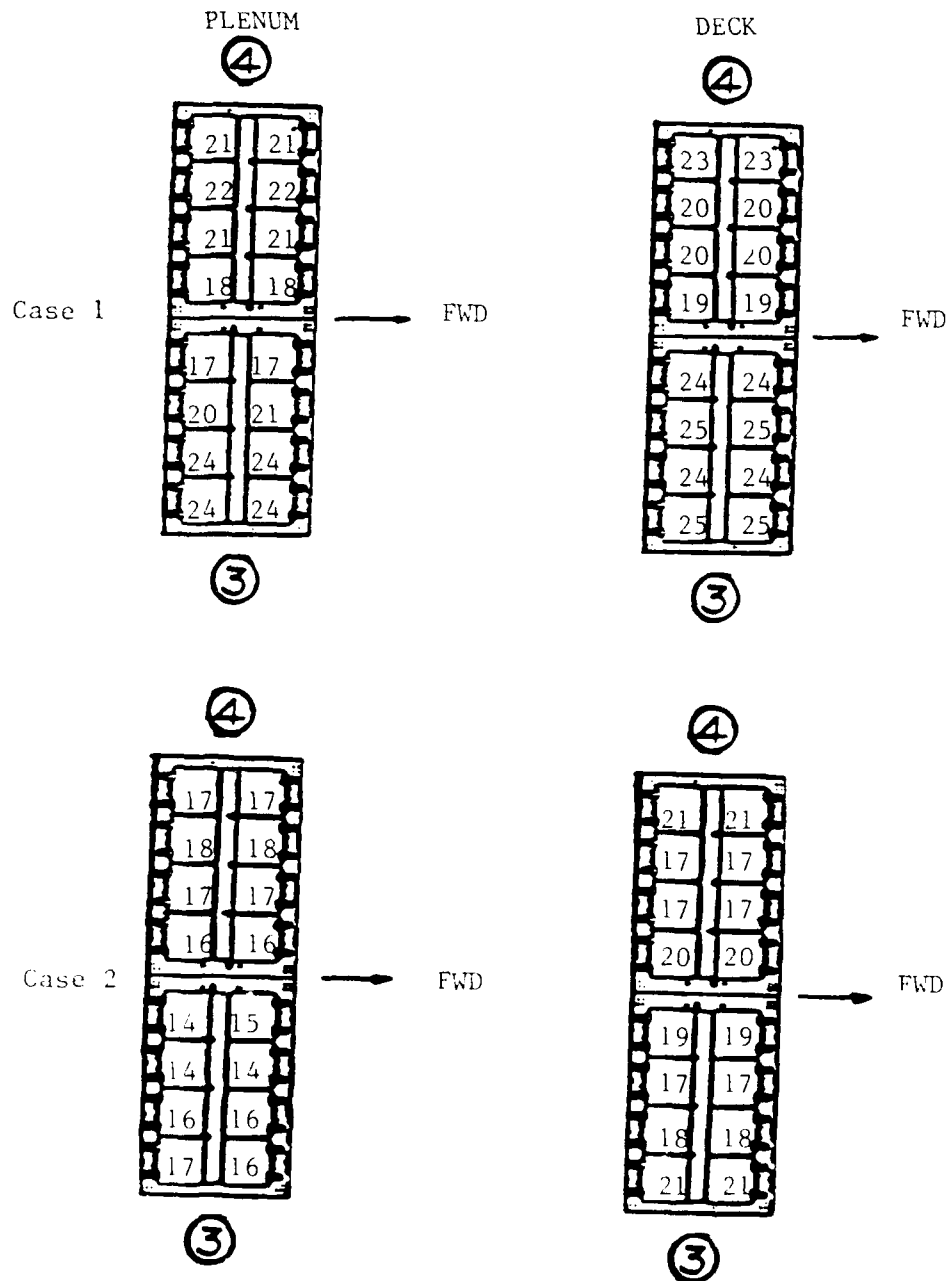


Figure 21. Vertical Accelerations (G's) at Plenum/Canister base and Deck level Light Loadout, Aft Launcher

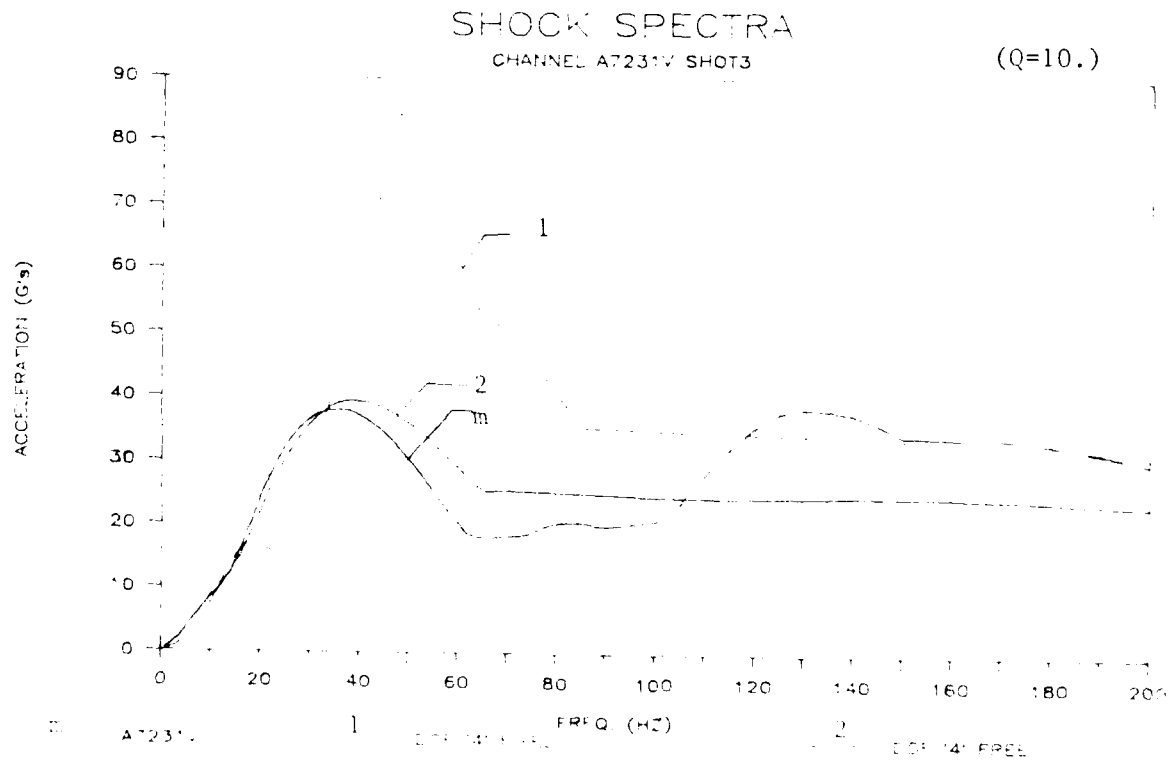
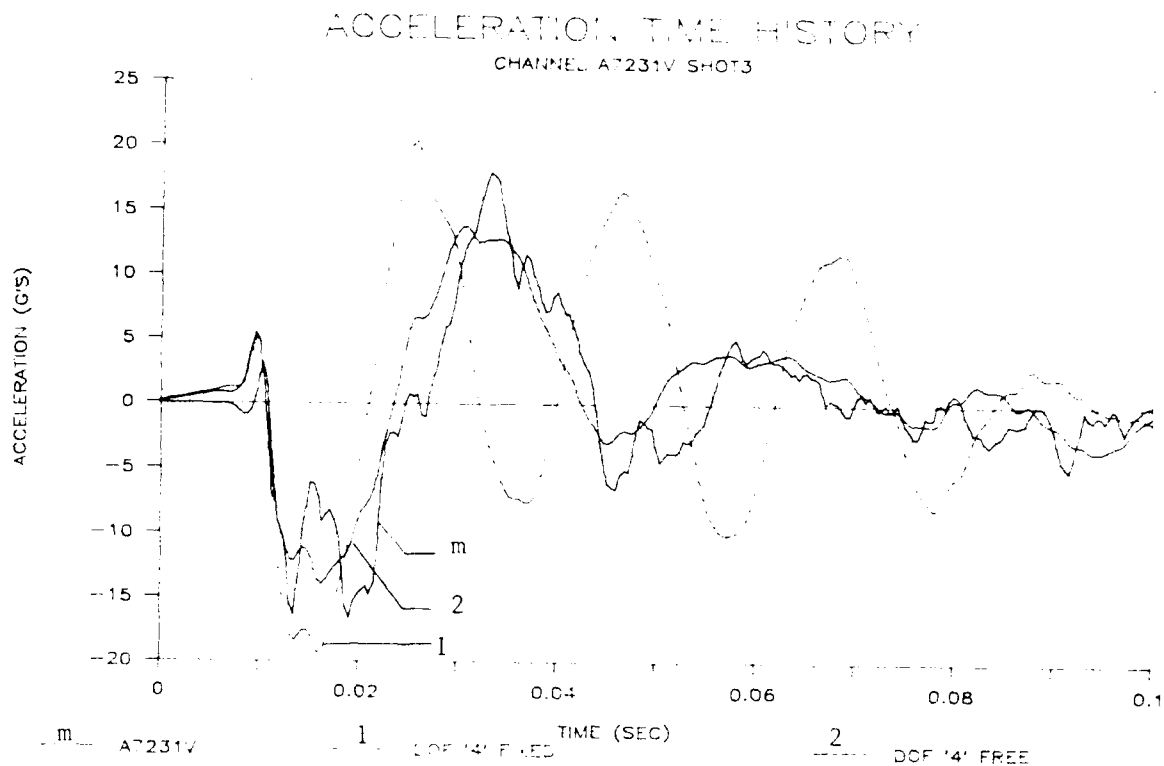


Figure 22. Charge side acceleration response comparison between Shot Four measured vs analytical, light loadout, aft launcher

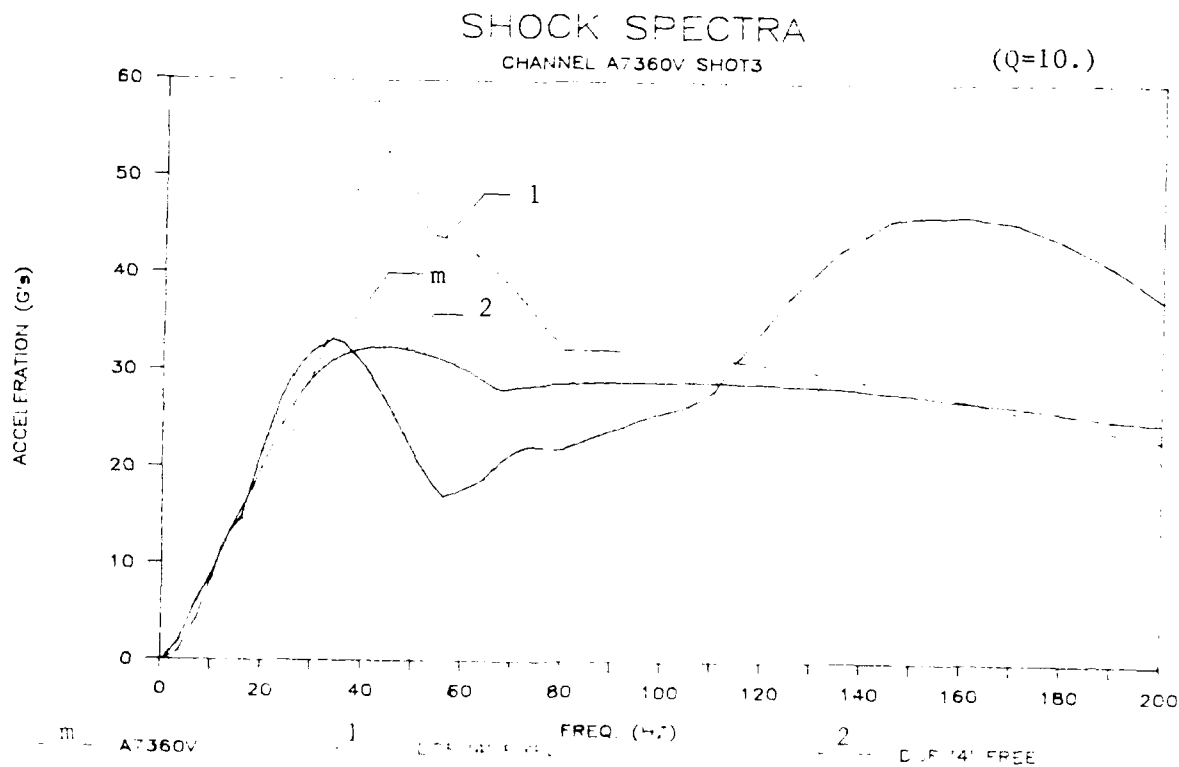
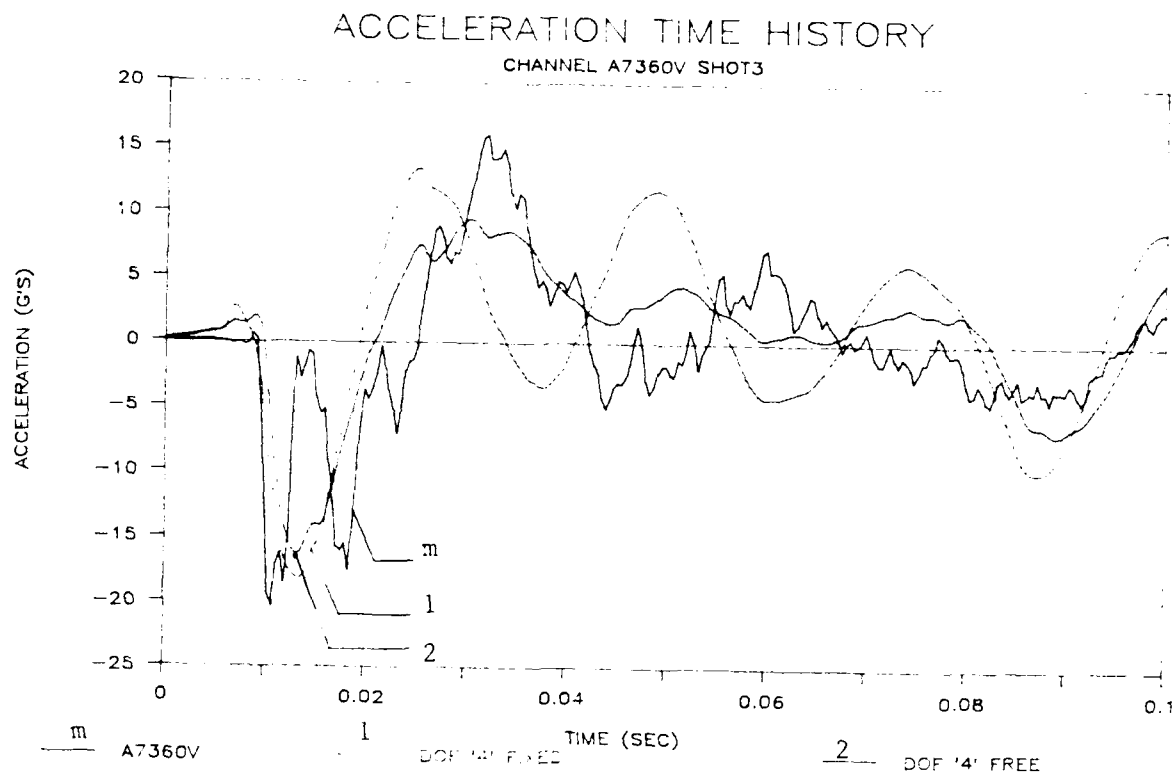


Figure 23. Shadow side acceleration response comparison between Shot Four measured vs analytical, light loadout, aft launcher

Shock Trials data and the two cases shows Case 2 to be closer to the measured data.

For the heavy loadout configuration with DDG 51 subbase model all input loading was at the subbase feet, which were connected to the ship foundation. There were no connections with ship bulkheads. Note that this configuration is similar to the CG 53 aft foundation whereas the forward foundation outboards are connected to the ships longitudinal bulkheads port and starboard. Because of the way in which the subbases were connected to each other and assuming symmetry about the center line of the subbases themselves, no additional mass distributions needed to be simulated. This configuration was analysed for Case 1 and Case 2. Figure 24 shows the peak accelerations at the plenum top/canister base and deck level for the two cases. Analysis shock spectra and time history plots are presented in Figures 25 and 26. The peak acceleration response data shows a shadow side effect for both cases. The comparison of shock spectra between the two cases shows Case 2 response frequency is closer to the frequency of CG 53 heavy loadout Case 2. The VLS with DDG 51 Subbase also showed the Shadow Side Effect, but the peak response of the VLS was 20 percent lower for the DDG 51 subbase case than the CG 53 foundation case.

CONCLUSIONS AND RECOMMENDATIONS

Transient analysis for the shadow side study was performed using several different finite element models. It was noted that changing the athwartship load did not vary the vertical response of the model. From the analytical response data it is clear that it is not enough to look at the peak accelerations. Time history and shock spectra plots of acceleration response provide a better understanding of the shadow side effect. Ship roll motion (Case 2) when introduced in the model gives better correlation to the measured data than Case 1 when roll motion is constrained. This study was able to reproduce a similar response for the VLS by using measured data as input to the mathematical models and changing the boundary constraints. The methodology explained in this report can be readily adaptable to other ship hull structures.

MMA&NS analytical models for the VLS showed good correlation with the CG 53 measured data. Any discrepancies which may be present can further be reduced by using translational and rotational inputs at the keel. The input loads for the keel and the ship structure surrounding the VLS should be generated using a method similar to one used by Reference 3. In the case of CG 53 only one velocity gage data was available at the keel.

The VLS model response for the CG 53 heavy loadout was evaluated with the CG 53 foundation and the DDG 51 subbase. A comparison of results for these two cases shows that the average vertical acceleration response was 20 percent higher for the CG 53 foundation case than for the DDG 51 subbase case. Also, a comparison of shock response spectra indicates that the shadow side response was 50

VERTICAL ACCELERATION (G's) AT
PLENUM/CANISTER BASE AND DECK LEVEL

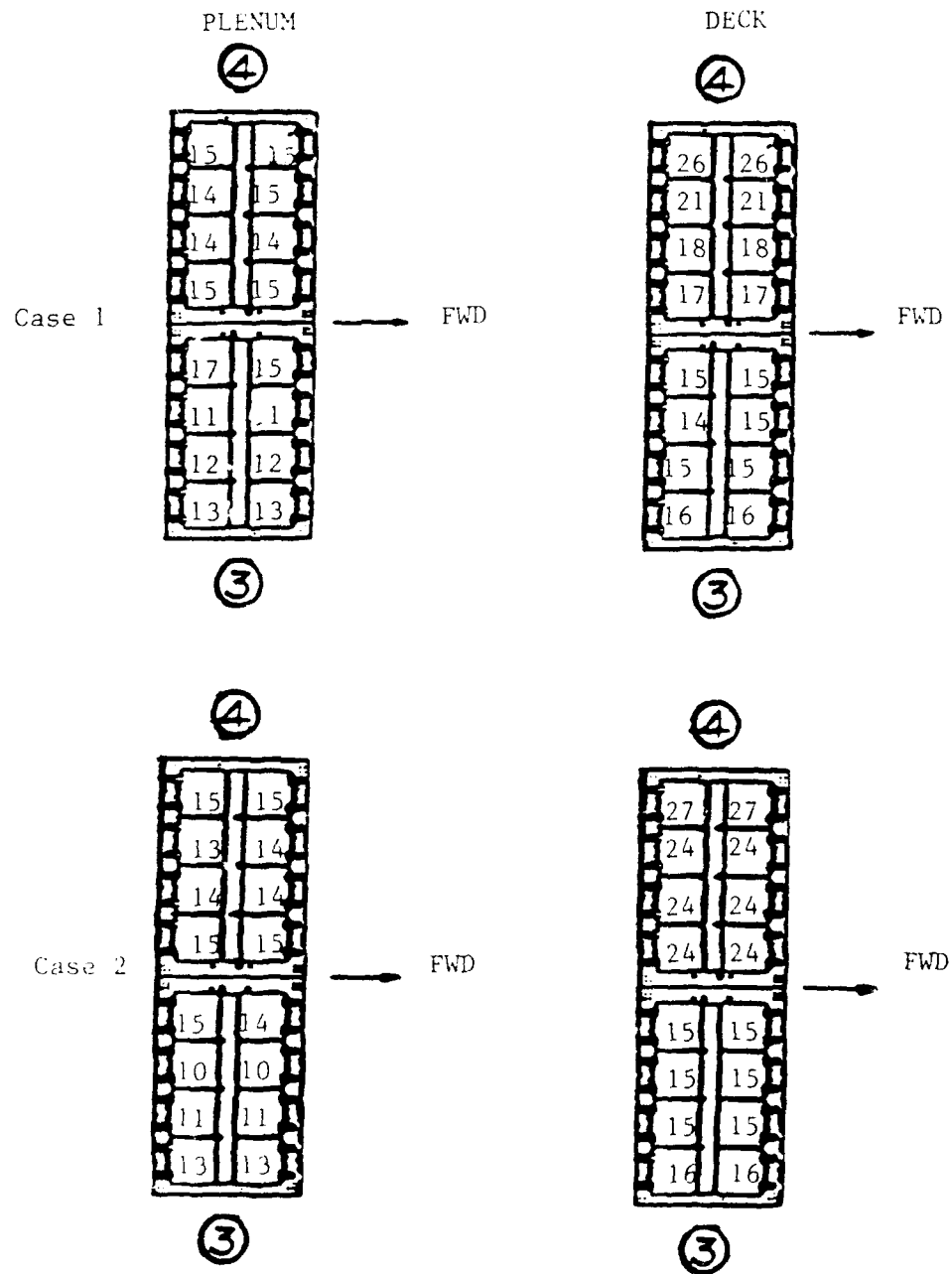


Figure 24. Vertical Accelerations (G's) at Plenum/Canister base and Deck level, Heavy Loadout with DDG 51 subbase, Forward Launcher

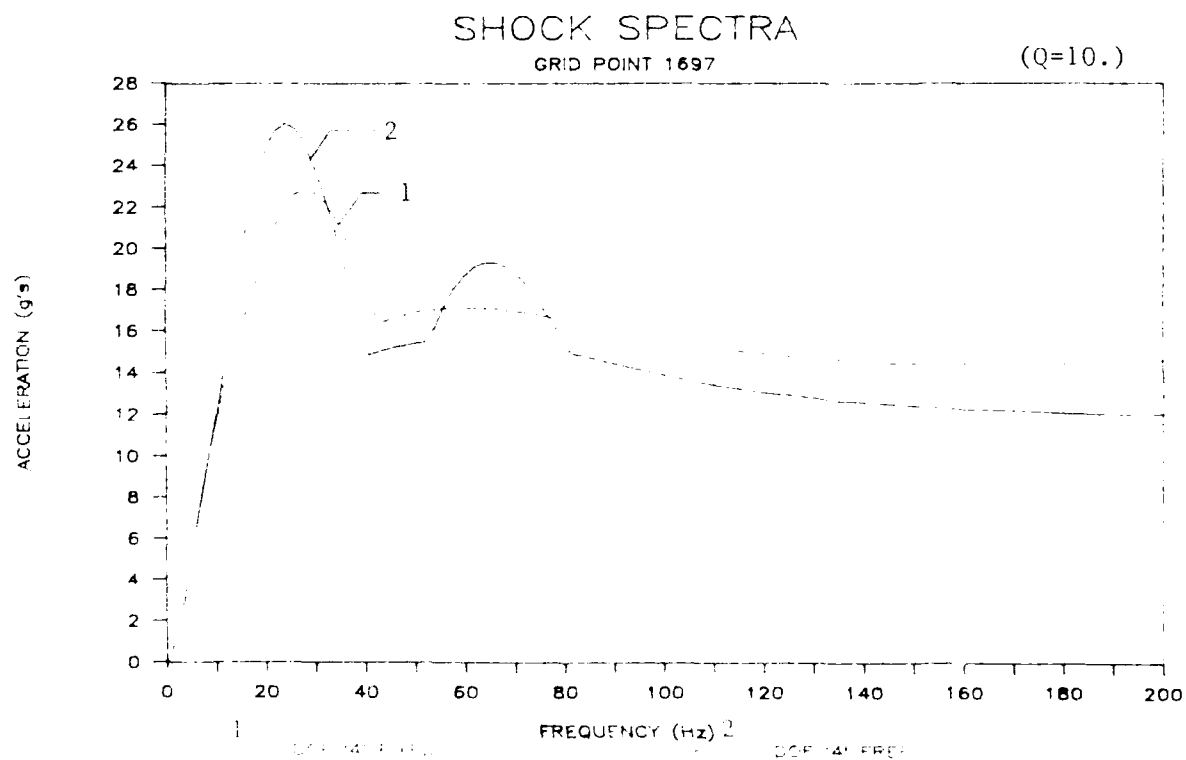
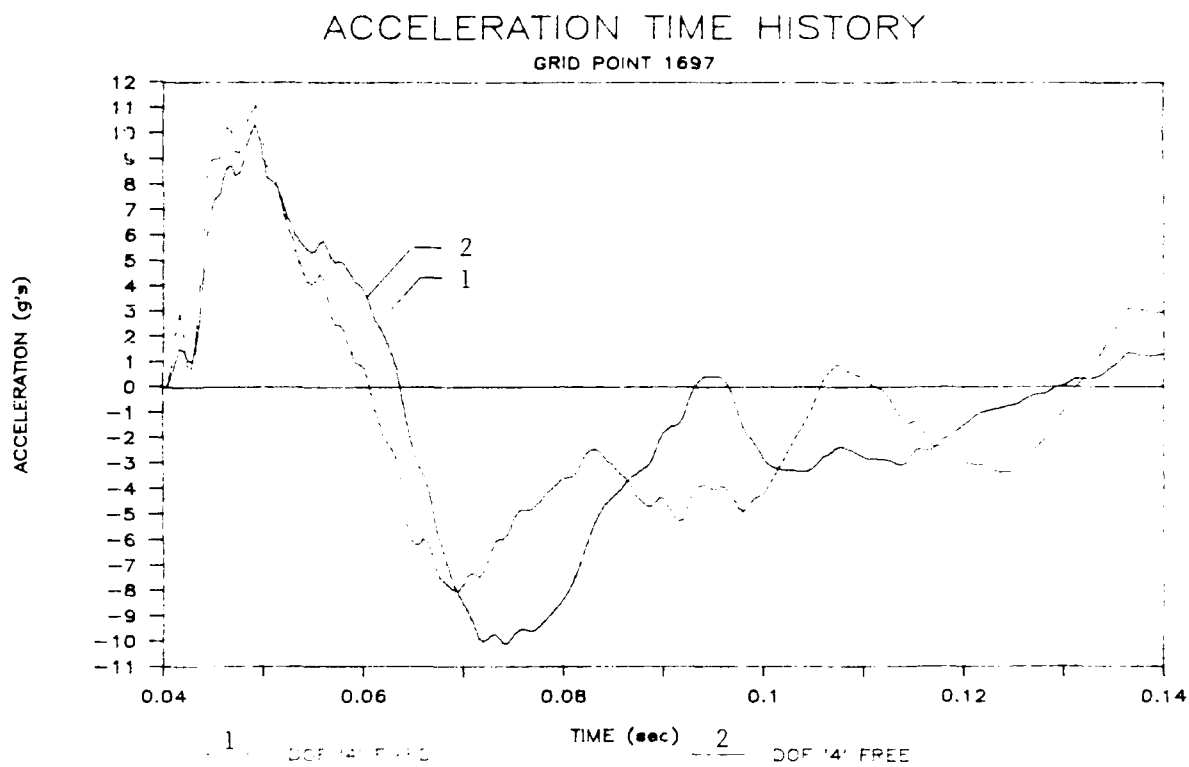


Figure 25. Charge side acceleration response comparison between analytical Case 1 and analytical Case 2 for CG 53 heavy loadout, forward launcher w/DDG 51 subbase

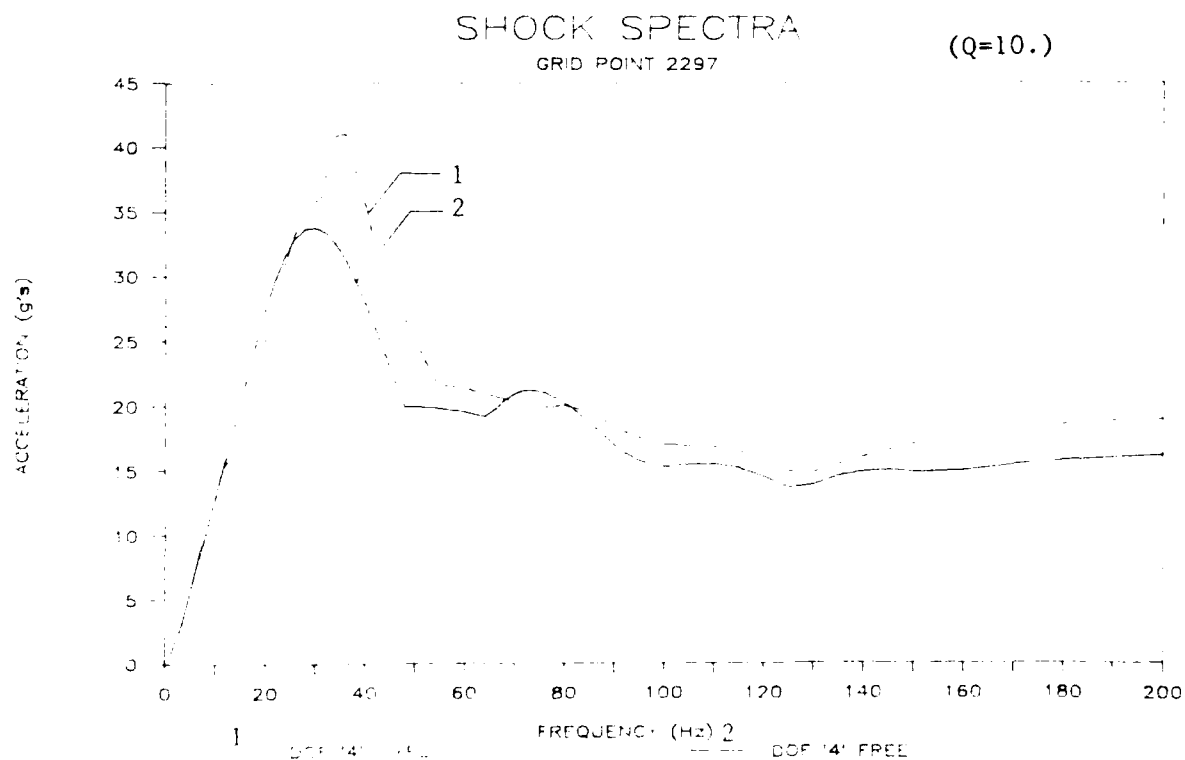
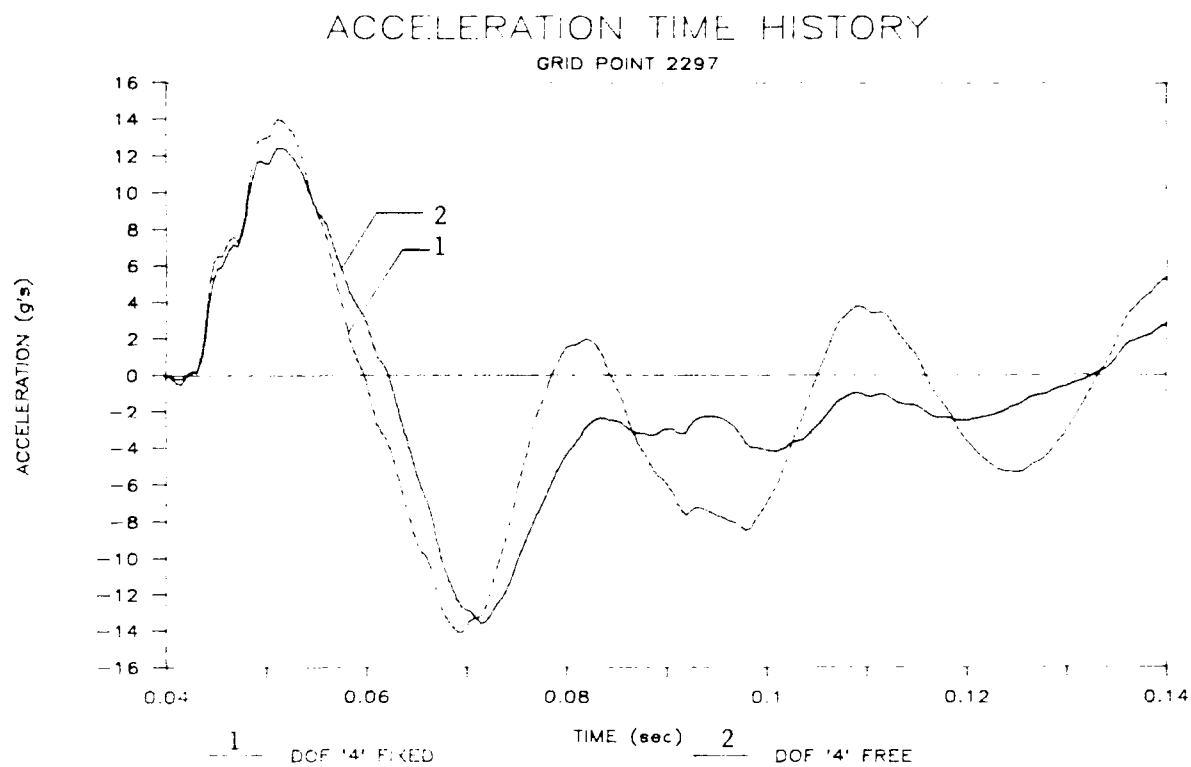


Figure 26. Shadow side acceleration response comparison between analytical Case 1 and analytical Case 2 for CG 53 heavy loadout, forward launcher w/DDG 51 subbase

percent higher than charge side for the CG 53 foundation case compared to 30 percent for the DDG 51 subbase case.

A second phase of Shadow Side Effect Study is ongoing at Martin Marietta Aero and Naval Systems. The analytical model for this part of the Study will include a part of the ship structure surrounding the VLS. Input loads will be the CG 53 Shock Trials measured data at the ship hull for a gage located near the center line of the ship. Input loads at the other locations on the ship structure will be adjusted for the impact time phasing and the amplitude change of the pulse. Delta time will be defined by the radial distance away from the center line of the ship divided by the speed of sound in water. And, the transient load amplitude change accross the hull will be determined by keel shock factor formula [11].

ACKNOWLEDGEMENT

This study was conducted under a contract from RCA, Electronic Systems Department, Borton Landing Road, Moorestown, New Jersey, 08057.

REFERENCES

1. "VLS Transient Analysis Pretest Report for CG 53 Shock Trials", BR110, Martin Marietta Baltimore Aerospace, February 1987.
2. "NAVSEA S9072-AF-RPT-010, -20/(C) CG 48, USS YORKTOWN (CG 48) Shock Trials(U)", Volume I and II, December, 1984.
3. "Vertical, Athwartship and Fore/Aft Shock Response of the Mk26 Guided Missile Launching Systems Mounted on the CG 47 Class Ship", NAVSEA N00024-79-C-4372 NKF Report No. 8200-214, November, 1983.
4. "DDG 993 MK 26 Guided Missile Launching Systems Vertical and Athwartship Response , NAVSEA N00024-79-C-4372-32123, NKF Report No. 8001-103 , March 1981.
5. "VLS Dynamic Design Analysis Method (DDAM) Pretest Report for CG 53 Shock Trials", BR101, Martin Marietta : Baltimore Aerospace, December 1986.
6. "VLS Dynamic Design Analysis Method (DDAM) Post Test Report for CG 53 Shock Trials", Vol 1 , BR00,606, Martin Marietta Aero & Naval Systems, December 1987.
7. "VLO ANA 20720330-001 CG 53 Shock Trials Data Analysis for VLS", Martin Marietta Aero and Naval Systems, October, 1987.

8. "Vertical Launching System MOD 1 Launcher DDAM Report", Vol 1, Mathematical Model, 2, November 1981, Martin Marietta Corporation, Orlando Aerospace.
9. Gockel, M.A., "MSC/NASTRAN Handbook For Dynamic Analysis", The Macneal Schwendler Corporation, 815 Colorado Blvd., Los Angeles, CA 90041.
10. Gockel, M.A., "MSC/NASTRAN Handbook for Superelement Analysis", the Macneal-Schwendler Corporation, Los Angeles, CA.
11. "NAVSEA T9CGO-BV-RPT-010(I), -020(II)/(C) CG 53, USS Mobile Bay (CG 53) Shock Trials(U)", Volume I and II, March, 1988.
12. "Shock Dynamic Design Analysis Report For DDG 51 Class Ships", Volume II, Book 1, BR103, Martin Marietta Aero & Naval, August, 1987.
13. "Study On VLS Shadow Side Effect During CG 53 Shock Trials", VL1 ANA 20021000-1, Vol I-IV, Martin Marietta Aero and Naval Systems, June, 1988.

DYNAMIC RESPONSE OF PIPE SUBJECTED TO HIGH IMPACT LOADS

R. J. Scavuzzo and P. C. Lam
Department of Mechanical Engineering
University of Akron
Akron, OH 44325

An instrumented pressurized simply supported 1 1/2" schedule 40 pipe was subjected to starting velocity shock using a drop test fixture. Velocities as high as 21 ft/sec were imposed on the 4' length of pipe. Elastically calculated stresses exceeded the yield strength by over a factor of three. The plastic pipe deflection is about 1/4". Design criteria based on an allowable plastic pipe deflection is suggested.

INTRODUCTION

Allowable dynamic stresses of piping in naval combatant ships are normally limited to values between the yield strength and twice the yield strength. These same limits are also used in the ASME Boiler and Pressure Vessel Code, Section III, Division I for nuclear piping subjected to seismic or other dynamic loads [1,2]. In this study the response of piping to both static (pressure) stresses and dynamic stresses associated with shock loading are experimentally investigated.

Piping subjected to naval shock never fails in the center of a pipe span. Failures, if present, occur in threaded or soldered joints or in the hangers supporting the pipe. Thus, based on the experience, design effort should be concentrated on the joint design or hanger design and not in the hanger spacing to limit pipe bending stresses.

Recent evidence indicates that piping systems can absorb considerably more dynamic energy than permitted by the upper limit of $2S_y$. Studies of power plants that have been subjected to large earthquakes without having been designed to resist earthquakes show that the piping neither failed nor showed evidence of large plastic deformation as long as it was properly anchored [3]. Because of the economic potential, the current Code criteria for nuclear piping are being re-examined to determine whether more liberal allowable stresses can be safely permitted. Work being done for the nuclear industry can be applied to piping in naval

combatants.

One argument for permitting higher allowable stresses for the dynamic loads is based on the concept of limited available energy for structural deformation. For static loads such as internal pressure (from gas or steam) and dead weight, the available energy is large compared with the energy required to deform and, subsequently fail the structure. However, for certain types of dynamic loads such as an earthquake, drop-impact, and shipboard shock, the available energy is limited and may not be sufficient to cause either unacceptable plastic deformation or rupture.

As a result, an experimental study was sponsored by the PVRC [3] dynamic task group to measure the dynamic response of pressurized stainless steel piping subjected to high dynamic loads. Specifically, the objectives the experimental portion of this research program were to:

- (1) Superpose dynamic stresses in piping onto static pressure stresses so that current allowable stress criteria of the ASME Boiler and Pressure Vessel Code [1] are exceeded.
- (2) Obtain experimental dynamic strains in the piping specimen to compare with various analytical predictions.
- (3) Measure plastic deformation to compare with analyses.

Data provided from the first objective were used to experimentally evaluate the significance of exceeding Code allowable stresses. Data provided on the second and third objectives were used both to evaluate experimental results and to compare with various analytical solutions so that the ability of a designer to calculate dynamic elastic-plastic stresses and strains in very simple structures could be accessed. These analytical comparisons are discussed in Reference [4-7].

DESCRIPTION OF TEST EQUIPMENT

Pipe Specimens

All pipe specimens were 1 1/2 in. NPS Schedule 40-type 304 stainless-steel seamless pipe. The nominal inside and outside pipe diameters were 1.90 in. and 1.61 in., respectively. The D/t ratio was 12.1 where D is the mean diameter.

Two tensile tests were conducted on the 304 stainless-steel pipe material. Both tests were conducted on the first length of the pipe which was used for the four pipe specimens. The first test was conducted using a mechanical extensometer to measure strains. An electric resistance strain gage was used in the

1/4-in. diameter steel rods 9 ft high. The fixture was dropped from different heights onto a steel channel on the floor for each test.

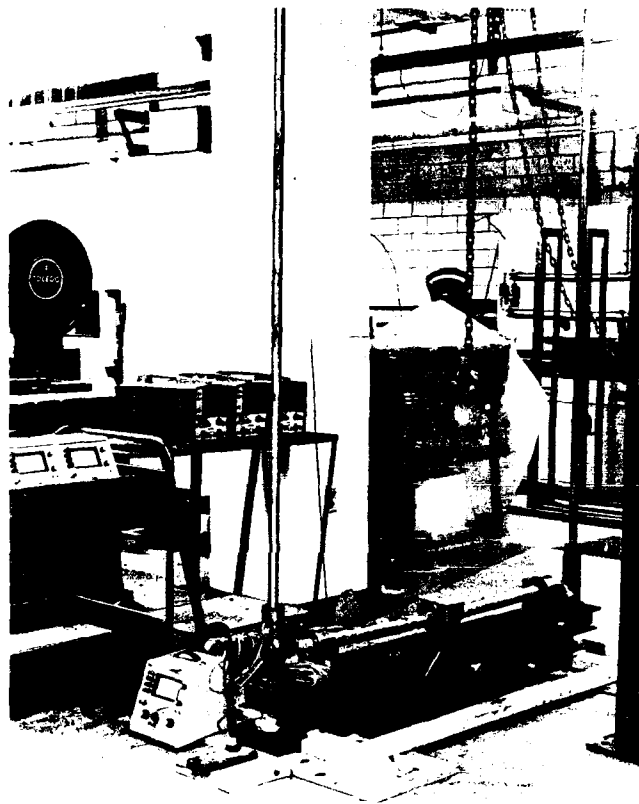


Fig 1--Overview of entire test fixture with concentrated weight on pipe specimen

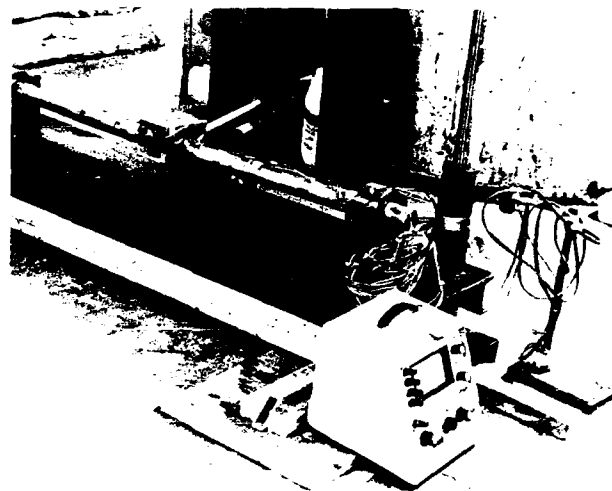


Fig 2--Pipe specimen, strain gaged and mounted in loading fixture

Both uniform pipe and pipe with a 14 lb. mass at the center of the span were tested. Output from electric resistance strain gages at various positions on the pipe were recorded using storage oscilloscopes. In this manner, strain-time history data were obtained. Specimens were loaded first elastically and then into the plastic range. Without the center mass as many as eight tests were conducted on one pipe specimen. Five of the tests plastically deformed the pipe. For the pipe specimens with the center mass only two tests into the plastic range could be conducted. After a particular specimen reached a center deflection of approximately 1/2-in., it was discarded and replaced with a new pipe specimen. A total of eight different pipe specimens were tested to evaluate the response of piping to high dynamic stresses.

second test. Data from the second test are judged to be more accurate. The yield strength was determined from both tests. Data from the tests were also to determine the tangent modulus.

The measured yield strengths were 27,000 psi and 29,600 psi, respectively. The measured elastic modulus was 28.5 million psi. The tangent modulus varied with strain. An average value of 5.5 million psi was estimated over the plastic strain range obtained during testing. Material properties are summarized in Table 1.

Table 1—Elastic and Inelastic Material Properties

Source	$E \times 10^{-3}$ (ksi)	ν	σ_y^a (ksi)	$E_t \times 10^{-3}$ (ksi)	ρ (lb/in. ³)
Handbook ^b	28.5	0.3	30	1.32	0.283
Test ^c	28.5	0.3	29.6	5.50	0.283

^a Initial yield stress.

^b Nuclear Systems Materials Handbook for 304 SS @ 70° F.

^c Average values from tensile tests conducted at the University of Akron.

Table 2—Test Instrumentation and Equipment

Test Equipment	Instrumentation and Equipment		
	Manufacturer	Model	Comments
Bridge amplifier and meter	Vishay Instruments	BAM-1	0-20 K Hz
Storage oscilloscope	Textronix	Type-T912	0-10 M Hz
B&K electromagnetic shaker	Bruel and Kjaer	Type 812	0-445 N (0-100 lb)
B&K power amplifier	Bruel & Kjaer	Type 2107	—

Test Facilities and Instrumentation

Facilities of the Mechanical Engineering Laboratory at the University of Akron were used in this program. Strain gages were mounted on all pipe specimens and dynamic strains were recorded on a storage oscilloscopes. Each strain gage signal was amplified through a bridge amplifier to the oscilloscope. A permanent record of data was made with photographs of the scope trace. Plastic deformation between the center of the pipe specimen and fixture was measured after each test in a series. These centerline deflections were measured with inclined gage blocks and a micrometer. Data could be duplicated to within 0.002 in. with these instruments. Instrumentation and equipment used in this test program are listed in Table 2.

A test fixture was designed to load pipe specimens by dropping the entire fixture at a known height (see Figs. 1 and 2). In this manner, a starting-velocity shock loads the pipe. The fixture tests a 1 1/2-in. NPS Schedule 40 pipe specimen 48 in. long simply supported at each end. The simple support is obtained from hardened steel pins that extend from a collar through a steel yoke. Two lubricated bronze bushings were press fitted into each yoke to provide bearings with low energy losses. These yokes were fixed to a frame fabricated from two steel channels covered with a 1/4-in. steel plate. One yoke was free to move in the axial direction of the pipe. Steel blocks welded to the frame under each yoke provided a very stiff support to the foundation. The movable portion of the fixture is guided by ball bushings by 1

The location of strain gages varied from one test series to the next. Strain gage locations are shown on Figs. 3-5; strain gage data from test series (or pipe specimens) 2, 3, 5 and 8 were analyzed to determine damping in both the elastic and plastic regimes. Specimens 2 and 3 were uniform pipe sections without a center mass. Peak strains of approximately 3500 micro-in./in. were obtained. Specimens 5 and 8 had a center mass of 14 lb. (Fig. 2). For this case, peak strains over 7000 micro-in./in. were developed. Typical high-strain data (Test Series 8) are shown on Fig. 6.

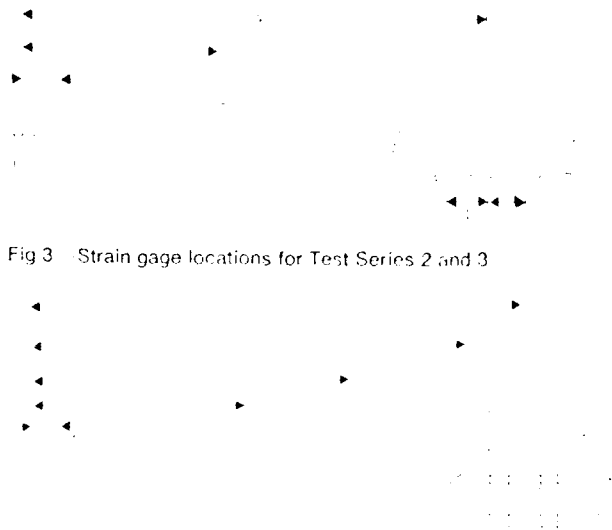


Fig 3 Strain gage locations for Test Series 2 and 3

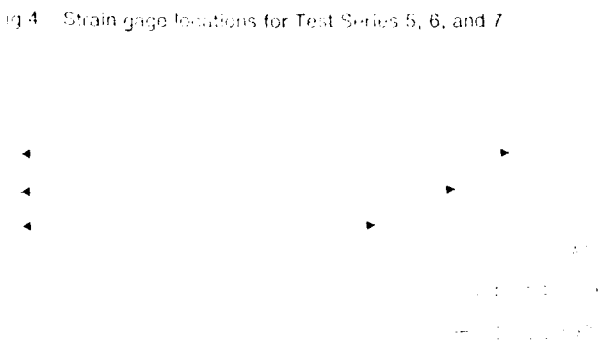
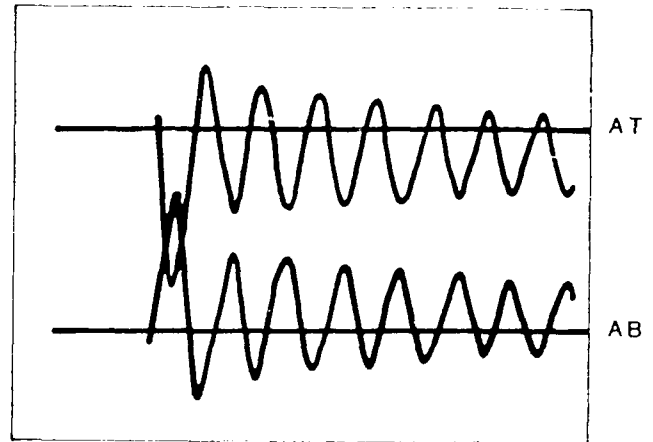


Fig 4 Strain gage locations for Test Series 5, 6, and 7



Fig 5 Strain gage locations for Test Series 8 and 9

TEST 8-3



TEST 8-4

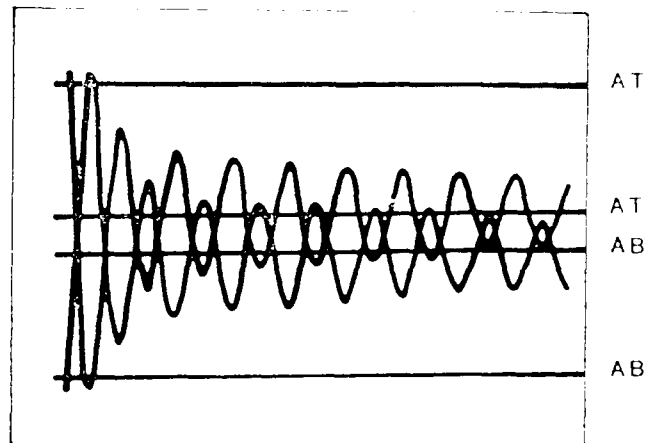


Fig 6 Strain gage data, Test Series 8, Tests 3 and 4, from gages AT and AB

The two ends of the pipe were fitted with plugs and O-ring seals so that the pipe could be pressurized using a hydraulic

pump. Pressures up to 3000 psi could be obtained with the fittings in the system. Thus, dynamic stresses developed from impact are superposed onto the static pressure stresses. A closed up view of the pin support with the yoke and bushing is shown in Figure 7.



Fig 7 - View of pin support showing the yoke and bushing.

DISCUSSION OF RESULTS

A total of nine test series were conducted on eight different pipe specimens. Tests 1, 2, and 3 were conducted on uniform diameter pipe specimens without a center mass. Preliminary tests for pipe specimens with a 14 lb. mass at the center were conducted on the third pipe specimen by turning the specimen over and bending the pipe in the opposite direction. Tests in this pipe are called Test Series 4. Test Series 5 through 9 were conducted on pipe specimens with a 14 lb center mass. Test Series 9 was conducted to determine if the center weight tended to flatten the pipe during impact. Peak strains from all the tests are tabulated in Reference [4].

Data from each test on the pipe specimens without a concentrated mass at the midspan are listed on Table 3. Data from pipe specimens with the 14 lb center mass are listed in Table 4. In Tables 3 and 4, the drop height is listed for each test. The initial hydrostatic internal pressure is also tabulated. Axial stresses from the hydrostatic pressure are added to the peak elastically calculated dynamic stress to obtain the maximum elastic elastically calculated stress intensity, SI. Peak dynamic strains measured by the strain gages multiplied by the elastic modulus is also listed. As seen in Table 3 these pseudo stresses, $E \times \text{strain}$, determined from strain gage data exceed the elastically calculated values by as much as 50% for the higher impacts (Tests 2-6, 2-7). Thus, elastic analyses from this impact loading underestimated the maximum strains that occurred. The

strain-gage data from the first test appears faulty but is provided for completeness.

Midspan (incremental) plastic deformation caused by a particular test is also listed in Tables 3 and 4. The total midspan deformation in a specimen is cumulative and can be obtained by adding all values for a particular test series. Plastic deflections obtained from tests without a center weight are plotted in Fig. 8. A drop of approximately 20 in. was needed to initiate measurable plastic deformation.

Deflection data for Test Series 4 through 9 are plotted in Fig. 9. It should be noted that deflections obtained during Test Series 5 and 6 without internal pressure were lower than values obtained during Series 7 and 8 indicating that internal pressure increased plastic strain in the pipe. Permanent deflections of approximately 0.3 in. were measured for a 60 in. drop, which is

9-2

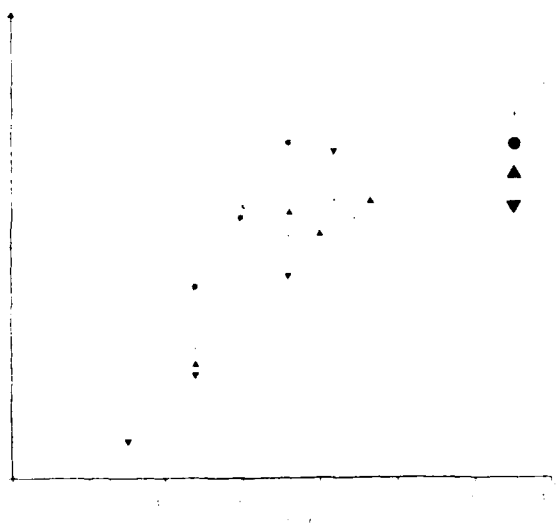
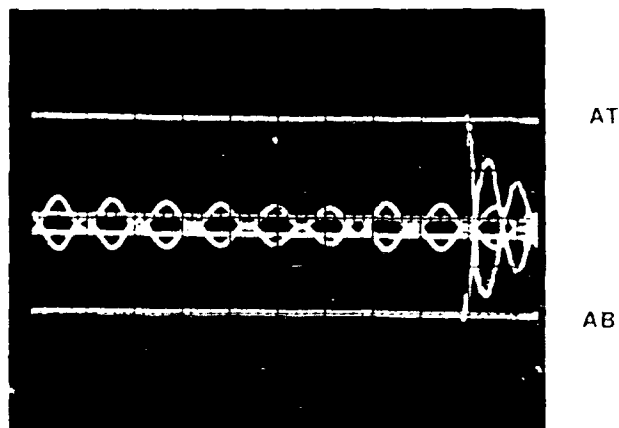


Fig. 8 Plastic deformation vs. drop height - no center mass



9-2

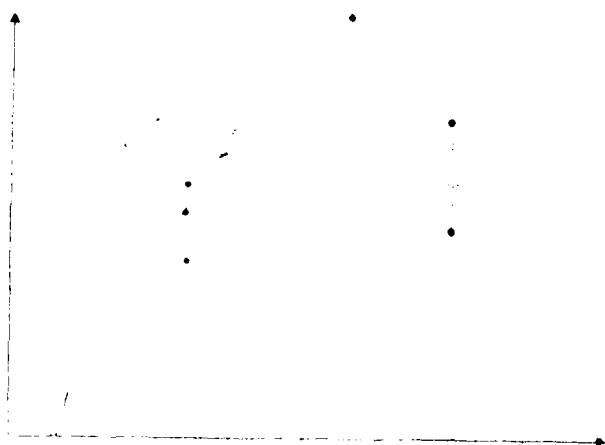


Fig. 9 Deflection data for Test Series 4 through 9

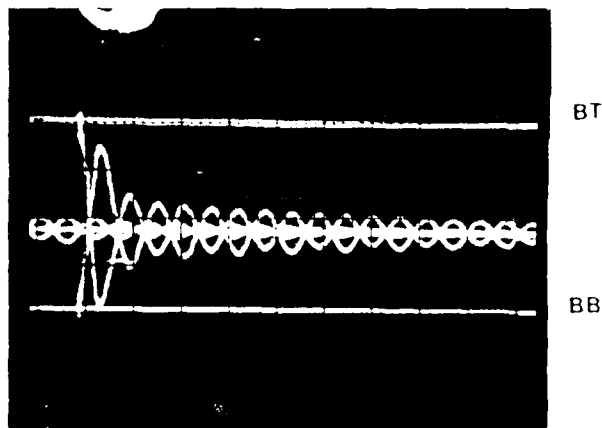


Fig. 10 Strain gage data from Test Series 10, indicating plastic deformation at B and BB

Table 3—Elastically Calculated Stresses for Specimens Without Concentrated Mass

Test No.	Drop Height (in.)	Pressure (ksi)	Design Stress (ksi)			Experimental $E\epsilon_p$ (ksi)	Deflection ^a δ (in.)
			σ_z ^c	σ_{z1} ^b	S_T ^d		
1-1	9	0	0.36	18.56	18.81	15.68	
1-2	18	1.0	2.80	26.36	29.16	31.55	
1-3	48	2.0	5.35	33.91	38.99	24.23	0.061
1-4	72	2.0	5.35	52.72	58.97	33.48	0.139
1-5	80	2.0	5.35	55.56	60.91	33.48	0.128
1-6	93	2.0	5.35	65.26	70.61		0.146
2-1	12	2.4	6.37	21.52	27.89	25.65	0
2-2	12	2.4	6.37	21.52	27.89	25.65	0.091
2-3	12	2.4	6.37	21.52	27.89	23.94	0.091
2-4	15	2.4	6.37	24.96	30.43	27.08	0
2-5	48	2.4	6.37	33.91	39.41	56.72	0.059
2-6	72	2.4	6.37	52.72	59.09	90.09	0.126
2-7	84	2.4	6.37	56.95	63.82	92.91	0.145
3-1	12	2.4	6.37	21.52	27.89	26.51	0
3-2	12	2.4	6.37	21.52	27.89	24.23	0
3-3	15	2.5	6.62	24.96	30.68	28.50	0.002
3-4	30	2.48	6.57	34.93	40.60	47.31	0.019
3-5	48	2.30	6.11	43.94	49.15	61.56	0.054
3-6	72	2.40	6.57	52.72	59.09	77.52	0.105
3-7	84	2.45	6.50	56.95	63.45	83.22	0.170

$\sigma_z = \frac{a^2 p}{b^2 - a^2} + \frac{M b}{I}$ $M = \frac{W L^2}{8} = 83.2 \text{ lb in.}$ $I = 0.3078 \text{ in.}^4$
 $a = 0.805 \text{ in.}$ $b = 0.95 \text{ in.}$
^a σ_{z1} = 223.58 V_1
^b $S_{allowable} = 3S_m = 2S_u$ for Class 1, Level D = 60 ksi at room temperature.
^c S_T = elastically calculated stress intensity.
^d $E\epsilon_p$ = peak dynamic strain times elastic modulus, $E = 28.5 \times 10^6 \text{ psi}$.
^e δ_0 = midspan plastic experimental pipe deformation.

Table 4—Elastically Calculated Stresses for Specimens with 14-lb Concentrated Mass

Test No.	Drop Height (in.)	Pressure (ksi)	Design Stress (ksi)			Experimental $E\epsilon_p$ (ksi)	Deflection ^a δ (in.)
			σ_z ^c	σ_{z1} ^b	S_T ^d		
4-1 ^e	18	2.00	5.87	89.63	95.50	38.18 ^f	0.349
4-2	45	0	0.78	89.63	90.41	44.18	0.307
4-3	48	0	0.78	89.63	90.41	48.17	0.23
5-1	10	0	0.78	40.91	41.69	46.46	0.0
5-2	10	0	0.78	40.91	41.69	46.46	0.0
6-1	24	0	0.78	63.38	64.16	92.91	0.045
6-2	60	0	0.78	100.21	100.99	204.92	0.279
6-3	10	0	0.78	40.91	41.69	48.17	0.0
6-4	10	0	0.78	40.91	41.69	48.17	0.0
6-5	10	0	0.78	40.91	41.69	48.17	0.0
6-6	24	0	0.78	63.38	64.16	88.97	0.041
6-7	60	0	0.78	100.21	100.99	185.54	0.269
7-1	10	0	0.78	40.91	41.69	39.99	0.0
7-2	10	2.40	6.89	40.91	47.80	43.82	0.0
7-3	24	2.48	7.19	63.38	70.48	—	0.056
7-4	60	2.49	7.12	100.21	107.33	—	0.342
8-1	10	2.50	7.15	40.91	48.06	52.73	0.0
8-2	10	2.50	7.15	40.91	48.06	44.75	0.0
8-3	24	2.50	7.15	63.38	70.53	84.65	0.053
8-4	60	2.50	7.15	100.21	107.36	—	0.352

$\sigma_z = \frac{a^2 p}{b^2 - a^2} + \frac{M b}{I}$ $M = 251.23 \text{ lb in.}$ $I = 0.3078 \text{ in.}^4$
 $a = 0.805 \text{ in.}$ $b = 0.95 \text{ in.}$
^a σ_{z1} is obtained from STRUDL Finite Element Program.
^b $S_{allowable} = 3S_m = 2S_u$ for Class 1, Level D = 60 ksi at room temperature.
^c S_T = elastically calculated stress intensity.
^d $E\epsilon_p$ = peak dynamic strain times the average measured elastic modulus $E = 28.5 \times 10^6 \text{ psi}$.
^e δ_0 = midspan plastic experimental pipe deformation.
^f Used test specimen from Test Series 3 with reverse bend.
^g Gage F located on the tensile side of the specimen 12 in. from center.

equivalent to an initial impact velocity of 17.9 ft./sec. Strains measured on pipes with the center mass reached values over 7000 micro-in./in. which is six times the strain yield.

Test Series 8 was instrumented to observe ratcheting that might have been caused by cyclic plastic bending superposed onto the tensile static internal pressure stresses. It was expected that permanent set or plastic strains measured in compression by the top gage would be less than the tensile strains measured by the bottom gage. Actually, the opposite occurred; compression set exceeded the tensile set. Therefore, an eighth pipe specimen (Test Series 9) was tested. In this test, data was obtained to determine possible local bending from the concentrated mass. Pipe diameter measurements were taken to determine possible changes from high impact. None were observed. As shown in Fig. 10, the permanent set observed with the strain gages was similar to the permanent set measured in Test Series 8. Higher strains were also measured in compression than in tension in this test.

Elastic stress calculations are compared to Code allowable values for the uniform pipe specimens and specimens with the center weight in Tables 3 and 4, respectively. Code allowable stress values vary depending upon the Class and Service level from 1.5-3.0 S_m or $2S_y$, whichever is smaller. For 304 stainless-steel seamless pipe the Code [1] gives $S_m = 20$ ksi. The maximum Service level D limit is thus 60 ksi. Maximum experimentally measured pseudostresses ($E \times \text{strain}$) reached 107 ksi. The effect on the pressurized pipe was that a permanent set of 3/8 in. occurred with no other structural damage. Furthermore, this set can be estimated as discussed in Part III of this report.

Results listed in Table 4 clearly demonstrate that the upper limit of Code-allowable value be exceeded by a factor of over 6 (Test 5-4) without rupture or even significant plastic deformation of the pipe. In that test, the peak measured strain was 7190 micro-in./in. with a corresponding elastic pseudostress ($E \times \text{strain}$) of 204,820 psi. A centerline displacement of 0.279 in. resulted.

APPLICATION TO NAVAL SHOCK ANALYSIS

The pipe can be analyzed assuming a starting velocity equal to the velocity at impact. For a 5' drop height, the velocity at impact is

$$V = 17.9 \text{ ft./sec.} \quad (1)$$

The first mode natural frequency of the 13.9 lb. oil filled pipe with a 14 lb. center weight is approximately 42 Hz.

The effective G load is:

$$G = V^2 \pi F / g \quad (2)$$

$$G = 146.7 \text{ g's} \quad (3)$$

Thus, the calculated dynamic stress, S_d , based on a center weight of 27.9 lbs is

$$S_d = 152,400 \text{ psi}$$

This stress is clearly unacceptable by current Naval allowable stress standards for a material with a 30,000 psi yield strength. As seen in Table 4 the permanent deflection of the pipe is between 0.28" to 0.35". Deflections of this magnitude are usually insignificant in shipboard applications.

SUMMARY and CONCLUSIONS

- (1) A total of 9 straight pipe specimens in 10 test series were tested with a starting velocity shock and internal pressure.
- (2) Strains of 7190 micro-in./in. (for which $E \times \text{strain} = 204,900$ psi), and permanent deflections of up to 0.3 in. were obtained for a 1 1/2 in. Schedule 40-type 304 SS simply supported pipe 4 ft. long with internal pressure of 2500 psi. Other than the bend in the pipe, there was no adverse effects on the integrity of the pipe.
- (3) Experimental data indicate that allowable stresses based on the yield strength for dynamic impact loads can be increased significantly without affecting the integrity of the pipe.
- (4) Criteria should be based on an allowable permanent displacement of the pipe rather than a stress criteria. Also the criteria should emphasize the strength of joints and pipe hangers.

ACKNOWLEDGMENTS

The authors wish to acknowledge the support of the Pressure Vessel Research Committee of the Welding Research Council and the Nuclear Regulatory Commission for their support in this project.

REFERENCES

- [1] ASME Boiler and Pressure Vessel Code, Sec. III, Div. 1
Nuclear Power Plant Components Design, ASME, New York, 1986

- [2] S. E. Moore and E. C. Rodabauch, "Background for Changes on the 1981 Edition of the ASME Nuclear Power Plant Components Code for Controlling Primary Loads in Piping Systems," ASME, Jr Pressure Vessel Technology, Vol. 107, Nov. 1982, pp. 351-361.
- [3] United States Nuclear Regulatory Commission, Piping Review Committee, "Summary and Evaluation of Historical Strong Motion Earthquake Seismic Response and Damage to Above Ground Industrial Piping," NUREG-1061, Vol. 2, Addendum, Apr. 1985.
- [4] Scavuzzo, R. J. and P. C. Lam, "Investigations of Design Criteria for Dynamic Loads on Nuclear Power Piping," WRC Bulletin 324, June 1987.
- [5] Lam, P. C. and Scavuzzo, R. J., "Test-to-Analysis Correlations with Relevance to Dynamic Stress Criteria," "ASME Pressure Vessel and Piping Div., PVP Vol. 98-6, June 1985.
- [6] Scavuzzo, R. J., Lam, P. C., and Scavuzzo, S. A., "Damping of Pipes-Plastic Regime," ASME Vessel and Piping Div., PVP Vol. 98-6, June 1985.
- [7] Scavuzzo, R. J. and Lam, P. C., "Allowable Stress Criteria for Dynamic Loads," "ASME Pressure Vessel and Piping Div., PVP Vol. 98-6, June 1985.

DYNAMIC ANALYSIS

BUBBLE JET CALCULATIONS USING THE DYSMAS/E FINITE DIFFERENCE CODE

Stephen A. Wilkerson
Naval Surface Weapons Center
10901 New Hampshire Ave.
Silver Spring, MD 20903-5000

and

Dr. Hans Schittke
Industrietalagen-Betriebsgesellschaft
Abteilung Finite Berechnungsverfahren
8012 Ottobrunn bei München
Federal Republic of Germany

A method of calculating underwater bubble collapse using the DYSMAS/E code is presented. The effects on bubble growth and collapse of a nearby rigid boundary and the free surface are included in the analysis. The solution methodology is described and the advantages and disadvantages of compressible flow theory are compared to incompressible flow theory. The approach is shown to give reasonable results in comparison to observed explosion bubble behavior. The paper also contains a preliminary look at the formation of a bubble jet .

BACKGROUND

The formulation of the DYSMAS/E code was based on an existing one dimensional finite difference code. The code employs the basic conservation of momentum, mass and energy laws. The original one dimensional model was extended to include one and two dimensional cylindrical coordinate systems and one, two and three dimensional cartesian coordinate systems. The present DYSMAS/E finite difference code is still undergoing development. The code makes use of state-of-the-art discretization, material models, equation of state formulations and failure criteria. The present version of DYSMAS/E utilizes the FLIC (FLuid In Cell) finite difference method of Gentry Martin and Daly¹. The method is second order with exception of the convective phase. In this phase a donor cell upwind differencing method is used. Other methods are also under development.

The material model uses an elastic-plastic strength formulation with a linear-elastic constitutive relation for isotropic materials and a Von Mises yield criterion which takes into account the effects of strain, strain-rate, temperature and pressure effects. Further,

the code includes several burn models including constant velocity burn, the C-J volume burn, burn to detonation and forest fire burn²⁻⁴. The code contains specific models for water, including cavitation affects; air, accounting for high energy dissociation and ionization; compacting soils, as well as an extensive list of high explosives. Among the equation of state models is the Jones Wilkins Lee (JWL) equation of state for explosives. In all the code has an internal data bank of about 60 materials.

The failure criteria that can be used in DYSMAS/E provide for failure due to exceeding the maximum allowable distention of a material, the maximum effective stress, the maximum effective strain, or the hydrodynamic pressure. These criteria account for strain rate, temperature and load state. After failure, the code simulates failure propagation in a material cell by introducing a small failed region which can grow according to an assumed load-dependent rate law. In this model a fully failed material will support no tensile load. However, recompression of a failed material is possible.

PROBLEM DEFINITION

The purpose of this study was to explore the applicability of the DYSMAS/E code to the analysis of the underwater explosion bubble collapse. In particular, DYSMAS/E's ability to predict the formation of a bubble jet, toward a rigid boundary during the bubble's collapse phase, was of primary importance. The problem chosen for analysis was that of a small explosive charge (1.4 grams of TNT) situated between a free surface and a rigid flat plate such that the bubble should collapse onto the rigid flat plate during its collapse phase. The location of the charge was approximately 3/4 of the expected maximum radius from the plate. At this location, a bubble jet was expected to form and impact on the rigid boundary near the end of the first bubble period. Figure 1 shows the geometry being studied. Selection of this configuration permits the problem to be easily duplicated experimentally.

The DYSMAS/E code offers a variety of detonation models including a fully exploded model, a C-J Constant Volume burn model, the burn to detonation model by Mader, initiation and growth model by Lee and Tarver and the forest fire model by Mader. In the interest of simplicity a fully exploded model was chosen for the TNT explosive. In this model the original volume of TNT converted to a high pressure, high temperature gas, thus providing the initial conditions for the dynamic expansion and contraction of the explosion products. The problem under consideration is axisymmetric and a cylindrical coordinate system is used.

In order to take full advantage of DYSMAS/E rezoning features an initial grid of 40 by 40 cells was used. Since the change in each cell must be calculated during a cycle, and the shock wave can only propagate one cell per cycle, it would be inefficient to include a large grid initially. Therefore, use of a small grid reduces the computation time required for each cycle and the rezoning feature can be used when required to expand the grid for the outward propagation

of the explosion's shock wave. DYSMAS/E rezoning can be performed using an integer factor. For example, a factor of 2 along a coordinate axis would combine the information of two cells into one along that axis. Figure 2 shows the initial 40 by 40 grid and the location of the TNT cells within the grid. It was initially important to choose a sufficient number of cells being occupied by the TNT gaseous products and a sufficient number of fluid cells. Having sufficient cells occupied by the TNT gaseous products allows the detailed examination of the bubble jetting phenomena. An insufficient number of TNT gas cells would obscure the resolution, details, and accuracy of the compilation. Furthermore, the initial grid size and proportions become important when a rezoning is performed. This rezoning must be done in a way that preserves the initial grid's ratio of fluid cells to TNT gas cells. If this is not done correctly, the total number of cells will grow, thus increasing the computational time or the loss of TNT cells will result in a degradation of computational accuracy. Furthermore, the best way to estimate proper proportions appears to come with experience. In order to gain experience several grid configurations in a one dimensional system as well as several configurations in a two dimensional system were experimented with before choosing the final grid given in Figure 2. The importance of consistent rezoning procedures is due to the code's time dependence on shock wave speed. As the initial shock wave propagates outward, roughly at the speed of sound in water, the explosive gases continue to expand outward dropping the internal pressure of the TNT's gas products. This drop in gas pressure results in a decreasing outward momentum which is clearly time dependent. When the shock wave reaches the outer fluid cells the analysis must be stopped and a rezoning must be performed before the analysis can continue. If at that time the bubble's gases have not expanded sufficiently, the total ratio of TNT to fluid cells will not be preserved after rezoning. This in turn will become a worsening problem with each additional rezone and a real problem throughout the analysis.

After the initial choice of grid sizes the problem was rezoned 4 additional times. The final grid was utilized until the bubble jet formed and impacted on the rigid boundary. One additional rezoning would have increased the accuracy near the end of the collapse phase of the bubble period. However, the results obtained up to that point were sufficient for the purpose of this analysis and no final rezoning was performed. The rezoning procedures in DYSMAS/E were very efficient, and the total rezoning process became so routine that a 5 to 10 minute operator time delay per rezone was all that was required before continuing the analysis. A plot showing the rezoning process and the amount of time in terms of computation cycles is shown in Figure 3. The first and second choice of grids resulted in a larger number of cells being needed in the 3rd and 4th rezoning. However, after the 4th rezoning the bubble was sufficient in size so that the final rezoning was the last required. The final configuration consisted of a 60 by 65 grid with gradually expanding cells along the x and y axes. The final grid extended several meters high and 10 meters out. A large grid limits the influence of a reflected shock wave from a boundary which reduces surrounding

boundary constraints and allows the influence of the flat plate on bubble collapse to be studied accurately.

RESULTS

The results showed that the interaction of the bubble with the flat plate and the bubble's proximity to the free surface extended the bubbles period slightly, which was expected. When compared with empirical rules, the DYSMAS/E's predicted bubble period was 10 to 15 percent longer than an equivalent free field detonation which seemed reasonable. A number of plots were made throughout the analysis, showing the behavior of the bubble and surrounding fluid. Several notable plots are shown here which duplicate expected bubble behavior during its growth and collapse in the proximity of a rigid boundary and near a free surface. Initially the gaseous products from the explosive detonation become nearly spherical. The initial tin can shaped charge used in this analysis became nearly spherical after only 15 cycles, 1.024×10^{-06} seconds, into the analysis. A velocity plot showing the outward movement of gaseous products and the beginning of the formation, of the now nearly spherical shock wave, is shown in Figure 4. In Figure 5 the outer circle, highlighted by the velocity vectors, is the shock wave in the fluid and the darker inner circle shows the expanding bubble gases. As indicated, this velocity distribution is representative of expected shockwave formation and early time bubble growth and is very early in the analysis (5.315×10^{-06} seconds). One additional velocity distribution is given in Figure 6. Figure 6 shows the rebounding shockwave from the rigid boundary which is seen propagating outward behind the initial shock wave. The dark inner velocity vectors show the near spherical expansion of the bubble's explosive gases.

In order to show the phenomena of bubble jetting as well as the magnitude of the bubble jet strength, several momentum distribution plots are presented. These plots indicate the magnitude of each cell's momentum relative to the other cells. In-other-words, higher momentum cells will be highlighted by larger vectors which can be seen as darkened areas on the plots. These larger momentum vectors become of interest in estimating the magnitude of the force being exerted on the rigid boundary by the bubble jet. Additionally, the bubble's boundary can be estimated by recalling that momentum is the product of mass and velocity for each cell. Since the TNT gaseous products are of a very low density, and the plot is scaled in accordance with the highest momentum, areas occupied by the TNT gas bubble are shown with little or no momentum. These areas are surrounded by high momentum fluid vectors and can be identified on the figures. Figure 7 shows a momentum distribution near maximum bubble expansion. The outward bubble expansion is highlighted by a dark ring of momentum vectors. Further, the interaction with the free surface can also be seen by the mish-mash of momentum vectors extending from the upper portion of the bubbles surface to the free surface of the water. Figure 8 shows the initial contraction of the bubble and the beginning of the formation of a bubble jet near the top of the bubble surface. Finally, Figure 9 shows definite formation of a bubble jet and Figure 10 shows the jet impacting on

the rigid boundary. The results show conclusively that a bubble jet will form and impact on the rigid boundary under the initial conditions imposed by this study. Further, the results indicate that the momentum in the area of the bubble's jet could be significant in deforming a non-rigid boundary.

CONCLUSION

The DYSMAS/E code represents a major contribution to the field of computational fluid dynamics and offers the opportunity to study complex physical phenomenon in detail. The code is easy to use, well written and offers an abundance of features. In particular the present study offers only limited results. However, the results presented indicate that the code is easily adapted for specific underwater applications. In particular, the code is well suited for the study of shock wave propagation as well as the study of underwater explosion bubble collapse.

The DYSMAS/E code offers a number of advantages over an incompressible irrotational flow theory approach in analyzing an underwater explosion bubble collapse. The code methodology avoids the problems that occur in incompressible theory when the bubble jet penetrates the opposite surface of the bubble. Additionally, the effects of the energy loss after the bubble minimum are also partially accounted for in DYSMAS/E. DYSMAS/E will also allow the consideration of a deformable boundary. Incompressible theory currently does not address these complex phenomena which occur near the bubble minimum. The one negative aspect of DYSMAS/E is that the code is very computationally intensive and requires a large amount of computer time. In conclusion, DYSMAS/E offers the opportunity to study particular cases of bubble jet collapse in detail, but is not well suited for parametric studies on bubble collapse. Such studies are better suited for incompressible flow theory, where multiple parameters can be studied, prior to bubble jet penetration, in a fraction of the computational time required by DYSMAS/E.

ACKNOWLEDGMENT

This work was sponsored by the Undersea Warheads and Fuzes Block Program at the Naval Surface Warfare Center (NSWC) White Oak and the German Federal Ministry of Defense in Bonn. The study represents a cooperative one month effort which was conducted at the Industrietalagen-Betriebsgesellschaft (IABG) Company in Munich. The IABG cooperation was established jointly in 1961 by the Federal Ministry of Defense and the German Aerospace Industry to provide technical support, in test and evaluation, for the Federal Republic of Germany. The purpose of this study was the investigation of underwater explosion bubble collapse with the German developed code DYSMAS/E. The preliminary results from this study show that the DYSMAS/E code represents a significant advancement in analytical approaches to underwater explosion research. The authors gratefully acknowledge the help and support of Mr. Pfrang of IABG and Mr. Farley of NSWC who's continued support made this study possible.

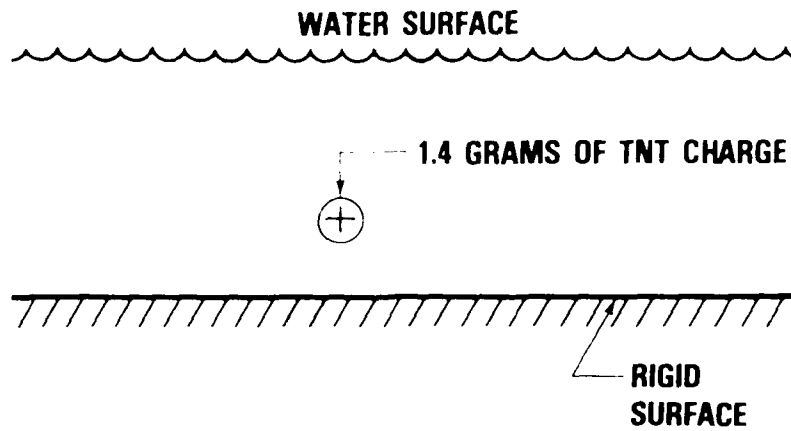


Figure 1. Shot Geometry

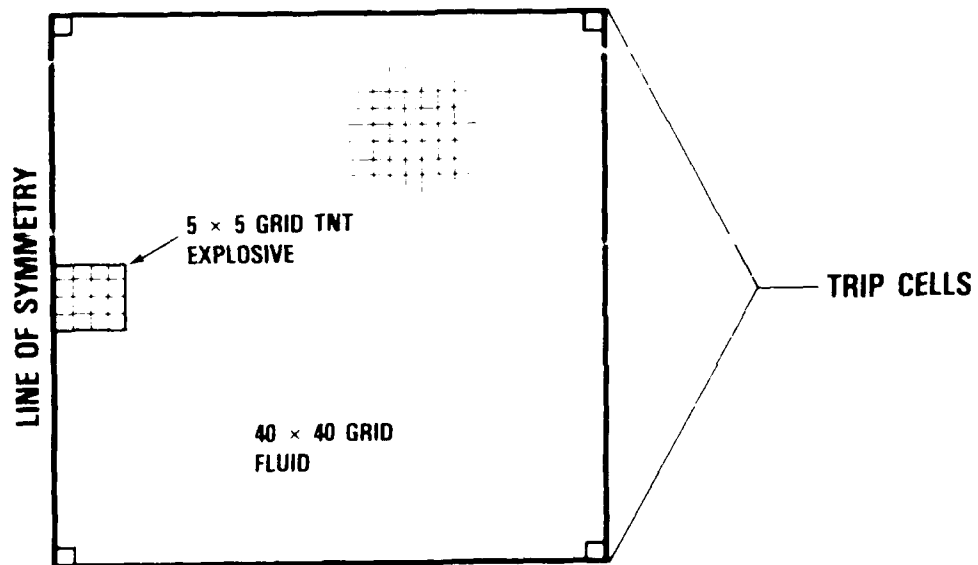


Figure 2. Initial Conditions

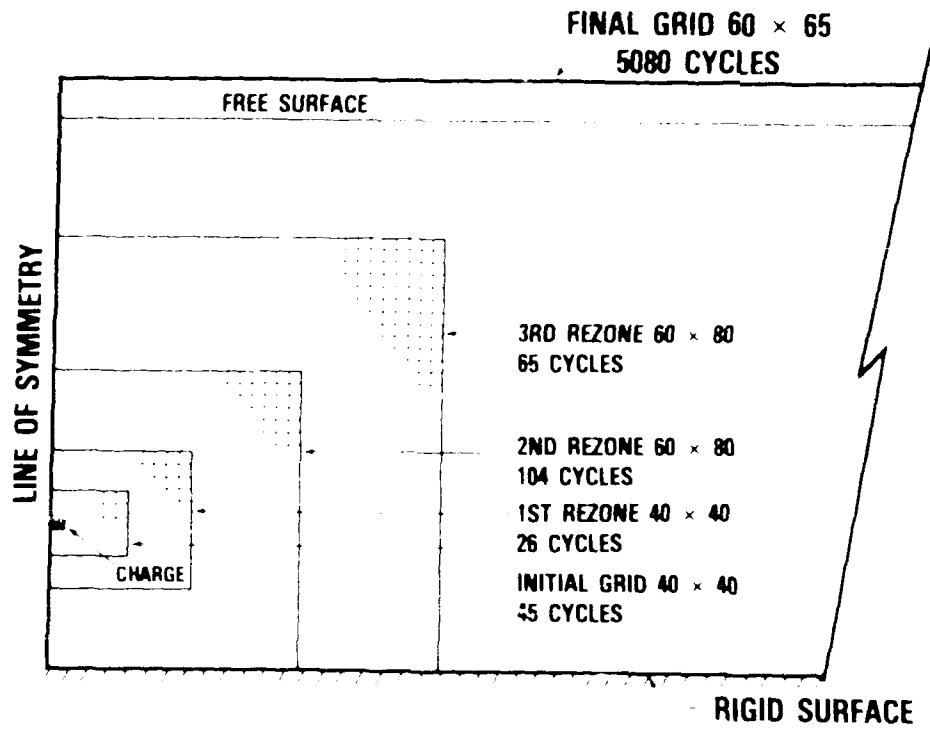


Figure 3. Rezoning Plan

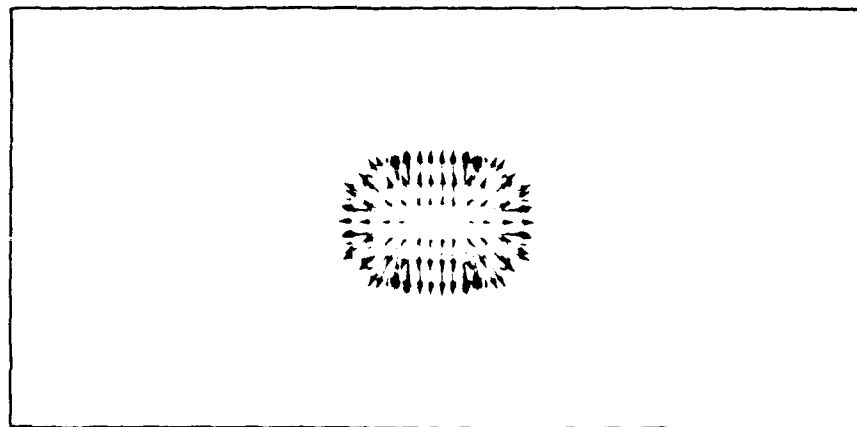


Figure 4. Velocity Distribution
(CYCLE 15 1.024×10^{-6} SEC)

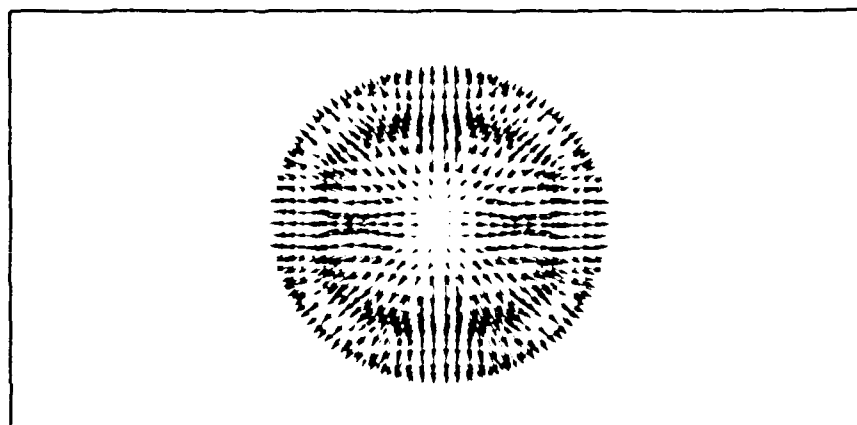


Figure 5. Velocity Distribution

(CYCLE 45 5.315×10^{-6} SEC)

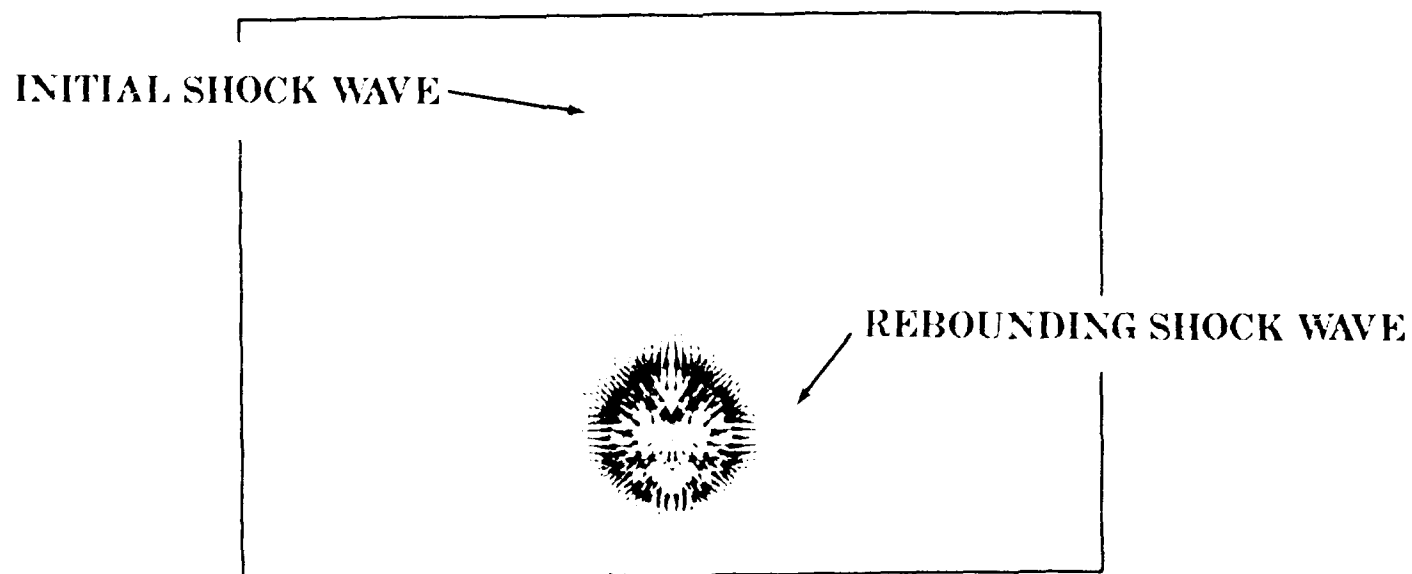


Figure 6. Velocity Distribution

(2ND REZONE CYCLE 104 1.657×10^{-4} SEC)

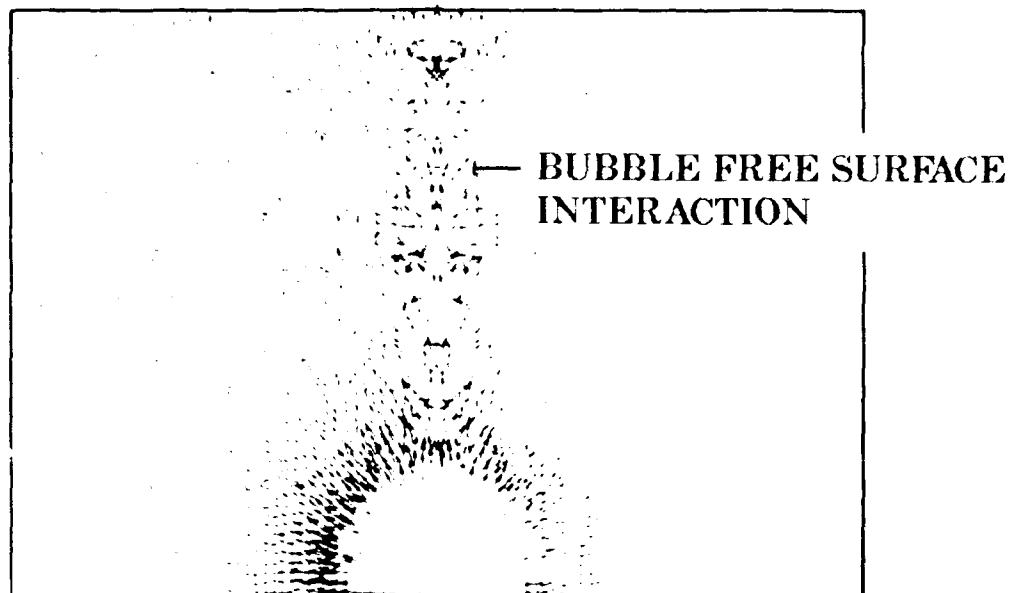


Figure 7. Momentum Distribution
 (FINAL GRID CYCLE 1400 1.008×10^{-2} SEC)

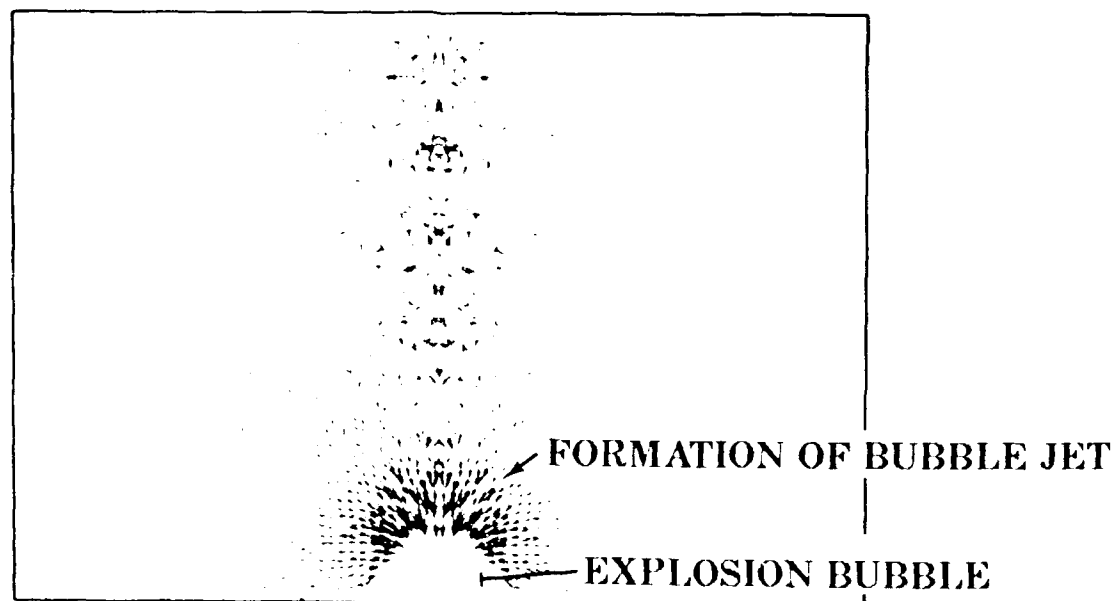


Figure 8. Momentum Distribution
 (FINAL GRID CYCLE 3800 2.685×10^{-2} SEC)

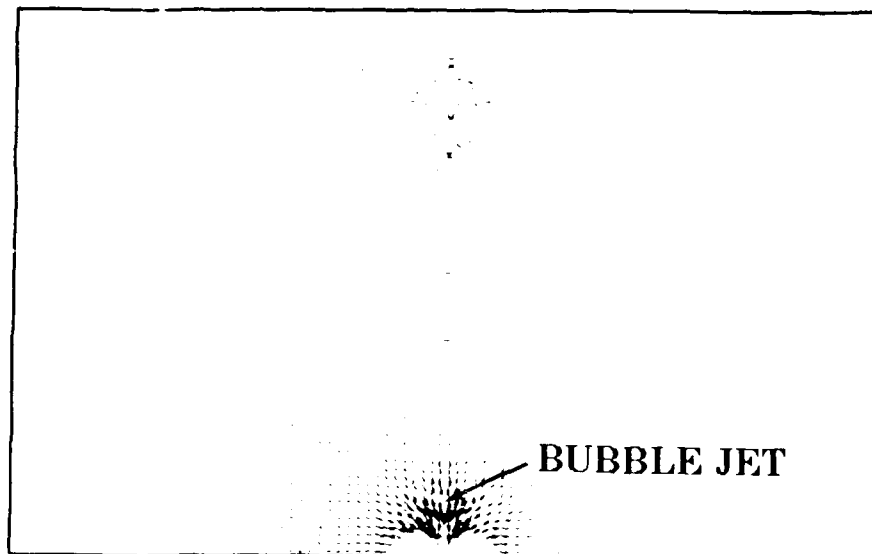


Figure 9. Momentum Distribution
(FINAL GRID CYCLE 4840 3.408×10^{-2} SEC)

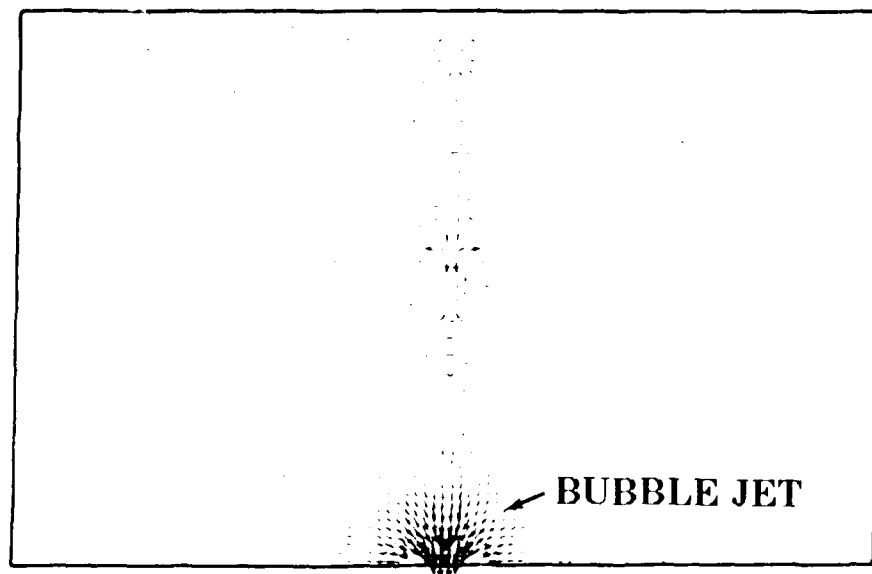


Figure 10. Momentum Distribution
(FINAL GRID CYCLE 5080 3.573×10^{-2} SEC)

REFERENCES

1. Gentry, R. A., Martin, R. E., and Daly, B. J. "An Eulerian Differencing Method for Unsteady Compressible Flow Problems", J. Comp. Phys. Vol. 1, pp. 87-118, 1966.
2. Mader, C. L. "Numerical Modeling of Detonations", U. of California Press, Berkeley, CA, 1979.
3. Lee, E. L., and Tarver, C. M. "Phenomenological Model of Shock Initiation in Heterogeneous Explosives", Phys. Fluids, Vol. 23, No. 12, pp. 2362-2372, Dec. 1980.
4. Forest, C. A. "Burning and Detonation", Los Alamos Scientific Laboratory UC-45, La-7245, July 1978.

CONVERGENCE OF FINITE ELEMENT FREQUENCY ANALYSIS FOR A THIN WALLED CYLINDER

Joseph M. Santiago and Henry L. Wisniewski
US Army Ballistic Research Laboratory
Aberdeen Proving Ground, MD 21005-5066

The natural frequencies of a thin walled cylindrical shell are computed using the ADINA finite element computer program and compared with the frequencies from a Rayleigh-Ritz solution of the Kirchhoff shell equations. The rate of convergence of the finite element solution is investigated by using three progressively refined mesh discretizations. Models based on the 16-node quadrilateral curved shell element and the 3-node triangular plate element are generated for each mesh. The subspace iteration solution method is employed to solve for the first 100 frequencies and results are used to estimate rates of convergence and limit frequencies. Comparison of the solutions calculated by the three finite element meshes reveals that frequencies converge predominantly from above and that the quadrilateral element converges faster than the triangular element. Convergence correlates with the mode shape rather than the frequency, with modes having few oscillations being closest to convergence. Comparison with the Rayleigh-Ritz solutions reveals that while the finite element frequencies are markedly closer to converging for less complex mode shapes, as the oscillations in the modes increase, the frequencies predicted by the Rayleigh-Ritz analysis become superior.

INTRODUCTION

This paper investigates how the accuracy of finite element calculations for the natural frequencies of a thin walled cylindrical shell is effected by the type and number of elements employed. Such analyses are often useful as a preliminary means of selecting an appropriate finite element model for subsequent transient response computations. In fact, the present investigation is an outgrowth of such a study [1]. The commercially available ADINA computer program [2] is used for this study. Convergence of the finite element solution is investigated by using three progressively refined mesh discretizations, comprising 325, 703, and 1225 nodes. Finite element models based on the 16-node quadrilateral curved shell element and the 3-node triangular plate element are developed for each of the three meshes. The subspace iteration solution method [3; pages 672-695] resident in the ADINA program is used to calculate the first 100 frequencies for each mesh and element combination. For each element type, the frequencies predicted by the three mesh models are used to estimate the

rate of convergence and a limit frequency for each mode by assuming a power convergence formula. An independent Rayleigh-Ritz analysis of the Kirchhoff shell equations for the cylinder is used to calculate the frequencies corresponding to the modes computed by the finite element analysis. As an estimate of the error in the finite element solutions, the computed frequencies and the limit frequencies for each element type are compared using the Rayleigh-Ritz frequencies as a basis.

BACKGROUND

It is commonly accepted that the accuracy with which a finite element analysis reproduces the transient response of a structure, in particular when the response is predominantly elastic, is a function of how well the frequency spectrum of the structure is modeled. This is because the accuracy of the transient solution is limited by the frequency spectrum associated with the finite element discretization irrespective of the time integration scheme used to solve the equations of motion, see Bathe [3; pages 499-547]. For this reason, a frequency analysis can prove useful as a preliminary step in selecting an appropriate finite element model for subsequent dynamic analyses.

However, it is well known that the frequency spectrum of a finite element model does not duplicate exactly the frequency spectrum of the corresponding continuous body. First, the spectrum of the continuous body is infinite, while that of the finite element model is finite and equal to the number of degrees-of-freedom. Second, the process of discretization, in particular, the choice of mass matrix, distorts the frequency spectrum relative to the associated modes. A consistent mass formulation will overpredict frequencies, while a lumped mass formulation may underpredict frequencies [4]. Moreover, the accuracy of a finite element frequency analysis depends on how closely the finite element shape functions approximate mode shapes. This means that accuracy will diminish as modes become more oscillatory. Since highly oscillatory modes are often associated with the higher frequencies, this means that the high frequency end of the spectrum will be poorly calculated by the finite element model. That is, these high frequencies will be more a reflection of the discrete modeling, sensitive to the total number of nodes and the type of elements used, but having little resemblance to the actual structure's spectrum. If, however, as most often happens, the loading on the structure is fairly smooth in time and space, the response will be governed by the lower frequencies, since the higher frequencies will be only slightly excited and will hardly contribute to the total response. Moreover, for sufficiently severe loading, plastic deformation will tend to dampen the higher frequencies so that the lower ones predominate after a short while. That is why a finite element analysis will often predict the transient response of a structure quite accurately when only the lower frequency modes are modeled adequately. However, some care is required in choosing appropriate elements and in using a sufficient number of nodes.

To some extent, these observations reflect the conclusions reached in our first investigation into the problem [1]. There, the ADINA program was used to reproduce the transient deformations measured on a cylindrical shell subjected to an enveloping blast wave in a shock tube experiment [5]. A preliminary frequency analysis was used to select an appropriate discretization and element type, and compared with a counterpart Rayleigh-Ritz analysis. This comparison revealed some of the features described above, in particular, that the Rayleigh-Ritz predictions became noticeably superior to the finite element predictions as the mode shapes became more oscillatory, although at that time we did not fully understand the reason for this. Moreover, at the time it was mistakenly found that the frequencies predicted by the triangular plate element model were closer to converging

than those predicted by the quadrilateral element model. This was contrary to our expectations because the cubic shape function of the quadrilateral element seemed better suited to modeling the oscillatory pattern of the modes than the linear shape function of the triangular plate element. The increased computational power resulting from the replacement of the Cyber 7600 computer by the Cray XM-P/48 computer at the Ballistic Research Laboratory in late 1986, provided the opportunity to reinvestigate this problem and answer some of the questions raised by the earlier study.

CYLINDER SPECIFICATIONS

The cylinder analyzed in this paper, as in our first study [1], is taken from an experimental investigation [5] and has the following dimensions:

L	= length between clamped ends	= 0.8 m (31.5 in.)
D	= inside diameter	= 0.3048 m (12.0 in.)
h	= wall thickness	= 1.016 mm (0.04 in.)

These give a D/h ratio of 300, well within thin shell theory. The mechanical properties of the

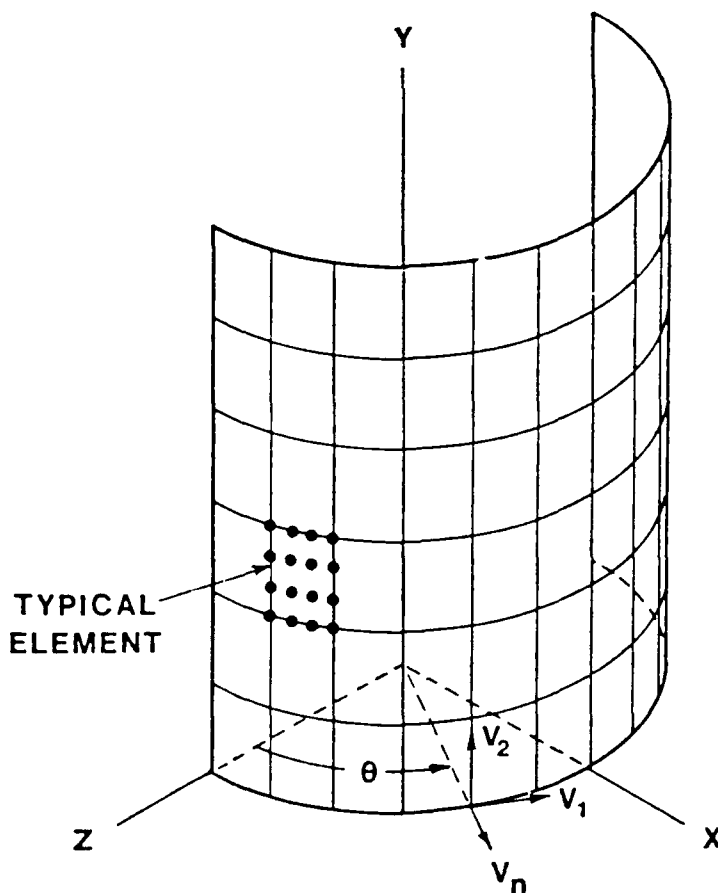


Figure 1: The 18x36 mesh model of the quarter cylinder using 703 nodes and 72 16-node shell elements.

cylinder are taken as the nominal values for 6061-T6 aluminum sheet:

$$\begin{aligned} E &= \text{Young's modulus} = 64.73 \text{ GPa (9388 ksi)} \\ \nu &= \text{Poisson's ratio} = 0.3285 \\ \rho &= \text{mass density} = 2700 \text{ kg/m}^3 (5.24 \text{ slug/ft}^3) \end{aligned}$$

The cylinder is assumed clamped at both ends, so that these edges neither translate nor rotate. Moreover, only modes of vibration symmetric with respect to the mid-plane between the two ends are investigated.

FINITE ELEMENT MODELS

Since only modes of vibration symmetric with respect to the mid-plane are of interest, the problem employs two planes of symmetry (one through the axis and the other perpendicular to the axis midway between the fixed ends) to reduce the computational model to one quarter of the cylinder. This is depicted in Figure 1, where symmetry boundary conditions are imposed on the edges in the y - z and z - x coordinate planes and clamped boundary conditions are applied to the top edge only. The figure depicts the finite element model of the quarter cylinder employing 72 16-node quadrilateral shell elements, which was also the model used in the previous study. It also shows the local shell coordinates (V_1 and V_2 tangential and V_n normal) used by quadrilateral elements to specify the rotational degrees-of-freedom (DOF). The boundary conditions are set by limiting the displacement and rotational DOF at boundary nodes as follows: at the symmetry boundaries only displacements in the plane of symmetry and rotations about the normal to the plane are allowed, while on the clamped edge no displacements or rotations are permitted at all.

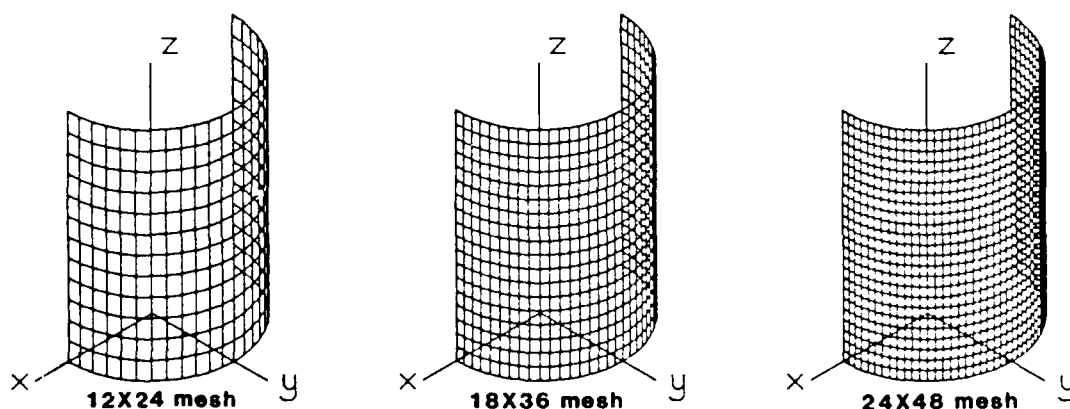


Figure 2: Mesh models for quarter cylinder.

To study the rate of numerical convergence, the present study employs three different mesh discretizations involving 325, 703, and 1225 nodes, as shown in Figure 2, where mesh intersections indicate node locations. Notice, this figure differs from the previous one which shows the element mesh rather than the node mesh. The meshes maintain the same aspect ratio as they are refined and can be characterized by the number of increments in the longitudinal and circumferential directions as follows: 12×24 , 18×36 , and 24×48 . Hence, the meshes subtend angles of 7.5 degrees, 5.0 degrees,

and 3.75 degrees, respectively, in the circumferential direction. These mesh models are used as grids to generate finite element models based on the 16-node quadrilateral shell element and the 3-node triangular plate element.

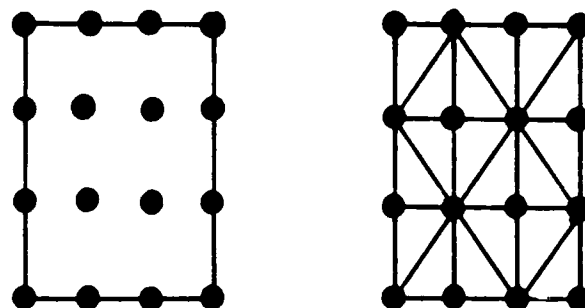


Figure 3: Equivalence of a single 16-node shell element to 18 triangular plate elements.

Applying the ADINA quadrilateral curved shell element with 16 mid-surface nodes to these three meshes results in models consisting of 32, 72, and 128 elements; the 72 element model is shown in Figure 1. The quadrilateral element [6] is based on Mindlin plate theory and has 2 rotational DOF (rotations about the shell normal are undefined) in addition to the usual 3 displacement DOF. Taking into account the constraints imposed by the boundary conditions, the resulting finite element models are found to have 1402, 3184, and 5686 DOF. Application of the ADINA triangular plate element [7] with 3 mid-surface nodes to the three meshes results in models with 576, 1296, and 2304 elements. Notice that the triangular element model uses many more elements than the corresponding quadrilateral element model, because 18 triangular elements are required to replace a single quadrilateral element, as shown in Figure 3. This figure also shows how the triangular elements are arranged in an alternating geometric pattern so as not to introduce directional bias. Unlike the quadrilateral element, the triangular element has a full 6 DOF per node, the additional rotational DOF being required to accommodate the difference in element normals at common nodes. Moreover, the rotational DOF are with respect to the global, rather than local shell coordinate axes. Hence, the finite element models based on this element require 1655, 3779, and 6767 DOF, approximately 20% more than the corresponding quadrilateral element models. The pertinent parameters for these finite element models are summarized in the following table.

Table 1: Specification of finite element models.

Element Type	Mesh	Circumferential Mesh Spacing	Number of Nodes	Number of Elements	DOF
16-Node Quadrilateral	12×24	7.5 degrees	325	32	1402
	18×36	5.0 degrees	703	72	3184
	24×48	3.75 degrees	1225	128	5686
3-Node Triangular	12×24	7.5 degrees	325	576	1655
	18×36	5.0 degrees	703	1296	3779
	24×48	3.75 degrees	1225	2304	6767

Rather than describing the finite element analysis next, we present a brief description of the

Rayleigh-Ritz method and results obtained thereby in order to give insight into interpreting the subsequent finite element results.

RAYLEIGH-RITZ ANALYSIS

As an independent check on how closely the finite element calculations simulate the cylinder frequencies, an approximate solution for the frequencies of the cylinder based on a Rayleigh-Ritz analysis of the Kirchhoff shell equations has been developed. Typically, the analysis employs a set of approximate displacement functions satisfying the essential boundary conditions and determines the associated displacement coefficients by requiring that the equations of equilibrium be satisfied in a Galerkin or integral sense. By way of illustration, the method of analysis is applied in Appendix A to the somewhat simpler Donnell equations for a cylindrical shell. This is taken from Kraus's textbook on elastic shells, but with corrections, since the the final results presented there are in error.

Based on a Rayleigh-Ritz analysis of the more general Kirchhoff shell equations, a small program has been written to compute the frequencies of the cylinder. As explained in detail in Appendix A, to calculate cylinder frequencies by this method, the oscillations in a mode must first be specified in terms of the number of longitudinal *half* waves, m , and the number of circumferential *full* waves, n ; the program then computes the corresponding frequency. Figures 5-9 illustrates the definitions of m and n by examples. It turns out that the frequency spectrum of the cylinder is best examined in terms of these numbers.

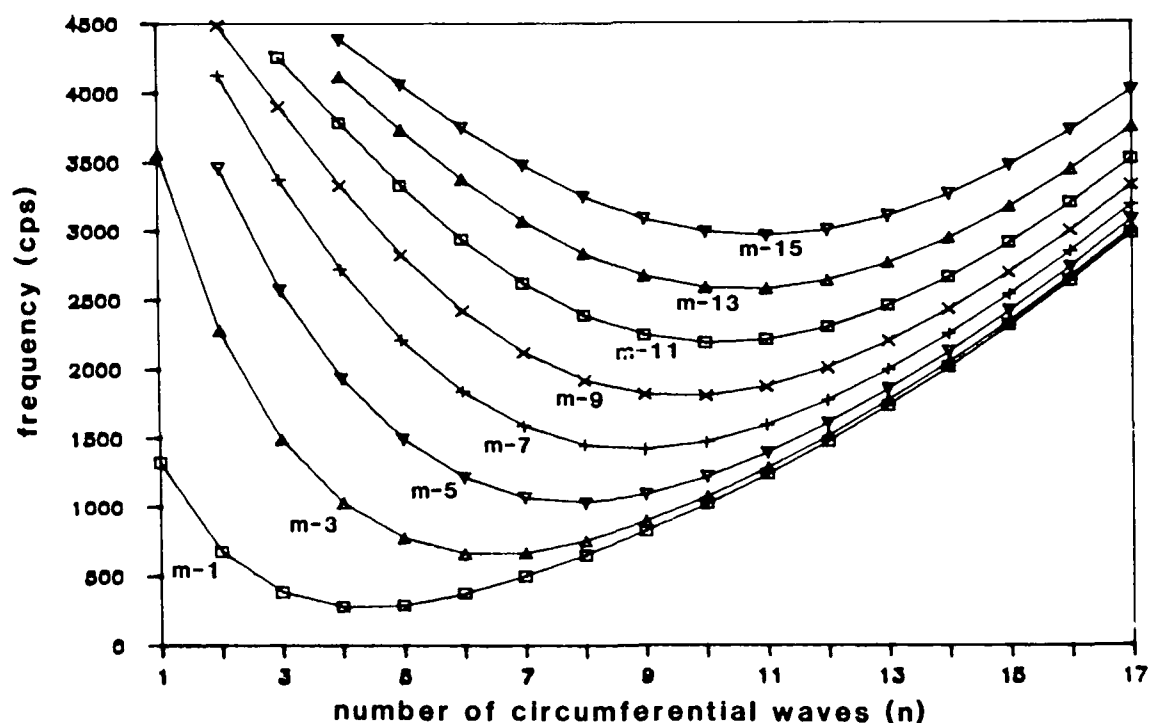


Figure 4. Frequencies of clamped end cylinder as computed by the Rayleigh-Ritz method.

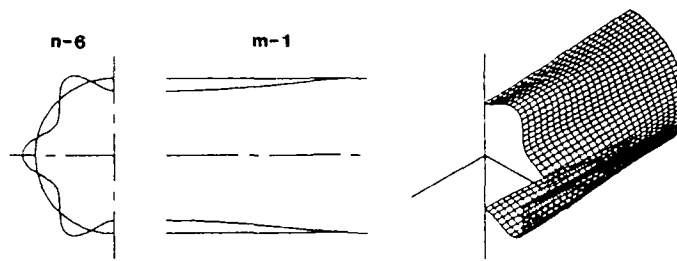
In Figure 4 the frequencies obtained by the program for the cylinder under consideration are plotted against the number of circumferential waves for ascending numbers of longitudinal half waves. This method of representation clearly illustrates the anomalous character of the frequency spectrum of the cylinder, which is unlike that of simpler structures, such as beams and plates, where the natural frequency increases with the complexity of the corresponding mode shape. Here we notice that while the frequencies of the cylinder increase monotonically with the number of longitudinal half waves, m , the trend with respect to the number of circumferential waves, n , is unusual in that at first the frequencies show an unexpected decrease to a minimum followed by the more usual monotonic increase. For this reason, frequencies higher than the minimum occur not only for higher values of n , but also lower values. This behavior is explained by Arnold and Warburton [9] as due to a balance in the strain energy stored in membrane deformation (decreasing with higher n) and the flexural deformation (increasing with higher n) causing the lowest frequency to occur at an intermediate value of n where the total energy is a minimum. Finally, it should be emphasized that because the Rayleigh-Ritz method uses approximate displacement functions satisfying the equilibrium in an integral sense only, the frequencies calculated by this method can be expected to overpredict the true natural frequencies of the cylinder.

FINITE ELEMENT FREQUENCY ANALYSIS

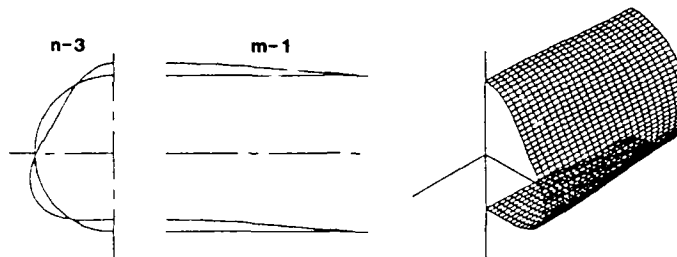
Using the ADINA eigen-frequency analysis option, the first 100 frequencies and associated mode shapes are calculated for each of the six finite element models previously described. The calculations employ the subspace iteration method of solution exclusively [3; pages 672-695], since our previous investigation [1] established that this method gives essentially the same answers as determinant search method (also available in ADINA), but with relatively less computational effort as the DOF of the models increase. A consistent mass formulation is employed throughout, so that the analysis overpredicts the true cylinder frequencies [10; page 226].

The ADINA program calculates frequencies in ascending order starting with the fundamental. Figures 5-9, showing the first 20 frequencies and associated mode shapes obtained with the most refined mesh (24×48) using the quadrilateral element, typifies the results obtained from the ADINA computations. Notice that the number of circumferential waves does not necessarily increase with the frequency; for example, for modes with one longitudinal half wave, the number of circumferential waves in mode 3 is less than that in mode 2, the number in mode 6 is less than that in mode 5, and so on. This is to be expected in light of the Rayleigh-Ritz analysis, Figure 4, since for each family of longitudinal half waves, there are higher frequencies to the left as well as to the right of the minimum frequency. The times required by the finite element models to calculate the first 100 frequencies on the Cray X-MP/48 computer are in the order of 2-3 minutes for the 12×24 mesh, 6-7 minutes for the 18×36 mesh, and 13-15 minutes for the 24×48 . In general, the solution times, in addition to reflecting the DOF of the models, are influenced by the values of the parameters used in the subspace iteration method and the available computer storage, but are not affected much by the type of element employed.

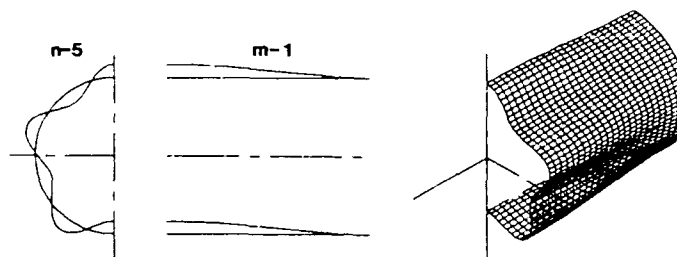
The results of the finite element frequency calculations, as well as the those for the Rayleigh-Ritz analysis, are arranged in order of ascending wave numbers in Appendix B for the quadrilateral element models and in Appendix C for the triangular element models. Since the finite element analysis calculates frequencies in ascending order, to generate these tables it is necessary to assign



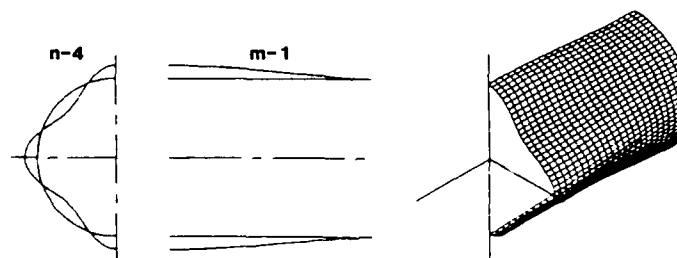
Mode Shape 4 Frequency 378 cps



Mode Shape 3 Frequency 368 cps

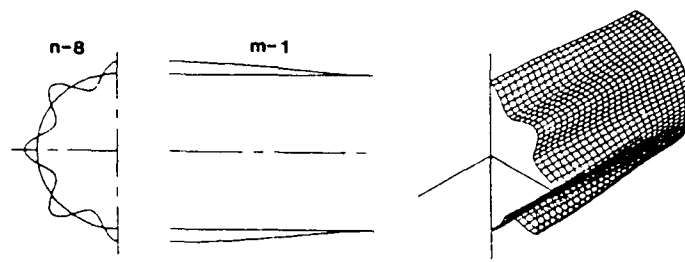


Mode Shape 2 Frequency 290 cps

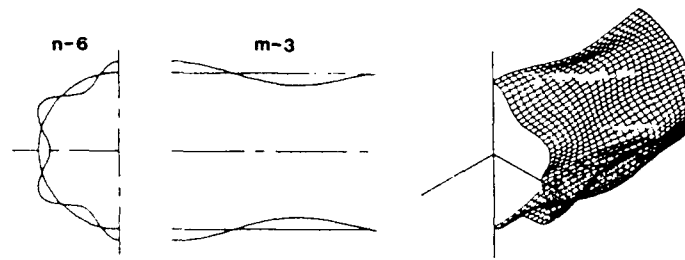


Mode Shape 1 Frequency 272 cps

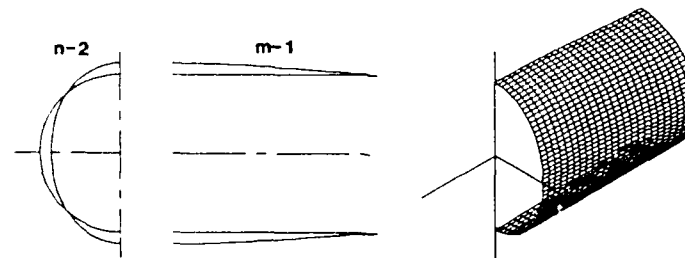
Figure 5: Frequencies and mode shapes for the 24x48 mesh 16-node quadrilateral element model: modes 1-4.



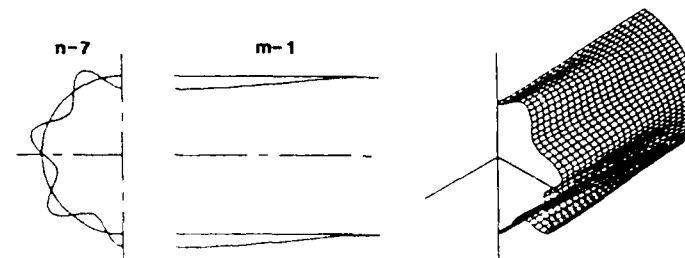
Mode Shape 8 Frequency 656 cps



Mode Shape 7 Frequency 648 cps

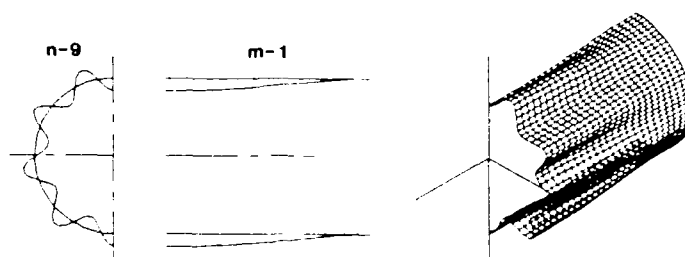


Mode Shape 6 Frequency 632 cps

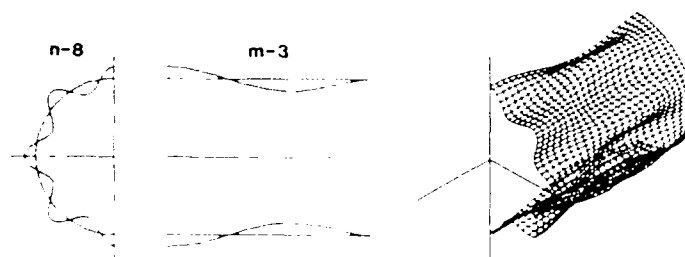


Mode Shape 5 Frequency 504 cps

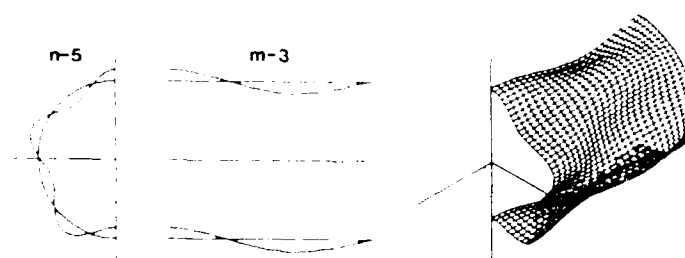
Figure 6: Frequencies and mode shapes for the 24x48 mesh 16-node quadrilateral element model: modes 5-8.



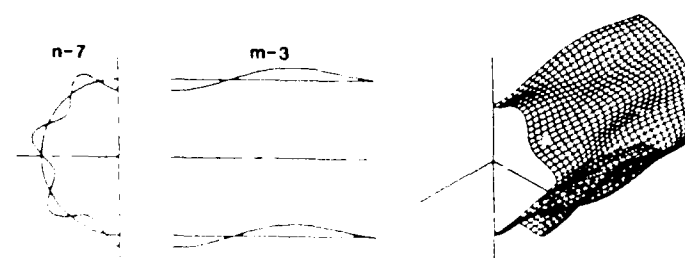
Mode Shape 12 Frequency 831 cps



Mode Shape 11 Frequency 753 cps

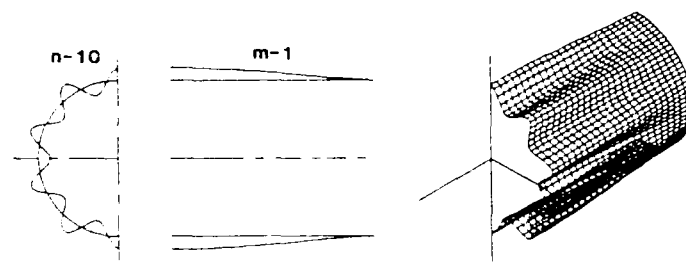


Mode Shape 10 Frequency 744 cps

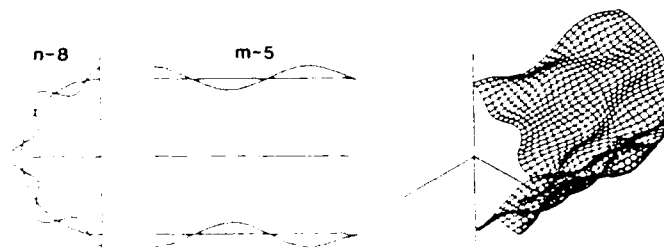


Mode Shape 9 Frequency 661 cps

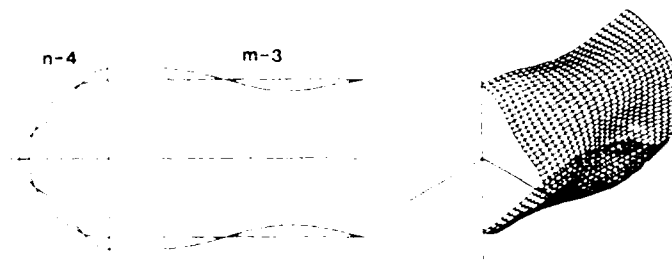
Figure 7. Frequencies and mode shapes for the 24x48 mesh 46 node quadrilateral element model, modes 9-12



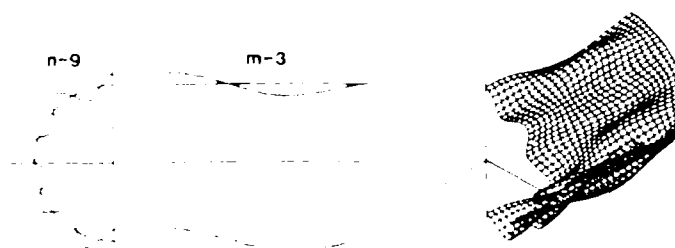
Mode Shape 16 Frequency 1027 cps



Mode Shape 15 Frequency 1023 cps

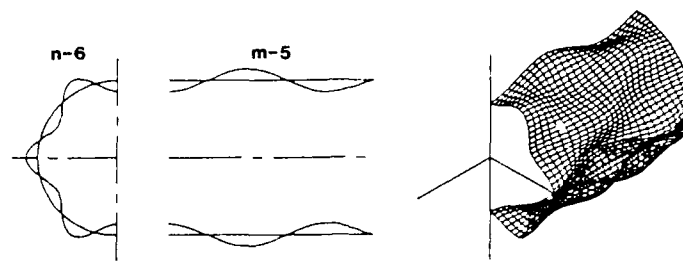


Mode Shape 14 Frequency 976 cps

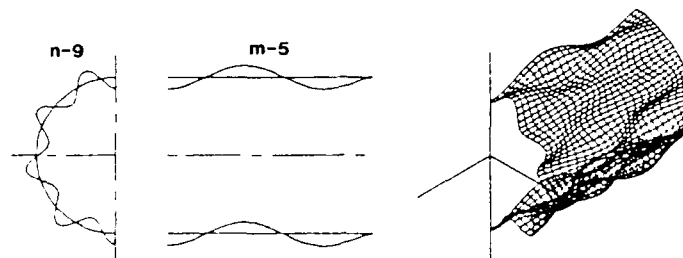


Mode Shape 13 Frequency 947 cps

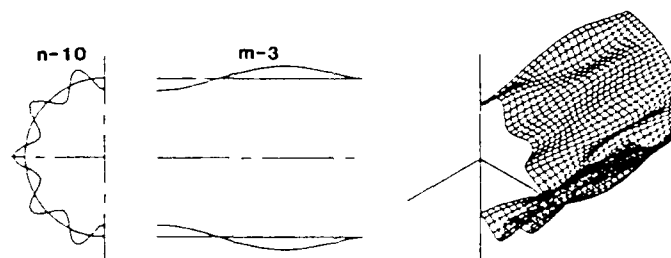
Figure 8. Frequencies and mode shapes for the 24x48 mesh 16 node quadrilateral element model, modes 13-16.



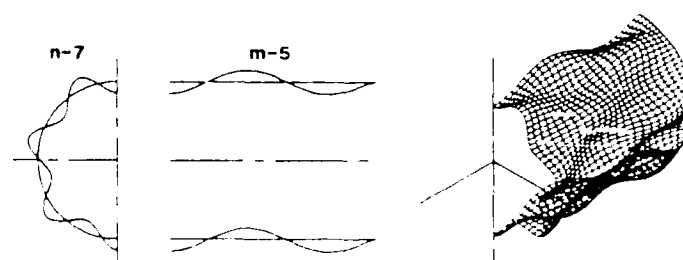
Mode Shape 20 Frequency 1181 cps



Mode Shape 19 Frequency 1088 cps



Mode Shape 18 Frequency 1078 cps



Mode Shape 17 Frequency 1046 cps

Figure 9. Frequencies and mode shapes for the 24x48 mesh 16 node quadrilateral element model, modes 17-20

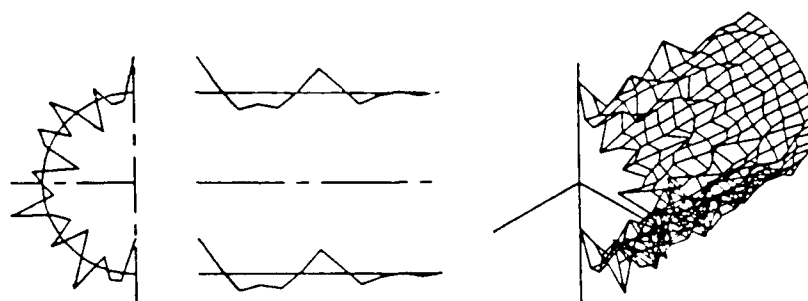


Figure 10: Mode 92 calculated with the 12x24 mesh model using 3-node triangular elements.

wave numbers m and n to each frequency based on identifying the number of waves in the deflection pattern. The process is not difficult for the more refined meshes, see Figures 5-9, but for the coarsest mesh (12x24), identification can become uncertain as the number of waves increases. In some cases involving the triangular element model, identification becomes impossible, giving rise to gaps in the coarse mesh data in Appendix C for the highly oscillatory modes. Figure 10 illustrates this dilemma for mode 92 obtained with triangular elements and the 12x24 mesh; here, not only is the circumferential pattern very irregular, but it is impossible to determine the number of longitudinal half waves. When the frequencies obtained from the ADINA calculations are graphed as functions of the number of circumferential waves for ascending numbers of longitudinal half waves, the curves are found to have the same general characteristics as those obtained by the Rayleigh-Ritz method, Figure 4. Therefore, rather than showing these very similar graphs for the finite element calculations, we prefer to graph the differences in the frequencies calculated by these models in terms of deviations from the Rayleigh-Ritz frequencies later in the paper in Figures 11-15.

The tables in Appendices B and C show that, with the exception of some simple modes with few oscillations, the frequencies predicted by both the quadrilateral and the triangular element models converge from above as the finite element mesh is refined, in agreement with the use of a consistent mass analysis. Moreover, as the mesh is refined, the frequencies for modes with few oscillations change less than those for highly oscillatory modes, indicating that the former are closer to converging. This causes frequencies of some modes with few oscillations to be replaced in the tables by those of modes with many oscillations as the mesh is refined, since only the lowest 100 frequencies are computed by the program. Consequently, there is a shift in the tabular data with more highly oscillatory modes being included as the mesh is refined at the expense of losing modes with few oscillations. In general, with the exception of some modes with few oscillations, the quadrilateral element frequencies are lower than the corresponding triangular element frequencies, indicating that for a given degree of refinement the quadrilateral element will predict frequencies closer to converging and hence is superior¹.

Comparison of the frequencies predicted by the finite element models and the the Rayleigh-Ritz analysis reveals an interesting trend. While finite element frequencies for modes with few oscillations are markedly closer to converging than the corresponding Rayleigh-Ritz frequencies, as the oscillations increase the converse becomes true. Looked at in detail for a fixed number of longitudinal half waves, m , and a given mesh refinement, we see that as the number of circumferential

¹ This result corrects an erroneous result in our previous investigation[1]. In that work, a mistake in modeling boundary conditions with the quadrilateral element gave unrealistically high frequency predictions. Recalculation of results reported there indicates that the error had been corrected before further calculations were performed and that the remainder of the results concerning the dynamic buckling of the cylinder are correct.

waves, n , increases, the frequencies from the two methods approach a cross-over frequency and thereafter the superiority of the Rayleigh-Ritz solution steadily increases. The apparent reason for this is that the sinusoidal functions used in the Rayleigh-Ritz analysis become better approximations of the displacements than the element shape functions as the oscillations in the modes increase. Hence, the fact that the Rayleigh-Ritz formulation satisfies the equations of motion in an integral sense and not exactly becomes less significant with increasing oscillations. It is true that by refining the finite element mesh, the cross-over frequency is delayed and some improvement in the accuracy of the finite element solutions for the higher values of n is achieved, but in all cases for the highest number of circumferential waves considered, the Rayleigh-Ritz frequencies are closest to converging. These points will be dealt with again below in comparing the deviation of the finite element solutions from the Rayleigh-Ritz solution.

CONVERGENCE ANALYSIS

In order to evaluate how close the frequencies computed by the finite element models are to converging, an estimate of the limit frequency is needed. In general, discrete numerical algorithms converge as some power of the mesh increment. Indeed, Tong and Pian[1] have shown that the rate at which each frequency computed by a finite element model converges to its limit value can be bounded by an expression of the form:

$$f_\epsilon = f + \kappa \epsilon^\eta \quad (1)$$

where ϵ is a characteristic mesh length, usually the mesh increment, f_ϵ is the frequency computed by the finite element model with the given mesh, f is the converged value of the frequency, obtained in the limit as $\epsilon \rightarrow 0$. κ and η are model parameters that are assumed to be independent of the mesh increment ϵ , although they both can be influenced by the type of element used and, in particular, κ can depend on the frequency being considered. These parameters can be interpreted as follows: η is an exponential measure of the rate at which the finite element model is converging to the limit frequency and κ is a measure of the closeness of the model to that limit frequency.

Taking this equation for our estimate on convergence, the frequencies computed using the three mesh refinements are used to determine the three unknowns f , κ , and η for each mode. The resulting values of the limit frequencies f are listed in Appendices B and C, and the values of the rate of convergence exponents η are tabulated in Tables 2 and 3 for the quadrilateral and triangular elements. The tables clearly show that the quadrilateral element converges at a faster rate, with an average exponential rate of convergence of 5.5786 compared to 1.7621 for the triangular element. A comparison of frequencies in Appendices B and C show that although the frequencies calculated with the triangular element are higher than the corresponding quadrilateral element frequencies, their limit frequencies are lower. This we attribute to the slow rate of convergence of the triangular element, as illustrated in Table 3, resulting in an inaccurate limit frequency. We shall return to this point again in the next section, where the deviations of the limit frequencies from Rayleigh Ritz frequencies are compared.

The gaps appearing in Tables 2 and 3, as well as those in the limit frequencies columns in Appendices B and C are due to a number of causes. The principal cause is that the limit analysis cannot be applied to modes that do not have data from all three mesh calculations. Moreover, the analysis cannot be used if the frequencies for a mode are not monotonic. Also, certain cases involving the triangular element, where the rate of convergence exponent is found to be less than

one, are excluded as being unreasonable.

Table 2: Rate of convergence exponents for the 16-node quadrilateral element calculations.

$\begin{matrix} m \\ n \end{matrix}$	1	3	5	7	9	11	13	15
2	6.0734							
3	5.6355	11.5008						
4	5.6901	6.0780	11.0451	10.7949				
5	5.4316	5.6659		7.1314	7.1157			
6	5.3847	5.5294	3.8910	6.5487	6.6586	6.6089		
7	5.3902	5.3958	4.1984	6.4439	6.4974	6.5442	5.1608	
8	4.5346	6.0074	7.0628	7.3185	7.3439	7.2336	5.9967	5.1817
9	5.3157	5.2851	5.6039	4.6614	5.1830	5.5903	4.8821	4.5157
10	5.2417	5.2227	5.3451	4.9409	5.2430	5.6208	5.1029	4.9403
11	5.1739	5.1624	5.3321	5.0016	5.2334	5.6371	5.3107	5.2768
12	6.3212	6.1602	5.4696	4.4996	3.8266	3.6086	3.3694	3.5631
13	5.0408	5.0412	5.0296	5.0170	5.0935	5.2124	4.8341	4.7201
14	5.0034	5.0042	5.0075	5.0095	5.1023	5.2519	5.0074	
15	4.9319	4.9319	4.9404	4.9616	5.0728	5.2346		

Table 3: Rate of convergence exponents for the 3-node triangular element calculations.

$\begin{matrix} m \\ n \end{matrix}$	1	3	5	7	9	11
2	1.9980					
3	2.0629	1.7110				
4	2.0693	1.9828	1.6387		1.1371	
5	2.0733	2.0440	1.9063	1.6142	1.5170	
6	3.1869	2.0754	1.9960	1.8306	1.6823	
7	2.0199	2.0920	2.0390	1.9214	1.7530	1.1877
8	1.9971	2.0759	2.0605	1.9628	1.7662	1.2706
9	1.9736	2.0274	2.0519	1.9715	1.7241	1.2362
10	1.9416	1.9656	2.0026	1.9414	1.6073	1.0280
11	1.8985	1.8936	1.9139	1.8587		
12	1.8375	1.7948	1.7567	1.6531		
13	1.7586	1.7089	1.6443	1.5195		
14	1.6492	1.5807	1.4624	1.3044		
15	1.5006	1.4159	1.2404			
16	1.2900	1.1816	1.0224			

COMPARISON OF FREQUENCIES

In this section we compare the deviations of the frequencies computed with the three finite element meshes and the limit frequencies obtained from the convergence analysis for the two element

types relative to the Rayleigh-Ritz frequencies as a basis. Ideally, we would prefer to use the true cylinder frequencies as a basis for comparison, but these are unavailable. The next choice might be the limit frequencies, except that the limits computed using the two element types are at wide variance, indicating possible inaccuracy in reproducing the true frequencies. Moreover, the limit frequencies are based on the corresponding finite element frequencies, which are themselves sensitive to the accuracy with which the finite element analysis simulates the mode shapes. Hence, an error in any one of the three finite element frequencies due to a faulty simulation of a mode shape would be perpetuated in the limit frequency. Some sensitivity to mode modeling is, in fact, discovered in the following analysis. For these reasons we chose the Rayleigh-Ritz data as the basis for comparison.

For purposes of comparison the deviation for each mode is represented as an error:

$$\text{error} = \frac{\text{computed frequency} - \text{Rayleigh-Ritz frequency}}{\text{Rayleigh-Ritz frequency}} \quad (2)$$

For the computer frequency we use either the frequencies successively computed by the three finite element meshes or the related limit frequency. When a computed frequency is lower than the Rayleigh-Ritz frequency, the error will be negative, an indication that it is closer to converging than the Rayleigh-Ritz. Figures 11-13 show graphically the results of the error analysis for the quadrilateral element and Figures 14-15 for the triangular element.

Focusing on the results from the quadrilateral element calculations, Figure 11 shows that for modes with one longitudinal half wave, $m = 1$, if a mode has five or less circumferential waves, the errors from all three mesh calculations are negative and practically indistinguishable from each other, signifying that the finite element frequencies are very close to their limit values and, hence, more accurately computed than the corresponding Rayleigh-Ritz frequency. As the number of circumferential waves increase, the error in each mesh calculation increases until each becomes progressively positive, indicating that the corresponding frequencies are farther away from converging than the Rayleigh-Ritz frequencies. The error curves for each mesh give an indication of the rate of convergence, showing that the 24×48 mesh frequencies are relatively close to converging and, although not easy to see, that the limit frequencies are slightly below the Rayleigh-Ritz frequencies. These trends for the most part persist for modes with three and five longitudinal half waves, except that in the latter case the smoothness in the error curve for the 12×24 mesh is disrupted by a positive jump in the value at $n = 8$.

Figure 12 shows that the tendency for a jump in the error curve of the 12×24 mesh at $n = 8$ persists into modes with seven, nine, and eleven longitudinal half waves. Moreover, a similar positive jump begins to appear in the error curves for the 18×36 mesh at $n = 12$, which apparently effects the error curve for the limit frequencies by causing a negative jump at this point. The figure also shows how the curves for the 12×24 mesh no longer coincide with the other curves at the lower values of circumferential wave numbers. Moreover, the figure more clearly illustrates that the limit frequencies are below the Rayleigh-Ritz frequencies over the entire range. Figure 13 shows that this tendency for jumps in the error curves of the 12×24 mesh at $n = 8$ and the 18×36 at $n = 12$ continues for modes with thirteen and fifteen longitudinal half waves.

These jumps in the error curves appear to be related to a coincidence between the number of circumferential waves and the number of circumferential elements; in both cases the number of elements used by the finite element model in the circumferential direction equals exactly twice the number of circumferential wave over *half* the cylinder circumference. This means that each wave is modeled by exactly two elements in this direction. That the solution should be effected by the sim-

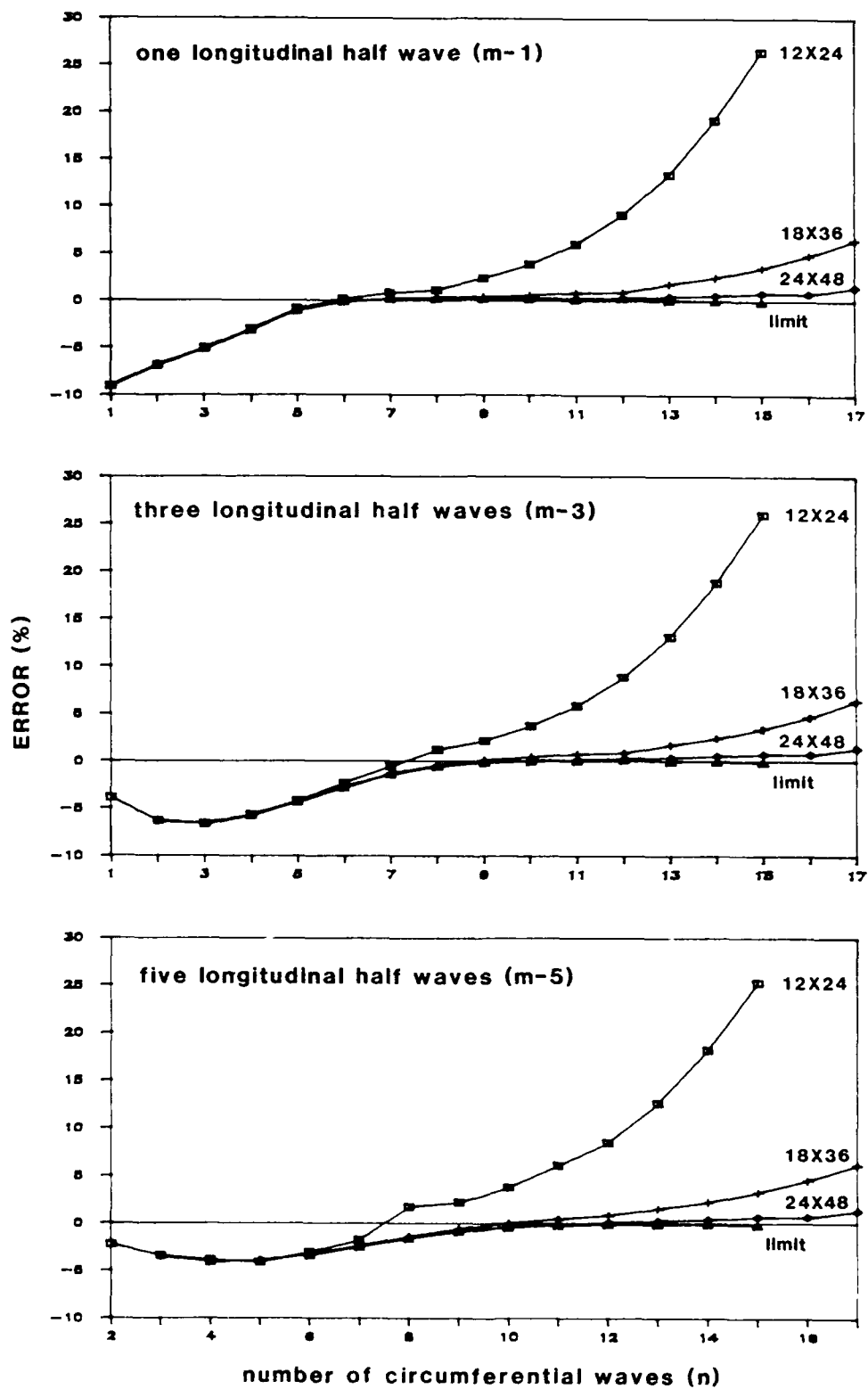


Figure 11: Error graphs for quadrilateral element calculations: $m = 1, 3, 5$.

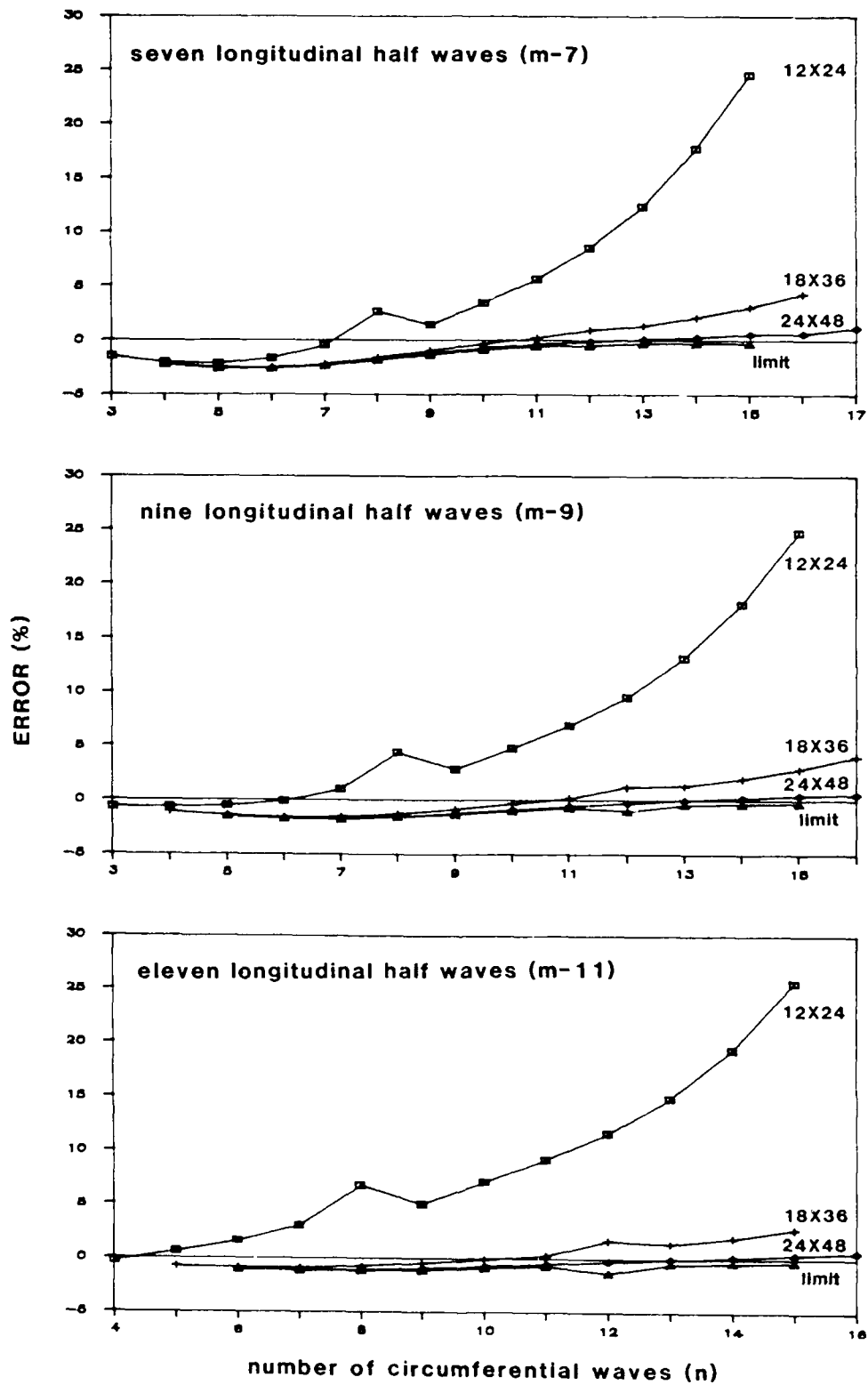


Figure 12: Error graphs for quadrilateral element calculations: $m = 7, 9, 11$

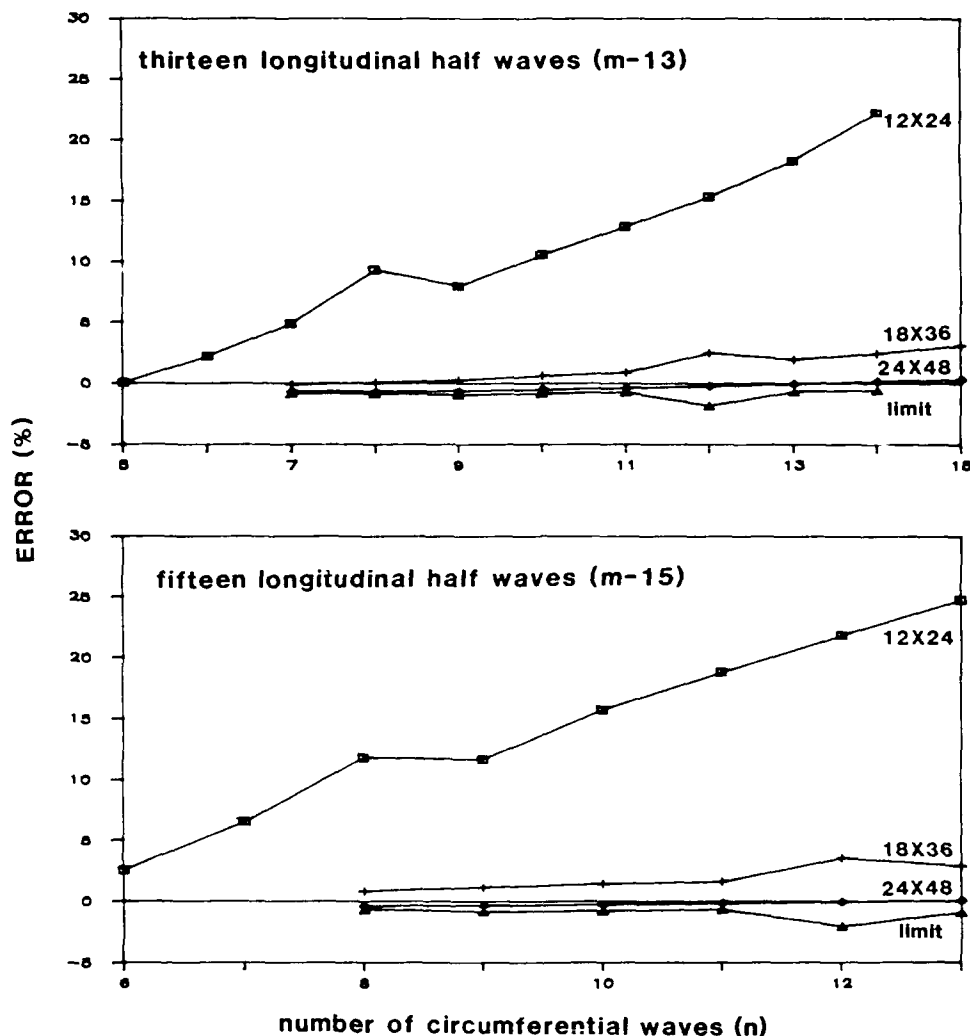


Figure 13: Error graphs for quadrilateral element calculations: $m = 13, 15$.

ilarity in element distribution and deformation pattern is not altogether surprising; what is strange is that rather than the solution improving, it worsens. Intuitively, it seems reasonable to expect that the more closely the element distribution conforms to the wave pattern of the deformation, the nearer the energy function will be to its minimum, since the element shape functions would then reproduce the sinusoidal deformation more accurately, and, hence, the closer the solution will be to converging. That these calculations apparently indicate the contrary to be true is puzzling and needs to be investigated further to see if this result is true in general for finite element frequency analyses.

Figures 14-15 show that the overall performance of the triangular element is poorer than that of the quadrilateral element. Comparing Figure 14 with Figure 11, we notice that the error curves of the triangular element become positive at lower values of n than those of the quadrilateral element, indicating that the corresponding frequencies are less accurately calculated earlier than the quadrilateral element frequencies. Moreover, the separation between the frequencies for the different mesh calculations at the lower values of n is greater with the triangular element models than with the quadrilateral element models. Figure 14 also shows a peculiar crossing over of the error curves of the three and five longitudinal half wave calculations. This is caused by the frequency calculated with

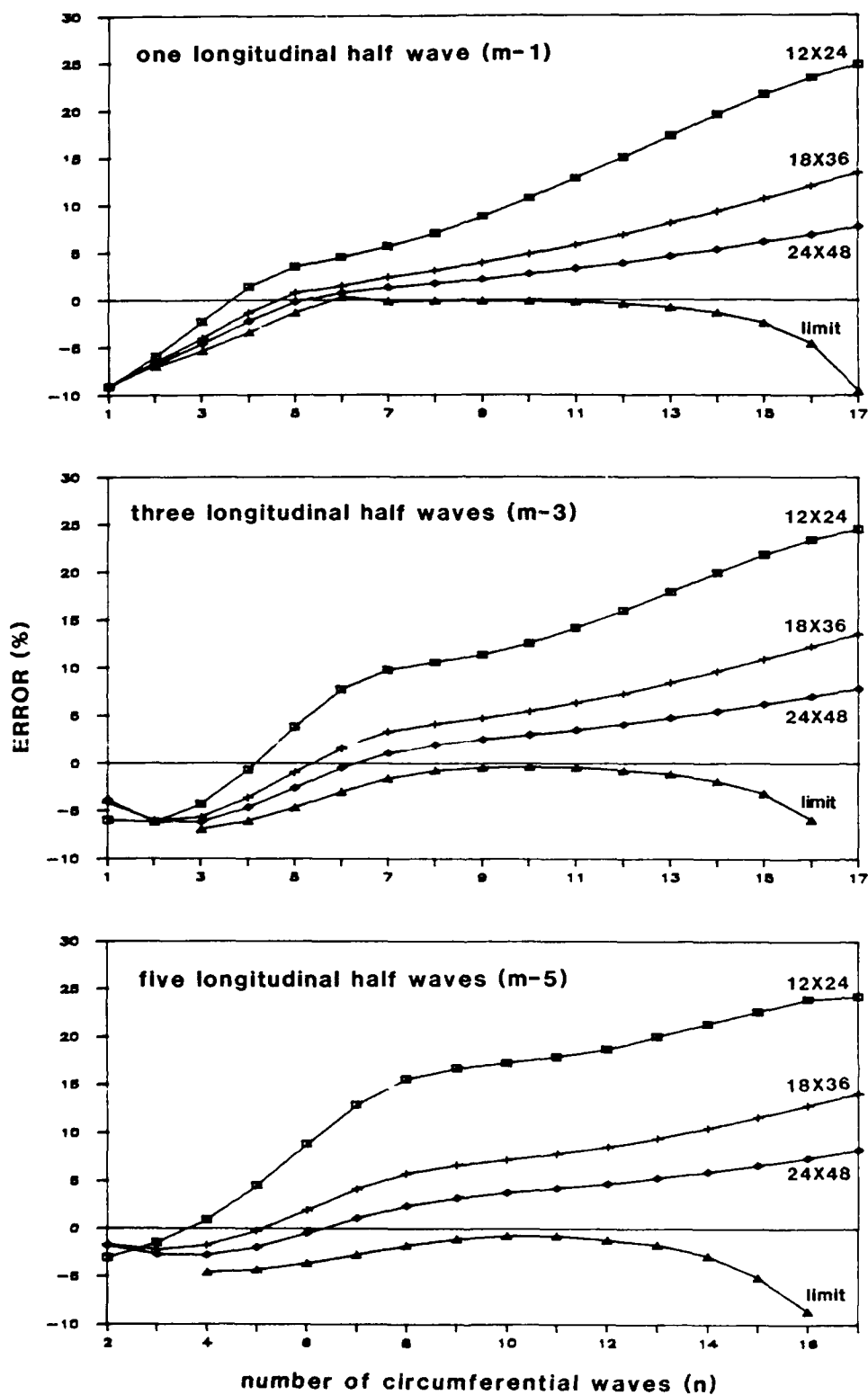


Figure 14: Error graphs for triangular element calculations: $m = 1, 3, 5$.

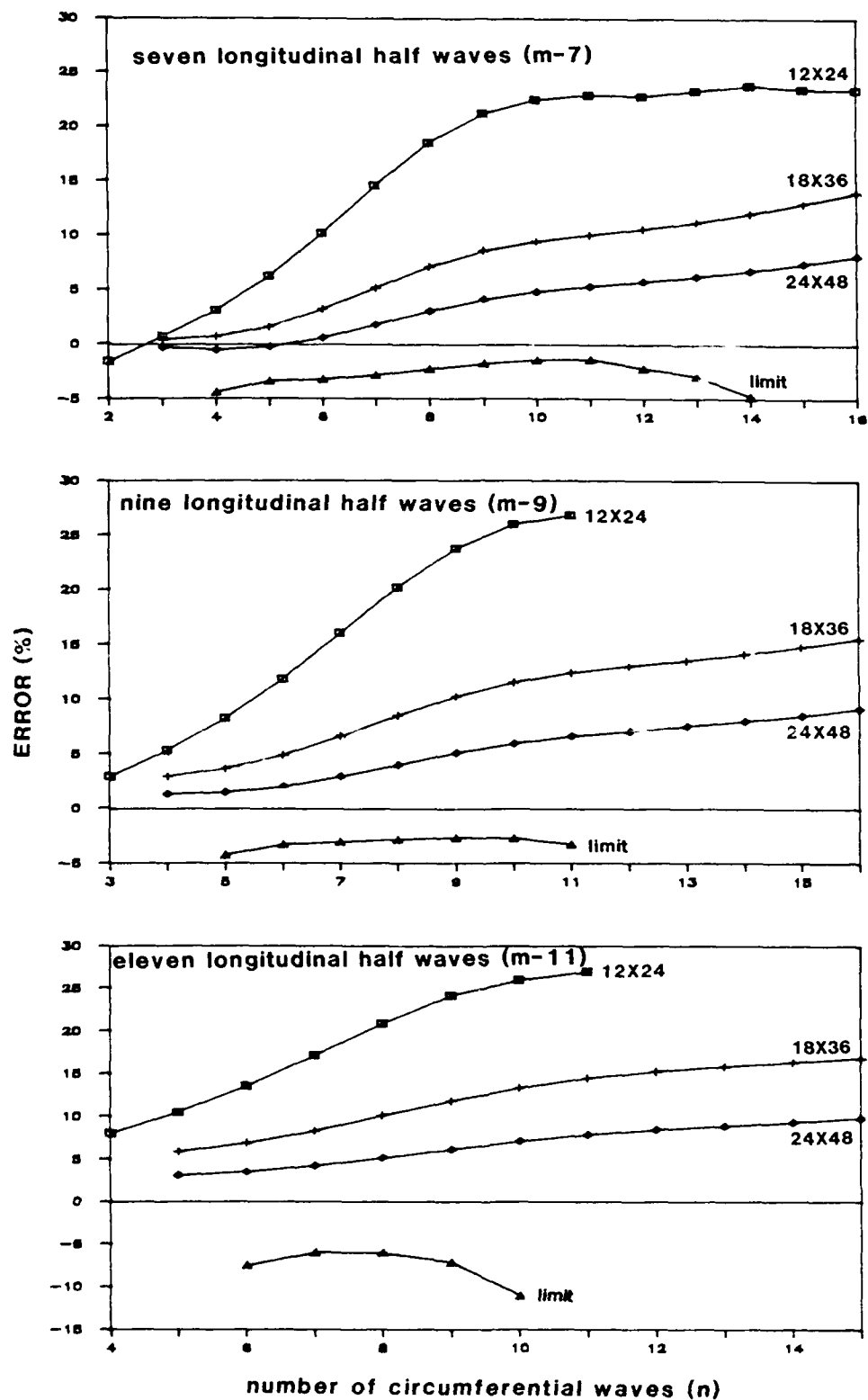


Figure 15: Error graphs for triangular element calculations: $m = 7, 9, 11$.

the coarsest mesh for the lowest value of n being lower than the corresponding frequencies computed with the refined meshes, a violation of the convergence from above requirement. Lastly, the limit curves indicate a peculiar trend in the limit frequencies: they show that the limit frequencies are considerably below the Rayleigh-Ritz frequencies at the lower values of n , which is to be expected, that they approach the Rayleigh-Ritz frequencies at the intermediate values of n , again expected, but then, unexpectedly, that they are once more considerably below the Rayleigh-Ritz frequencies at the higher values of n , even though now the frequencies for the three mesh calculations are considerably above those of the Rayleigh-Ritz frequencies. The last result is clearly wrong because it implies that the poor frequency predictions calculated by the finite element models at the higher values of n yield limit frequencies that are closer to converging than the more accurate frequency predictions at the intermediate values of n . Moreover, we know from the quadrilateral element comparisons, Figures 11-13, that for modes with many oscillations, the Rayleigh-Ritz frequency predictions are very close to the limit values. Most of the above observations continue to hold true in the error comparisons for the seven, nine, and eleven longitudinal half waves results, Figure 15, and need not be discussed further. The thirteen and fifteen longitudinal half waves data is too sparse for meaningful comparison and is hence omitted. Basically, the poor performance of the triangular element models in reproducing the cylinder frequencies, especially for modes with many oscillations, can be attributed to the element's poor simulation of the more complex deformation patterns, as exemplified in Figure 10, and its low rate of convergence, Table 3.

SUMMARY OF RESULTS

Comparison of the first 100 natural frequencies of the cylinder calculated by using three progressively refined finite element meshes for both the 16-node quadrilateral shell element and 3-node triangular plate element—the triangular element models confirms that frequencies converge predominantly to their true values from above, in agreement with the use of a consistent mass analysis. The frequencies computed by quadrilateral element models are closer to converging than the corresponding frequencies computed by triangular element models, despite the fact that the latter models required 20% more degrees-of-freedom. In particular, the convergence study shows that the quadrilateral element on the average converges three times faster than the triangular element. Moreover, as the number of oscillations in the modes increase, it becomes progressively more difficult to clearly identify the number of oscillations in the modes computed by the triangular element models. The only drawback found in using the quadrilateral element is that for mode shape and mesh combinations where each wave in the circumferential direction is modeled by exactly two elements, the frequency calculated by the finite element model is slightly less accurate than normal—the reason for this puzzling result remains unexplained. Overall, the quadrilateral element has been found to be superior in most respects to the triangular element and is recommended for frequency calculations.

The calculations also reveal that accuracy in computing the frequencies of a cylinder is not necessarily better for the lower frequencies, but correlates with mode oscillations—the less oscillations a mode contains, the closer its frequency is to converging. As an indirect result of this, it has been found by comparing the finite element solutions with the Rayleigh-Ritz solutions that, while the finite element frequencies are markedly closer to converging for the less complex mode shapes, as the number of oscillations in the mode shapes increase, the frequencies predicted by Rayleigh-Ritz analysis improve steadily and are substantially closer to converging for highly oscillatory modes. The reason for this is that as the oscillations in the modes increase, the sinusoidal functions used in

the Rayleigh-Ritz analysis becoming better approximations of the displacements than the element shape functions. This result can be significant for situations where high frequency response associated with many oscillations must be accurately modeled, since improvements in the accuracy of the finite element method are usually attained by refining the mesh and the degree of refinement is limited by the storage capacity of the computer. On the other hand the utility of the Rayleigh-Ritz approach, although more accurate for large numbers of oscillations, is limited to simple geometries for which good analytical approximations to mode shapes are available.

Generally, although these calculations succeeded in meeting the objectives of study, revealing the effects of mesh refinement on the accuracy of the frequency predictions, showing the overall better performance of a complex element over a simple element, clarifying some issues raised by our earlier study, and giving insight into the properties of the frequency spectrum for cylinders, they also raise some intriguing questions. Among these are, why does the simple element performed so poorly? Why is the quadrilateral element not as accurate when the element configuration and deformation pattern coincides? More fundamentally, can the accuracy of finite element frequency predictions be improved for highly oscillatory modes without undue demands on computer memory? One possible approach to the last is to combine the consistent mass formulation, which overpredicts frequencies, with the lumped mass formulation, which in certain situations underpredicts frequencies, in order to achieve accuracy in a given frequency range. In summary, these calculations have answered some question, but have also pointed out areas in which further work needs to be done to better understand finite element frequency analysis.

REFERENCES

1. J. M. Santiago, M. H. Klaus and H. L. Wisniewski, "Buckling of Blast Loaded Cylinder," Technical Report BRL-TR-2863, US Army Ballistic Research Laboratory, October 1987.
2. "ADINA, A Finite Element Program for Automatic Dynamic Incremental Nonlinear Analysis, Users Manual," Report AE 84-1, ADINA Engineering Inc., December 1984.
3. K.-J. Bathe, *Finite Element Procedures in Engineering Analysis*, Prentice-Hall, Englewood Cliffs, NJ, 1982.
4. P. Tong, T. H. H. Pian and L. L. Bucciarelli, "Mode Shapes and Frequencies by Finite Element Method Using Consistent and Lumped Masses," *Computers and Structures*, Vol. 1, pp. 623-638, Dec. 1971.
5. R. J. Pearson, H. L. Wisniewski, P. D. Szabados and A. W. Wilson, "The Effects of Thermal/Blast Synergism on the Nuclear Vulnerability of a Generic Aircraft Structure," Technical Report ARBRL-TR-02540, US Army Ballistic Research Laboratory, January 1984.
6. K.-J. Bathe and S. Bolourchi, "A Geometric and Material Nonlinear Plate and Shell Element," *J. Computers and Structures*, Vol. 11, pp. 23-48, 1980.
7. K.-J. Bathe and L. W. Ho, "A Simple and Effective Element for Analysis of General Shell Structures," *J. Computers and Structures*, Vol. 13, pp. 673-681, 1981.
8. H. Kraus, *Thin Elastic Shells*, John Wiley & Sons, New York, 1973.
9. R. N. Arnold & G. B. Warburton, "Flexural Vibrations of the Walls of Thin Cylinders," *Proc. I. Mech. E.*, Vol. 167, pp. 62-74, 1953.
10. G. Straug and G. J. Fix, *An Analysis of the Finite Element Method*, Prentice-Hall, Englewood Cliffs, NJ, 1973.

APPENDIX A: RAYLEIGH-RITZ ANALYSIS OF DONNELL SHELL

The Rayleigh-Ritz method of analysis is applied in this appendix to the Donnell equations for a cylindrical shell. This is taken from Kraus's textbook on elastic shells, but with corrections, since the final results presented there [8; pages 300-301, equations 8.14g & 8.14j] are in error.

The Donnell approximation to the equilibrium equations for a cylindrical shell, after the standard frequency substitution of $\cos \omega t$ to eliminate the time dependence, can be written as follows [8; page 297, equations 8.13]:

$$\begin{aligned} L_x &= \frac{\Omega^2}{a^2} u + \frac{\partial^2 u}{\partial x^2} + \frac{1-\nu}{2} \frac{\partial^2 u}{\partial y^2} + \frac{1+\nu}{2} \frac{\partial^2 v}{\partial x \partial y} + \frac{\nu}{a} \frac{\partial w}{\partial x} = 0 \\ L_\theta &= \frac{\Omega^2}{a^2} v + \frac{\partial^2 v}{\partial y^2} + \frac{1-\nu}{2} \frac{\partial^2 v}{\partial x^2} + \frac{1+\nu}{2} \frac{\partial^2 u}{\partial x \partial y} + \frac{1}{a} \frac{\partial w}{\partial y} = 0 \\ L_r &= \frac{\Omega^2}{a^2} w - \frac{h^2}{12} \nabla^4 w - \frac{1}{a^2} w - \frac{\nu}{a} \frac{\partial u}{\partial x} - \frac{1}{a} \frac{\partial v}{\partial y} = 0 \end{aligned} \quad (3)$$

where

- u = axial displacement
- v = circumferential displacement
- w = radial displacement
- x = axial coordinate
- y = $a\theta$ = circumferential coordinate
- ω = circular frequency
- a = mean radius of cylinder
- h = thickness of cylinder

Moreover,

$$\nabla^2 = \frac{\partial^2}{\partial x^2} + \frac{\partial^2}{\partial y^2}$$

is the Laplacian operator

$$\Omega = \sqrt{\frac{(1-\nu^2)\rho}{E}} a \omega$$

is a dimensionless circular frequency and E , ν , and ρ are the material constants introduced earlier in the section entitled CYLINDER SPECIFICATIONS.

As already mentioned, the Rayleigh-Ritz method uses a set of functions with unspecified coefficients to approximate the displacements. For the shell equations, it is convenient to approximate the mode shapes by displacement functions employing beam bending functions in the longitudinal direction and trigonometric functions in the circumferential direction:

$$u = A \xi'_m(x) \cos n\theta, \quad v = B \xi_m(x) \sin n\theta, \quad w = C \xi_m(x) \cos n\theta \quad (4)$$

where m corresponds to the number of longitudinal *half* waves and n the number of circumferential *full* waves in the mode. Figures 5-9 in the body of the paper illustrates the definitions of m and n by examples.

The beam bending functions

$$\xi_m(x) = \sin \frac{\mu L}{2a} \cosh \frac{\mu x}{2a} + \sinh \frac{\mu L}{2a} \cos \frac{\mu x}{2a} \quad (5)$$

will satisfy the clamped boundary condition at $x = L/2$ and the symmetry boundary condition at $x = 0$ when μ satisfies

$$\tan \frac{\mu L}{2a} + \tanh \frac{\mu L}{2a} = 0 \quad (6)$$

Solutions of this transcendental equation for μ can be associated with the number of longitudinal half waves m through the equation

$$\mu = \frac{a\pi}{L} \left(m + \frac{1}{2}\right) \quad (7)$$

where m is the nearest integer satisfying the equation. In actuality, the previous expression is used in an inverse way: an integer value of m is substituted in (7), which is solved for a value of μ , which is then used as the initial guess in a Newton's method solution of (6). Because (6) is derived on the basis that modes are symmetric about the plane $x = 0$, only odd values of m will give valid solutions.

The assumed displacement functions (4) with the resulting bending functions (5) can be shown not to satisfy the equations of equilibrium (3) exactly. Consequently, in order to impose equilibrium on (3) in an integral or Galerkin sense, the Rayleigh-Ritz method is applied to the variational equation of the problem

$$\int_{-L/2}^{L/2} \int_0^{2\pi} (L_x \delta u + L_y \delta v + L_z \delta w) dx dy = 0 \quad (8)$$

Substituting (3), (4), and (5) in (8) and integrating leads to the homogeneous matrix equation

$$\begin{pmatrix} a_{11} + \Omega^2 & a_{12} & a_{13} \\ a_{21} & a_{22} + \Omega^2 & a_{23} \\ a_{31} & a_{32} & a_{33} + \Omega^2 \end{pmatrix} \begin{pmatrix} \dot{A} \\ B \\ C \end{pmatrix} = 0 \quad (9)$$

where

$$\begin{aligned} a_{11} &= \mu^2/P + \frac{1}{2}n^2 & a_{12} = a_{21} &= -\frac{1}{2}v\sqrt{P}\mu n \\ a_{22} &= \frac{1}{2}v^2P\mu^2 + n^2 & a_{23} = a_{32} &= n \\ a_{33} &= 1 + \frac{b^2}{12a^2}(\mu^4 + 2P\mu^2n^2 + n^4) & a_{31} = a_{13} &= -v\sqrt{P}\mu \end{aligned}$$

$$P = \tan^2 \frac{\mu L}{2a} + \frac{2a}{\mu L} \tanh \frac{\mu L}{2a}$$

and

$$A = \frac{\mu}{a} \sqrt{PA}$$

Since (9) can have nontrivial solutions only if its determinant vanishes, a cubic equation for the nondimensional frequencies Ω^2 results.

Hence, to solve for the frequencies of the cylinder by this method, the corresponding mode shape is first specified by picking the number of longitudinal half waves m and circumferential wave n . The associated value of μ is determined from (6) and μ and n are substituted in the determinant of (9), which is then solved for Ω^2 . The three frequencies resulting from the solution of the cubic can be distinguished as predominantly longitudinal, torsional, or flexural based on which coefficient, A , B , or C , is largest, as determined from (9). Usually, as in the body of the paper, the flexural modes produce the lowest frequencies.

APPENDIX B: FREQUENCIES COMPUTED BY QUADRILATERAL ELEMENT MODELS

The frequencies computed using the three quadrilateral element models are listed, row-wise, in ascending order according to the number of axial half waves (m) and circumferential waves (n) contained in the mode shape, and, column-wise, in increasing degree of mesh refinement. For comparison, they are flanked on the left by the frequencies from the Rayleigh-Ritz analysis and on the right by the limit frequencies from the convergence analysis of the finite element frequencies. In the majority of cases, the frequencies calculated by the finite element method for a given mode converge from above. Also, it should be noticed that, with very few exceptions, the frequencies for a given mode computed with the quadrilateral element models are lower and, hence, closer to converging than the corresponding frequencies computed with the triangular element models in Appendix C.

Wave Numbers		Rayleigh -Ritz Analysis	Finite Element Analysis			
m	n		Mesh Configuration			Limit Values
			12×24	18×36	24×48	
1	1	1327.086	1206.830	1206.835	1206.835	1206.835
1	2	678.316	632.211	632.204	632.204	632.204
1	3	387.831	368.197	368.153	368.149	368.148
1	4	281.115	272.878	272.732	272.719	272.716
1	5	291.060	291.435	291.038	290.999	290.989
1	6	379.028	379.682	378.602	378.494	378.465
1	7	503.196	507.281	504.395	504.107	504.029
1	8	654.887	662.114	656.911	656.194	655.927
1	9	829.201	848.849	832.765	831.114	830.657
1	10	1025.093	1064.513	1031.245	1027.733	1026.734
1	11	1242.067	1316.880	1252.715	1245.765	1243.738
1	12	1479.922	1611.985	1493.766	1485.286	1483.613
1	13	1738.566	1971.921	1769.641	1746.601	1739.511
1	14	2017.959	2405.434	2069.078	2030.222	2018.147
1	15	2318.080	2931.534	2399.962	2336.876	2316.735
1	16	2638.917		2766.615	2659.853	
1	17	2980.161		3174.656	3024.036	
3	1	3561.922	3423.025			
3	2	2280.207	2136.150	2136.179	2136.207	
3	3	1497.200	1398.008	1397.862	1397.860	1397.860
3	4	1035.952	977.173	976.613	976.570	976.561
3	5	778.478	746.031	744.610	744.515	744.485
3	6	667.170	651.742	648.974	648.712	648.615
3	7	670.590	666.909	661.898	661.399	661.265
3	8	757.302	766.242	754.187	753.236	753.031
3	9	899.070	917.786	899.673	897.792	897.266
3	10	1078.472	1117.631	1082.661	1078.946	1077.881

Wave Numbers		Rayleigh -Ritz Analysis	Finite Element Analysis			
<i>m</i>	<i>n</i>		Mesh Configuration			Limit Values
			12×24	18×36	24×48	
3	11	1286.789	1361.362	1295.883	1288.760	1286.674
3	12	1519.893	1654.395	1532.729	1523.676	1521.822
3	13	1775.824	2008.077	1805.354	1782.267	1775.194
3	14	2053.608	2439.253	2103.021	2064.191	2052.128
3	15	2352.740	2963.266	2432.700	2369.732	2349.628
3	16	2672.952		2798.473	2691.965	
3	17	3014.094		3205.820	3055.572	
5	2	3461.230	3384.730			
5	3	2580.316	2490.989	2490.551	2490.664	
5	4	1940.536	1864.819	1861.729	1861.695	1861.693
5	5	1502.061	1440.108	1443.138	1442.901	
5	6	1222.484	1185.421	1182.288	1181.739	1181.472
5	7	1074.652	1055.860	1049.333	1048.313	1047.878
5	8	1039.798	1057.742	1025.522	1023.828	1023.572
5	9	1097.144	1120.928	1090.877	1088.112	1087.423
5	10	1223.682	1269.495	1223.797	1219.158	1217.888
5	11	1400.350	1485.475	1407.005	1399.000	1396.798
5	12	1614.612	1751.439	1627.995	1616.042	1612.915
5	13	1859.160	2094.509	1887.461	1863.778	1856.490
5	14	2129.911	2517.888	2178.112	2138.922	2126.763
5	15	2424.593	3036.549	2503.185	2440.088	2420.008
5	16	2741.919		2865.753	2759.685	
5	17	3081.147		3270.739	3120.947	
7	3	3375.185	3324.916			
7	4	2726.938	2671.625	2666.688	2666.628	2666.625
7	5	2217.967	2170.050	2160.714	2160.236	2160.165
7	6	1844.246	1813.105	1796.928	1795.891	1795.705
7	7	1594.062	1586.580	1558.890	1557.012	1556.698
7	8	1457.133	1495.457	1433.658	1430.715	1430.306
7	9	1422.803	1443.209	1409.511	1405.117	1403.549
7	10	1476.508	1527.674	1472.067	1465.490	1463.397
7	11	1600.817	1691.606	1604.842	1594.812	1591.693
7	12	1779.613	1931.242	1796.526	1777.716	1770.615
7	13	2000.738	2249.111	2028.282	2002.902	1995.055
7	14	2256.081	2655.937	2303.753	2263.162	2250.577
7	15	2540.549	3164.345	2618.453	2554.388	2534.163
7	16	2851.017		2973.746	2868.132	
7	17	3185.567			3223.682	
9	3	3905.701	3879.897			
9	4	3333.383	3311.660	3296.222		
9	5	2833.760	2818.207	2792.543	2791.221	2791.025
9	6	2430.024	2428.119	2390.510	2388.199	2387.799

Wave Numbers		Rayleigh -Ritz Analysis	Finite Element Analysis			
			Mesh Configuration			Limit Values
<i>m</i>	<i>n</i>		12×24	18×36	24×48	
9	7	2127.870	2149.023	2094.588	2091.029	2050.379
9	8	1926.892	2011.736	1902.267	1897.105	1896.395
9	9	1823.906	1875.357	1808.699	1801.504	1799.413
9	10	1812.125	1899.263	1806.263	1796.450	1793.661
9	11	1880.507	2010.461	1883.963	1870.567	1866.746
9	12	2015.589	2208.207	2010.672	2010.604	1995.619
9	13	2204.483	2494.824	2233.452	2204.268	2195.501
9	14	2436.801	2879.289	2485.786	2441.995	2428.883
9	15	2705.036	3375.476	2783.848	2717.270	2697.414
9	16	3004.075		3126.997	3021.520	
11	4	3783.651	3773.219			
11	5	3333.722	3354.133	3308.480		
11	6	2942.815	2989.940	2917.090	2912.527	2911.725
11	7	2627.794	2707.528	2604.686	2598.082	2596.896
11	8	2396.649	2558.943	2378.991	2370.135	2368.872
11	9	2252.404	2365.960	2242.073	2230.615	2227.746
11	10	2194.016	2350.331	2191.976	2177.499	2173.913
11	11	2216.166	2420.128	2222.769	2204.838	2200.423
11	12	2309.926	2579.046	2348.399	2303.523	2278.919
11	13	2464.692	2832.008	2498.792	2463.223	2453.000
11	14	2670.295	3189.092	2723.369	2674.392	2660.520
11	15	2918.283	3667.123	3000.089	2929.482	2909.355
11	16	3202.235			3221.445	
13	5	3734.785	3736.686			
13	6	3379.644	3454.967			
13	7	3077.585	3228.478	3073.939	3057.117	3052.188
13	8	2841.679	3106.450	2843.119	2822.260	2817.738
13	9	2679.437	2892.793	2687.413	2662.577	2654.496
13	10	2593.975	2867.584	2609.393	2580.667	2572.068
13	11	2584.250	2917.271	2606.894	2574.973	2566.125
13	12	2645.442	3051.027	2712.370	2640.396	2596.406
13	13	2770.108	3276.810	2825.194	2769.584	2751.455
13	14	2949.825	3605.960	3021.927	2954.561	2933.659
13	15	3176.615		3276.083	3188.136	
15	6	3752.579	3848.832			
15	7	3478.184	3705.163			
15	8	3254.517	3640.293	3281.795	3243.079	3231.824
15	9	3091.654	3452.838	3127.139	3081.937	3064.981
15	10	2995.412	3466.507	3038.771	2988.168	2972.063
15	11	2967.820	3526.299	3016.590	2963.492	2948.590
15	12	3007.125	3662.924	3114.577	3006.078	2945.370
15	13	3108.833	3878.803	3198.876	3111.483	3081.221

APPENDIX C: FREQUENCIES COMPUTED BY TRIANGULAR ELEMENT MODELS

The frequencies computed using the three triangular element models are listed, row-wise, in ascending order according to the number of axial half-waves (m) and circumferential waves (n) contained in the mode shape, and, column-wise, in increasing degree of mesh refinement. For comparison, they are flanked on the left by the frequencies from the Rayleigh-Ritz analysis and on the right by the limit frequencies from the convergence analysis of the finite element frequencies. In the majority of cases, the frequencies calculated by the finite element method for a given mode converge from above. Also, it should be noticed that, with a few exceptions, the frequencies for a given mode computed with the triangular element models are higher and, hence, further from converging than the corresponding frequencies computed with the quadrilateral element models in Appendix B.

Wave Numbers		Rayleigh -Ritz Analysis	Finite Element Analysis			
			Mesh Configuration			Limit Values
m	n		12×24	18×36	24×48	
1	1	1327.086	1206.398	1207.115	1207.091	
1	2	678.346	638.348	634.171	632.708	630.825
1	3	387.831	379.025	372.268	369.956	367.102
1	4	281.445	285.489	277.776	275.143	271.907
1	5	294.060	304.475	296.349	293.579	290.183
1	6	379.028	396.089	384.575	381.958	380.215
1	7	503.496	531.777	515.515	509.864	502.693
1	8	654.887	701.142	675.112	665.992	654.244
1	9	829.201	901.989	861.416	847.080	828.324
1	10	1025.093	1134.796	1074.118	1052.430	1023.442
1	11	1242.067	1400.927	1313.828	1282.210	1238.695
1	12	1479.922	1701.707	1581.525	1536.931	1472.911
1	13	1738.566	2038.377	1878.351	1817.268	1724.505
1	14	2017.959	2410.895	2205.518	2123.994	1989.714
1	15	2318.080	2818.120	2564.226	2457.950	2261.096
1	16	2638.917	3256.121	2955.606	2820.023	2518.297
1	17	2980.164	3718.058	3380.631	3211.130	2694.810
3	1	3561.922	3347.865	3413.926	3422.865	3426.129
3	2	2280.207	2140.167	2141.986	2139.471	
3	3	1497.200	1432.309	1412.748	1405.153	1393.209
3	4	1035.952	1028.569	998.237	987.555	973.665
3	5	778.478	807.894	770.977	758.259	742.370
3	6	667.170	718.608	677.885	664.014	647.031
3	7	670.590	736.033	692.491	677.748	659.887
3	8	757.302	837.286	788.452	771.821	751.465
3	9	899.070	1001.115	941.727	921.445	895.152
3	10	1078.472	1213.901	1137.348	1110.220	1074.538

Wave Numbers		Rayleigh -Ritz Analysis	Finite Element Analysis			
			Mesh Configuration			Limit Values
<i>m</i>	<i>n</i>		12×24	18×36	24×48	
3	11	1286.789	1468.739	1368.067	1331.457	1280.902
3	12	1519.893	1761.997	1630.962	1581.591	1508.543
3	13	1775.824	2094.501	1925.231	1859.459	1755.872
3	14	2053.608	2462.879	2251.070	2164.909	2015.263
3	15	2352.740	2866.006	2609.117	2498.290	2277.864
3	16	2672.952	3298.585	3000.145	2860.216	2514.585
3	17	3014.094	3755.553	3424.869	3251.442	
5	2	3461.230	3355.516	3401.357	3399.229	
5	3	2580.316	2512.094	2522.693	2509.334	
5	4	1940.536	1958.133	1906.640	1886.123	1852.057
5	5	1502.061	1569.586	1498.522	1472.797	1437.580
5	6	1222.484	1330.702	1245.965	1216.264	1177.975
5	7	1074.652	1213.489	1118.927	1086.292	1045.387
5	8	1039.798	1201.633	1099.483	1064.501	1021.259
5	9	1097.144	1280.636	1170.203	1132.267	1085.113
5	10	1223.682	1435.063	1312.328	1269.411	1214.326
5	11	1400.350	1651.233	1510.118	1459.174	1389.794
5	12	1614.612	1916.959	1753.123	1690.543	1595.375
5	13	1859.160	2231.987	2035.427	1957.265	1828.038
5	14	2129.911	2584.787	2354.043	2256.132	2068.934
5	15	2424.593	2973.233	2707.659	2585.710	2301.323
5	16	2741.919	3398.683	3095.802	2945.558	2506.209
5	17	3081.147	3828.915	3518.316	3335.789	
7	2	4126.153	4060.614			
7	3	3375.185	3397.749	3389.028	3364.992	
7	4	2726.938	2810.767	2745.350	2712.164	2607.702
7	5	2217.967	2355.869	2253.410	2212.227	2142.546
7	6	1844.246	2032.293	1902.926	1854.806	1785.392
7	7	1594.062	1826.608	1676.460	1622.401	1549.152
7	8	1457.133	1727.203	1560.709	1501.650	1423.821
7	9	1422.803	1724.667	1544.807	1481.208	1397.885
7	10	1476.508	1808.964	1616.541	1547.758	1455.809
7	11	1600.817	1968.490	1762.096	1686.094	1578.589
7	12	1779.613	2186.558	1968.632	1882.246	1740.375
7	13	2000.738	2468.309	2226.298	2125.676	1942.145
7	14	2256.081	2793.593	2528.453	2409.411	2148.093
7	15	2540.549	3137.612	2870.947	2729.382	
7	16	2851.017	3519.641	3251.205	3083.205	
9	3	3905.701	4019.463			
9	4	3333.383	3510.013	3430.127	3375.807	
9	5	2833.760	3066.642	2936.560	2874.598	2714.473
9	6	2430.024	2717.863	2548.830	2478.489	2349.934

Wave Numbers		Rayleigh -Ritz Analysis	Finite Element Analysis			
			Mesh Configuration			Limit Values
<i>m</i>	<i>n</i>		12×21	18×36	24×48	
9	7	2127.870	2468.816	2268.263	2189.591	2063.210
9	8	1926.892	2316.775	2090.603	2004.100	1872.204
9	9	1823.906	2256.855	2010.490	1916.709	1775.078
9	10	1812.125	2282.467	2021.167	1920.189	1762.936
9	11	1880.507	2384.428	2113.649	2004.542	1818.946
9	12	2015.589		2277.195	2158.153	
9	13	2204.483		2502.659	2370.025	
9	14	2436.801		2780.773	2631.305	
9	15	2705.036		3105.478	2935.660	
9	16	3004.075		3472.012	3278.909	
11	4	3783.651	4087.586			
11	5	3333.722	3683.735	3529.118	3435.578	
11	6	2942.815	3342.217	3145.522	3045.188	2723.387
11	7	2627.794	3078.884	2846.807	2738.226	2471.633
11	8	2396.649	2897.778	2638.055	2520.065	2252.686
11	9	2252.404	2796.397	2518.992	2391.419	2092.706
11	10	2194.016	2764.219	2487.142	2349.969	1951.357
11	11	2216.166	2814.289	2537.577	2390.381	
11	12	2309.926		2663.177	2504.788	
11	13	2464.692		2855.729	2684.207	
11	14	2670.295		3107.089	2920.094	
11	15	2918.283		3409.943	3205.376	
13	6	3379.644	3876.442			
13	7	3077.585	3598.511	3399.578	3251.558	
13	8	2841.679		3181.159	3025.118	
13	9	2679.437	3219.377	3043.798	2877.238	
13	10	2593.975		2986.919	2809.436	
13	11	2584.250		3008.951	2819.980	
13	12	2645.442		3105.470	2904.354	
13	13	2770.108		3270.310	3056.189	
13	14	2949.825		3496.284	3268.449	
15	9	3091.654		3577.143	3362.892	
15	10	2995.442		3508.036	3283.849	
15	11	2967.820		3512.993	3277.701	
15	12	3007.125		3589.352	3342.485	

INTEGRAL METHOD FOR FREE EDGE PLATES WITH STIFFENERS

B. P. Wang and S. Nomura

Department of Mechanical Engineering
University of Texas at Arlington
Arlington, TX 76019

ABSTRACT

A computer aided implementation of the Ritz method is presented to calculate the natural frequency of a plate with interior support points reinforced by stiffeners. Symbolic algebra software, REDUCE, is used to generate permissible Galerkin functions for the deflection of the plate that satisfy both the free boundary conditions and support constraints. The effect of stiffeners can be handled by additional line integrals. REDUCE is also used to calculate matrix elements for the generalized eigenvalue problem. The method has advantages over purely numerical methods and is particularly suitable for the sensitivity analysis.

INTRODUCTION

A computer-aided implementation of classical Ritz procedure is presented to treat free vibration of a plate reinforced by stiffeners. An integral method which has been successfully applied to the analysis of transient heat conduction is adopted and symbolic algebra software, REDUCE [1], is used for the analysis.

Of various boundary conditions of the plate problems, the free edge poses the most difficulty and receives the least attention. This is because the boundary conditions associated with free edges ("natural boundary conditions") involve higher order derivatives of the plate lateral displacement.

An integral method, which takes advantage of both numerical techniques and symbolic algebra software, has been used in heat transfer problems and it has proven to be a powerful and accurate method for various problems in transient heat conduction [2-3]. By combining the standard Galerkin method with symbolic algebra software, improved accuracy and reduced computer time are possible.

The lateral displacement in free edge plates with stiffeners is expressed as a series of polynomials each of which satisfies the free boundary conditions. Coefficients of these polynomials are determined by the standard Ritz method using the Galerkin functions. Symbolic algebra software is essential to perform necessary algebraic operations to generate admissible Galerkin functions and generalized mass and stiffness matrices for the generalized eigenvalue problem [4]. The presence of stiffeners is handled by additional integrations over stiffener phases [5]. The obtained expression is in closed form and unlike purely numerical methods such as finite element or finite difference methods, this method does not require excessive computational time nor huge memory storage.

It is also possible to compute the sensitivity of eigenvalues with respect to variation of support locations based on the Galerkin method and computer algebra. This sensitivity will be useful in choosing support locations and can be also used in automated programs to find the optimal support locations to maximize the fundamental natural frequency.

Numerical examples are also presented.

ANALYSIS

A stiffened two-dimensional plate supported at interior points with free edges is considered. The governing equations for the plate and stiffeners are expressed as

$$\rho_p \frac{\partial^2 w}{\partial t^2} + D \left(\frac{\partial^4 w}{\partial x^4} + 2 \frac{\partial^4 w}{\partial x^2 \partial y^2} + \frac{\partial^4 w}{\partial y^4} \right) = 0 \quad (1)$$

$$\rho_s \frac{\partial^2 w}{\partial t^2} \bigg|_{y=y_1} + EI \frac{d^4 w}{dx^4} \bigg|_{y=y_1} = 0 \quad (2)$$

$$\rho_s \frac{\partial^2 w}{\partial t^2} \bigg|_{x=x_1} + EI \frac{d^4 w}{dy^4} \bigg|_{x=x_1} = 0 \quad (3)$$

where ρ_p and ρ_s are the mass densities of the plate and stiffeners, respectively, w is the lateral deflection and D and EI are the flexural rigidities of the plate and stiffeners, respectively. The plate is reinforced by stiffeners in both x - and y - directions along as $x=x_1$ and $y=y_1$.

If the plate is square whose region is expressed in non-dimensionalized form as $((x,y), -1 < x < 1, -1 < y < 1)$, the free boundary conditions are expressed as

$$x = \pm 1 \quad \partial^2 u / \partial x^2 + \nu \partial u^2 / \partial y^2 = 0 \quad (4)$$

$$\partial^3 u / \partial x^3 + (2-\nu) \partial^3 u / \partial x \partial y^2 = 0 \quad (5)$$

$$y = \pm 1 \quad \partial^2 u / \partial y^2 + \nu \partial u^2 / \partial x^2 = 0 \quad (6)$$

$$\partial^3 u / \partial y^3 + (2-\nu) \partial^3 u / \partial y \partial x^2 = 0 \quad (7)$$

where ν is the Poisson's ratio of the plate.

In addition, constraint conditions at interior support points are expressed

as

$$w(x_a, y_a, t) = 0 \quad (8)$$

$$a = 1, 2, \dots, N$$

where the plate is supported at a point (x_a, y_a) .

In order to find the free vibration of such a plate, a time-harmonic solution is assumed as

$$w(x, y, t) = W(x, y) e^{i\omega t} \quad (9)$$

With this substitution, eqns (1)-(3) become

$$D \left(\frac{\partial^4 W}{\partial x^4} + 2 \frac{\partial^4 W}{\partial x^2 \partial y^2} + \frac{\partial^4 W}{\partial y^4} \right) = \rho_p \omega^2 W \quad (10)$$

$$EI \left. \frac{d^4 W}{dx^4} \right|_{y=y_i} = \rho_s \omega^2 W \left|_{y=y_i} \quad (11)$$

$$EI \left. \frac{d^4 W}{dy^4} \right|_{x=x_i} = \rho_s \omega^2 W \left|_{x=x_i} \quad (12)$$

Equations (10)-(12) can be solved by applying the Ritz method using a Galerkin function [5] by assuming a solution in the form of a linear combination of base functions as

$$W(x,y) = \sum_a c_a \psi_a(x,y) \quad (13)$$

where $\psi_a(x,y)$ is a polynomial that satisfies the homogeneous boundary conditions as well as support constraint conditions of eqn (8) and c_a 's are unknown coefficients to be determined. According to the Ritz method, the following matrix eigenvalue problem is obtained [5]:

$$A c = \lambda B c \quad (14)$$

$$\begin{aligned} (a_{a\beta}) = & (1-\nu) \iint \left(\frac{\partial^2 \psi_a}{\partial x^2} \frac{\partial^2 \psi_\beta}{\partial x^2} + 2 \frac{\partial^2 \psi_a}{\partial x \partial y} \frac{\partial^2 \psi_\beta}{\partial x \partial y} + \frac{\partial^2 \psi_a}{\partial y^2} \frac{\partial^2 \psi_\beta}{\partial y^2} \right) dS \\ & + \nu \iint \Delta \psi_a \Delta \psi_\beta dS \\ & + \left(\int_0^1 \frac{\partial^2 \psi_a}{\partial x^2} \bigg|_{y=y_1} \frac{\partial^2 \psi_\beta}{\partial x^2} \bigg|_{y=y_1} dx + \int_0^1 \frac{\partial^2 \psi_a}{\partial y^2} \bigg|_{x=x_1} \frac{\partial^2 \psi_\beta}{\partial y^2} \bigg|_{x=x_1} dy \right) \quad (15) \end{aligned}$$

$$\begin{aligned} (b_{a\beta}) = & \iint \psi_a \psi_\beta dS \\ & + \eta \left(\int_0^1 \psi_a \bigg|_{y=y_1} \psi_\beta \bigg|_{y=y_1} dx + \int_0^1 \psi_a \bigg|_{x=x_1} \psi_\beta \bigg|_{x=x_1} dy \right) \quad (16) \end{aligned}$$

where

$$\lambda = \frac{\rho_p \omega^2}{D} \quad (17)$$

and

$$\gamma = \frac{E I}{D} \quad (18)$$

$$\eta = \frac{\rho_s}{\rho_p} \quad (19)$$

Once the eigenvalue problem defined in eqn (14) is solved, the m-th mode shape, $W_m(x,y)$, corresponding to the m-th eigenvalue, λ_m , can be computed by using the eigenvector, (c_m) , in eqn (14). Additionally, the sensitivity of eigenvalue with respect to design parameters can be obtained by direct differentiating eqn (14). That is,

$$\frac{\partial \lambda_m}{\partial z} = c_m^T \left(\frac{\partial A}{\partial z} - \lambda_m \frac{\partial B}{\partial z} \right) c_m / (c_m^T B c_m) \quad (20)$$

where z is a design parameter such as plate thickness, rigidity of stiffeners, or support location. It should be noted that if closed form of the elements of the matrices, A and B , of the design parameters were available, the eigenvalue sensitivity analysis can be carried out readily.

SOLUTION PROCEDURE

Equation (14) is a generalized eigenvalue problem whose solution routine is readily available once the components of the matrices, A and B , are found. However, the evaluation of $a_{\alpha\beta}$ and $b_{\alpha\beta}$ involves formidable amount of algebra by human hands and is best carried out by symbolic algebra software. First, a trial polynomial function $\psi(x,y)$ that satisfies the support constraint conditions of eqn (8) as well as the free boundary conditions of eqns (4)-(7) is sought.

It is assumed that $\psi_j(x,y)$ is constructed from a series of polynomials as

$$\psi_j(x,y) = \sum_i h_i^j u_i(x,y) \quad (21)$$

where

$$u_i(x,y) = x^{L_i} y^{M_i} \quad (22)$$

(L_i and M_i are integers)

The coefficients, h_i , can be determined so as to satisfy the given boundary conditions and support constraints. The minimum order of polynomials, $\psi(x,y)$, is chosen in such a way that the number of unknowns (h_i 's) equals or exceeds the number of constraints plus the number of boundary conditions. For this case, the boundary conditions at each side (eqs (4)-(7)) yield $4 \times (2N-3)$ conditions. If the number of supporting points is M and the order of polynomials is N , N has to be chosen to satisfy the following inequality:

$$(N+1)(N+2)/2 \geq 4(2N-3) + M \quad (23)$$

For example, if there are four supporting points ($M=4$), the minimum order of polynomial (for both x and y) is twelve ($N=12$). Symbolic algebra software, REDUCE, has been used to generate a FORTRAN compatible code by actually evaluating eqs (4)-(7) for eqn (21), which yields coefficients of a set of simultaneous equations for unknown h_i^j 's. This set of indefinite simultaneous equations can be solved by a routine numerical method, thus, a polynomial that satisfies both the free-edge boundary conditions and the supporting condition can be obtained. REDUCE was also used to facilitate eqs (15)-(16) by expressing each component of the matrices, $a_{\alpha\beta}$ and $b_{\alpha\beta}$, as functions of h_i^j 's, thus avoiding time-consuming numerical integrals. Once the components of A and B are at hand, the generalized eigenvalue problem (eqn (14)) can be easily carried out by a routine numerical method. It is believed that this is the first time a systematically automated procedure is used to produce trial

functions that satisfy the natural boundary conditions.

For a given problem once we solve the generalized eigenvalue problem of eqn (14), the eigenvalue sensitivity can be computer using eqn (20). It should be noted that the required matrix derivatives, $\partial A/\partial z$ and $\partial B/\partial z$, can be carried out analytically for specific design parameters.

NUMERICAL RESULTS AND DISCUSSION

As an illustrative example, a square plate (unit length) supported at four interior points $((x,y)=(\beta,\beta),(1-\beta,\beta),(\beta,1-\beta),(1-\beta,1-\beta), 0<\beta<1)$ is selected for this study since a comparison with finite element is possible for the same geometry without stiffeners [6]. The plate is reinforced by four stiffeners that pass each support point $(x=\beta,1-\beta, y=\beta,1-\beta)$.

As was discussed in the previous section, $\psi(x,y)$ is assumed to be a twelfth-order polynomial on both x and y . A simple calculation reveals that seven linearly independent solutions for h_1 's are available for this geometry which yields seven distinct eigenvalues. Table 1 shows a result of the lowest three eigenvalues for different aspect ratios, β , as well as the different flexural rigidity ratios of the plate to the stiffeners, γ . For simplicity, the mass density ratio, η , was set to be unity. Table 1 also shows the results for the same geometry without stiffeners compared with those calculated by finite element method [6]. The effect of stiffeners is clearly demonstrated.

Several extensions are possible using this approach. Orthotropic plates or anisotropic plates can be easily handled. Addition of extra stiffeners is incorporated by additional integrals in eqs (15)-(16).

The present approach is particularly suitable for sensitivity analysis as

Aspect ratio β		No stiffeners	$\gamma=2$	$\gamma=5$	$\gamma=10$	FEM (no stiffeners) [6]
0.1	$\lambda_1=$	10.14	13.29	19.18	26.02	12.89
	$\lambda_2=$	21.30	18.93	35.04	35.04	19.69
	$\lambda_3=$	25.17	22.78	44.15	44.15	23.97
0.2	$\lambda_1=$	17.22	20.06	28.84	39.21	19.69
	$\lambda_2=$	23.84	29.54	43.11	58.72	23.13
	$\lambda_3=$	37.37	34.08	47.56	64.21	32.56
0.3	$\lambda_1=$	13.88	16.99	24.78	33.95	19.31
	$\lambda_2=$	23.03	27.64	39.36	51.47	19.72
	$\lambda_3=$	28.09	29.79	39.94	53.45	24.30

Table 1. Natural frequency, λ , of square plate with stiffeners. γ is the ratio of flexural rigidity of stiffeners to the plate.

it can retain all the relevant parameters in the formulation. Results will be reported subsequently.

REFERENCES

- [1] A. Hearn, *REDUCE User's Manual*, Rand Corporation, Santa Monica, CA (1987).
- [2] A. Haji-Sheikh, "On Solution of Parabolic Partial Differential Equation Using Galerkin Functions," *Integral Methods in Science and Engineering*, F. Payne, et al., Eds, Hemisphere Pub., 467-479 (1986).
- [3] S. Nomura and A. Haji-Sheikh, "Analysis of Transient Heat Conduction in Complex Shaped Composites," Journal of Engineering Materials and Technology, vol.110, pp.110-112 (1988).
- [4] S. Nomura and B.P. Wang, "Free Vibration of Plate by Integral Method", Computers & Structures, in press (1988).
- [5] S.P. Timoshenko and S. Woinowsky-Krieger, *Theory of Plates and Sheels*, McGraw-Hill, New York (1959).
- [6] R.D. Blevins, *Formulas for Natural Frequency and Mode Shape*, Van Nostrand Reinhold Company, New York (1979).

VIBRATION CONTROL

SHOCK ISOLATION USING AN ACTIVE MAGNETOSTRICTIVE ELEMENT

Robert S. Reed
Associate Professor
Systems Engineering Department
U.S. Naval Academy
Annapolis, MD 21402-5025

ABSTRACT

Materials with a high degree of magnetostriction have been developed at The Naval Surface Warfare Center. Devices have been constructed and tested to demonstrate the ability of this material to actively modify the vibration characteristics of structures. The effort reported here demonstrates the ability of these materials to isolate a platform in the presence of shock inputs at the base using magnetostrictive elements with appropriate feedback. A small vibrator was constructed using a magnetostrictive actuator. The device was attached to a massive base. Models were developed, experiments were completed and a controller was designed to demonstrate the ability of the magnetostrictive actuator to reduce the shock levels at the platform.

INTRODUCTION

The magnetostrictive effect in materials, changes in geometry when exposed to a magnetic field, was first discovered and studied in 1940 [1]. The reference, which is current, gives a brief history of the discovery and development of the materials. At that time the amount of strain which could be generated was restricted to 50 ppm (parts per million). Dr. Arthur E. Clark [2] and other researchers at Naval Surface Warfare Center have developed highly magnetostrictive materials which are alloys of iron (Fe) with the rare earths dysprosium (Dy) and Terbium (Tb). They have been given the name Terfenol. The materials were further developed and manufacturing techniques improved by O. D. McMasters of Ames Laboratory [1]. These highly magnetostrictive materials, 2000 ppm, are now commercially available in a variety of configurations from Edge Technologies Inc., Ames Iowa, and are finding application as high force low displacement actuators. A magnetostrictive actuator was fabricated and modeled [3] in a previous effort. The actuator was then used to actively reduce the response of a platform which was attached to a base which was undergoing sinusoidal vibration [4]. The effort reported here will focus on the application of the magnetostrictive actuator to the reduction of shock levels on a platform which is supported by a base which is experiencing shock inputs.

THE VIBRATOR

In order to demonstrate the application of the material to the shock and vibration isolation problem, a magnetostrictive vibrator was fabricated. Figure 1 below shows the magnetostrictive vibrator which was used to study the shock and vibration applications of the actuator. Also shown in the figure are the external disturbances and readily available feedback transducers which could be used to accomplish the desired control. Figure 1 also shows a block which is the potential controller of the device. The block accepts the feedback signals and sends the correcting currents to the device. The design of this controller although not the main purpose of this effort will be discussed below. Figure 1 shows the feedback signals namely strain, or relative displacement, base acceleration and finally the platform acceleration. The purpose of this effort is to reduce the activity of the platform accelerometer.

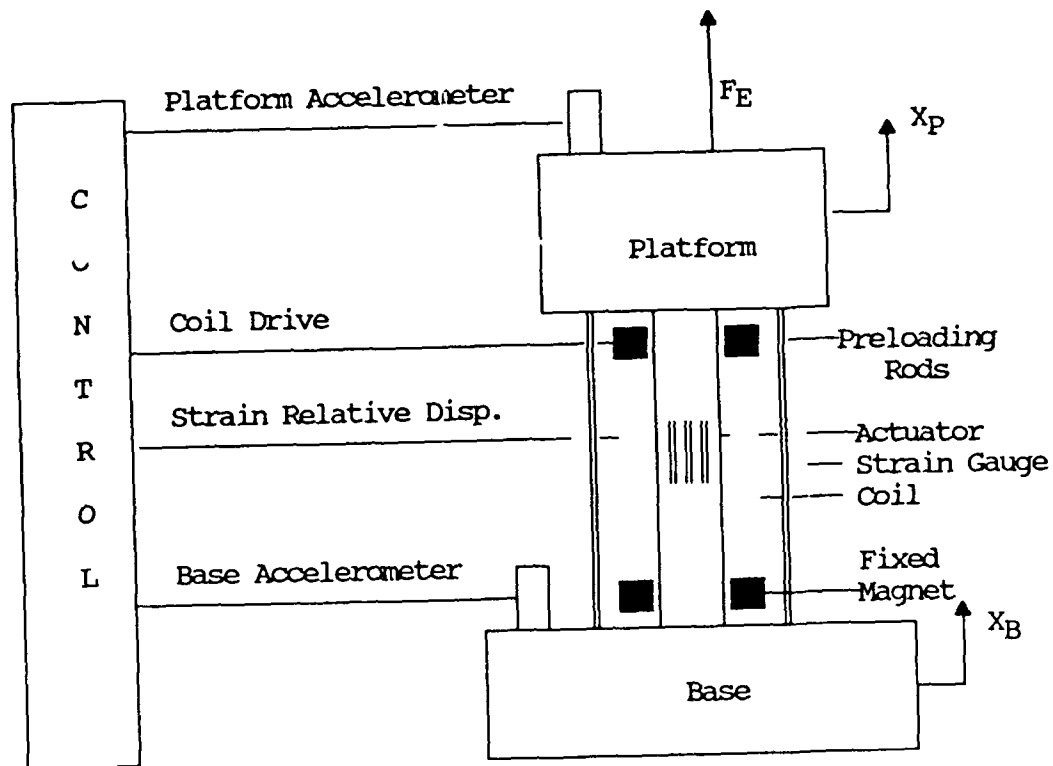


Figure 1 Instrumented Magnetostrictive Vibrator

THE ACTUATOR

The performance of these actuators has been studied in static [2] as well as dynamic [3],[4] situations. Reference [2] gives the strain versus magnetic field strength for several different alloys. The alloy $Tb_{.27} Dy_{.73} Fe_{1.95}$ was used for this effort. Experiments have indicated that the performance is influenced by loading. Since the actuator is preloaded and is opposing a spring like resistance, the performance will differ from the constant load curves of reference [2]. The strain versus current was measured for currents between plus and minus five

amperes and also for a one ampere peak sinusoidal input with a one ampere bias. The results are shown in Figure 2. It is important to note that the material elongation versus magnetic field strength is symmetric about the strain axis [2]. The actuator must therefore be operated with a bias in order to have bidirectional control. The coil for these test was fabricated with fixed magnets at the ends. This supplies a small bias to the actuator which is evident in the end points of Figure 2. The figure is not intended to indicate the extremes of the actuator displacement. The amplifier was limited to five amperes. If higher current values were used in the testing it would be necessary to cool the test apparatus. The actual limits of the elongation for a three inch rod would be approximately 0.006 inches in a single direction or 0.003 in a bidirectional application. For a single cycle 1 kilohertz sinusoidal input the displacement limitation translates to plus and minus 100 G's. The actuator was operated at a moderate 1 ampere bias figure 2. for all dynamic test. This will also, hopefully, reduce the affects or the non-linearity of the device.

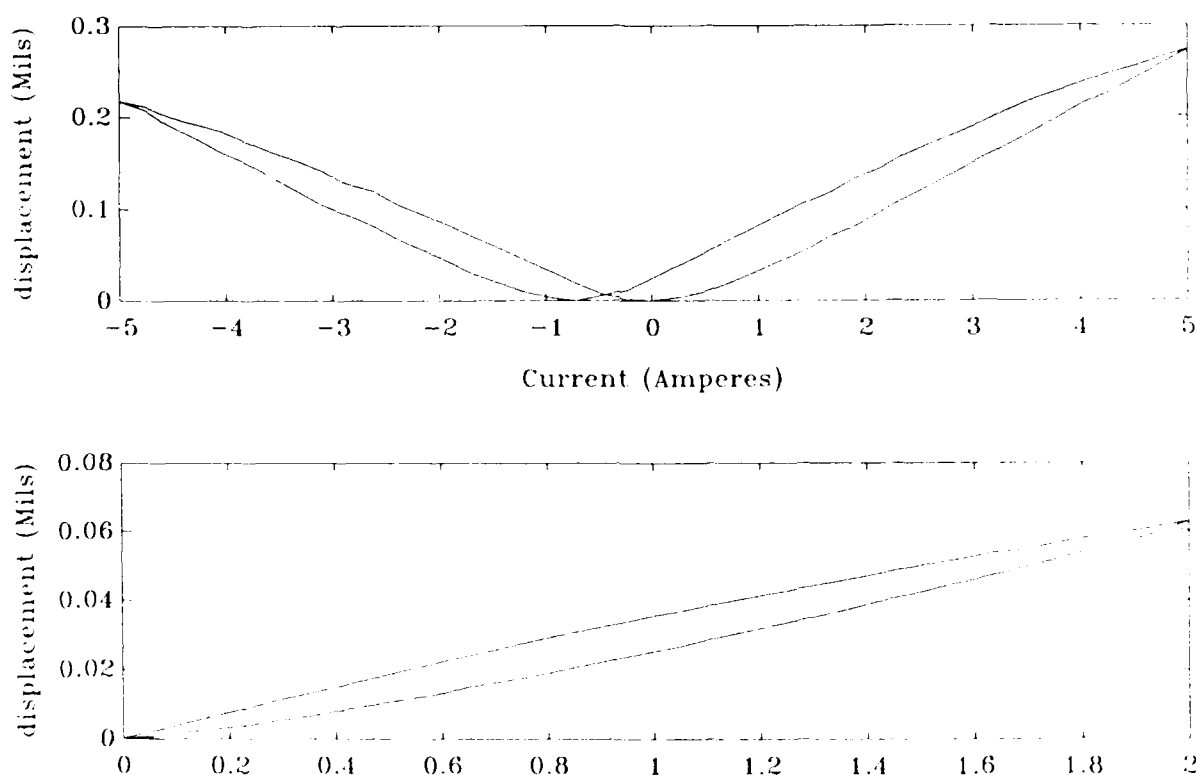


Figure 2 Displacement vs. Current for Actuator

SYSTEM MODEL

In order to study the behavior of the vibrator, a model was developed. The block diagram is shown in Figure 3. The model includes the inputs X_B -base motion, F_E -external force and E_I -input voltage. The relative motion between the base and platform is shown as X_R . The platform motion, the output, is shown as X_T . The additional constants in the model include A -amplifier gain, R -coil resistance, L -coil inductance, K_F -actuator force constant, M -mass, K -stiffness, C -damping, and K_B -actuator feedback voltage constant. In addition, the block diagram includes two feedback paths H_1 and H_2 . The H_1 and H_2 feedbacks represent the relative motion

sensors, which might be a strain gauge, and total motion sensors, which might be an acceleration. In order to eliminate the phase lag and attenuation caused by the coil a current feedback loop was added to the model and is shown in the Figure 3 as unity feedback on the amplifier. The transfer function platform motion for applied voltage with feedback was computed and is shown in equation (1). The platform motion over base motion is shown in equation (2). The objective here is to control the platform response in the presence of the external disturbances. Using the model with voltage E_I input is convenient for both the experiments and the modeling.

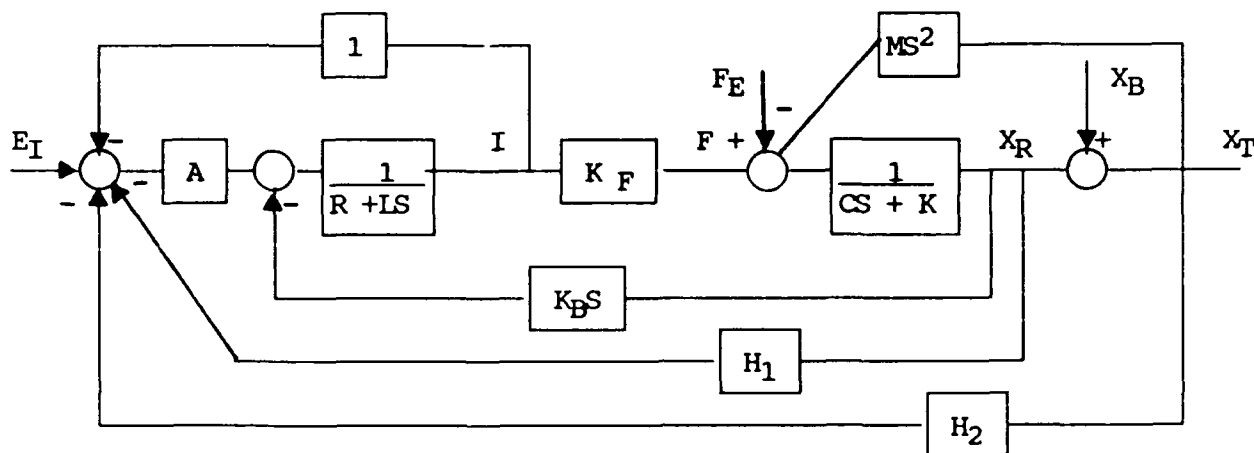


Figure 3 Block Diagram of Vibrator With Feedback

$$\frac{X_T}{E_I} = \frac{AK_F}{MLS^3 + (LC+MR+MA)S^2 + (KL+RC+AC+K_F K_B)S + (RK+AK+AK_F(H_1+H_2))} \quad (1)$$

$$\frac{X_T}{X_B} = \frac{LCS^2 + (LK+RC+AC+K_F K_B)S + (KR+KA+AK_F H_1)}{MLS^3 + (LC+MR+MA)S^2 + (KL+RC+AC+K_F K_B)S + (RK+AK+AK_F(H_1+H_2))} \quad (2)$$

If it is assumed that the electrical elements of the system are much faster than the mechanical elements, a standard practice in low frequency servo systems, the system model simplifies. If amplifier gain A approaches infinity, the transfer functions simplify and are shown in equations (3) and (4). These equations will be useful for studying the effects of feedback.

$$\frac{X_T}{E_I} = \frac{K_F}{MS^2 + CS + K + K_F H_1 + K_F H_2} \quad (3)$$

$$\frac{X_T}{X_B} = \frac{CS + K + K_F H_1}{MS^2 + CS + K + K_F H_1 + K_F H_2} \quad (4)$$

Experiments have indicated, as will be shown later, that the system contains at least four poles. The true characteristics of the compensated amplifier A add a pole to the system and change equation (1) and (2) significantly. The simplification to two poles is useful for visualizing the effects of feedback on system performance.

The important thing to note in the equations is that the relative feedback occurs in both the numerator and denominator. The total motion feedback appears only in the denominator. This has an interesting implication. If for example, the effective stiffness is increased using strain feedback the low frequency gain will be unaffected. If total platform displacement is used for displacement feedback, only the denominator constant term is increased. This will reduce the low frequency gain of the system, causing less platform motion. This is the objective of this effort. The other possible use of the relative displacement feedback would be to change the system to a low frequency system. This could be done with positive displacement feedback and negative acceleration feedback. This would therefore increase the apparent mass and reduce the apparent stiffness. This approach was not attempted here. For this effort only relative motion feedback of the strain rate will be considered. The strain rate feedback would be useful to synthetically increase damping and thus reduce the resonant amplification. The alternate approach to design of a controller is to sense the base motion and input the negative to the actuator. This would be an open-loop system but it is an attractive approach because of the simplicity. This will not be studied in any detail here.

Consider using devices, that sense the actual platform motion and the first two derivatives. For this case the $K_F H_2$ feedback takes the form of equation (5). Here the h_A is acceleration gain, h_V is velocity gain and h_D is displacement gain of the feedback device.

$$K_F H_2 = h_A S^2 + h_V S + h_D \quad (5)$$

The strain rate feedback could be modeled as shown in (6). Here the strain rate gain is given by e_R .

$$K_F H_1 = e_R S \quad (6)$$

With these feedbacks included in equation (4), the transfer function becomes equation (7) below.

$$\frac{X_T}{X_B} = \frac{(C + e_R)S + K}{(M + h_A)S^2 + (C + h_V + e_R)S + (K + h_D)} \quad (7)$$

These effects of the various feedbacks were modeled using MATLAB [4] and are shown below along with a hypothetical input. The model was made to be consistent with the actual device. That is, natural frequency 1585 Hertz and fraction of critical damping of 0.05. The input is a 1 khz single cycle 100 G base acceleration. Figure 4 shows the input acceleration, velocity and displacement. This input also shows graphically the displacement and velocity extremes of a

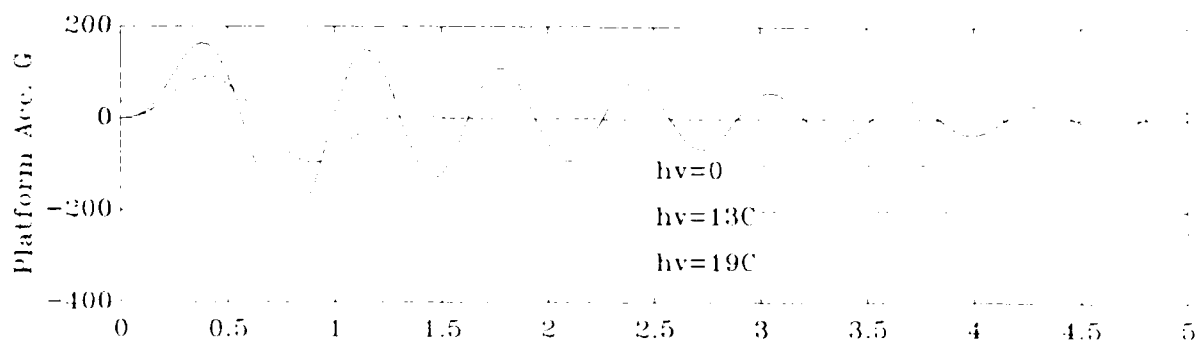
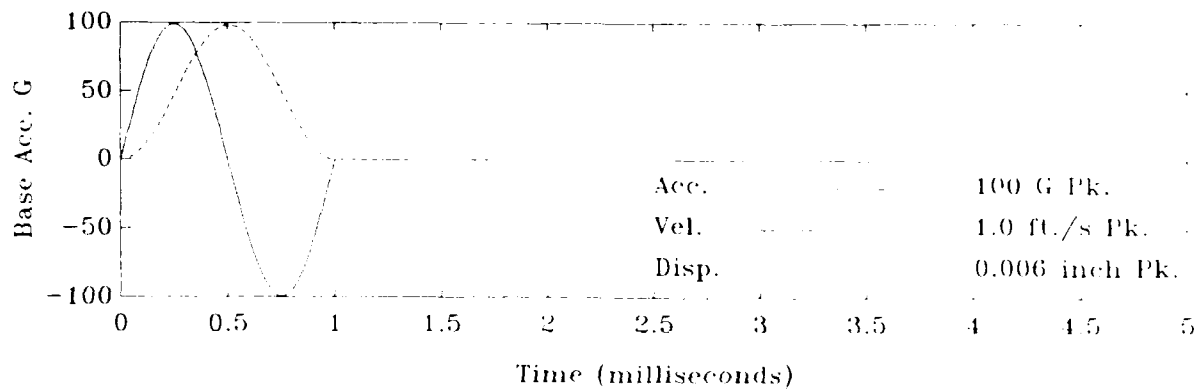


Figure 4 Input and Response with Rate Feedback

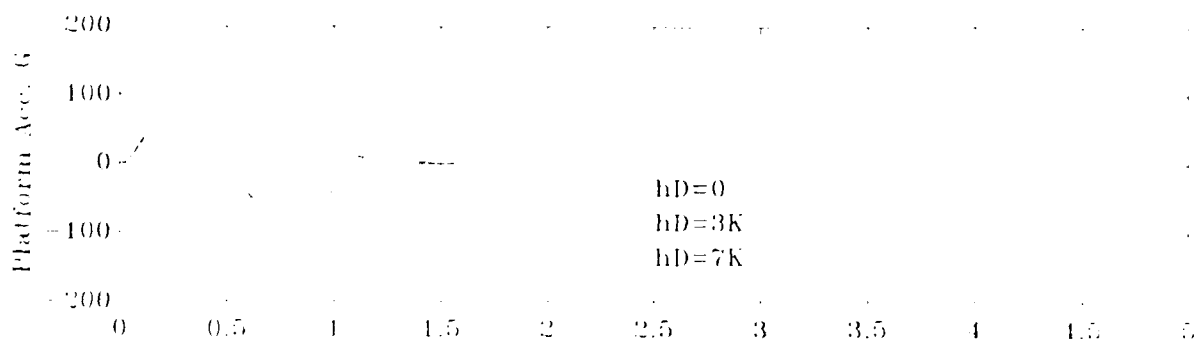
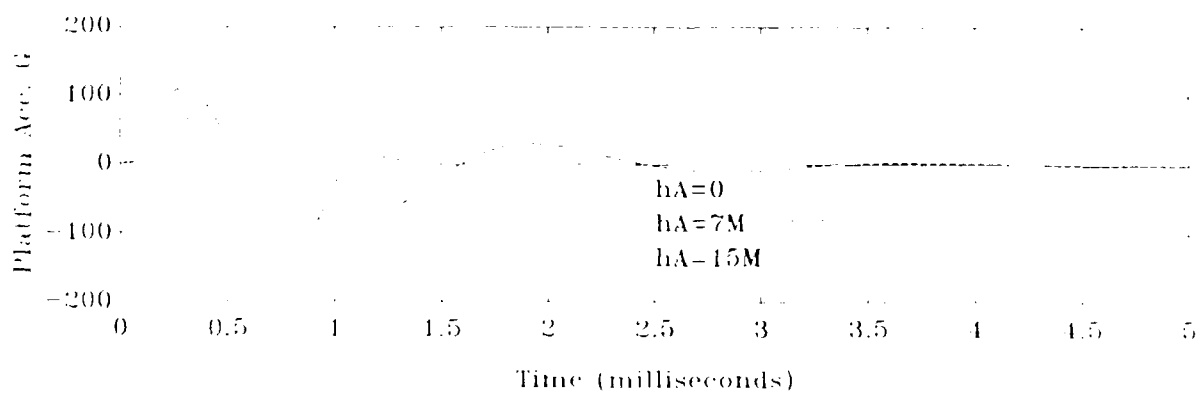


Figure 5 Effects of Displacement and Acceleration Feedback

three inch actuator for this particular input. The affects of total velocity feedback are shown for several h_v values. As a reference on the value of h_v note that $h_v=19C$ would be critical damping as a result of making c 20 times the current value.

Figure 5 shows the effects of the total velocity and total acceleration feedback. Here again $h_A=3M$ indicates the apparent mass is four times the actual value and $h_D=3k$ indicates the apparent stiffness is four times the original value. In both cases the h_v feedback was set to $h_v=13C$ which results in 0.707 for fraction of critical damping in the denominator.

EXPERIMENTS

The vibrator and base mass of Figure 1 were placed on a soft support, in order to eliminate any effects from the structure supporting the apparatus. In the realistic application, the base impedances would be seen as an additional feedback loop in Figure 3. This would have a significant affect on the controller design. The vibrator was then driven with a sinusoidal input voltage (50 mv-pk) to measure the frequency response function (Bode Plot [6]). The measured Bode diagram platform acceleration over drive voltage is show in Figure 6 with the symbol (*).

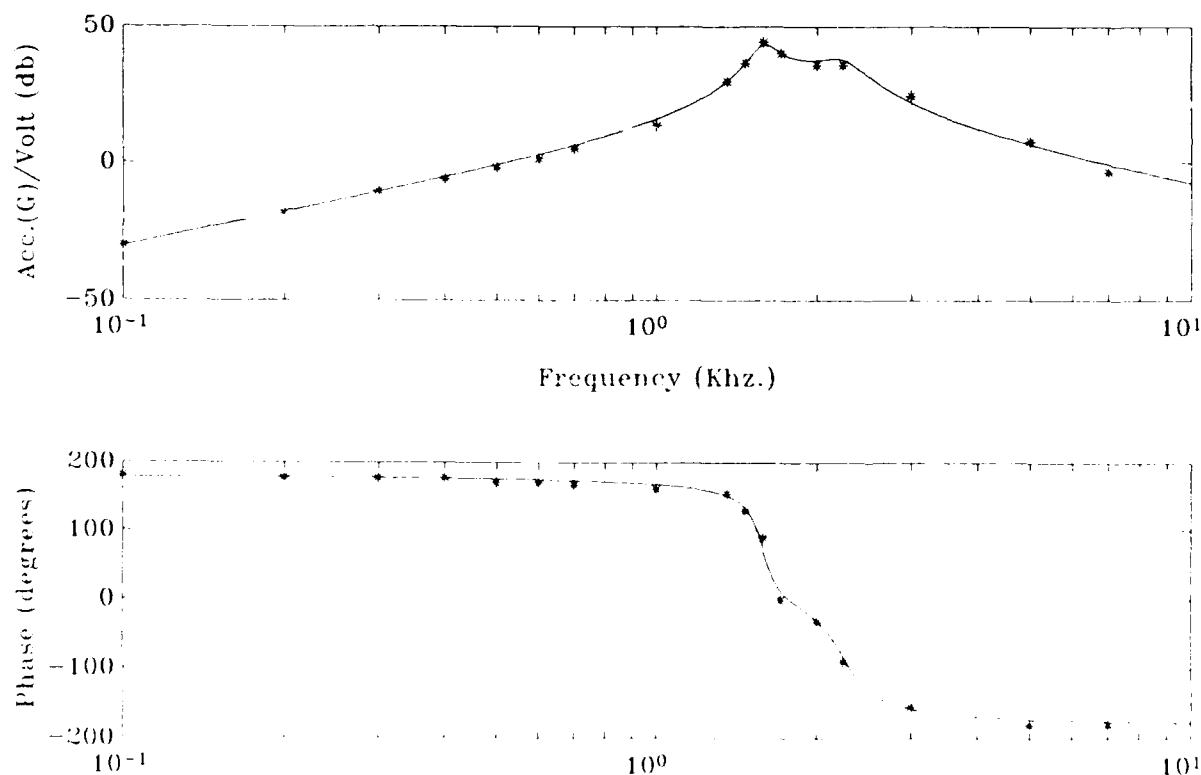


Figure 6 Measured and Modeled Transfer Function

The rapid 360 degree phase transition indicates that two complex conjugate pairs

of roots are needed to model the system. A system model is also shown in Figure 6 with solid lines. The system was determined to have natural frequencies at 1585 Hertz and 2239 Hertz with fraction of critical damping of 0.05 in the first and 0.10 in the second.

The expression for the transfer function is shown in equation (8). The equation has been time scaled by making the substitution of $S=2000\sqrt{s}$. The roots of the denominators are now in kilohertz and the fraction of critical damping is unaffected. The displacement over drive voltage Bode diagram was calculated from the acceleration transfer function and is shown in Figure 7. This is consistent with the measurements of strain over drive voltage. The displacement transfer function is flat enough at low frequencies that an open-loop controller would probably be adequate for low frequency shock inputs. The addition of filters could eliminate the dual resonant rise and extend this useful frequency range.

$$\frac{\ddot{X}_T}{E_I} = \frac{39.4S^2}{(S^2 + 0.159S + 2.51)(S^2 + 0.448S + 5.01)} \quad (8)$$

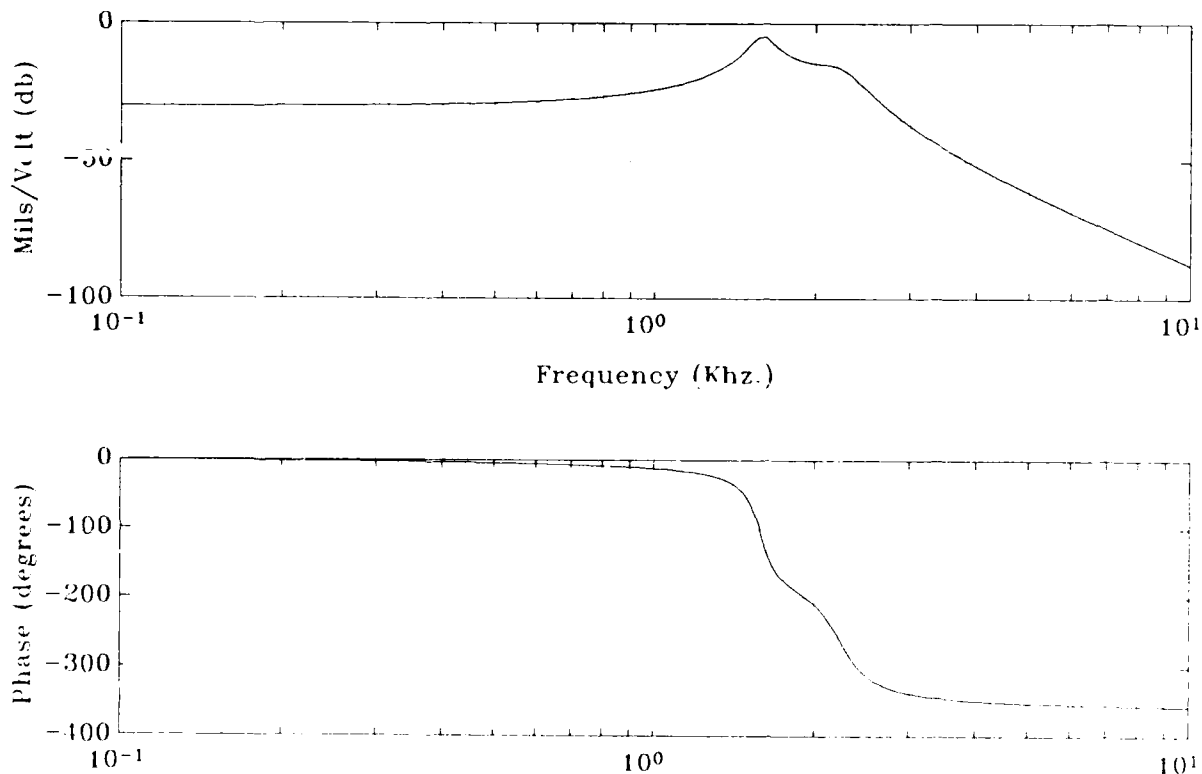


Figure 7 Displacement/Volts Transfer Function

Controller Design

The transfer function Figure 6 indicates the direct accelerometer feedback could be applied without reaching the conditions for instability (gain 1, 180 degrees phase lag [6]). This is in fact not quite true. Gains which were high enough to

significantly influence the frequency response were very close to the unstable condition. The phase margin was very small. With the acceleration gain at these high levels any disturbance of the apparatus caused unstable oscillations. This is believed to be a combination of the low gain margin, additional higher frequency poles and the fact that the non-linearity in the actuator shows up as increasing slope, or gain, when the current levels are increased. Several attempts to design the controller using Lag-Lead compensation [7] proved inadequate. The system therefore required a more complicated controller. The system was compensated using an observer [8]. This was accomplished by programming an analog computer to duplicate, in terms of input/output, the actual system. The added feedback required to change the performance was determined. This additional feedback was readily available in the analogous system. In order to modify the pole locations in the systems, an additional feedback term is required. The rate of change of acceleration (jerk) must be added to the feedback expression (5). The feedback with the added term, h_J , is shown in equation (9).

$$K_F H_2 = h_J S^3 + h_A S^2 + h_V S + h_D \quad (9)$$

The transfer functions, analogous and real, were changed by this feedback so that the new roots of the denominators occur as two complex pairs at 1600 and 3000 Hertz each with fraction of critical damping of 0.707. The compensated transfer function, acceleration over drive voltage, is shown in Figure 8.

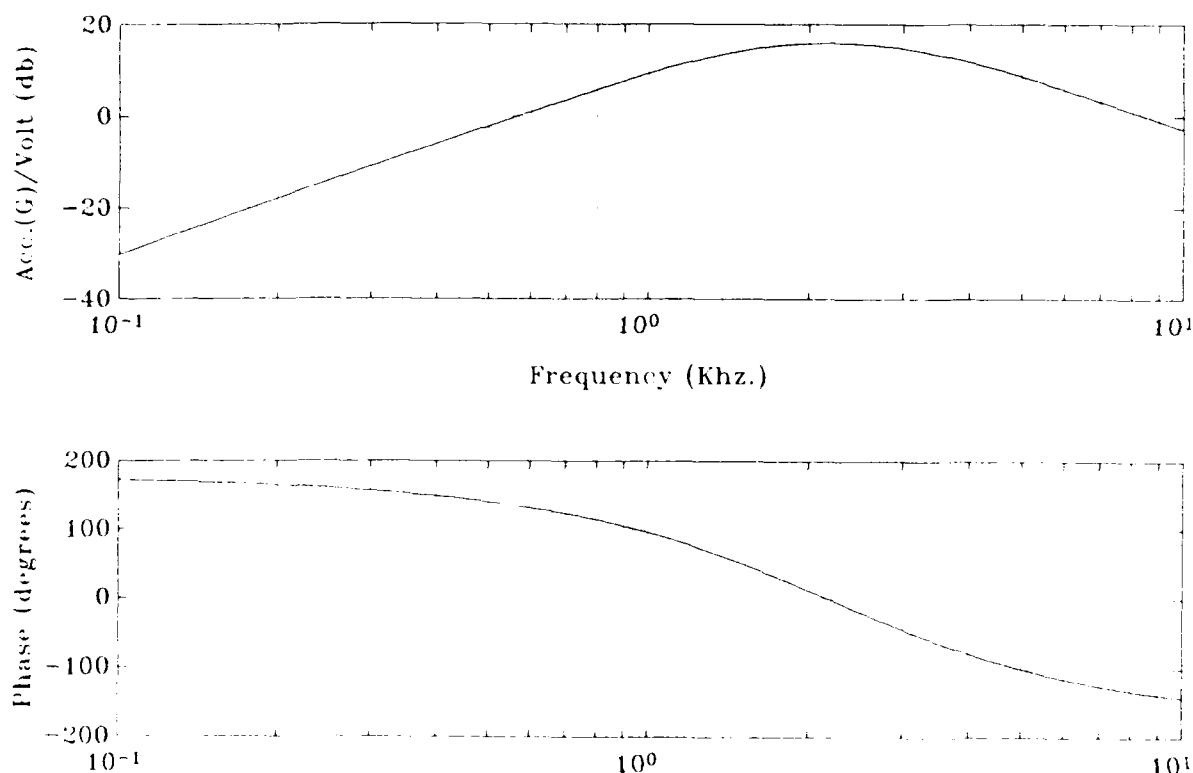


Figure 8 Compensated System Transfer Function

The acceleration over drive voltage transfer function is shown in equation (10)

below. The feedback terms in the denominator were calculated from the above requirements. Equation (11) shows the total motion over base motion transfer function.

$$\frac{\ddot{X}_T}{E_I} = \frac{39.4S^2}{(S^4 + (0.61+h_J)S^3 + (7.59+h_A)S^2 + (1.92+h_V+e_R)S + (12.6+h_D))} \quad (10)$$

$$\frac{X_T}{X_B} = \frac{S^4 + 0.61S^3 + 7.59S^2 + (1.92+e_R)S + 12.6}{(S^4 + (0.61+h_J)S^3 + (7.59+h_A)S^2 + (1.92+h_V+e_R)S + (12.6+h_D))} \quad (11)$$

The acceleration, h_A term, is the only readily available feedback from the real system. With this control approach [8] the error signal, in this case platform acceleration is input to the model as an acceleration disturbance. This acceleration disturbance to the duplicate system causes the appropriate corrections to be input to the real system.

The final test was run by striking the base of the apparatus and measuring the response with and without acceleration feedback. The base acceleration and platform acceleration with and without feedback are shown in Figure 9. Inspection of the figure reveals that the feedback changed the natural frequency and increased the damping.

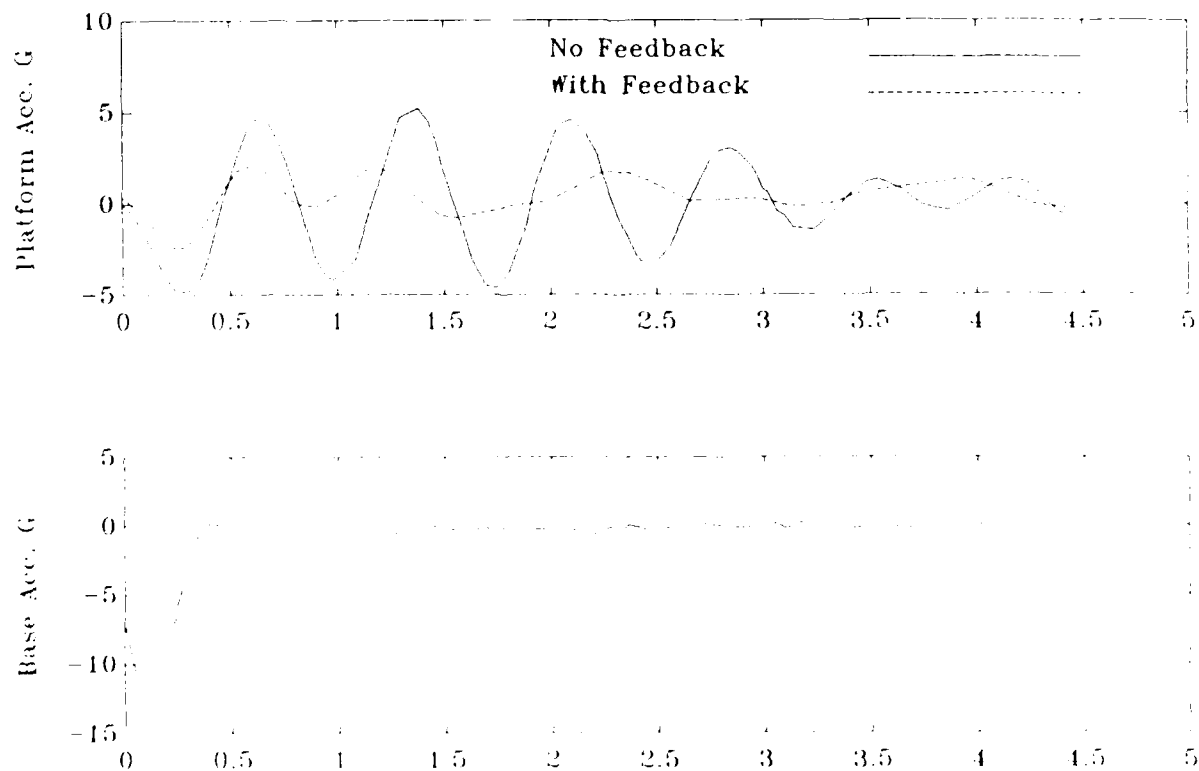


Figure 9 Measured Platform Response and Base Input

The magnetostrictive actuator is very obviously reducing the platform response in the presence of the base input. The response to the 11.5 G input to the base is approximately 5 G peak and is lightly damped in the uncontrolled vibrator. The compensated system has a peak of about 2 G and is more heavily damped.

RESULTS AND CONCLUSIONS

The tests have shown that, for this simple system, the shock response of the platform can be reduced using a magnetostrictive actuator. The particular isolation problem studied, that of reducing platform motion in the presence of base motion, should have numerous applications. The developers of the material [2] have indicated that results from tests using small samples scale well when used in larger applications. The controller did not eliminate entirely the motion of the platform. Current efforts are focusing on eliminating completely the platform response in the presence of base motion and other disturbances using some combination of the available feedback signals and optimization techniques.

ACKNOWLEDGEMENTS

The effort reported here was partly supported by the Naval Surface Warfare Center where the material was developed. Dr. Arthur E. Clark, one of the developers of the material, was very helpful in the original formulation of this problem and has been very supportive in this and other studies of the applications of the material.

REFERENCES

1. Butler, J. L., Application Manual for Design of Etrema Terfenol-D Magnetostrictive Transducers, Edge Technologies Inc, Ames, Iowa, 1988.
2. Clark, A. E., Spano M. L. and Savage H. T., "Effect of Stress On Magnetostriction and Magnetization of Rare Earth-Fe Alloys", IEEE Transaction On Magnetics, VOL. MAG-19, No. 5, September 1983.
3. Reed, R. S. and Uldrick, J. P., "Model of a Magnetostrictive Actuator with Application to Simple Systems", Modeling and Simulation Vol 19, 1988.
4. Reed, R. S., "Active Vibration Isolation Using a Magnetostrictive Actuator", Modeling and Simulation Vol 19, 1988.
5. Moler, C., Little, J., Bangert, S. and Kleiman, S., PC-MATLAB, The MathWorks, Inc. 1987
6. Ogata K., Modern Control Engineering, Printice-Hall Inc., Englewood Cliffs, N. J., 1970
7. Elbert, T. F., Estimation and Control of Systems, Van Nostrand Reinhold, New York, 1984

PREDICTION OF MODAL CHARACTERISTICS AND HARMONIC RESPONSE OF VISCOELASTICALLY DAMPED STRUCTURES

H. T. Zhou*, J. Der Hagopian, G. Ferraris, M. Lalanne I.N.S.A.,
Laboratoire de Mécanique des Structures
U.A. C.N.R.S. 255-20, avenue Albert Einstein 69621
Villeurbanne, France

This work is concerned with the modal characteristics and the harmonic response of viscoelastically damped structures which contain a large number of degrees of freedom and with non proportional damping. A pseudo-modal method is recalled, and an application is presented. The influence of the number of modes used is shown and the comparison between experiment and prediction is satisfactory.

INTRODUCTION

Structure vibration control is more and more necessary today and the use of viscoelastic elements is now common in engineering structures to get a significant damping. The prediction of the dynamic behavior of structures with viscoelastic elements is of great interest as shown in [1], [2]. More specifically it is frequently necessary to be able to predict modal characteristics - frequencies of resonance and associated modal damping - and the steady state response to harmonic excitation forces. Previously [3], [4] a method was proposed. Basically the structure is modelled using finite elements, then because of the high number of degrees of freedom, the response of the structure to a harmonic excitation is quite impossible to obtain. A pseudo-modal method was then developed and used, the number of degrees of freedom was thus highly reduced and the method was applied to engineering structures such as in [5]. The first aim of this work is to check the influence of the number of modes on the response to a harmonic excitation force. The other aim is to present a relatively complex viscoelastically damped structure with all the data. This structure was tested and all the characteristics are given in such a way that they could be used by others involved in prediction problems to check methods.

PSEUDO-MODAL METHOD

The method has been presented in [3], [4] and is briefly recalled. In complex notation the steady state harmonic response of the structure is given by the solution of the system :

$$(-\Omega^2 M + j\eta_v K_v + K)X = F \quad (1)$$

* On leave 11-87, 11-88 from Jiao Tong University - Shanghai.

where M and K are respectively the mass and the stiffness matrices of the entire structure and K_v , the stiffness matrix of the viscoelastic element. The order of equation is N and η_v is the structural damping factor of the viscoelastic material. The harmonic excitation force $F(t)$ and the displacement vector $x = x(t)$ are such that :

$$x = X e^{j\Omega t} \quad (2)$$

$$= (X_r + jX_i) e^{j\Omega t} \quad (3)$$

$$F(t) = F e^{j\Omega t} \quad (4)$$

$$= (F_r + j F_i) e^{j\Omega t} \quad (5)$$

where Ω is the excitation frequency and r and i the subscripts of the real and imaginary parts.

At first the modes of the structure supposed undamped are sought. They come from the solution of the eigenvalue-eigenvector problem associated with :

$$Mx'' + Kx = 0 \quad (6)$$

An average value E_{v0} of $E_v = E_v(\Omega)$, real part of the Young's modulus of the viscoelastic material is used to determine K . Then the $n \ll N$ lowest frequencies and the corresponding modes ϕ_1, \dots, ϕ_n are used to transform the initial equation by :

$$x = (\phi_1, \dots, \phi_n) \begin{vmatrix} q_1 \\ \vdots \\ q_n \end{vmatrix} \quad (7)$$

$$= \phi \cdot q \quad (8)$$

Because of (2) and (4) :

$$q = Q e^{j\Omega t} \quad (9)$$

$$= (Q_r + jQ_i) e^{j\Omega t} \quad (10)$$

Premultiplying (1) by ϕ^t , where t is here the matrix transposition symbol, and using (5), (8) and (10) :

$$(-\Omega^2 \phi^t M \phi + j\eta_v \phi^t K_v \phi + \phi^t K \phi)(Q_r + jQ_i) = F_r + jF_i \quad (11)$$

The n equations of the system (11) are not independent as the matrix product $\phi^t K_v \phi$ has no reason to give a diagonal matrix but as n is small the system is now easy to solve. The identification of the real and the imaginary terms in (11) gives :

$$\begin{vmatrix} \phi^t K \phi - \Omega^2 \phi^t M \phi & ; & -\eta_v \phi^t K_v \phi \\ \eta_v \phi^t K_v \phi & ; & \phi^t K \phi - \Omega^2 \phi^t M \phi \end{vmatrix} \begin{vmatrix} Q_r \\ Q_i \end{vmatrix} = \begin{vmatrix} F_r \\ F_i \end{vmatrix} \quad (12)$$

System (12) is now solved for given values of Ω . The matrix product $\eta_v \phi^t K_v \phi$ is also a function of Ω as $\eta_v = \eta_v(\Omega)$ and as $\phi^t K_v \phi$ is proportional to $E_v = E_v(\Omega)$. Then from (12), $Q_r = Q_r(\Omega)$, $Q_i = Q_i(\Omega)$ are known and using (3) and (8) gives at last $X_r = X_r(\Omega)$, $X_i = X_i(\Omega)$.

In addition if the modes, as it often happens, are reasonably uncoupled the system can be conveniently modelled around the p^{th} resonance frequency of resonance ω_p by the equation :

$$(-\Omega^2 \phi_p^T M \phi_p + \phi_p^T K \phi_p + j\eta_{vp} \cdot \phi_p^T K_v \phi_p) Q = F \quad (13)$$

then a modal loss factor can be defined in comparing equation (13) and :

$$(-\Omega^2 \phi_p^T M \phi_p + \phi_p^T K \phi_p + j\eta_{gp} \cdot \phi_p^T K \phi_p) Q = F \quad (14)$$

Equations (13) and (14) gives :

$$\eta_{gp} = \eta_{vp} \frac{\phi_p^T K_v \phi_p}{\phi_p^T K \phi_p} \quad (15)$$

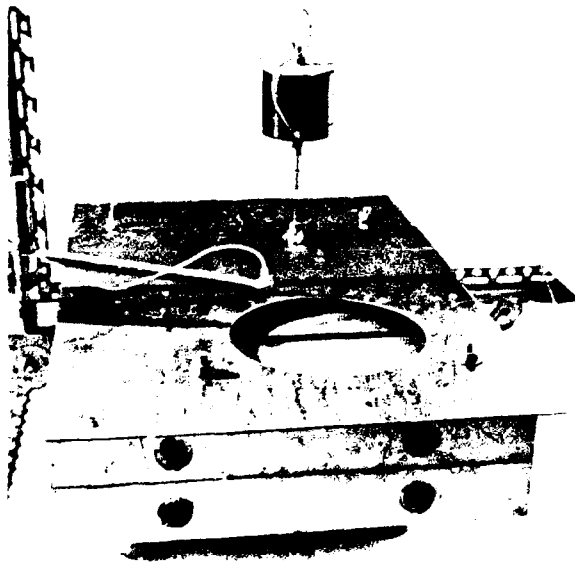
The quantities $\phi_p^T K_v \phi_p$ and $\phi_p^T K \phi_p$ are easily obtained when (6) is solved, but as the frequencies and modes are obtained with E_{vo} and as at $\Omega = \omega_p$, $E_v = E_v(\omega_p) = E_{vp}$ equation (15) has to be modified :

$$\eta_{gp} = \eta_{vp} \cdot \frac{E_{vp}}{E_{vo}} \frac{\phi_p^T K_v \phi_p}{\phi_p^T K \phi_p} \quad (16)$$

The modal loss factor η_{gp} is then obtained from (16) and the values of E_v , η_v (table 1).

APPLICATION

The application is the viscoelastically damped plate shown in photograph 1, the dimensions of which are given in millimeter figure 1. The dimensions of the steel element and of the viscoelastic element are respectively 600 x 398.5 x 2.06 and 398.5 x 160 x 2.



Photograph 1 : Damped plate

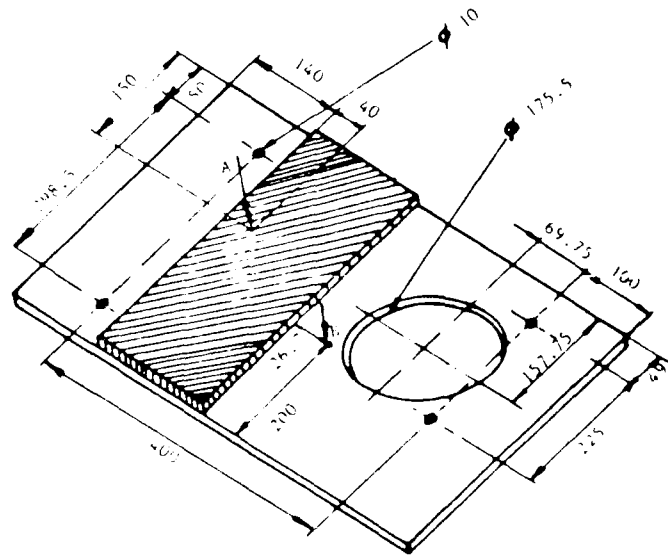


Figure 1 : Damped plate

The characteristics of the steel used are :

$$E = 1.97 \cdot 10^{11} \text{ N/m}^2 ; \quad \nu = 0.3 ; \quad \rho = 7870 \text{ kg/m}^3$$

with,

E , Young's modulus

ν , Poisson's ratio

ρ , mass per unit volume.

The structure was tested at 22.5°C and the characteristics $E_v(\Omega)$, $\eta_v(\Omega)$ of the viscoelastic material have been obtained, as described in [3], from the response of a beam damped on both sides and submitted to a harmonic force of excitation. The values are given in table 1.

Frequency Hz	19.7	60	120	160	220
$10^{-9} E_v \text{ N/m}^2$	2.05	2.4	2.8	3.1	3.4
η_v	0.74	0.74	0.73	0.71	0.65

Table 1 : E_v and η_v at 22.5°C as a function of frequency.

Poisson's ratio is taken equal to $\nu_v = 0.49$ and the mass per unit volume is $\rho_v = 1750 \text{ kg/m}^3$. A Solartron transferometer, characterised by a 120 db dynamic range, was used to drive the experiment. The force gage is small and the displacement is measured by an eddy current transducer. The experiments and calculations show d/F , where F is the amplitude of the force of excitation acting at point A and d the amplitude in the direction perpendicular to the plate of the displacement at point B, (figure 1).

The structure is modelled by the classical 16 nodes thick shell isoparametric element which has three degrees of freedom per node. The mass matrix is consistent and the structure has been modelled regularly with 171 finite elements. The number of nodes is 1105 which gives 3315 degrees of freedom. The mountings are such (see photograph 1) that the plate is supposed to be clamped at the four bolts, at a diameter of 0.02 m. The response d/F has been measured and calculated in the range 0-180 Hz. The response with $E_v = 3.10^9$ has been calculated as a function of the number of modes : $n = 1, 2, \dots, 8$ to show the influence of the modes, (figure 2). In figure 3 the results with $n = 10$ modes have been shown in a larger scale than in figure 2. The response is the same as for $n = 8$ and these results show a good agreement between measured and calculated results. Addition of supplementary modes $n = 11, 12, \dots$ does not change the results.

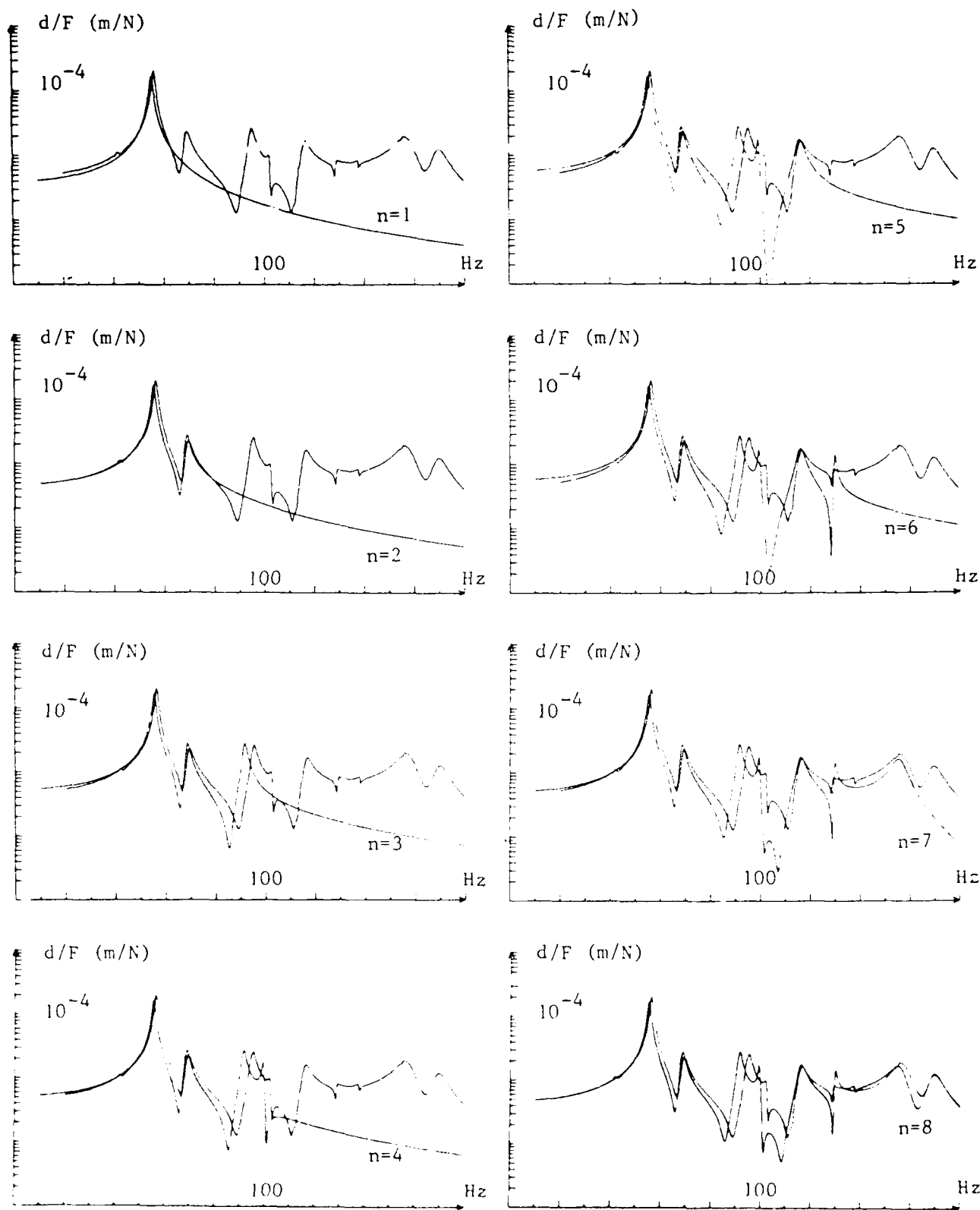


Figure 2 : Response d/F as a function of frequency for different number n of modes used for prediction.

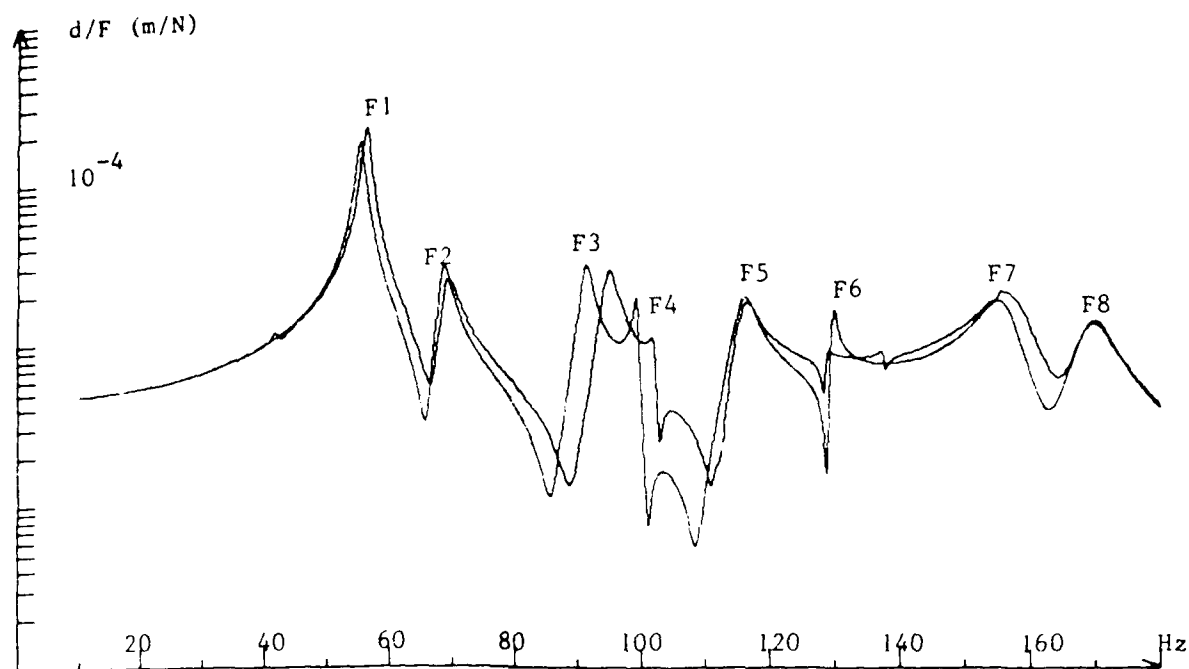


Figure 3 : Response d/F as a function of frequency with 10 modes.

In addition the modal loss factors are calculated using equation (16) and measured by the - 3 db bandwidth using the well known formula :

$$\eta_{gp} = \frac{\Delta \Omega}{\omega_p} \quad (17)$$

In table 2 the values of the frequencies of the resonance of the modal loss factor calculated (C) and measured (M) are presented and the agreement is satisfactory.

MODE		1	2	3	4	5	6	7	8
F Hz	M	56.4	69.5	95.3	105	117	129	158	170
	C	55.4	68.8	91.7	99.4	116	130	155	170
$10^2 \eta_g$	M	2.3	3.7	2.6	--	3.4	--	4.9	3.4
	C	2.3	2.6	2	0.8	2.8	0.7	3.8	3.2

Table 2 : Measured (M) and calculated (C) values of the 8 first resonance frequencies of resonance and modal dampings.

CONCLUSION

A pseudo modal method has been applied to a relatively complex structure the characteristics of which have been given. The comparison of the measurements and predictions has been made as a function of the number of modes and the agreement is shown to be satisfactory.

ACKNOWLEDGEMENTS

The authors are indepted to METRAVIB for having provided the viscoelastic material.

REFERENCES

- [1] J. Soovere, M.L. Drake, "Aerospace structure technology damping design guide," AFWAL-TR-84-3089, 1985
- [2] A.H. Nashif, D.I.G. Jones, J.P. Henderson, "Vibration damping," J. Wiley, 1985
- [3] M. Lalanne, M. Paulard, P. Trompette, "Response of thick structures damped by viscoelastic material with applications to layered beams and plates," 45th Shock and Vib. Bull., 1975
- [4] M. Lalanne, P. Berthier, J. Der Hagopian, "Mechanical vibrations for engineers," J. Wiley, 1983
- [5] P. Trompette, M. Paulard, M. Lalanne, D.I.G. Jones, M. Parin, "Prediction of modal damping of jet engine stator vanes using finite element techniques," A.S.M.E. Paper 76-GT-60, 1976

NEW STRUCTURE DESIGN CRITERIA OFFER IMPROVED POINTING AND LOWER WEIGHT

L. Porter Davis and Dr. James F. Wilson

Honeywell Inc.
Satellite Systems Division
Glendale, AZ

A new design approach for large space structures, based on dynamic performance, offers significant pointing performance improvements. Passive damping is employed as a dynamic structural element working in conjunction with conventional static structural elements to provide optimal performance. Comparisons of various aspects of space structure performance are discussed and structure figures of merit are examined. Settling time emerges as the most significant performance parameter. Through an integrated stiffness-damping design process, it is possible to maximize the ratio of these parameters (settling time/weight). Quantitative results are obtained and compared for a specific application.

INTRODUCTION

A revolution will take place over the next decade in the way spacecraft structures will be designed and built. The change will come about because of damping. However, it is not simple to change the way engineers approach the design problem, the way they think, or the structure design criteria they use. That is primarily what this paper is about: a new way to guide the design of space structure. Once this is understood, it will become clearer why so much is being said about damping and why a revolution in design of space structure is underway. An example will be provided to show how a structure using new design criteria significantly out-performs a design based on maximum stiffness-to-weight ratio.

To introduce the subject of design criteria, it might be helpful to relate a conversation that took place in 1986 when we were discussing space structure design while developing the Hubble Space Telescope Reaction Wheel Assembly (RWA) Isolation System. Taking a viewpoint contrary to the use of the combination of compliance and damping, Dr. Wilson said, "Give me the weight that you use for damping and I will improve the structure by making it stiffer." My reply was, "Take the shocks off my automobile, use the weight to stiffen the springs, and see if it gives me a better ride." Obviously it would not. This example helped clarify that a combination of compliance and damping can be a better solution for certain needs (in this case vibration suppression) than stiffness alone. It is interesting that, although all of us are familiar with isolation systems when it comes to our automobile (and use them without exception), very few isolation systems (certainly even fewer damped isolation systems) are used in spacecraft. The Hubble Space Telescope RWA Isolation System [1] is, however, one exception. (See Fig. 1.) This automobile story is an introduction to the fact that high stiffness, low weight is

not always correct. This figure of merit is usually further conditioned by the rule: get the first mode an order of magnitude above the control bandwidth; if you can't do that, get it five times the bandwidth. This rather cavalier statement of structural design criteria is used because it characterizes the way system controls engineers sometimes provide requirements to structural design engineers. It is a simplifying process that somewhat decouples active control dynamics from structural dynamics. It makes both engineering jobs easier, but in some cases, it does not work.

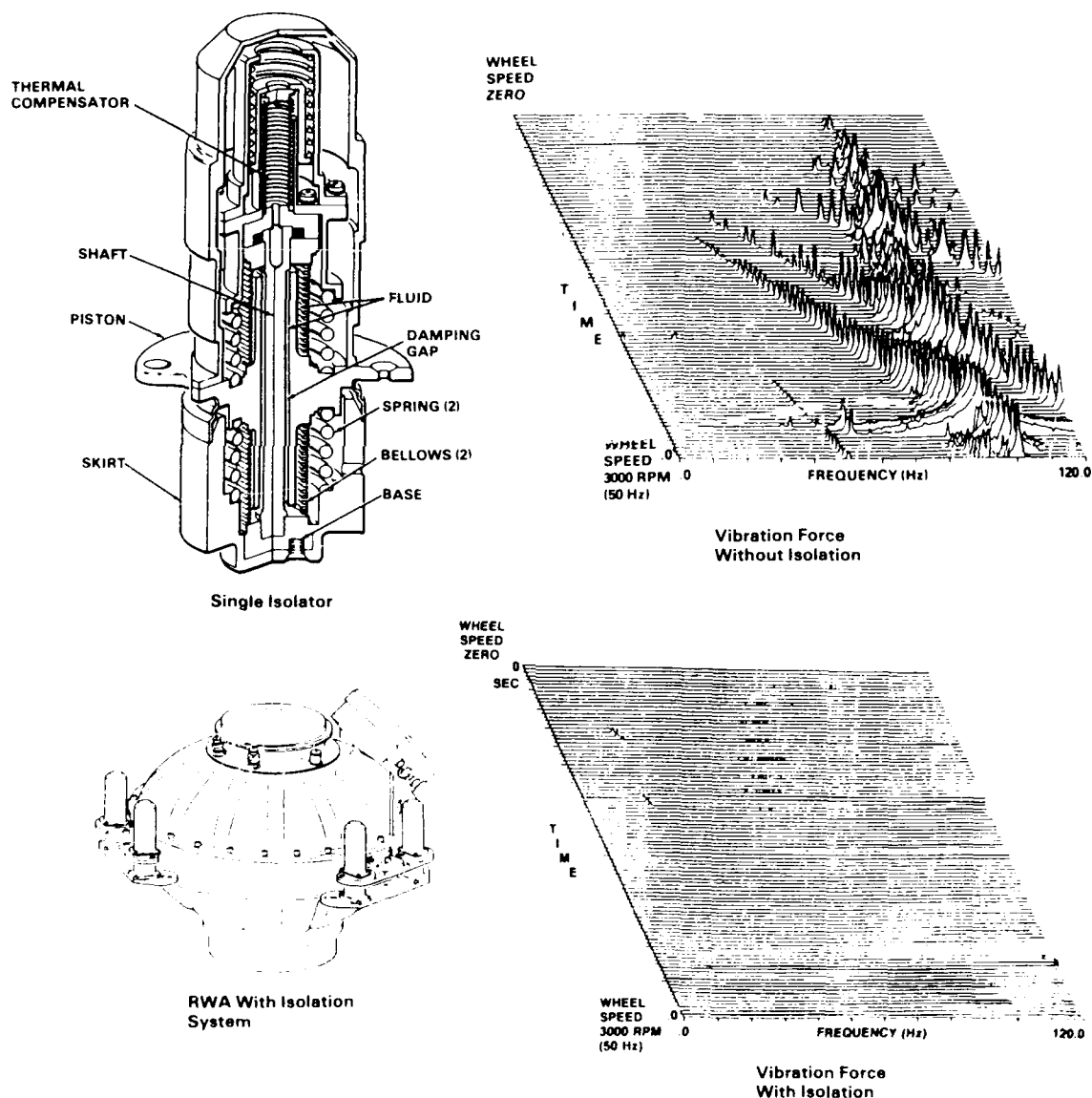


Fig. 1 Hubble space telescope reaction wheel assembly isolation system

DESIGN CRITERIA - STIFFNESS TO WEIGHT

If we were to restate the criteria in a more technically accurate and complete manner, but without any basic change, it might read:

- Stiffness - Structural resonances must be high enough to not affect active control. Generally, an attempt is made to keep all modes a factor of 10 above the control bandwidth. In certain situations, depending on structural damping and other control factors, a factor of 5 may be acceptable.
- Stiffness/Weight - With stiffness satisfied, weight should be minimized.
- Strength - It can generally be assumed that if stiffness requirements are satisfied, strength will have excess margin.

Although for years these criteria have been somewhat of a standard for the industry and have been used quite successfully, they are deficient in at least two aspects:

- They give only casual consideration to damping, and active control failures can result.
- They do not provide the lightest weight or optimum design for applications where structural dynamics and vibration amplification or settling time are important to performance.

The fairly well-known problem of launch vehicle POGO is an example of too little consideration for structural damping. Here, structural vibrations caused by low damping destabilized the active control system. When large, controlled amounts of damping are not built into a structure, joint slip and related phenomena produce significant changes in damping that cannot be accurately predicted. This results in high structural amplifications that create the problem.

Maximizing stiffness to weight will not produce the best design when structural dynamics or vibration settling time directly influence performance. A significant sacrifice in stiffness, and thus a major weight reduction, can be obtained by increasing damping to an optimum level. Pointing accuracy, jitter, tracking, and retarget time are examples of performance requirements that fit into this category. Structural dynamics becomes more of a problem as spacecraft become larger. SDI vehicles and the Space Station are prime examples.

With larger vehicles and more demanding accuracy requirements, the 10-to-1 ratio between bandwidth and structural modes becomes an increasing problem. Bandwidths need to be higher to improve accuracy and speed, and structural modes need to be lower to reduce weight.

Damping, either passive or active, will contribute to a solution of this problem. Active damping can be used to make a soft structure appear to be much stiffer. This enables pointing, tracking and retargeting of a variety of systems to be performed more accurately and more quickly. Passive damping performs the same function. Although it does not increase static stiffness, it increases dynamic stiffness and enables a structure to be maneuvered more quickly and to settle to a given pointing accuracy or velocity jitter in less time. In addition, passive damping reduces the destabilizing influence that a high Q structure has on associated active controls.

Significantly improved performance results when damping can be optimized at very high values. For most designs, this will mean 20 to 50 percent damping. The space industry has given very little consideration to structures with this level of damping because design techniques which provide it have not existed. Research by the Government and private enterprise, however, is changing this situation. Honeywell's DSTRUT system, which uses viscous damping, is a prominent example [2], [3]. (See Fig. 2.) The Air Force and Martin, through the PACOSS program, are using viscoelastic materials to provide similar results. The Air Force and TRW, through the JOSE' program, are developing active damping techniques.

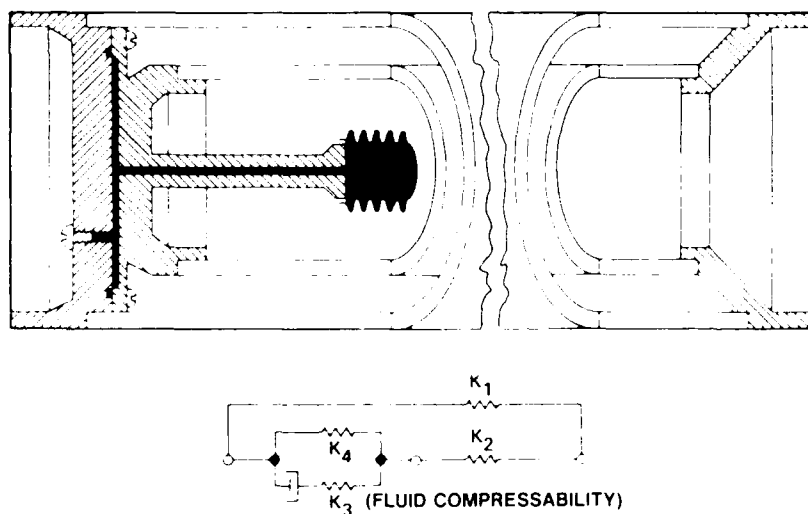


Fig. 2 DSTRUT

DESIGN CRITERIA - STRUCTURE TIME CONSTANT

If we assume that structures can be built with high damping ratios, then we should alter our structural design criteria to account for the effect and to provide a more-accurate basis for design optimization. Consider the following:

- Figure of merit is to minimize the structural time constant
 $(t = Q/\pi f)$ as a function of weight (1)

where Q is the modal amplification factor $= 1/2 \zeta$

ζ is the damping ratio

f is the modal frequency

- Stiffness Adequate stiffness will result from time constant optimization.
- Strength In most applications, this will not dictate major design factors if the time constant is satisfied.

Structural time constant will normally dictate the design and can be optimized as a function of weight or, in other words, become the figure of merit because it is most directly related to the basic purpose of most missions, i.e., how quickly after retargeting will accuracy or jitter limits be obtained and how soon will the function be able to be performed or, after being disturbed, how quickly can the

function be performed? Further, time constant constraint will control both stiffness and damping, but only in product ($T_c = Q/\pi f$). This will (2) allow the two parameters to be optimally selected, affording the potential for better results than those obtained when stiffness is optimized to weight. It will provide a means for evaluating the effect of increased damping as opposed to simply increased stiffness.

The following example shows the importance of the time constant design criterion and how the addition of damping enables stiffness and weight to be reduced. Fig. 3 shows a generic truss structure such as might be used for the Space Station or other large space structures. The frequencies of the first 20 modes are tabulated. The assumed goal of the structure designer is to make the longest system time constant as small as possible. The lowest mode is at 1.55 Hz for the lightly damped structure. If the damping associated with this mode is one percent ($Q = 50$), the time constant will be $1/.01 \times 2 \times \pi \times 1.55 = 10$ seconds. If highly damped truss elements are used [4], the frequency of the first mode

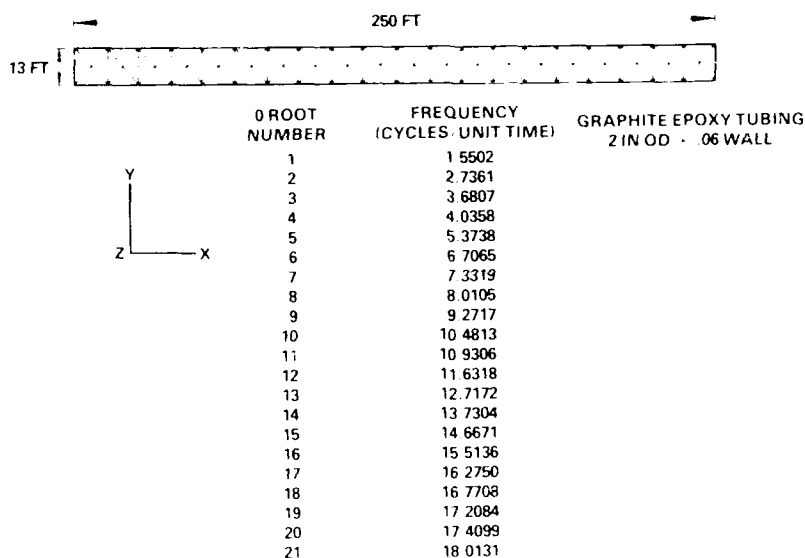


Fig. 3 Generic Truss

would drop to 1.33 Hz, but the time constant will become $1/.175 \times 2 \times \pi \times 1.33 = 0.68$ second. Fig. 4 provides visual comparison between a time constant of 10 seconds and 0.68 second. To achieve the same time constant reduction by stiffening the structure would require raising the first mode to over 27 Hz, an improbable goal. The time constant reductions for the lowest few modes are shown in Fig. 5. Only the lower modes with long time constants are selected.

Fig. 6 shows the effect of high passive damping on structural control considerations. Control bandwidth is often limited by the requirement to provide some level of margin, such as the 6 dB shown at the first structural resonance. Resonances with Q s of 3 and 50 are shown occurring at the same frequency. The very low Q system can implement approximately one order of magnitude higher bandwidth because of the greatly reduced gain at the first resonance. This illustrates that stiffness should not be a fixed value related to control bandwidth and that time constant as a design criterion has the advantage over stiffness to weight. The time constant criterion treats the space structure design problem more appropriately as a dynamics problem than a statics problem. Bandwidth increase will enormously benefit damping which, in turn, should result in major improvements in spacecraft structural design.

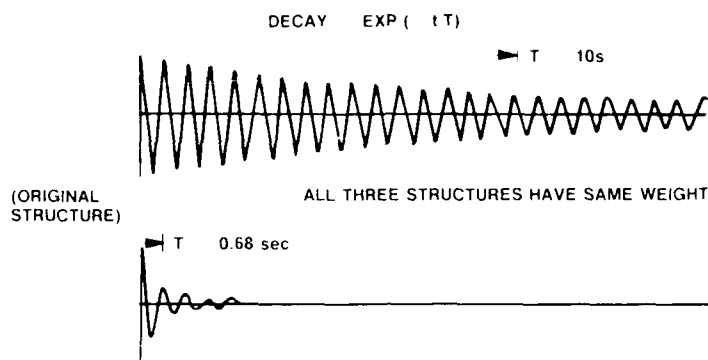


Fig. 4 System time constant is significant figure of merit for settling time

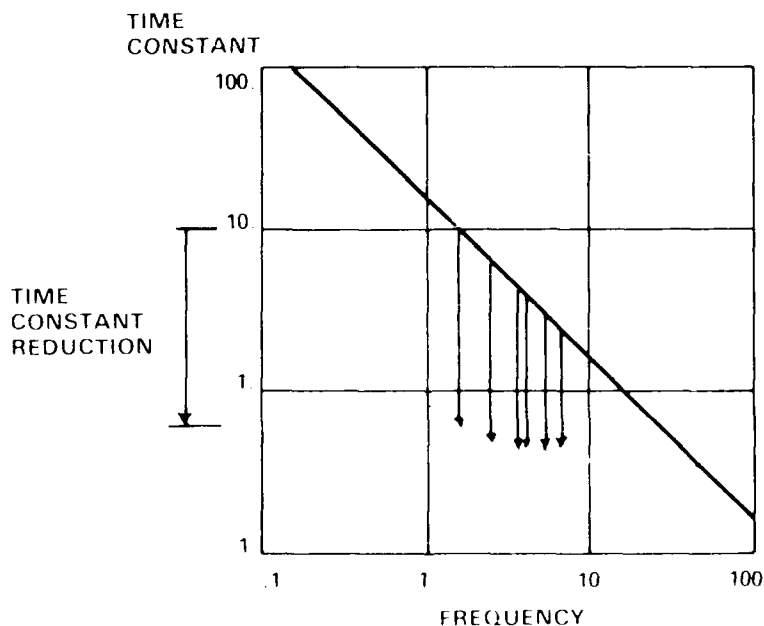


Fig. 5 Time constant reduction for generic truss

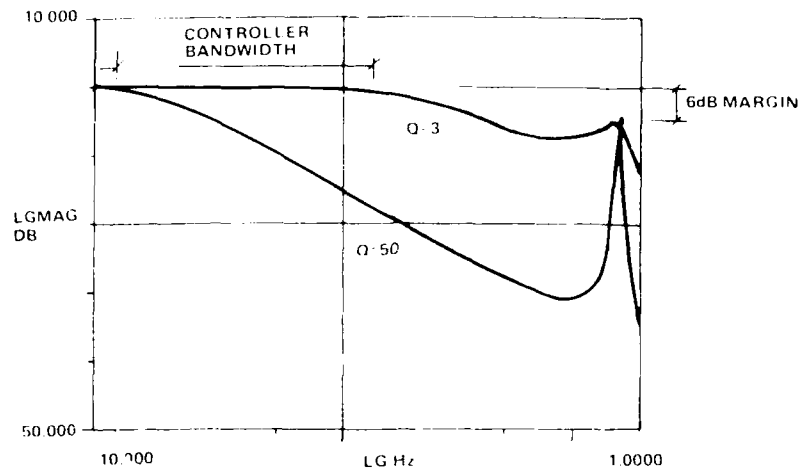


Fig. 6 Bandwidth increase for highly damped structure

A major by-product of damping, other than improvement of operational performance, is launch-load reduction. This helps reduce cost and weight penalties of the various spacecraft components and payloads and allows these elements to be more universally used on spacecraft and launch vehicles. These are sometimes called Soft Launch Systems. Currently, Honeywell is developing a Soft Launch System for Fairchild and NASA Goddard to reduce launch loads transmitted to components being resupplied, via the shuttle, to the Hubble Space Telescope. This system will replace an undamped compliant system. Analyses promise significant improvement in the level of isolation. Other systems are being developed that isolate launch loads from an entire satellite.

CONCLUSION

- 1) Damping should and will be used more often in space structures and payload isolation systems to:
 - Improve payload and spacecraft performance during orbital operation
 - Reduce stiffness requirements to reduce weight
 - Reduce launch vibrations
- 2) Designs with higher levels of damping are more predictable and ensure less interaction between active controls and structural dynamics.
- 3) Structural design criteria should include a structural time constant to better-optimize structural stiffness and damping. This will provide lighter weight designs with more dependable performance.

REFERENCES

1. J. J. Rodden, H. J. Dougherty, L. F. Reschke, M.D. Hasha, L. P. Davis, "Line of Sight Performance Improvement with Reaction Wheel Isolation," AAS Guidance and Control Conference, Keystone, Co., February 1986
2. Dr. James F. Wilson and L. Porter Davis, "Very High Damping in Large Space Structures," ASME Vibrations Conference, Boston, MA, 1987
3. Highly Damped Structure for Reduced Settling Time and Jitter, Sperry Corporation, Aerospace and Marine Group. 1986
4. "Viscous Damped Space Structure for Reduced Jitter," 58th Shock and Vibration Symposium, Huntsville, AL, 1987

AIRBLAST

THE EFFECTS OF HEAVY TUNGSTEN CASINGS ON THE AIRBLAST CHARACTERISTICS OF A CYLINDRICAL CHARGE

Mr. Kirk A. Marchand
Mr. Luis M. Vargas

Southwest Research Institute
Department of Civil Engineering
and Energetic Systems
San Antonio, TX

Mock munitions were developed to simulate the effects of detonation of a special munition in terms of airblast and fragmentation characteristics. Bare and cased charges were developed. Bare charges were designed to be used alone when only airblast loads were required in testing. The developed munitions were designed to be used to provide close in airblast and fragment loadings to protective barrier walls.

INTRODUCTION

The purpose of the overall study of which the work reported herein was an integral part, was to study alternative barrier wall concepts as improvements to the conventional sandbag dividing walls. The alternative barrier walls were to prevent sympathetic detonation of special munitions due to fragmentation hazards require less floor space than current designs, be easily reconfigured, require low maintenance, and be cost effective. Concepts were to be directed towards protection of the group of munitions in the storage compartment, rather than the individual munitions.

Alternative barrier wall concepts were developed by identifying a number of trial systems and subjectively selecting four for further analysis. Four concepts of reasonably different description were selected rather than ones with only minor differences which could evolve during engineering development of the barrier systems. Subjective criteria used in selecting the four candidates included:

- *ability to stop fragment threat*
- *ability to withstand blast loads*
- *ability to be accommodated in existing structures*
- *reduction of floor space used*
- *ease of reconfiguration*
- *low maintenance requirements*
- *low cost*

After reviewing four concepts, the sponsor directed Southwest Research Institute (SwRI) to perform evaluations through four interrelated research areas:

- *Analysis*
- *Preliminary 1/2 scale testing*
- *Configuration design*
- *Replica 1/2 scale testing*

Testing of the barrier concepts included work accomplished in five tasks. The development of a mock munition for barrier testing was done to support the preliminary testing of the barriers. This paper specifically discusses the results of mock munition tests. Mock munitions were developed such that they could represent the detonation of an actual special munition in terms of airblast and fragmentation characteristics. Bare and cased charges were developed. Bare charges

were designed to be used alone when only airblast loads were required in testing. The developed munitions were designed to be used to provide close in airblast and fragment loadings to the barrier walls.

MOCK MUNITION DESIGN AND FABRICATION

Uncased Charge Design and Fabrication

For both the uncased and cased charge tests, an appropriate simulant explosive was used to approximate the 16.5 lbs. of PBX-9404 contained in the actual munition. Based on an equivalence factor of approximately 1.1 for PBX 9404 and pentolite, where

$$1.1 = \frac{\text{explosive energy of PBX 9404}}{\text{explosive energy of Pentolite}} \quad (1)$$

from Reference 1, an equivalent full scale charge consisting of 18.0 lbs. of cast Pentolite was selected. When scaled, the 1/2 scale weight can be determined as

$$W_{scaled} = \frac{W_{actual}}{SF^3} \quad (2)$$

where

W_{scaled} = scaled charge weight

W_{actual} = weight of modeled munition

and

SF = scale factor

The scale factor for the tests performed in this series is 2.0. Thus, the actual weight can be determined for the scaled munition as

$$18.0 / SF^3 = \frac{18.0}{8} = 2.2 \quad (3)$$

and the scaled munitions designed and fabricated for the tests performed consisted of 2.2 pounds of cast Pentolite, with a cast density of approximately .061 lb./in³.

A steel canister was fabricated to a set of scaled dimensions based on the interior description of the actual munition. Based on the density reported above, and the volume of the canister, the dimensions of the scaled munition were selected to be 7.5 in. long by 2.825 in. in diameter, excluding the scaled tungsten exterior case. The mock munition design is shown in Figure 1.

Cased Charge Design and Fabrication

The tungsten case selected for the mock munition was scaled from the actual munition (References 2, 3 and 4) and was chosen because of its high density and relatively high ductility. The dimensions of the case were scaled according to the laws of replica scaling, thus the dimensions scale linearly with the scale factor of 2.0. The material properties of the sintered, swaged and strain aged W91 case (90% pure tungsten) are as follows:

Tungsten content - 90.2 %
 Density - 17.2 gm/cc
 Rockwell Hardness - 26 (c scale)
 Ultimate tensile Strength - 131,000 psi
 Yield strength - 100,400 psi
 Elongation - 12.2 %

This material complies with MIL-T-21014B, Type II, Class I requirements.

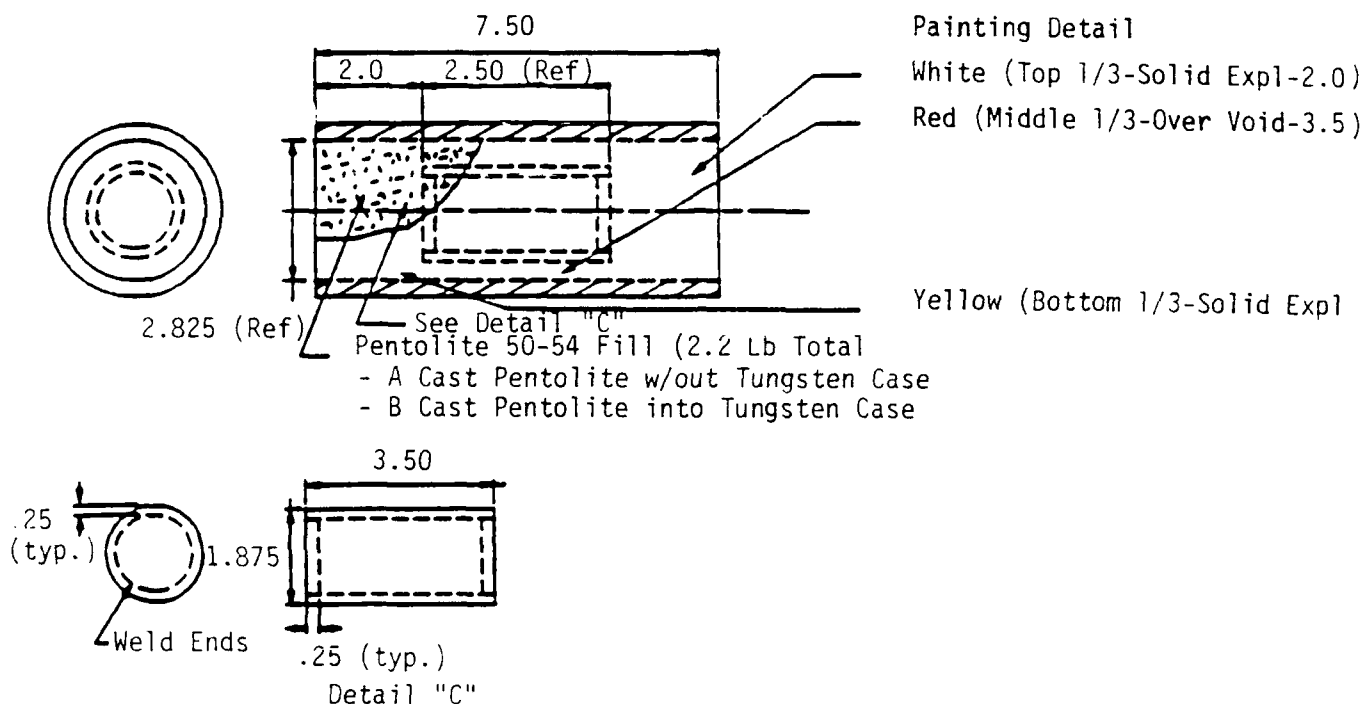


Figure 1. Mock Munition Design.

The uncased and cased weights of the fabricated charges are included as Table 1 below.

Table 1. Measured Weights of Fabricated Explosive Charges

Charge No.	Charge Type	Explosive Weight (lbs.)	Case and Liner Weight (lbs.)	Total Weight (lbs.)
1	Uncased	2.08	1.47	3.558
2	Uncased	2.18	1.47	3.654
3	Uncased	2.13	1.47	3.607
4	Uncased	2.28	1.47	3.747
5	Cased	2.23	10.32	12.550
6	Cased	2.23	10.32	12.553
7	Cased	2.30	10.32	12.630

MOCK MUNITION UNCASD (AIRBLAST ONLY) EQUIVALENCY TESTS

Test Setup and Instrumentation

Three tests were conducted using the uncased 2.2 pound pentolite charges. The charges were placed vertically in a reaction structure at the location and standoff shown in Figures 2a and 2b. Side-on pressure measurements were recorded at standoffs of 15 in. and 38 in. from the charge. All data was recorded on magnetic tape.

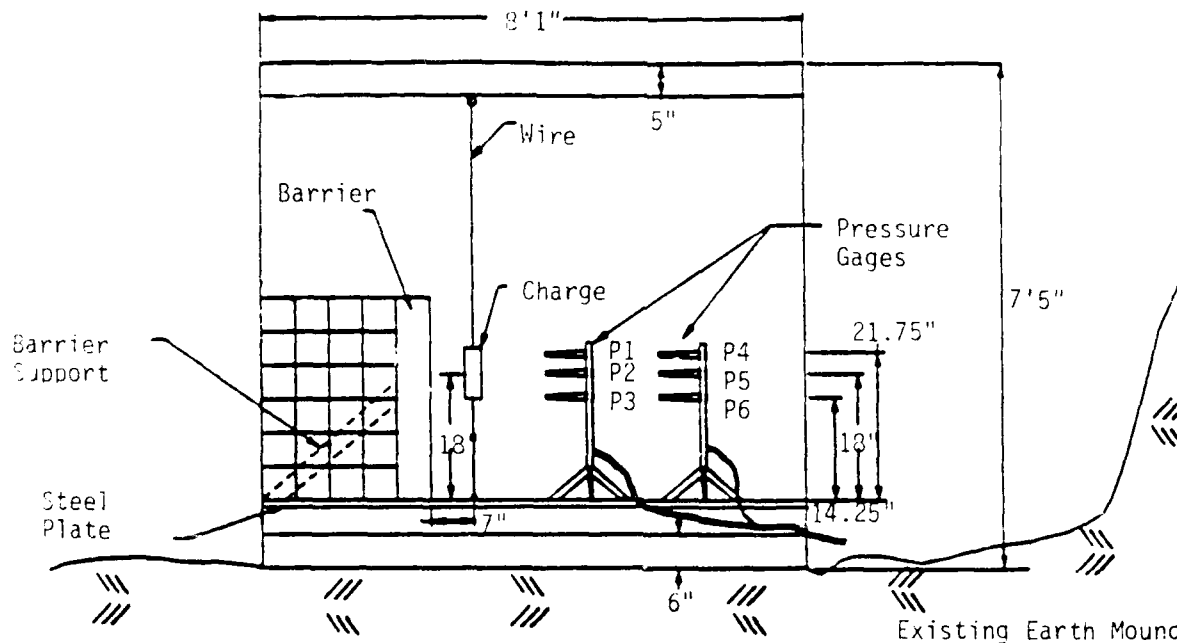


Figure 2a. Schematic of Reaction Structure Showing Barrier and Charge Location - Side View.

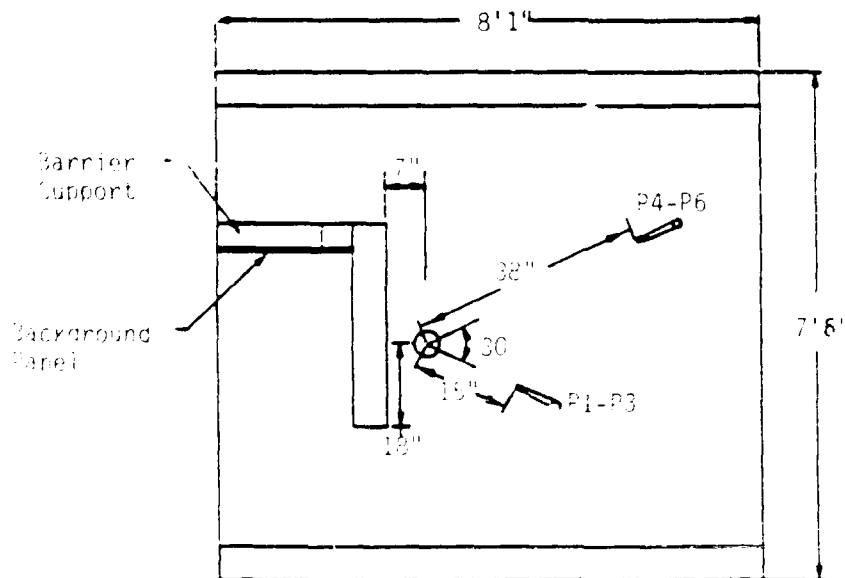


Figure 2b. Schematic of Reaction Structure Showing Barrier and Charge Location - Top View.

PCB model 137A pressure probes were selected for side-on pressure measurements. Two arrays of three transducers were used, one array located 15 in. from the charge centerline, the other 38 in. away from the centerline. PCB model 137A21 transducers, with a 0-5000 psi range were used at the 15 in. standoff, while PCB model 137A11 transducers, with a range of 0-500 psi were used at the 38 in. standoff. The transducer array located at the 38 in. standoff was protected from fragment impact expected during the cased charge tests by including a fragment deflector in the path of expected fragments. Figure 3 shows the detail of the transducer assembly.

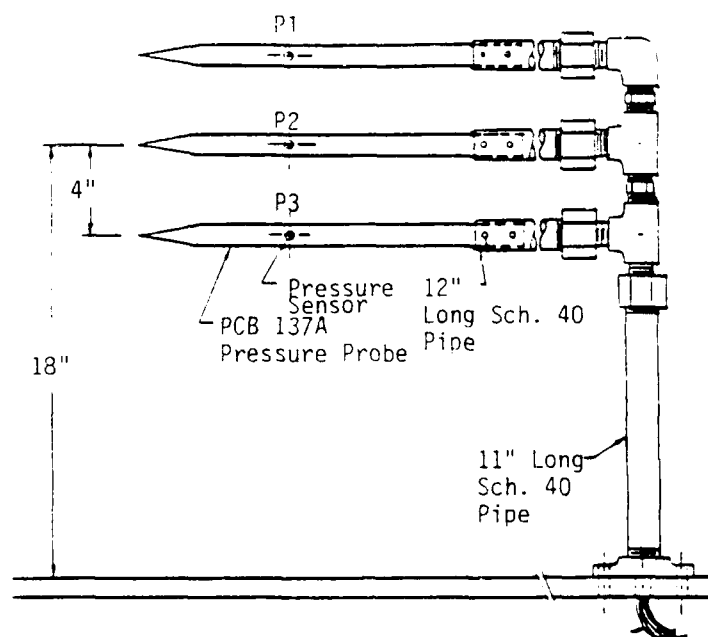


Figure 3. Elevation View of the 15 in. Standoff Transducer Assembly.

Airblast Equivalency Test Results

Pressure Records and Impulse Calculations - The predicted and observed side-on pressures expected for the 15 in. and 38 in. standoffs for the uncased munition tests (2.2 lb. pentolite charge) are presented in Table 2 below:

Table 2. Uncased Charge Tests Predicted and Measured Pressures and Impulses

Test No.	Standoff (in.) (Gage Nos.)	Predicted Side-on Pressure (psi)	Predicted Side-on Impulse (psi-msec)	Observed Side-on Pressure (psi)	Observed Side-on Impulse (psi-msec)
1	15.0 (1-3)	1000	33	360	26
1	38.0 (4-6)	300	26	207	25
2	15.0 (1-3)	1000	33	575	24 (P2,P3)
2	38.0 (4-6)	300	26	222	22

The predicted values of Table 2 were taken from Reference 5 for surface burst high explosive charges. The charge weight of the Pentolite was corrected by the equivalency factor of 1.1, thus a charge weight of $(2.2) \cdot (1.1)$ or 2.42 lbs. of TNT equivalent. The data presented above shows that the observed pressures recorded in the uncased charge tests (for tests Nos. 1 and 2) are approximately 53% less than predicted at the 15 in. standoff, and 29% less than predicted at the 38 in. standoff. The recorded impulses, which are a much more appropriate comparator for explosive energy, are approximately 24% less than predicted for the 15 in. standoff and only 10% less than predicted for the 38 in. standoff. For pressure and impulse comparisons presented here and in later sections, the recorded values just prior to the appearance of the apparent first reflection (from the side walls of the enclosure) were used. The calculated impulses after the arrival of subsequent reflections are increasing and not meaningful in this comparison.

MOCK MUNITION CASED (AIRBLAST AND FRAGMENTS) EQUIVALENCY TESTS

The cased charge tests were identical to the bare charge tests with the exception of the addition of the fragment bundles set up to measure fragment velocity and to recover the fragments for distribution, size and weight data. The cased charges were substituted for the bare charges in these tests. Three cased charge tests were performed.

Test Setup and Instrumentation

Figures 4a and 4b show the test setup for the cased charge tests. Figures 5a and 5b are schematics of the breakscreen and fragment catcher bundle setup. Imprinted paper was used for the breakscreens. The paper was mounted on cutout sheets of 1/2 in. plywood with cutouts for the front 12 screens, located 10 ft. from the charge. Celotex was used to capture fragments.

Fragment Collection and Data Reporting - The Celotex bundles described above were taken apart at the conclusion of each of the 3 tests to observe the trajectory and final location of the impacting fragments. The fragment impacts were numbered and tracked by designating each observed penetration as to its final location. This marking on the Celotex was done every 5 sheets (depending on average fragment penetration depth) so that when a fragment was found, its trajectory and initial entry point would be known. Each fragment found was washed in acetone, weighed and labeled.

Pressure Measurement - The instrumentation setup for these tests was slightly different than that of the uncased tests, as was previously described. The front set of pressure gages (gages P1, P2 and P3) were removed. Additionally, a fragment deflector (vertical steel pipe) was added in front of the gages remaining (P4-P6). Figure 6 shows the transducer setup for the cased charge tests.

Airblast and Fragments Equivalency Test Results

Fragment Mass and Geometry Analysis and Comparison With Predicted and Observed Full Scale Results - Fragments from both tests nos. 5 and 6 were collected, weighed and measured in accordance with the procedure presented in the paragraphs above.

The data gathered was first used to determine the distribution of mass and length to diameter ratio for all fragments collected. For fragments collected after the tests, approximately 60% of the fragments had a mass of less than 1 gram, while the remaining fragments had masses from 1 to 4.9 grams. Fragment L/D was similarly evaluated. About 60% of the fragments were of L/D less than 2, while 30% varied from 2 to 4.0. The fragment data here compares well with the full scale data presented in References 2 and 3, where fragment L/D ranged up to about 4, and the largest fragment mass observed was approximately 40 grams. When the largest fragment observed in the SwRI tests (4.9 grams) is scaled to full scale (mass scales by the (scale factor)³ = $(2)^3 = 8$) the largest fragment mass observed is 39.2 grams, very close to the 40 gram fragment from References 2 and 3.

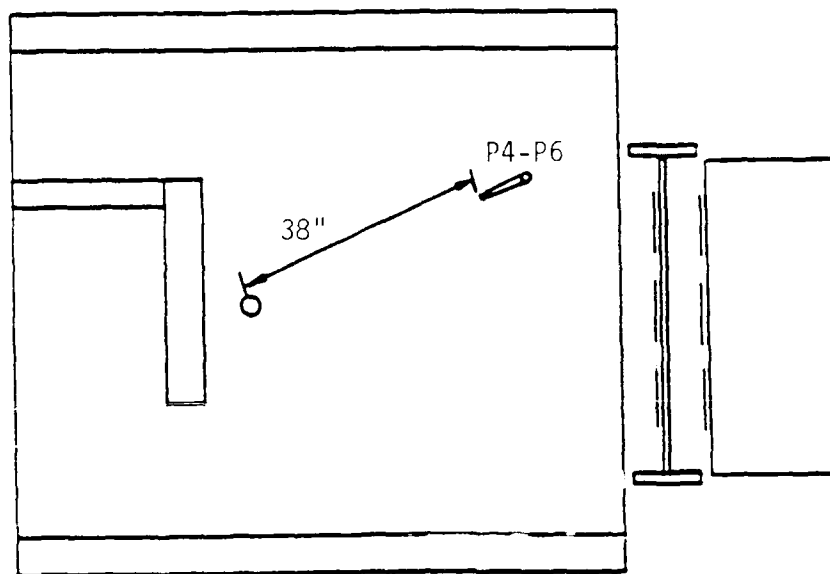


Figure 4a. Test Setup for the Cased Charge Tests - Top View.

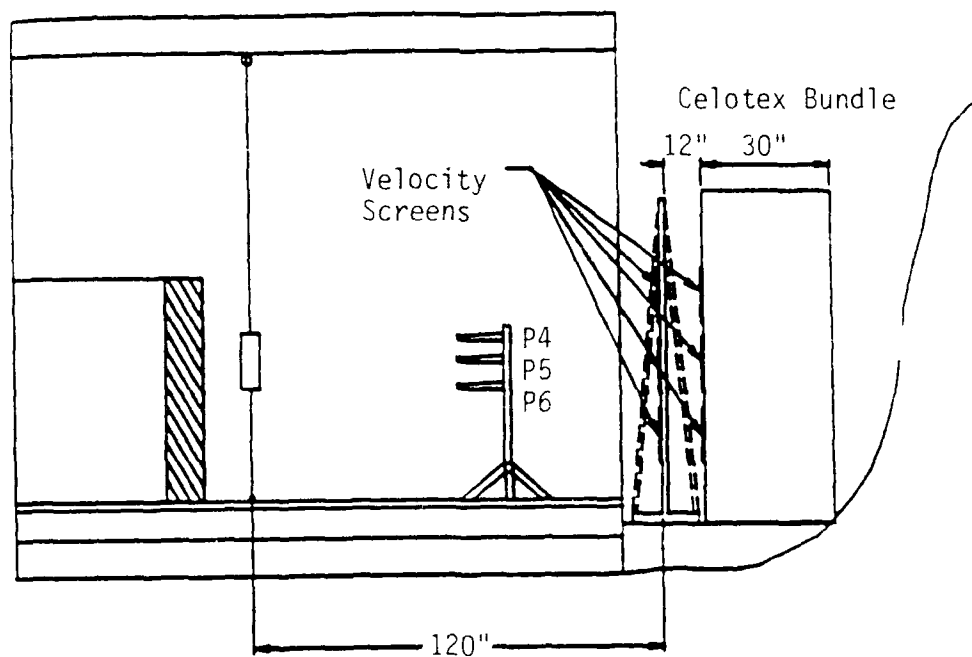


Figure 4b. Test Setup for the Cased Charge Tests - Side View.

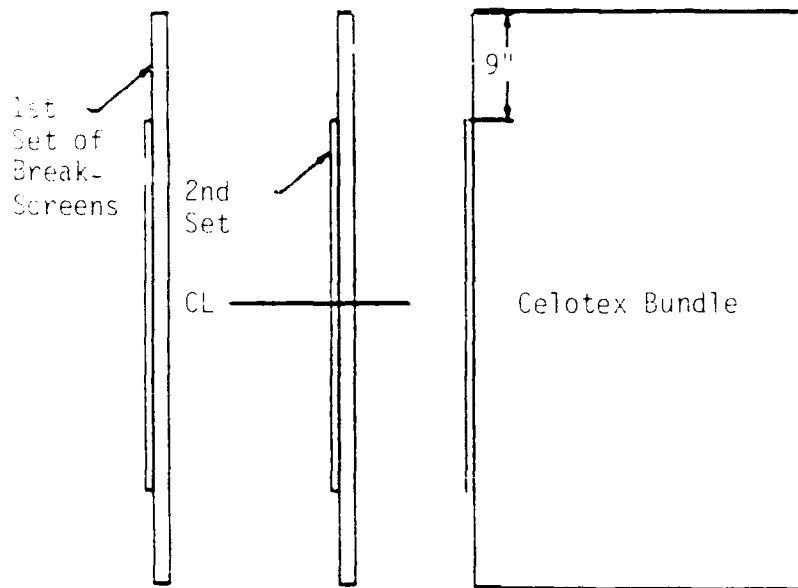


Figure 5a. Breakscreen and Catcher Bundle Schematic - Top View.

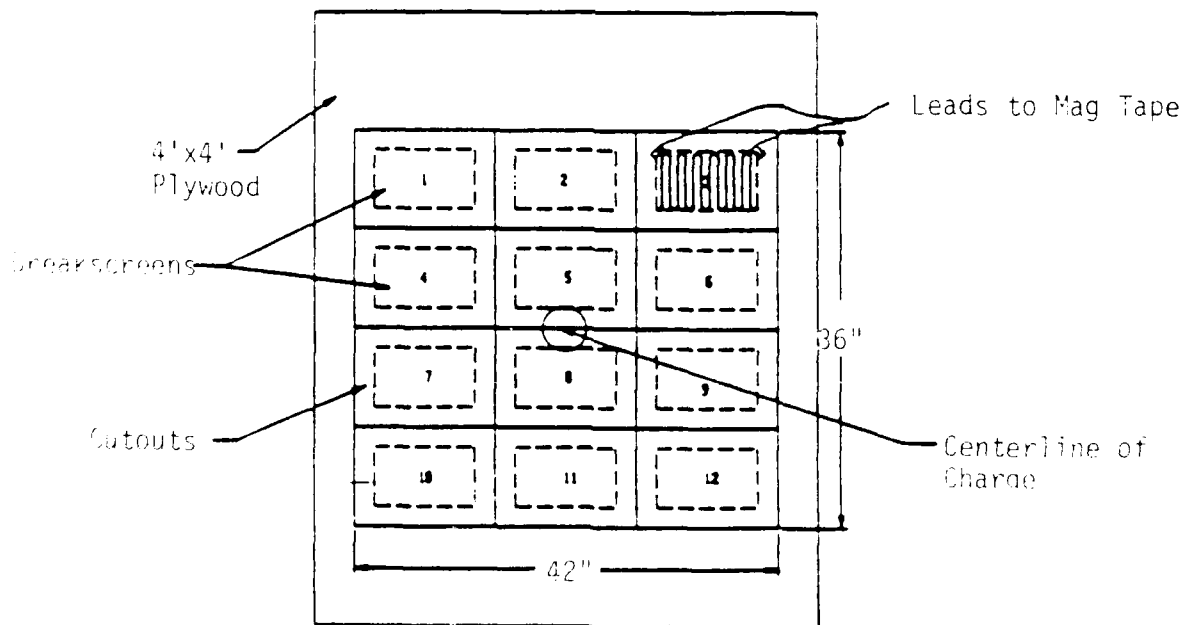


Figure 5b. Breakscreen and Catcher Bundle Schematic - Side View.

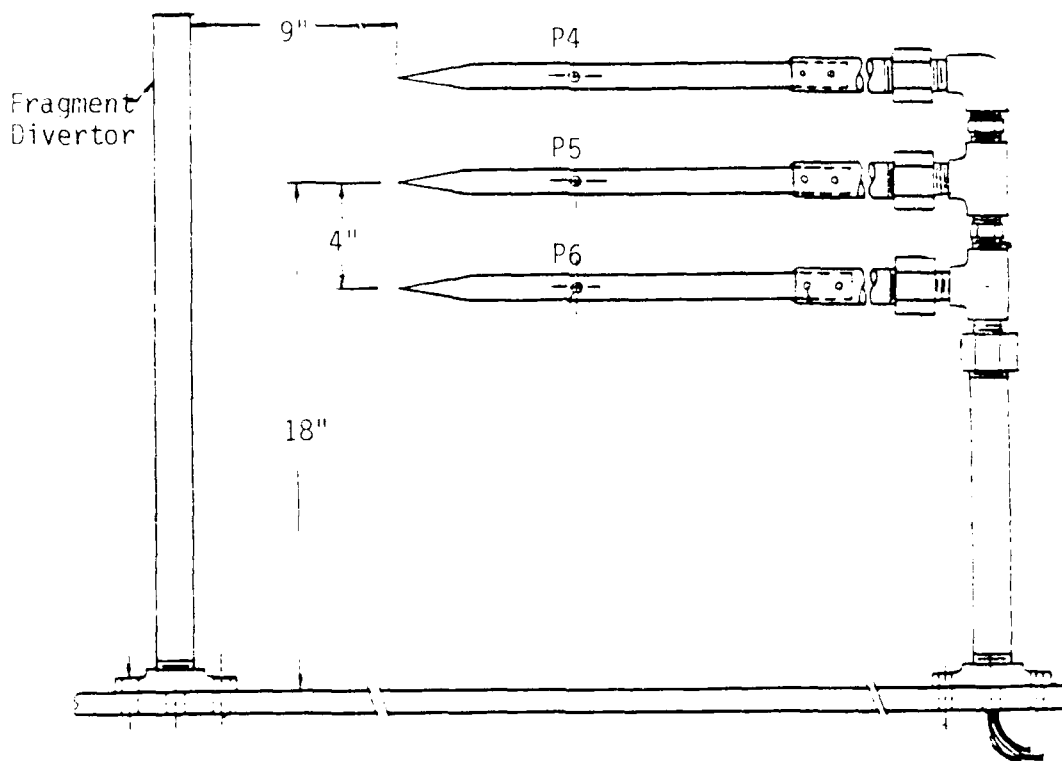


Figure 6. Transducer Setup for the Cased Charge Tests.

Fragment Velocity Analysis and Fragment Load Prediction - Reference 6 gives a relationship for fragment penetration into Celotex as follows:

$$V = 447.40(eA)^{0.75}w^{-0.75} \quad (4)$$

where

- e = penetration depth, in.
- A = presented area, in²
- w = weight of fragment, grains
- V = velocity, ft./sec.

When a velocity for each fragment is known, momentum applied to the target can be calculated and compared with initial assumptions concerning fragment impulse. Combining this calculated momentum with the catcher bundle size additionally allows specific momentum or momentum per unit area (specific fragment impulse on the target) to be calculated.

Figures 7-9 illustrate the distribution of fragment mass, calculated impact velocity and calculated fragment momentum on the Celotex target at the 10.0 ft. standoff distance for tests nos. 5 and 6 respectively.

When these impulses are scaled to full scale (impulse scales as a function of the scale factor, 2.0) they are considerably lower than the initial predicted fragment impulses (which were based on the 40 gram, 4900 fps fragment). The predicted full scale fragment impulse at the 16 in. standoff was 11.95 psi-sec. This is greater than three times the scaled up impulse of (2)*(1.6229) or 3.25 psi-sec predicted from the cased charge tests.

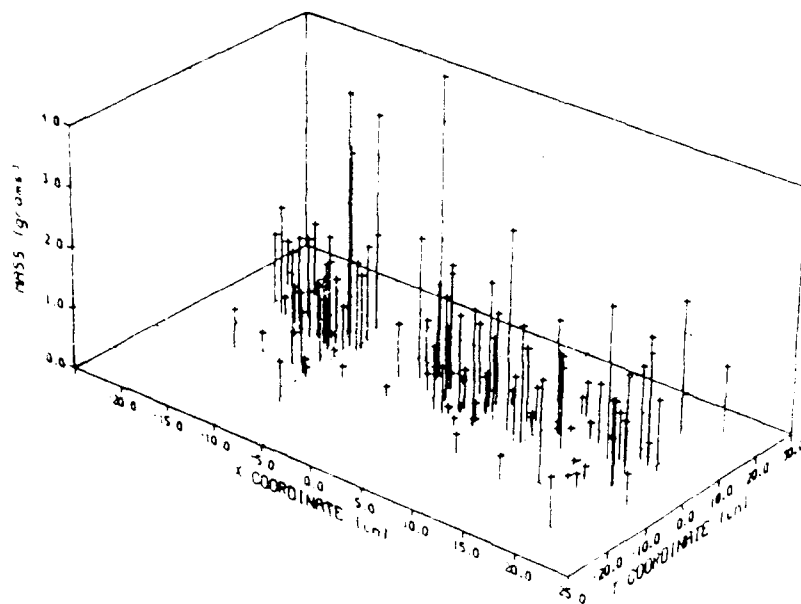


Figure 7. Fragment Mass Versus Impact Location.

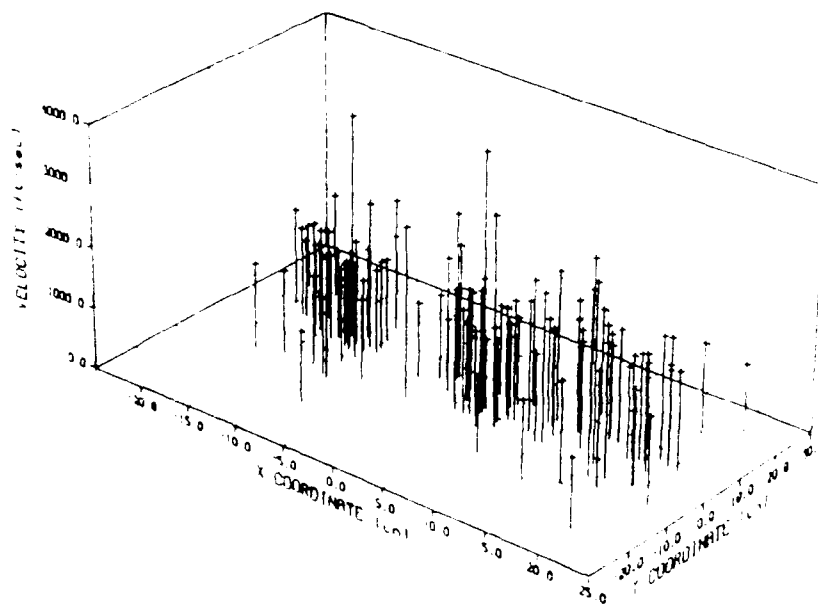


Figure 8. Fragment Impact Velocity Versus Impact Location.

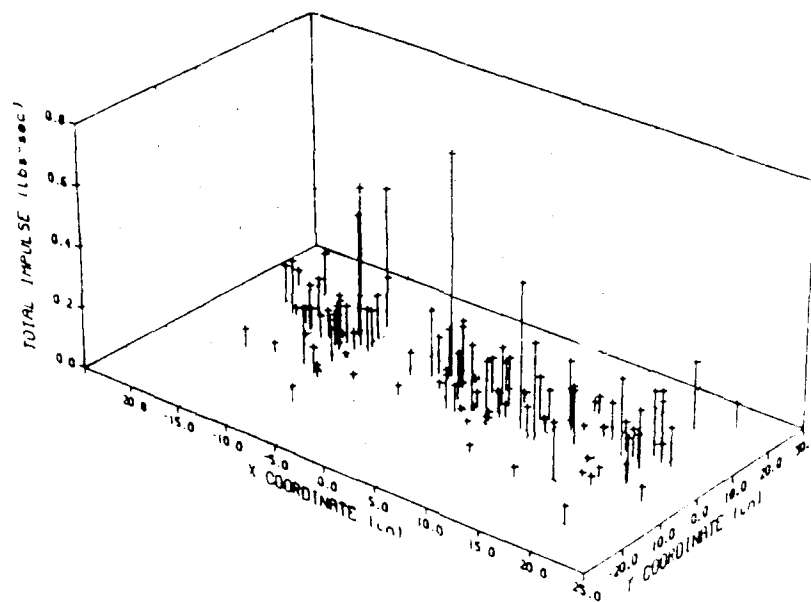


Figure 9. Calculated Fragment Impulse Versus Impact Location.

Fragment Velocity Comparison With Predicted and Observed Full Scale Results - Tests nos. 5 and 6 were instrumented for fragment velocity determination with break screens as described above.

Instrumentation problems prevented velocities recorded in test no. 5 to be reliably use and evaluated. Velocities from test no. 6 were used, however. The magnitude of the highest velocity fragment for each of the cutout sections 1-12 shown in Figure 5 was determined as the difference between time of arrival pulses for each screen divided by the separation distance, equal to 1.0 ft. for each screen. These velocities were then compared with the predicted velocity from equation 4, with the calculated maximum velocities reported above, and with the observed maximum velocity of 4900 ft./sec. from References 2 and 3. The results of this comparison are shown in Table 3

below.

Table 3. Comparison of Measured Fragment Velocities With Calculated and Full Scale Results

Break Screen #	TOA Screen # 1 (ms)	TOA Screen # 2 (ms)	Measured Fragment Velocity (fps)	THOR Fragment Velocity (fps)	Gurney Maximum Fragment Velocity (fps)
1	2.950	3.200	4000	3657	5300
2	2.850	3.187	2963	2731	5300
3	3.180	3.090	----	2844	5300
4	2.625	2.900	3604	2399	5300
5	2.438	2.873	2301	2171	5300
6	2.650	3.060	2439	2451	5300
7	2.625	2.920	2439	1559	5300
8	2.625	2.625	----	3427	5300
9	2.893	3.188	3396	2999	5300
10	3.375	3.780	2469	2038	5300
11	3.000	3.188	5333	----	5300
12	3.158	3.600	2260	1873	5300

Table 3 shows that the recorded velocities compare favorably with the calculated velocities determined from equation 4. The 5300 ft./sec. maximum predicted velocity of the fragment is very close to the maximum 5333 ft./sec. velocity measured in test no. 6 on panel no. 11. These velocities also compare quite favorably with the 4900 ft./sec. velocity measured from radiographs as reported in References 2 and 3.

Pressure Records and Impulse Calculations - As reported above, side-on airblast measurements were made for tests nos. 5 and 6 with the three transducers located at the 38 in. standoff.

The important comparisons to be made in the uncased and cased charge tests are the pressures and impulses recorded. Transducer records from locations 4-6 in test nos. 1 and 2 and 5 and 6 were evaluated to compare peak side-on pressures and calculated impulses derived from direct time integration of the pressure records. Table 4 below presents the results of the comparison.

Table 4. Measured Pressures and Impulse for Uncased and Cased Charge Tests

Location	Uncased Test Avg. Side-on Pressure (psi)	Uncased Test Avg. Impulse (psi-msec)	Cased Test Avg. Side-on Pressure (psi)	Cased Test Avg. Impulse (psi-msec)
4	111	23	159	10
5	260	25	242	17
6	270	23	95	12

Impulse Reduction and Time-of-Arrival Discrepancies and Possible Explanation - It can be observed in Table 4 above, that a reduction in recorded side-on impulse is seen for the cased charge tests. Additionally, a significant difference in arrival time of the pressure front can be observed between the cased and uncased tests. For test no. 1 at location 5 the pulse arrives at the 38.0 in. standoff gage at 0.32 ms. For test no. 6 at location 5 the pulse is seen to arrive approximately 0.43 ms later, or at a time of 0.75 ms.

The pressure records described above suggest that some reduction of impulse and delay of fragment arrival exists due to the case expansion and fracture in the cased charge tests. Computational modeling of explosive filled cylinders as reported by Anderson et al. in Reference 7 indicates that gas leakage from cracks forming in a munition case begins to occur at an expansion ratio for the case (radius/original radius) of about 1.75. At this expansion ratio the case velocity is seen to be about 90% of its final velocity.

A time duration for this expansion and case rupture, which would equate to part of the pulse arrival delay since the pressure front does not form until after case rupture, can be calculated. If a median fragment velocity is selected from Table 3 as 3000 ft./sec., a delay time can be defined as follows:

$$\frac{(r/r_0)r_0}{12v_{avg.}} = \text{delay time} \quad (5)$$

$$\frac{1.75(2.825/2.0)}{(3000/2)(12)} = 0.000137 \text{ sec.}$$

where:

r_0 = original radius = 2.825 in.

r = expanded radius

$v_{avg.}$ = average velocity during expansion = (3000/2) ft./sec.

Thus, 0.14 ms of the observed 0.43 ms delay in pulse arrival can be attributed to case rupture. The remainder of the delay can be postulated to be a function of the reduced intensity of the pressure wave front due to the use of some portion of the initial available energy to rupture the case. This reduced wave front intensity can also be thought of as a reduced effective charge weight in the munition. A reduced charge would have a later time of arrival and a reduced side-on impulse as compared to the full 2.2 lb. uncased charge. Using the airblast curves of Reference 5 and the equivalence factor of 1.1 used in the comparisons of preceding paragraphs, a reduced charge can be postulated. If a 40% reduction in charge weight is assumed, an equivalent weight of 1.45 lb. of TNT results. From Reference 5 the side-on impulse expected and time of arrival at the 38.0 in. standoff are:

Predicted side-on impulse = 21 psi-ms

Predicted time of arrival = 0.57 ms

The predicted impulse of 21 psi-ms, when reduced by the 10-15% factor seen in the comparison of predicted to observed results for the uncased tests at the 38.0 in standoff, is 19 psi-ms which is close to an observed location 5 average for the cased charge tests. Also, the difference between the predicted arrival time of 0.57 ms for the reduced charge and the 0.32 ms arrival observed for the uncased full charge is .25 ms, which, when added to the expected rupture delay of 0.14 ms is:

$$(0.57 - 0.32) + 0.14 = .39 \text{ ms}$$

which is close to the observed delay of 0.42 ms.

Thus, a reduction in the equivalent uncased charge can be postulated when considering airblast equivalence of the heavily cased and uncased charges.

CONCLUSIONS

The data and analysis reported herein show that scale modeling of heavily cased explosive charges can adequately replicate the fragment and airblast loads produced by a full scale munition. This capability can be used to expediently and efficiently test structures subjected to these loads.

Additionally, the airblast from a heavily cased munition has been studied and a procedure has been developed to assess the reduction in blast pressure and impulse caused by the heavy case.

REFERENCES

1. Dobratz, B.M., Crawford, P.C., "LLNL Explosives Handbook," Lawrence Livermore National Laboratory, January 1985.
2. Wood, C.A., ARRAD-1, LLNL Document No. DOPJ83-139, April 1, 1983. (Secret)
3. Wood, C.A., ARRAD-2, LLNL Document No. DOPJ-85-009, August 12, 1985. (Secret)
4. Wood, C.A., "CERL-2, A Further Series of Gun Tests on Selected Armor Samples with the Representative Projectile (RP)," S-05-056, August 14, 1985. (Confidential)
5. Baylot, J. T., et al., "Fundamentals of Protective Design for Conventional Weapons," Structures Laboratory, US Army Engineer Waterways Experiment Station, Vicksburg, MS, p. 149, 1985.
6. "Project THOR Report No. 25-A Comparison of Various Materials in Their Resistance to Perforation by Steel Fragments; Empirical Relationships," Johns Hopkins University, Baltimore, MD, 1956.
7. Anderson, C.E., Predebon, W.W. and Karpp, R.R., "Computational Modeling of Explosive Filled Cylinders," International Journal of Engineering Science, No. 12, pp. 1317-1330, 1985.